Interactions involved in the permeation and distribution of ions and biomolecules inside charged microgels

TESIS DOCTORAL

Programa de Doctorado en Física y Ciencias del Espacio

Irene Adroher Benítez

Directores

Arturo Moncho Jordá
Gerardo Odriozola Prego

Grupo de Física de Fluidos y Biocoloides
Departamento de Física Aplicada
Universidad de Granada
2017

La doctoranda / *The doctoral candidate* Irene Adroher Benítez, y los directores de la tesis / *and the thesis supervisors* Arturo Moncho Jordá y Gerardo Odriozola Prego,

Garantizamos, al firmar esta tesis doctoral, que el trabajo ha sido realizado por la doctoranda bajo la dirección de los directores de la tesis y hasta donde nuestro conocimiento alcanza, en la realización del trabajo, se han respetado los derechos de otros autores a ser citados, cuando se han utilizado sus resultados o publicaciones.

Guarantee, by signing this doctoral thesis, that the work has been done by the doctoral candidate under the direction of the thesis supervisors and, as far as our knowledge reaches, in the performance of the work, the rights of other authors to be cited (when their results or publications have been used) have been respected.

Granada, a 24 de febrero de 2017,

Directores de la Tesis / *Thesis supervisors*:

Dr. Arturo Moncho Jordá
Prof. Titular de Universidad
Grupo de Física de Fluidos y Biocoloides
Departamento de Física Aplicada
Universidad de Granada

Dr. Gerardo Odriozola Prego
Prof. Titular de Universidad
Área de Física de Procesos Irreversibles
Div. Ciencias Básicas e Ingeniería
Universidad Autónoma Metropolitana
(CD de México, Mexico)

Doctoranda / *Doctoral candidate*:

Irene Adroher Benítez

A mi padre, mi madre y mi hermana,
por estar siempre ahí.

Contents

List of papers

The results and discussion section of this thesis is presented as an ensemble of the research papers in which I have worked as a doctoral candidate. The following publications are sorted according to their content:

Paper I   **Role of steric interactions on the ionic permeation inside charged microgels: theory and simulations.**
I. Adroher-Benítez, S. Ahualli, A. Martín-Molina, M. Quesada-Pérez, and A. Moncho-Jordá.
Macromolecules **2015**, *48*, 4645–4656.

Paper II   **Competition between excluded-volume and electrostatic interactions on nanogel swelling: effect of the counterion valence and nanogel charge.**
I. Adroher-Benítez, A. Martín-Molina, S. Ahualli, G. Odriozola, M. Quesada-Pérez, and A. Moncho-Jordá.
Phys. Chem. Chem. Phys. **2017**, DOI: 10.1039/C6CP08683G

Paper III   **The effect of electrosteric interactions on the effective charge of thermoresponsive ionic microgels: theory and experiments.**
I. Adroher-Benítez, S. Ahualli, D. Bastos-González, J. Ramos, J. Forcada, and A. Moncho-Jordá.
J. Polym. Sci. Part B: Polym. Phys. **2016**, *54*, 2038–2049.

Paper IV   **Conformation change of a poly(N-isopropylacrylamide) membrane: molecular dynamics.**
I. Adroher-Benítez, A. Moncho-Jordá and G. Odriozola.
Submitted to *J. Chem. Phys.*

Paper V   **Sorption and spatial distribution of protein globules in charged hydrogel particles.**
I. Adroher-Benítez, A. Moncho-Jordá and J. Dzubiella.
Submitted to *Langmuir*.

Paper VI   **Thermoresponsive microgels at the air-water interface: the impact of the swelling state on interfacial conformation.**
J. Maldonado-Valderrama, T. del Castillo-Santaella, I. Adroher-Benítez, A. Moncho-Jordá, and A. Martín-Molina.
Soft Matter **2017**, *13*, 230–238.

My contribution to each of the papers above was as follows:

Paper I   I developed the computational method to use the simulations output as an input for the integral equations and I carried out all the theoretical calculations, although I did not performed the Monte Carlo simulations. I was highly involved in the interpretation of data, and I significantly contributed to the writing and revision of the paper.

Paper II   As in Paper I, simulations were carried out by other members of the team and I was responsible for the theoretical calculations. I highly contributed to the presentation and discussion of the results and to the revision of the manuscript.

Paper III   I carried out the synthesis of the PVCL microgels, although I did not designed the synthesis method. I performed all the diameter and electrophoretic mobility measurements. I did not make the calculations to obtain the effective charge from the experimental data, but I carried out the numerical resolution of the OZ equations to fit the data and to obtain the theoretical effective charge. I actively participated in the discussion of the results, and I was highly involved in the writing and revision of the paper.

Paper IV I help to carry out the Molecular Dynamics simulations, although the oligomer and membrane systems were developed by my coworkers. I participated in the discussion of the results and in the revision of the manuscript.

Paper V I performed all the calculations needed to obtain the PMF and the state diagrams, although the model for the effective interaction Hamiltonian was proposed by my coworkers and other authors. I highly contributed to the interpretation and discussion of the results and I was significantly involved in the writing of the manuscript.

Paper VI I made the synthesis and characterization of the PVCL microgels, as in Paper III. I also performed the experimental measurements of the Langmuir monolayers, while the rest of experimental work was developed by other members of the team. I slightly contributed to the discussion, writing and revision of the paper.

According to the University of Granada rules for the doctoral programs, the following papers are not included in this thesis because they had been published before I obtained the Master's Degree:

Paper **Ion permeation inside microgel particles induced by specific interactions: from charge inversion to overcharging.**
A. Moncho-Jordá and I. Adroher-Benítez.
Soft Matter **2014**, *10*, 5810–5823.

Paper **Size-exclusion partitioning of neutral solutes in crosslinked polymer networks: A Monte Carlo simulation study.**
M. Quesada-Pérez, I. Adroher-Benítez, and J. A. Maroto-Centeno.
J. Chem. Phys. **2014**, *140*, 204910–7.

Abbreviations

AA	Acrylic acid
AFM	Atomic Force Microscopy
DLS	Dynamic Light Scattering
H_2O DDI	Double deionized water
HNC	Hypernetted-chain approximation
IUPAC	International Union of Pure and Applied Chemistry
KPS	Potassium peroxydisulfate
LCST	Lower Critical Solution Temperature
MBA	N,N'-methylenebis(acrylamide)
MC	Monte Carlo (simulations)
MD	Molecular Dynamics (simulations)
MSA	Mean-spherical approximation
$NaHCO_3$	Sodium bicarbonate
OZ	Ornstein-Zernike (formalism)
PB	Poisson-Boltzmann (formalism)
PEGDA	Poly(ethylene glycol) diacrylate
PNIPAM	Poly(N-isopropylacrylamide)
PVCL	Poly(N-vinylcaprolactam)
PY	Percus-Yevik approximation
SDS	Sodium dodecyl sulfate
SEM	Scanning Electron Microscopy
TEM	Transmission Electron Microscopy
VPTT	Volume Phase Transition Temperature

Introduction

1

Background

In 1949 Baker described a group of polybutadiene particles of nanometric size with the ability to swell in organic solvents in a paper entitled "Microgel, a new macromolecule"[1]. This is the first reported use of the term *microgel*, although it is thought that Staudinger and Husemann were the first to prepare microgel particles in the decade of the 1930's[2,3]. In contrast to the vague origin of these particles, nowadays microgels are well stablished responsive materials in the field of polymer science. The aim of this chapter is to present a brief description of microgel suspensions, as well as their main features and applications within the framework of this thesis.

1.1 Microgel suspensions

According to the IUPAC, a *gel* is a polymer network that is expanded throughout its whole volume by a fluid[4]. This is a familiar term in everyday life, given the strong presence of gels in cosmetic, food or pharmaceutical products. The term *microgel*, in contrast, is considerably unknown for the society, despite its promising applications. As its own name suggests, a microgel is a "small gel", that is, a polymer network with the entity of particle. Specifically, a particle which size falls within the colloidal range, between 10 and 1000 nm[5]. If their equivalent diameter is smaller than 100 nm, they are usually called *nanogels*[4]. A precise definition was also given by Pelton and Hoare, who described microgels as "colloidal dispersions of gel particles". As colloidal particles, microgels are dispersed in a solvent, usually forming stable solutions, although several fac-

tors can made them to aggregate or to form different structures[5]. The solvent may be organic, such as aromatic solvents (e.g. toluene[6]), or inorganic, such as water[7]. In this thesis we have focused on aqueous microgels, also known as *hydrogels*.

A picture of microgels at different length scales can be observed in Figure 1.1. The network structure of a microgel particle is formed by crosslinked polymer chains, which are molecules of high relative molecular mass made of the repetition of molecules of low relative molecular mass, called monomers. If some of the monomers have ionizable or ionic groups, then they form polyelectrolytes. A microgel made of polyelectrolytes is called *ionic* or *charged microgel*. In most of the cases, polymers in the microgel network are chemically crosslinked by covalent bonds. However, the network may also be formed through the physical aggregation of polymer chains, caused by entanglements, hydrogen bonds, crystallization, helix formation, complexation etc. The resulting microgels are termed physical or reversible microgels[4,8]. Either chemical or physical, the polymer network is a stable structure, which differentiates microgels from other colloidal particles such as micelles[5]. Even though polymer elasticity allows the particles to be deformed and compressed, two microgels cannot totally overlap due to the excluded-volume repulsion exerted by the polymer chains, that is, they are always distinguishable particles[9].
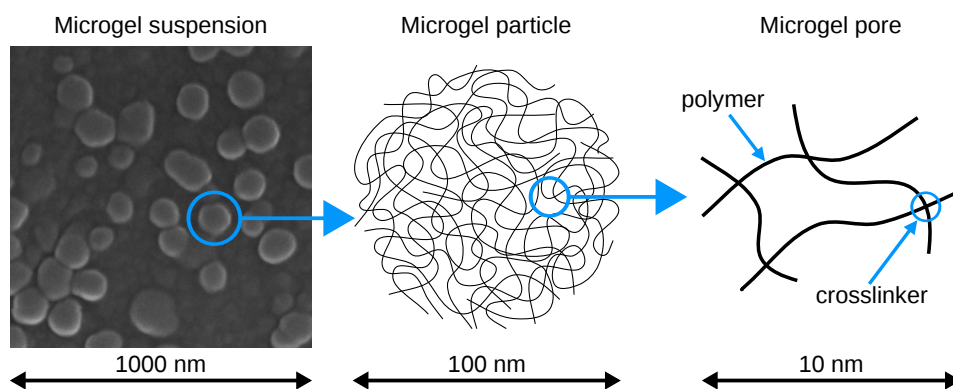
Figure 1.1: Microgels observed at different length scales. Left picture is a SEM micrograph of the PVCL microgels studied in Paper III. In this image particle structure is slightly deformed due to solvent evaporation.

But why has the scientific community put their attention towards microgels? The reason is that these particles join the main properties of macrogels with very useful features of colloidal suspensions[5]. The most important is that

microgels can absorb large amounts of solvent, so they can swell or shrink, drastically changing their size in response to many parameters such as temperature, pH, salt concentration, light, external fields, and specific solutes like glucose or other biomolecules[3,7,10–13]. This versatility allows microgels to be called "smart" or "responsive" materials. Event though macroscopic gels are also sensitive to external stimuli[14], microgels present some other advantages that made them suitable for many applications. First, they can swell eight orders of magnitude faster than macrogels, thanks to their high surface-volume ratio[15]. Moreover, as colloidal suspensions microgels are able to flow like liquids. The flow is roughly independent of the amount of crosslinkers in the microgel network, in contrast with macrogels, which can only flow if their crosslink density is low enough[5]. In addition, different structures may be formed by assembling microgel particles. As will be shown in Paper VI, the behaviour of microgel monolayers at air-water[16,17], oil-water[18,19], and other interfaces[20] has gained attention in recent years, and also other microgel 3D assemblies such as crystals[21,22], thin films and multilayers[23,24] have been explored by many researchers.

1.1.1 Thermoresponsive microgels

In this thesis we have paid particular attention to thermoresponsive aqueous microgels, formed by polymers that exhibit a lower critical solution temperature (LCST) above which they become hydrophobic. In Figure 1.2 we show an example of the volume change of these microgels. At temperatures below the LCST, hydrogen bonds are formed between water and the polymers, leading to an increase of the particle size. Even though the amount of crosslinks in the polymer network limits the microgel swelling degree, these particles can contain up to 99% of their volume of water in the swollen state.[3] In this situation in which polymer chains are hydrophilic, water is referred as a "good solvent". In contrast, when the system reaches the LCST, the microgel experiences a volume phase transition and the hydrogen bonds with water are disrupted as temperature increases, converting water in a "poor solvent" and leading to chain collapse[25]. Hence, above the LSCT thermoresponsive microgels shrink and expel water from their inside, though there is always some amount of solvent inside the particle. The proportion of microgel volume occupied by water in the collapsed state causes controversy among scientists because microgel molecular weight and internal structure is difficult to measure and so the exact water content inside it[5,26].

Most of the aqueous microgels reported in literature are based on LSCT polymers, since the techniques for their synthesis and characterization have
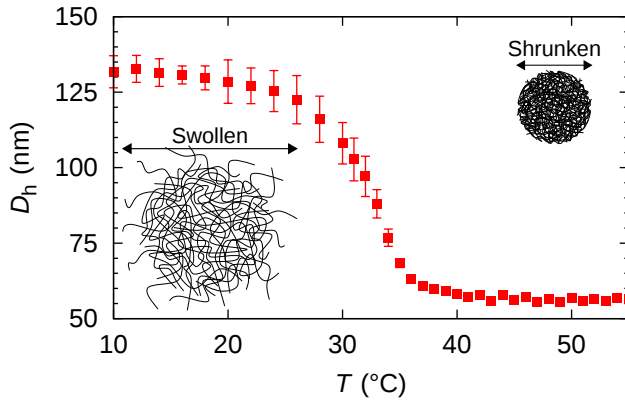
Figure 1.2: Hydrodynamic diameter of a PVCL thermoresponsive microgel as a function of temperature. Here we can observe the volume phase transition from the swollen state (good solvent) to the shrunken or collapsed state (poor solvent).

◀ ▶ ◀ ▶
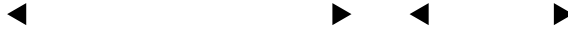
been well established for decades. In particular, the most studied microgels are known as PNIPAM, formed by poly(N-isopropylacrylamide) polymers. The first PNIPAM microgel was synthesized by Pelton and Chibante in 1978, though they could not publish their work until 1986[9,27]. A large amount of synthesis strategies, tuning and characterization have been published ever since[28–32]. Nowadays it is considered a model system in the field of polymer science, what results really useful for developing and testing theoretical and computational models for microgels[33–35], as will be shown later in the works presented in this thesis.

Another interesting family of thermoresponsive microgels that has been gaining attention recently is based in poly(N-vinylcaprolactam) polymers, abbreviated as PVCL. First synthesized in 1999 by Gao et al.[36], the strong point of these particles is their biocompatibility[37,38], which makes them available for biotechnological applications, as will be shown in section 1.2. Unlike PNIPAM, swelling behaviour of PVCL microgels depends on the polymer chain length and molecular weight[39]. Even though this feature may diminish our control over the processes of synthesis and characterization, it allows to tailor the microgel volume phase transition temperature (VPTT), bringing new possibilities of applications.

1.1.2 Ionic microgels in electrolyte solutions

Many microgels, especially those designed for biotechnological applications, are ionic microgels, so they bear an electric bare charge due to the polyelectrolytes that compound the microgel network. When such microgels are immersed in electrolyte solutions, the mobile ions of the salt permeate inside the porous network and distribute around the particle, creating the electric double layer. The swelling behaviour of these microgels results from the joint effect of electrostatic, elastic and solvent-induced interactions[5]. Indeed, the equilibrium swelling may be strongly affected by the electrolyte concentration and the valence of the ions present in the solution[28,40]. Furthermore, as will be shown in Papers I and II, for highly charged microgels, variations in the local concentration of counterions may lead to internal heterogeneities in the polymer structure[41,42].

The presence of electrolyte also determines the effective interaction between a microgel and other particles of the colloidal suspension, either microgels or other solutes. This is due to the charge screening caused by the oppositely charged counterions that diffuse through microgel pores, which can be freely moving or condensated inside the polymer network[43], as will be shown in Paper III. The overall screening is usually characterized by the microgel effective charge, which provides a global estimation of the charge that other microgel or incoming solute feels when approaching the particle from outside[35,44,45]. In addition, if the electrolyte solution presents ionic specificity (Hofmeister effects), microgel effective charge may be affected by charge inversion or overcharging effects[46–48].

Given the important role that the electrolyte solution plays on swelling response and on microgel-solute interactions, it is indispensable to understand the physical effects involved in the ionic distribution inside and around the microgel particle. In the bulk, Coulomb forces due to microgel effective charge control the local density of ions. However, when ions permeate through the polymer network, they are affected not only by the electrostatic interaction, but also by the steric repulsion[35,46]. This non-electric interaction arises because of the finite size of the ions that cannot overlap with other ions nor polymer chains. Therefore, this volume exclusion depends on the internal morphology of the polymer network and is especially relevant when the microgel de-swells.

1.2 Microgels for drug delivery

The development of "smart" polymer materials in last decades has opened up a whole new world of applications in fields such as coatings, textiles, biosensors, optical systems, tissue engineering, diagnostics, and drug delivery[49,50]. In particular, the design of stimuli-responsive drug transport and delivery systems has gained considerable attention in recent years[51–54], especially in the field of nanoscience, given that nanoparticles offer a number of advantages that allow to overcome many problems associated with traditional therapies[55]. This increase of interest is illustrated in Figure 1.3, where we can observe the growth of research in drug delivery systems since 1960.
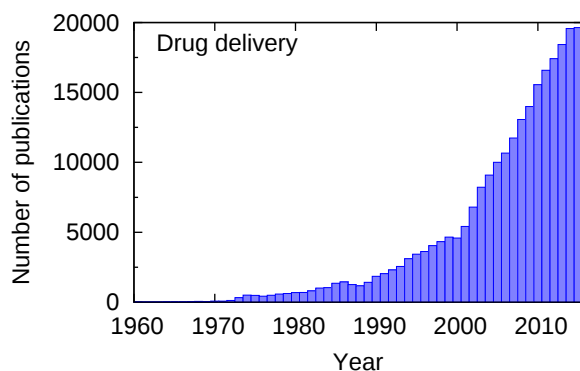
Figure 1.3: Number of publications related with drug delivery per year. The search has been performed looking for the term "drug delivery" within the title, abstract or keywords of the publications. Source: Scopus database (© Elsevier B.V.).

A drug delivery system is designed not only for improving the solubilization of poorly soluble drugs, but many other features such as controlled drug release rate, protection from chemical and enzymatic degradation, reduction of toxicity, and improvement of drug availability are also desirable[56]. In addition, by means of responsive materials, intelligent systems where the release of a molecule is triggered by changes in external stimuli can be developed.

Thanks to the combined properties mentioned in section 1.1, microgel particles are promising candidates for such purpose. The free volume inside the polymer network allows the encapsulation of different solutes, such as DNA, proteins, peptides and other biomolecules[57–61], either hydrophilic or hydrophobic, improving their solubility and protecting them from degradation[62]. In addition, the colloidal size of microgels is an advantage in areas where macroscopic

gels cannot be used, such as parenteral drug delivery, and their fast response is also a useful property to oral and nasal administration[63]. The swelling behaviour of microgel particles can be used for controlled and responsive drug uptake and release, and they even can be functionalized to enable specific targeting[64]. For all these reasons, a broad range of biotechnological and medical applications for microgels are being widely investigated[39,65–67].

The kind of microgels most studied for drug delivery are temperature and pH sensitive particles. On the one hand, thermoresponsive microgels with VPTT close to physiological temperature are very useful for the release of biomolecules in the human body[68], while by means of pH-responsive microgels electrostatic triggering can be achieved[69]. Therefore, a number of multiresponsive pH- and T-dependent microgels have also been investigated[70,71]. In addition, microgels which do not require any triggers are also interesting. These particles release the solutes by simple degradation of their polymer network[72]. Indeed, although biodegradability is a helpful feature for biomedical applications of microgels, biocompatibility is a must. In this sense, the use of PNIPAM for medical applications may be more limited than PVCL based microgels, since it shows higher cytotoxicity[37,38].

Compared with the considerable amount of experimental works published regarding the applications of microgels as nanocarriers, surprisingly little research have been done on describing such systems from a theoretical point of view[73–81]. As will be shown in Paper V, the permeation of biomolecules inside microgels is a complex process that depends on the features of the solvent (temperature, ionic strength, pH), microgel (charge distribution, network morphology, hydrophobicity) and biomolecule (size, shape and charge distribution). For this reason, knowing the microgel-biomolecule interactions is the cornerstone of the development of biomedical applications for microgel suspensions.

References

[1]   Baker, W. O. *Industrial & Engineering Chemistry* **1949**, *41*, 511–520.

[2]   Staudinger, H.; Husemann, E. *Berichte der deutschen chemischen Gesellschaft (A and B Series)* **1935**, *68*, 1618–1634.

[3]   Saunders, B. R.; Vincent, B. *Advances in colloid and interface science* **1999**, *80*, 1–25.

[4]   IUPAC, In *Compendium of Polymer Terminology and Nomenclature (IUPAC Recommendations 2008)*; Jones, R. G., Wilks, E. S., Metanomski, W. V., Kahovec, J., Hess, M., Stepto, R., Kitayama, T., Eds.; The Royal Society of Chemistry, 2009; p 443.

[5] Pelton, R.; Hoare, T. In *Microgel Suspensions: Fundamentals and Applications*; Fernandez-Nieves, A., Wyss, H. M., Mattsson, J., Weitz, D. A., Eds.; Wiley-VCH Verlag GmbH & Co. KGaA: Weinheim, Germany, 2011; pp 1–32.

[6] Antonietti, M.; Rosenauer, C. *Macromolecules* **1991**, *24*, 3434–3442.

[7] Sasa, N.; Yamaoka, T. *Advanced Materials* **1994**, *6*, 417–421.

[8] Rombouts, W. H. Composite Hydrogels of Bio-inspired Protein Polymers. Mechanical and Structural Characterization. Ph.D. thesis, Wageningen University, 2015.

[9] Lyon, L. A.; Serpe, M. J. In *Hydrogel Micro and Nanoparticles*; Lyon, L. A., Serpe, M. J., Eds.; Wiley-VCH, 2012; p 406.

[10] Murray, M. J.; Snowden, M. J. *Advances in Colloid and Interface Science* **1995**, *54*, 73–91.

[11] Zhang, Y.; Guan, Y.; Zhou, S. *Biomacromolecules* **2006**, *7*, 3196–3201.

[12] Saunders, B. R.; Laajam, N.; Daly, E.; Teow, S.; Hu, X.; Stepto, R. *Advances in colloid and interface science* **2009**, *147-148*, 251–62.

[13] Naficy, S.; Razal, J. M.; Whitten, P. G.; Wallace, G. G.; Spinks, G. M. *Journal of Polymer Science, Part B: Polymer Physics* **2012**, *50*, 423–430.

[14] Osada, Y.; Ross-Murphy, S. *Scientific American* **1993**, *268*, 82–87.

[15] Tanaka, T.; Fillmore, D. J. *The Journal of Chemical Physics* **1979**, *70*, 1214–1218.

[16] Zhang, J.; Pelton, R. *Langmuir* **1999**, *15*, 8032–8036.

[17] Maldonado-Valderrama, J.; del Castillo-Santaella, T.; Adroher-Benítez, I.; Moncho-Jordá, A.; Martín-Molina, A. *Soft Matter* **2016**, *8*, 6416.

[18] Li, Z.; Geisel, K.; Richtering, W.; Ngai, T. *Soft Matter* **2013**, *9*, 9939–9946.

[19] Scheidegger, L.; Fernández-Rodríguez, M. Á.; Geisel, K.; Zanini, M.; Elnathan, R.; Richtering, W.; Isa, L. *Phys. Chem. Chem. Phys.* **2017**,

[20] Li, Z.; Ngai, T. *Nanoscale* **2013**, *5*, 1399–1410.

[21] Lyon, L. A.; Debord, J. D.; Debord, S. B.; Jones, C. D.; McGrath, J. G.; Serpe, M. J. *Journal of Physical Chemistry B* **2004**, *108*, 19099–19108.

[22] Liétor-Santos, J. J.; Gasser, U.; Zhou, J.; Hu, Z.; Fernández-Nieves, A. *Hydrogel Micro and Nanoparticles*; Wiley-VCH Verlag GmbH & Co. KGaA: Weinheim, Germany, 2012; pp 337–368.

[23] Hendrickson, G. R.; Smith, M. H.; South, A. B.; Lyon, L. A. *Advanced Functional Materials* **2010**, *20*, 1697–1712.

[24] Hu, L.; Sarker, A. K.; Islam, M. R.; Li, X.; Lu, Z.; Serpe, M. J. *Journal of Polymer Science, Part A: Polymer Chemistry* **2013**, *51*, 3004–3020.

[25] Heskins, M.; Guillet, J. E. *Journal of Macromolecular Science: Part A - Chemistry* **1968**, *2*, 1441–1455.

[26] Ledesma-Motolinía, M.; Braibanti, M.; Rojas-Ochoa, L. F.; Haro-Pérez, C. *Colloids and Surfaces A: Physicochemical and Engineering Aspects* **2015**, *482*, 724–727.

[27]   Pelton, R. H.; Chibante, P. *Colloids and Surfaces* **1986**, *20*, 247–256.

[28]   Pelton, R.; Pelton, H. M.; Morphesis, A.; Rowell, R. L. *Langmuir* **1989**, *5*, 816–818.

[29]   Duracher, D.; Elaïssari, A.; Pichot, C. *Journal of Polymer Science, Part A: Polymer Chemistry* **1999**, *37*, 1823–1837.

[30]   Leobandung, W.; Ichikawa, H.; Fukumori, Y.; Peppas, N. A. *Journal of Applied Polymer Science* **2002**, *87*, 1678–1684.

[31]   López-León, T.; Ortega-Vinuesa, J. L.; Bastos-González, D.; Elaïssari, A. *The journal of physical chemistry. B* **2006**, *110*, 4629–36.

[32]   Tagit, O.; Tomczak, N.; Jafarpour, A.; Jańczewski, D.; Han, M. Y.; Vancso, G. J.; Herek, J. L. *Nanotechnology* **2011**, *22*, 265701.

[33]   Gottwald, D.; Likos, C. N.; Kahl, G.; Löwen, H. *The Journal of chemical physics* **2005**, *122*, 074903–11.

[34]   Quesada-Pérez, M.; Ramos, J.; Forcada, J.; Martín-Molina, A. *The Journal of chemical physics* **2012**, *136*, 244903–9.

[35]   Moncho-Jordá, A. *The Journal of chemical physics* **2013**, *139*, 064906.

[36]   Gao, Y.; Au-Yeung, S. C. F.; Wu, C.; Yibing Gao,; Steve C. F. Au-Yeung,; Chi Wu, *Macromolecules* **1999**, *32*, 3674–3677.

[37]   Vihola, H.; Laukkanen, A.; Valtola, L.; Tenhu, H.; Hirvonen, J. *Biomaterials* **2005**, *26*, 3055–3064.

[38]   Imaz, A.; Forcada, J. *Journal of Polymer Science Part A: Polymer Chemistry* **2010**, *48*, 1173–1181.

[39]   Ramos, J.; Peláez-Fernández, M. A.; Forcada, J.; Moncho-Jordá, A. In *Soft Nanoparticles for Biomedical Applications*; Callejas-Fernández, J., Estelrich, J., Quesada-Pérez, M., Forcada, J., Eds.; The Royal Society of Chemistry: Cambridge, 2014; Chapter 4, pp 1–37.

[40]   Daly, E.; Saunders, B. R. *Langmuir* **2000**, *16*, 5546–5552.

[41]   Quesada-Pérez, M.; Ahualli, S. A.; Martín-Molina, A. *The Journal of chemical physics* **2014**, *141*, 124903.

[42]   Rumyantsev, A. M.; Rudov, A. A.; Potemkin, I. I. *The Journal of Chemical Physics* **2015**, *142*, 171105–5.

[43]   Belloni, L. *Colloids and Surfaces A: Physicochemical and Engineering Aspects* **1998**, *140*, 227–243.

[44]   Denton, A. R. *Physical Review E* **2003**, *67*, 011804–10. *Erratum–ibid* **2003**, *68*.

[45]   Moncho-Jordá, A.; Anta, J. A.; Callejas-Fernández, J. *The Journal of chemical physics* **2013**, *138*, 134902.

[46]   Moncho-Jordá, A.; Adroher-Benítez, I. *Soft matter* **2014**, *10*, 5810–5823.

[47]   Rumyantsev, A. M.; Santer, S.; Kramarenko, E. Y. *Macromolecules* **2014**, *47*, 5388–5399.

[48]   Pérez-Fuentes, L.; Drummond, C.; Faraudo, J.; Bastos-González, D. *Soft Matter*

2015, *11*, 5077–5086.

[49] Cohen Stuart, M. A.; Huck, W. T. S.; Genzer, J.; Müller, M.; Ober, C.; Stamm, M.; Sukhorukov, G. B.; Szleifer, I.; Tsukruk, V. V.; Urban, M.; Winnik, F.; Zauscher, S.; Luzinov, I.; Minko, S. *Nature Materials* **2010**, *9*, 101–113.

[50] Wei, M.; Gao, Y.; Li, X.; Serpe, M. J. *Polym. Chem.* **2017**, *20*, 17–24.

[51] Mura, S.; Nicolas, J.; Couvreur, P. *Nature Materials* **2013**, *12*, 991–1003.

[52] Lee, S. M.; Nguyen, S. T. *Macromolecules* **2013**, *46*, 9169–9180.

[53] Du, A. W.; Stenzel, M. H. *Biomacromolecules* **2014**, *15*, 1097–1114.

[54] Lesher-Perez, S. C.; Segura, T.; Moraes, C. *Integr. Biol.* **2016**, *8*, 8–11.

[55] Sánchez-Moreno, P. Engineering lipid nanocapsule systems for intracellular delivery of anticancer drugs. Ph.D. thesis, Universidad de Granada, 2014.

[56] Malmsten, M. *Soft Matter* **2006**, *2*, 760–769.

[57] Ghugare, S. V.; Mozetic, P.; Paradossi, G. *Biomacromolecules* **2009**, *10*, 1589–1596.

[58] Bysell, H.; Månsson, R.; Hansson, P.; Malmsten, M. *Advanced Drug Delivery Reviews* **2011**, *63*, 1172–1185.

[59] Lü, S.; Liu, M.; Ni, B.; Gao, C. *Journal of Polymer Science, Part B: Polymer Physics* **2010**, *48*, 1749–1756.

[60] Smith, M. H.; Lyon, L. A. *Accounts of Chemical Research* **2012**, *45*, 985–993.

[61] Shin, J.; Cherstvy, A. G.; Metzler, R. *Physical Review X* **2014**, *4*, 021002.

[62] Vinogradov, S. V. *Nanomedicine (London, England)* **2010**, *5*, 165–8.

[63] Malmsten, M.; Bysell, H.; Hansson, P. *Current Opinion in Colloid and Interface Science* **2010**, *15*, 435–444.

[64] Blackburn, W. H.; Dickerson, E. B.; Smith, M. H.; McDonald, J. F.; Lyon, L. A. *Bioconjugate Chemistry* **2009**, *20*, 960–968.

[65] Ramos, J.; Imaz, A.; Callejas-Fernández, J.; Barbosa-Barros, L.; Estelrich, J.; Quesada-Pérez, M.; Forcada, J. *Soft Matter* **2011**, *7*, 5067–5082.

[66] Lu, Y.; Welsch, N.; Dzubiella, J.; Ballauff, M. In *Intelligent Hydrogels*; Sadowski, G., Richtering, W., Eds.; Springer International Publishing: Cham, 2013; pp 113–130.

[67] Ramos, J.; Forcada, J.; Hidalgo-Álvarez, R. *Chemical Reviews* **2014**, *114*, 367–428.

[68] Nolan, C. M.; Gelbaum, L. T.; Lyon, L. A. *Biomacromolecules* **2006**, *7*, 2918–2922.

[69] Das, M.; Mardyani, S.; Chan, W. C. W.; Kumacheva, E. *Advanced Materials* **2006**, *18*, 80–83.

[70] Hoare, T. R.; Pelton, R. *Langmuir* **2008**, *24*, 1005–12.

[71] Imaz, A.; Forcada, J. *Journal of Polymer Science Part A: Polymer Chemistry* **2011**, *49*, 3218–3227.

[72] Murthy, N.; Xu, M.; Schuck, S.; Kunisawa, J.; Shastri, N.; Frechet, J. M. J. *Proceedings of the National Academy of Sciences* **2003**, *100*, 4995–5000.

[73] Biesheuvel, P. M.; Wittemann, A. *Journal of Physical Chemistry B* **2005**, *109*, 4209–

4214.

[74] Wittemann, A.; Ballauff, M. *Physical Chemistry Chemical Physics* **2006**, *8*, 5269–5275.

[75] Leermakers, F. A. M.; Ballauff, M.; Borisov, O. V. *Langmuir* **2007**, *23*, 3937–3946.

[76] Hu, Y.; Cao, D. *Langmuir* **2009**, *25*, 4965–4972.

[77] Jung, S. C.; Oh, S. Y.; Chan Bae, Y. *Polymer* **2009**, *50*, 3370–3377.

[78] Yigit, C.; Welsch, N.; Ballauff, M.; Dzubiella, J. *Langmuir* **2012**, *28*, 14373–14385.

[79] Welsch, N.; Lu, Y.; Dzubiella, J.; Ballauff, M. *Polymer (United Kingdom)* **2013**, *54*, 2835–2849.

[80] Angioletti-Uberti, S.; Ballauff, M.; Dzubiella, J. *Soft matter* **2014**, *10*, 7932–45.

[81] Yigit, C.; Kanduc, M.; Ballauff, M.; Dzubiella, J. *Langmuir* **2017**, *33*, 417–427.

2

Justification

Once the main features of microgel suspensions have been presented, let us put our research in context. As has been explained in the previous chapter, microgels are soft colloidal particles whose unique characteristics made them promising for a number of biotechnological applications. Among them, the potential of microgels as drug transport an delivery systems has gained attention in recent years.

There is a wide range of microgel particles which respond to different external stimuli. Although the aim of this thesis is to provide knowledge that may be applicable to the large family of microgel suspensions, we have paid special attention to thermoresponsive ionic microgels. On the one hand, microgels with VPTT close to physiological temperature are expected to be very useful for applications in the human body. On the other hand, the presence of charged groups within the polymer network allows to control their behaviour when immersed in electrolyte solutions and their interaction with charged biomolecules.

Since the first microgel particles were synthesized, a great number of works have been published concerning their synthesis, characterization, modelling and applications, but only a small fraction of them aim to shed light on the behaviour of microgel in presence of charged solutes from a theoretical point of view. We firmly believe that a comprehensive understanding of the physical phenomena involved in the response of microgels to changes in their environment and the interactions between microgels and other particles will stimulate the development of innovative applications, will open new lines of research and in general will contribute to a deeper knowledge in the field of materials science.

2.1 Objectives

Having this idea in mind, the aims of this thesis may be summarized in the following points:

- Identify the different interactions involved in the permeation of ions and biomolecules inside charged microgel particles immersed in an electrolyte solution. Among them, determine to what extent the excluded-volume effects may hinder solute permeation and affect the spatial distribution of ions inside and around the microgel.

- Study the effect of the counterion permeation on the effective charge of microgel particles. Determine whether counterion valence has a relevant effect on the spatial distribution of electrolyte ions and on the internal structure of the charged microgel particle.

- Explore the potential of the Ornstein-Zernike integral formalism to reproduce and predict the radial distribution functions of ions inside and around microgel particles. In order to apply this formalism, find a model to properly represent the total microgel-ion interaction.

- Develop a microgel model for Molecular Dynamics simulations to study the microgel-ion interactions.

- Explore the interfacial properties of microgel particles at the air-water interface and their dependence with temperature and swelling behaviour. With this aim, construct Langmuir monolayers with thermoresponsive microgels in order to study the dependence of the spatial configuration of particles with the surface pressure.

2.2 Outline of the thesis

According to their content, we have classified the research works presented in this thesis in three main parts.

2.2.1 Microgel particles in presence of electrolyte

The aim of Papers I, II, III and IV was to study the interactions involved in the permeation of ions inside thermoresponsive ionic microgel particles in the limit of very diluted microgel suspensions. Bearing this idea in mind, we made use of

the Ornstein-Zernike integral formalism, Monte Carlo and Molecular Dynamics simulations, as well as experimental synthesis and characterization of microgel particles.

Paper I   The starting point of this thesis was the study of the effect of the steric interaction in the permeation of monovalent counterions inside a microgel particle. For this purpose, we developed a method that blended Ornstein-Zernike integral equations with Monte Carlo simulations, and we compared the ionic density profiles and the microgel effective charge obtained by the two methods for different swelling states of the microgels. This allowed us to test two different models for the steric interaction in order to determine which one was able to quantify more accurately the volume-exclusion effects that arose in this system. The role of the polymer charge distribution, electrolyte concentration and the ionic size were also addressed in this paper.

Paper II   In the same way as previous work, the combined technique of Monte Carlo simulations and Ornstein-Zernike equations was employed this time to determine the effect of two new variables on the swelling behaviour of the particle. On the one hand, results were obtained for 1:1 and 1:3 electrolyte to study the effect of counterion valence. In addition, two microgel particles, bearing different bare charge were considered. For the steric repulsion we employed the model that resulted more accurate in previous work, and also compared it with a different one.

Paper III   The reliability of the Ornstein-Zernike formalism was confirmed in this study, in which experimental results obtained for two different thermoresponsive ionic microgels were interpreted with the help of the integral equations. In this work we measured the hydrodynamic radius and electrophoretic mobility of PNIPAM and PVCL microgel suspensions for different salt valence and concentration. An experimental effective charge was obtained from these measurements, which was compared with the theoretical effective charge calculated for these systems. In this way, the effect of counterion valence and electrolyte concentration on the effective charge of the different microgel particles was analyzed, which allowed to draw interesting conclusions about counterion permeation and condensation inside the polymer network.

Paper IV To conclude this first part of our research, a completely different procedure was followed, based on all-atom Molecular Dynamics simulations. This approach allows to consider all the entangled interactions that arise when polymers are immersed an electrolyte solution. Given that constructing an exact microgel network to model the system is extremely demanding in all-atom simulations, an assembly of several PNIPAM chains was arranged into a membrane configuration. The thermosensitivity of the model was tested first with a infinitely diluted oligomer and then with a membrane in neat water, providing satisfactory results. Finally the membrane was immersed in two different electrolyte solutions to obtain the ionic density profiles for swollen and shrunken configurations.

2.2.2 Sorption and distribution of biomolecules in microgels

In addition to microgel-ion interactions, to assess the potential application of microgel as drug delivery systems we need a better understanding about the interactions between microgels and biomolecules. With this aim we performed the research described in the following publication.

Paper V We set aside the integral equations and simulations to carry out a relatively simple theoretical analysis of the uptake of a non-uniformly charged biomolecule by a microgel in presence of 1:1 electrolyte. Within the framework of mean field theory, we studied the total microgel-solute potential of mean force for different values of electric dipole moment and charge of the biomolecule. The effect of electrolyte concentration, excluded-volume repulsion and hydrophobic interactions was also considered. Five different sorption states were identified, from complete repulsion of the solute to its absorption deep inside the microgel.

2.2.3 Interfacial behaviour of thermoresponsive microgels

As mentioned in the introduction section, the assembling of microgel particles in different structures has gained attention in recent years. Therefore, with this concluding part of this thesis we aimed to open a new line in our research to study the interfacial characteristics of thermoresponsive microgels in order to explore their potential applications as stimuli responsive emulsion stabilizers.

Paper VI   The properties of charged thermoresponsive microgels at the air-water interface were investigated from both experimental and theoretical approaches. On the one hand, the experimental study was performed by means of a combination of several techniques, namely, adsorption, dilatational rheology and Langmuir monolayers. On the other hand, a qualitative interpretation for the surface pressure behaviour of the particle was provided in terms of microgel-microgel effective pair potentials.

Methodology

The aim of this chapter is to briefly introduce the most relevant theoretical, computational and experimental methods employed in this thesis. Given the wide variety of techniques considered in this work, we do not intend to describe them in depth, but to give a general view about the main procedures that have been useful to accomplish the goals of this research. More information about the specific details of each method will be provided in the corresponding chapters below.

3.1 Theoretical background

3.1.1 Radial distribution function and potential of mean force

In a system of N identical particles confined in a volume V at temperature T, in absence of external fields, the probability of finding any set of n particles at a specific configuration $\mathbf{r}^n = \{\mathbf{r}_1, ..., \mathbf{r}_n\}$, irrespective of the configuration of the rest of the particles, is given by the n-particle distribution function [1,2],

$$\rho_N^n(\mathbf{r}^n) = \frac{N!}{(N-n)!} \frac{1}{Z_N} \int e^{-\beta V_N} d\mathbf{r}^{(N-n)}, \tag{3.1}$$

where Z_N is the configuration integral and V_N the total potential energy of the system. To measure the extent to which the structure of a fluid deviates from complete randomness, that is, to describe the correlations between particles,

we define the n-particle correlation function,

$$g_N^n(\mathbf{r}^n) = \frac{\rho_N^{(n)}(\mathbf{r}_1, ...\mathbf{r}_n)}{\prod_{i=1}^{n} \rho_N^{(1)}(\mathbf{r}_i)}, \tag{3.2}$$

which for a homogeneous system reduces to

$$g_N^n(\mathbf{r}^n) = \frac{\rho_N^{(n)}(\mathbf{r}^n)}{\rho^n}. \tag{3.3}$$

The *pair correlation function* $g^{(2)}(\mathbf{r}_1, \mathbf{r}_2)$ is specially important because it can be experimentally determined and from it we can obtain the thermodynamic properties of the system. If the system is homogeneous and isotropic, $g^{(2)}(\mathbf{r}_1, \mathbf{r}_2)$ only depends on the relative distance between particles 1 and 2, $r_{12} = |\mathbf{r}_2 - \mathbf{r}_1|$. In this case we call $g^{(2)}(r_{12})$ the *radial distribution function*, denoted as $g(r)$, because the local density of particles at distance r about a fixed one is given by the product of $g(r)$ times the bulk density ρ_0,

$$\rho(r) = g(r)\rho_0. \tag{3.4}$$

From the pair correlation function we can define the *potential of mean force* (PMF), introduced in the 1930s by Kirkwood[3],

$$g^{(2)}(\mathbf{r}_1, \mathbf{r}_2) = e^{-\beta w(\mathbf{r}_1, \mathbf{r}_2)}, \tag{3.5}$$

which is the interaction between two particles, held at positions $\mathbf{r}_1$ and $\mathbf{r}_2$, when the rest $N - 2$ particles of the system are averaged over all configurations[1]. In the limit of very diluted systems, the two particles fixed a distance r_{12} are not affected by the remaining $N - 2$ particles, so $w(r_{12}) \rightarrow V(r_{12})$. Therefore, the radial distribution function is related with the effective pair potential so that[2]

$$\lim_{\rho_0 \rightarrow 0} g(r) = e^{-\beta V_{\mathrm{eff}}(r)}. \tag{3.6}$$

Another important quantity defined from $g(r)$ is the *total correlation function*,

$$h(r) = g(r) - 1, \tag{3.7}$$

which measures the influence of particle 1 on particle 2, situated at distance r from 1. Its Fourier transform $\hat{h}(k)$ multiplied by the bulk density ρ_0 provides the structure factor, which can be experimentally determined by scattering of electromagnetic radiation[1].

3.1.2 Ornstein-Zernike integral formalism

In 1914 Ornstein and Zernike [4] proposed to split the total correlation function $h(r)$ in two parts, one direct and other indirect, giving rise to the well known Ornstein-Zernike (OZ) integral equation:

$$h(r_{12}) = c(r_{12}) + \rho_0 \int c(r_{13}) h(r_{23}) \mathrm{d}r_3. \tag{3.8}$$

The term $c(r_{12})$ is called *direct correlation function* between particles 1 and 2. The second term of the right-hand side of the OZ equation stands for the indirect influence that particle 1 exerts on 2 by means of any other particle 3 of the system. This indirect effect is weighted with density and averaged over all particle positions [1].

The integration of equation (3.8) consists in a convolution of correlation functions $c(r)$ and $h(r)$. Making use of a Fourier transformation the equation is considerably simplified, given that the convolution becomes a product,

$$\hat{h}(k) = \hat{c}(k) + \rho \hat{c}(k) \hat{h}(k). \tag{3.9}$$

For a system of spherical particles formed by M different species, there are $M(M+1)/2$ coupled OZ integral equations. For a suspension of microgels in presence of electrolyte there are three types of particles, namely microgel (m), counterion (+) and coion (−). Therefore, a system of six equations is defined,

$$\hat{h}_{\mu\nu}(k) = \hat{c}_{\mu\nu}(k) + \sum_{\lambda=1}^{M} \rho_{0\lambda} \hat{c}_{\mu\lambda}(k) \hat{h}_{\lambda\nu}(k), \tag{3.10}$$

where $\rho_{0\lambda}$ is the bulk number density of particle λ, and μ and ν run over all species. In this way, ion-ion correlations give three equations,

$$\left. \begin{aligned} \hat{h}_{++} &= \hat{c}_{++} + \rho_{0+} \hat{c}_{++} \hat{h}_{++} + \rho_{0-} \hat{c}_{+-} \hat{h}_{+-} + \rho_{0m} \hat{c}_{+m} \hat{h}_{m+} \\ \hat{h}_{+-} &= \hat{c}_{+-} + \rho_{0+} \hat{c}_{++} \hat{h}_{+-} + \rho_{0-} \hat{c}_{+-} \hat{h}_{--} + \rho_{0m} \hat{c}_{+m} \hat{h}_{m-} \\ \hat{h}_{--} &= \hat{c}_{--} + \rho_{0+} \hat{c}_{+-} \hat{h}_{+-} + \rho_{0-} \hat{c}_{--} \hat{h}_{--} + \rho_{0m} \hat{c}_{-m} \hat{h}_{m-} \end{aligned} \right\}; \tag{3.11}$$

microgel-counterion and microgel-coion correlations are given by

$$\left. \begin{aligned} \hat{h}_{m+} &= \hat{c}_{m+} + \rho_{0+} \hat{c}_{m+} \hat{h}_{++} + \rho_{0-} \hat{c}_{m-} \hat{h}_{+-} + \rho_{0m} \hat{c}_{mm} \hat{h}_{m+} \\ \hat{h}_{m-} &= \hat{c}_{m-} + \rho_{0+} \hat{c}_{m+} \hat{h}_{+-} + \rho_{0-} \hat{c}_{m-} \hat{h}_{--} + \rho_{0m} \hat{c}_{mm} \hat{h}_{m-} \end{aligned} \right\}, \tag{3.12}$$

and microgel-microgel correlation provides the last equation,

$$\hat{h}_{mm} = \hat{c}_{mm} + \rho_{0+} \hat{c}_{m+} \hat{h}_{m+} + \rho_{0-} \hat{c}_{m-} \hat{h}_{m-} + \rho_{0m} \hat{c}_{mm} \hat{h}_{mm} \}. \tag{3.13}$$

In the limit of very diluted microgel suspensions, $\rho_{0m} \to 0$, so the fourth term of the right-hand side of these six equations vanishes. Hence, the equations become decoupled, which allows to solve the system step by step.

To find the solution we know the bulk concentration of particles (ρ_{0m}, ρ_{0+}, ρ_{0-}), but $\hat{h}_{\mu v}$ and $\hat{c}_{\mu v}$ correlation functions remain unknown. Therefore, six more equations are needed to have a determined system of equations. This is the aim of the closure relations, which relate $h_{\mu v}(r)$ with $c_{\mu v}(r)$ by means of the pair interaction potentials of the system, $V_{\mu v}(r)$. In this thesis we have made use of the *hypernetted-chain approximation* (HNC), developed independently by several authors[5,6],

$$h_{\mu v}(r) = e^{h_{\mu v}(r) - c_{\mu v}(r) - \beta V_{\mu v}(r)} - 1 = e^{\gamma_{\mu v}(r) - \beta V_{\mu v}(r)} - 1, \qquad (3.14)$$

where $\gamma_{\mu v}(r) \equiv h_{\mu v}(r) - c_{\mu v}(r)$ is known as *indirect correlation function*.

There is a number of closure relations, such as mean-spherical approximation (MSA)[7] or Percus-Yevik approximation (PY)[8]. None of them has demonstrated to be quantitatively best for all system under all conditions, but each one is more suitable for a specific problem. In this thesis we made use of the HNC relation because it has proved to be very accurate for the interactions involved in microgel suspensions in presence of electrolyte[9–11].

In this way, we have 6 OZ equations and 6 HNC approximations to find the unknown $\hat{h}_{\mu v}(k)$ y $\hat{c}_{\mu v}(k)$. However, is more simple to calculate $\hat{c}_{\mu v}(k)$ and $\hat{\gamma}_{\mu v}(k)$ and from them the rest of quantities we are interested in. Hence, the resulting OZ/HNC system of 12 equations derived from equations (3.11), (3.12), (3.13) and (3.14) is given by

$$\left. \begin{aligned} \hat{\gamma}_{++} &= \rho_{0+}\hat{c}_{++}(\hat{\gamma}_{++} + \hat{c}_{++}) + \rho_{0-}\hat{c}_{+-}(\hat{\gamma}_{+-} + \hat{c}_{+-}) \\ \hat{\gamma}_{+-} &= \rho_{0+}\hat{c}_{++}(\hat{\gamma}_{+-} + \hat{c}_{+-}) + \rho_{0-}\hat{c}_{+-}(\hat{\gamma}_{--} + \hat{c}_{--}) \\ \hat{\gamma}_{--} &= \rho_{0+}\hat{c}_{+-}(\hat{\gamma}_{+-} + \hat{c}_{+-}) + \rho_{0-}\hat{c}_{--}(\hat{\gamma}_{--} + \hat{c}_{--}) \end{aligned} \right\}, \qquad (3.15)$$

$$\left. \begin{aligned} \hat{\gamma}_{m+} &= \rho_{0+}\hat{c}_{m+}(\hat{\gamma}_{++} + \hat{c}_{++}) + \rho_{0-}\hat{c}_{m-}(\hat{\gamma}_{+-} + \hat{c}_{+-}) \\ \hat{\gamma}_{m-} &= \rho_{0+}\hat{c}_{m+}(\hat{\gamma}_{+-} + \hat{c}_{+-}) + \rho_{0-}\hat{c}_{m-}(\hat{\gamma}_{--} + \hat{c}_{--}) \end{aligned} \right\}, \qquad (3.16)$$

$$\hat{\gamma}_{mm} = \rho_{0+}\hat{c}_{m+}(\hat{\gamma}_{m+} + \hat{c}_{m+}) + \rho_{0-}\hat{c}_{m-}(\hat{\gamma}_{m-} + \hat{c}_{m-})\}, \qquad (3.17)$$

$$\left. \begin{aligned} c_{++} &= e^{\gamma_{++} - \beta V_{++}} - \gamma_{++} - 1 \\ c_{+-} &= e^{\gamma_{+-} - \beta V_{+-}} - \gamma_{+-} - 1 \\ c_{+-} &= e^{\gamma_{--} - \beta V_{--}} - \gamma_{--} - 1 \end{aligned} \right\}, \qquad (3.18)$$

$$\left.\begin{aligned} c_{\mathrm{m+}} &= e^{\gamma_{\mathrm{m+}} - \beta V_{\mathrm{m+}}} - \gamma_{\mathrm{m+}} - 1 \\ c_{\mathrm{m-}} &= e^{\gamma_{\mathrm{m-}} - \beta V_{\mathrm{m-}}} - \gamma_{\mathrm{m-}} - 1 \end{aligned}\right\}, \tag{3.19}$$

$$\left. c_{\mathrm{m+}} = e^{\gamma_{\mathrm{mm}} - \beta V_{\mathrm{mm}}} - \gamma_{\mathrm{mm}} - 1 \right\}. \tag{3.20}$$

To solve this system we followed a procedure based on the Picard method of successive approximation [12]. This approach is summarized in the following diagram:

$$
\begin{array}{ccc}
c_{\mu\nu}^{(0)}(r) & \gamma_{\mu\nu}^{(0)}(r) \xrightarrow{\text{HNC}} & c_{\mu\nu}^{(1)}(r) \\
\text{FT} \downarrow & \uparrow \text{FT}^{-1} & \\
\hat{c}_{\mu\nu}^{(0)}(k) \xrightarrow{\text{OZ}} & \hat{\gamma}_{\mu\nu}^{(0)}(k) &
\end{array}
\tag{3.21}
$$

The starting point is an initial guess of the direct correlation function, $c_{\mu\nu}^{(0)}(r)$, which is Fourier-transformed to $\hat{c}_{\mu\nu}^{(0)}(k)$. Then $\hat{\gamma}_{\mu\nu}^{(0)}(k)$ is calculated by solving the OZ equations (3.15), (3.16) or (3.17). Next, the inverse Fourier transform $\gamma_{\mu\nu}^{(0)}(r)$ is obtained and from it a new value of $c_{\mu\nu}^{(1)}(r)$ is calculated by means of the closure relations (3.18), (3.19) or (3.20). The new direct correlation function $c_{\mu\nu}^{(1)}(r)$ is mixed with the previous one $c_{\mu\nu}^{(0)}(r)$ to obtain a new starting value. Thus, the procedure is repeated until convergence of the two latter steps is achieved, so that the value

$$\int_{0}^{r_{\max}} |c_{\mu\nu}^{(n)}(r) - c_{\mu\nu}^{(n-1)}(r)|^2 \mathrm{d}r \tag{3.22}$$

is less than a given value chosen according to the numerical features of the problem.

Is important to note that, although for $\rho_{0\mathrm{m}} \to 0$ the OZ equations are decoupled, a specific order of resolution must be followed. Firstly, the ion-ion correlation functions are calculated from equations (3.15) and (3.18), which are independent of the rest. The physical meaning of this independence is that, in the limit of very diluted suspensions, ions interact among themselves as though microgels were not there. The solutions from the ion-ion equations are used to determine the microgel-ion correlations by means of equations (3.16) and (3.19). Finally, the resulting values of these equations are introduced in equations (3.17) and (3.20) to get the microgel-microgel solution. More specific and technical details of the numerical resolution of the OZ/HNC integral equations can be found in references [9–11] and Papers I, II and III of this thesis.

Once the direct and indirect pair correlation functions have been obtained,
is possible to calculate the radial distribution functions of the microgel-counterion-
coion system from equation (3.7),

$$g_{\mu\nu}(r) = h_{\mu\nu}(r) + 1 = \gamma_{\mu\nu}(r) + c_{\mu\nu}(r) + 1. \tag{3.23}$$

3.1.3   Poisson-Boltzmann formalism

When charged colloidal particles are dispersed in an electrolyte solution two
competing effects arise. On the one hand, counterions are attracted by the sur-
face to neutralize the particle charge; on the other hand, both positive and nega-
tive ions tend to spread into the bulk solution in order to maximize the entropy[2].
As a result, an electric double layer is formed in the surface of the colloidal
particles, to which both coions and counterions contribute, although coun-
terion concentration is much higher than coion concentration. The Poisson-
Boltzmann formalism is a powerful tool to describe the behaviour of such sys-
tems, which strongly depends on the distribution of the electrolyte ions (ρ_{el})
and on the electrostatic potential (ψ) that arises around the particle. Neverthe-
less, several assumptions must be born in mind when taking this approach[13]:

- The ions are considered point charges, that is, they have no volume and
  consequently they can overlap.
- Ion-ion correlations are not taken into account.
- The solvent is considered a dielectric continuum with a uniform relative
  dielectric permittivity ε_{r}.

The electrostatic potential at $\mathbf{r}$ in the solution, measured relative to the bulk
phase where $\psi(\infty) \to 0$, is given by the Poisson equation,

$$\triangle \psi(\mathbf{r}) = -\frac{\rho_{\mathrm{e}}(\mathbf{r})}{\varepsilon_{\mathrm{r}}\varepsilon_0}, \tag{3.24}$$

where $\triangle$ is the Laplacian, $\rho_{\mathrm{e}}(\mathbf{r})$ is the charge density at $\mathbf{r}$, ε_0 is de vacuum dielec-
tric permittivity, and ε_{r} the relative permittivity of the solvent.

The distribution of electrolyte, formed by N ionic species with valence z_i
and bulk number density c_i^∞, is given by Boltzmann's law, so that

$$c_{\mathrm{el}}(\mathbf{r}) = \sum_{i=1}^{N} c_i^\infty \exp\left(-\frac{z_i e \psi(\mathbf{r})}{k_{\mathrm{B}} T}\right), \tag{3.25}$$

where e is the elementary electric charge, k_{B} is the Boltzmann's constant and T
is the absolute temperature. Consequently, the charge density at $\mathbf{r}$ in the case

of a symmetric electrolyte with valence z and bulk concentration c_{el}^{∞} takes the form

$$
\begin{aligned}
\rho_{\text{el}}(\mathbf{r}) &= \sum_{i=1}^{N} z_i e c_i^{\infty} \exp\left(-\frac{z_i e \psi(\mathbf{r})}{k_B T}\right) \\
&= z e c_{\text{el}}^{\infty} \left\{ \exp\left[-\frac{z_i e \psi(\mathbf{r})}{k_B T}\right] - \exp\left[\frac{z_i e \psi(\mathbf{r})}{k_B T}\right] \right\} \\
&= -2 z e c_{\text{el}}^{\infty} \sinh\left[\frac{z_i e \psi(\mathbf{r})}{k_B T}\right].
\end{aligned} \tag{3.26}
$$

To particularize the problem for microgel suspensions, is important to note that microgels are spherical permeable particles of charge density $\rho_{\text{m}}(r)$. Therefore, the Poisson equation (3.24) is split into two parts, inside and outside the particle, and the symmetry of the system allows to write it in spherical coordinates:

$$
\triangle \psi(r) = \frac{d^2 \psi(r)}{dr^2} + \frac{2}{r}\frac{d\psi(r)}{dr} = \begin{cases} -\dfrac{\rho_{\text{el}}(r) + \rho_{\text{m}}(r)}{\varepsilon_r' \varepsilon_0}, & 0 < r < R_{\text{m}} \\ -\dfrac{\rho_{\text{el}}(r)}{\varepsilon_r \varepsilon_0}, & R_{\text{m}} < r < +\infty \end{cases}. \tag{3.27}
$$

Introducing (3.26) in (3.27), we obtain the Poisson-Boltzmann (PB) equation for a microgel in presence of symmetric electrolyte,

$$
\frac{d^2 \psi(r)}{dr^2} + \frac{2}{r}\frac{d\psi(r)}{dr} = \begin{cases} \dfrac{2 e c_{\text{el}}^{\infty}}{\varepsilon_r \varepsilon_0} \sinh\left[\dfrac{z e \psi(r)}{k_B T}\right] - \dfrac{z e c_{\text{m}}(r)}{\varepsilon_r \varepsilon_0}, & 0 < r < R_{\text{m}} \\ \dfrac{2 e c_{\text{el}}^{\infty}}{\varepsilon_r \varepsilon_0} \sinh\left[\dfrac{z e \psi(r)}{k_B T}\right], & R_{\text{m}} < r < +\infty \end{cases}, \tag{3.28}
$$

where $c_{\text{m}}(r)$ is the charge distribution of the microgel. Note that for simplicity the relative permittivity inside the particle ε_r' is assumed to be the same than the one of the bulk solution, $\varepsilon_r' = \varepsilon_r$.

We define the scaled electrostatic potential as $y(r) \equiv z e \psi(r)/k_B T$. In the low potential limit we can linearize the PB equation, so that

$$
|z e \psi(r)| \ll k_B T \;\Rightarrow\; |y(r)| \ll 1 \;\Rightarrow\; \sinh(y) \simeq y. \tag{3.29}
$$

This yields to the Debye-Hückel equation,

$$
y''(r) + \frac{2}{r} y'(r) = \begin{cases} \kappa^2 y(r) - \kappa^2 \dfrac{c_{\text{m}}(r)}{2 c_{\text{el}}^{\infty}}, & 0 < r < R_{\text{m}} \\ \kappa^2 y(r), & R_{\text{m}} < r < +\infty \end{cases}, \tag{3.30}
$$

where κ is the the inverse of the Debye screening length, $\kappa \equiv \lambda_D^{-1}$, also known as Debye-Hückel parameter,

$$\kappa = \left(\frac{2 z^2 e^2 c_{el}^\infty}{\varepsilon_r \varepsilon_0 k_B T} \right)^{1/2}.$$

To obtain the electrostatic potential from (3.30) we need to know $c_m(r)$, that is, the distribution of charged groups inside the ionic microgel. In Paper V of this thesis we have considered a uniform distribution inside the particle which decreases to zero at the microgel interface, being σ the microgel-water interface width. Nevertheless, if the electrolyte bulk concentration c_{el}^∞ is small, the Debye screening length is much greater than the interface width, $\lambda_D \gg \sigma$. Hence, in the limit of low salt concentration we can assume a vanishing σ, that is, a step charge distribution inside the microgel particle:

$$c_m(r) = \begin{cases} c_m^0, & 0 < r < R_m \\ 0, & R_m < r < +\infty \end{cases}. \tag{3.31}$$

In this limit the linearized PB equation is given by

$$y''(r) + \frac{2}{r} y'(r) = \begin{cases} \kappa^2 y(r) - \kappa^2 y_0, & 0 < r < R_m \\ \kappa^2 y(r), & R_m < r < +\infty \end{cases}, \tag{3.32}$$

where $y_0 \equiv \dfrac{Z c_m^0}{2 z c_{el}^\infty}$ is the scaled electrostatic potential at $r = 0$.

On the other hand, in the limit of high salt concentration, the microgel-water interface width is comparable to Debye length. In this case we can approximate the charge distribution as a error function, so that

$$c_m(r) = \frac{c_m^0}{2} \left[1 - \mathrm{erf}\left(\frac{r - R_m}{\sqrt{2}\,\sigma} \right) \right], \quad 0 < r < +\infty. \tag{3.33}$$

In this case the linearized PB equation is given by

$$y''(r) + \frac{2}{r} y'(r) = \kappa^2 y(r) - \kappa^2 y_0 \left[1 - \mathrm{erf}\left(\frac{r - R_m}{\sqrt{2}\,\sigma} \right) \right], \quad 0 < r < +\infty. \tag{3.34}$$

Electrostatic potential

In the low electrolyte concentration limit is possible to analytically solve the linearized Poisson-Boltzmann equation (3.32). This equation was solved by Ohshima[14]

for a spherical soft core-shell particle. The solution for our model is a particular case of this previous work:

$$y(r) = \begin{cases} y_0 \left[1 - (\kappa R_m + 1)e^{-\kappa R_m} \dfrac{\sinh(\kappa r)}{\kappa r} \right], & 0 < r < R_m \\[2em] y_0 R_m [\cosh(\kappa R_m) - \sinh(\kappa R_m)] \dfrac{e^{-\kappa r}}{\kappa r}, & R_m < r < +\infty \end{cases} . \quad (3.35)$$

In the high electrolyte concentration limit, however, the solution is much more straightforward. If the thickness of the charge layer is much greater than the Debye length ($\sigma \gg \lambda_D$), then the potential deep inside the particle becomes the Donnan potential ψ_D, which is obtained by setting electroneutrality at $r = 0$:

$$\psi_D = \frac{k_B T}{ze} \operatorname{arcsinh}\left(\frac{Z c_m^0}{2 z c_{el}^\infty} \right) = \frac{k_B T}{ze} \ln \left[\frac{Z c_m^0}{2 z c_{el}^\infty} + \sqrt{1 + \left(\frac{Z c_m^0}{2 z c_{el}^\infty} \right)^2} \right]. \quad (3.36)$$

In the limit of large electrolyte concentration, $c_{el}(r) \gg c_m(r)$, we can linearize the Donnan potential,

$$\psi_D \simeq \frac{k_B T}{ze} \frac{Z c_m^0}{2 z c_{el}^\infty}. \quad (3.37)$$

In this regime the electrostatic local effects decay very fast with distance to microgel centre, so electroneutrality is fulfilled at any r and thus the electrostatic potential is given by

$$y(r) \simeq \frac{Z c_m(r)}{2 z c_{el}^\infty} = \frac{y_0}{2} \left[1 - \operatorname{erf}\left(\frac{r - R_m}{\sqrt{2}\,\sigma} \right) \right]. \quad (3.38)$$

Electric field

Given that the system under study has spherical symmetry, the electric field can simply be obtained from the electrostatic potential,

$$\mathbf{E}(r) = -\nabla \psi(r) = \frac{d\psi(r)}{dr}\hat{r}. \quad (3.39)$$

We define the scaled electric field as $Y(r) \equiv zeE(r)/k_B T$. Therefore, applying (3.39) to (3.35) in the low electrolyte concentration limit, we obtain the following

scaled electric field:

$$Y(r) = \begin{cases} y_0(\kappa R_m + 1)e^{-\kappa R_m}\dfrac{\kappa r \cosh(\kappa r) - \sinh(\kappa r)}{\kappa r^2}, & 0 < r < R_m \\[2em] y_0[\kappa R_m \cosh(\kappa R_m) - \sinh(\kappa R_m)]\dfrac{(\kappa r + 1)e^{-\kappa r}}{\kappa r^2}, & R_m < r < +\infty \end{cases} \quad , \quad (3.40)$$

In the high electrolyte concentration limit, from (3.38) the electric field takes the form of a Gaussian distribution:

$$Y(r) = \frac{y_0}{\sigma\sqrt{2\pi}}e^{-\frac{(r - R_m)^2}{2\sigma^2}}. \tag{3.41}$$

3.2 Simulations

Computer simulations are essential tools in scientific research, complementing theoretical and experimental studies. Given that the analysis of the macroscopic properties of many-particle problems is highly complicated, scientific simulations play a specially relevant role in the field of statistical physics. In this thesis the two most spread simulation techniques have been employed, namely, Monte Carlo (MC) simulations and Molecular Dynamics (MD).

3.2.1 Monte Carlo simulations

The Monte Carlo method, introduced in the 1940s by Metropolis and Ulam [15], is based in a non-deterministic description of the system under study. That is, it does not attempt to follow the *real* evolution of the system with time, but to lead the system to equilibrium by means of a stochastic procedure which depends on a sequence of random numbers generated during the simulation [16].

In this way, in MC simulations the phase space of the system is sampled in order to estimate the equilibrium properties of the model. The space sampling may be performed in different ways. The most widely used technique is the importance sampling method, also known as the Metropolis algorithm [17]. According to this method, the different states of the system are not randomly sampled through successive independent states, but the sampling is performed following an stochastic process, known as Markov chain, in which every configuration is generated from a previous state using a transition probability which depends on the energy difference between the initial and final states. [16].

Is important to bear in mind that the sequence of states produced in MC simulations do not agree with the evolution that the real system follows throughout the time. That is, the MC method is not suitable to describe the system dynamics. However, this trajectories allow the system to reach the equilibrium in a very efficient way, which makes this technique really useful to study the macroscopic equilibrium properties of the system.

The MC simulations of a nanogel particle in presence of electrolyte that have been used in Papers I and II of this thesis were first developed by Quesada-Pérez et al.[18,19]. In these simulations the particle is described by a *bead-spring model*, in which each polymer chain is modelled as a sequence of spherical monomers connected by tetrafunctional crosslinkers. In order to provide electric charge to the particle to represent an ionic nanogel, a given number of beads of each chain is charged with the negative elementary charge. In Figure 3.1 two snapshots of the modelled nanogel are shown at initial configuration (a) and at the equilibrium state (b), reached after the system has evolved throughout a thermalization time. In this technique the solvent is modelled as a continuum with a constant dielectric permittivity, ε. More details about the concrete features of the simulations will be described in the corresponding chapters.
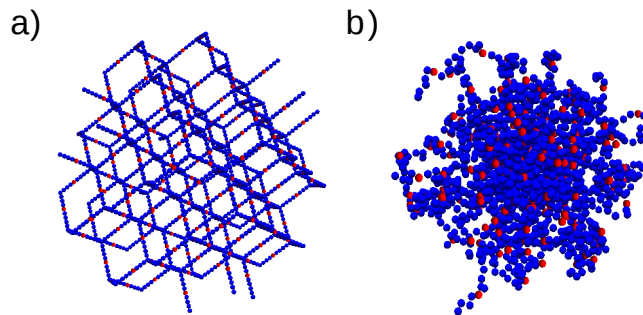
Figure 3.1: Snapshots of a nanogel modelled in Monte Carlo simulations at initial configuration (a) and once it has reached the equilibrium state (b).

3.2.2 Molecular Dynamics

Molecular Dynamics, developed in the late 1950s[20,21], is a simulation method which allows to study the equilibrium and transport properties of a many-body system[22]. Therefore, unlike Monte Carlo simulations, Molecular Dynamics provides information about the dynamical evolution of the system with time. With this purpose the particle trajectories are calculated by solving the classical New-

ton's equations of motion until the system reaches the equilibrium. Even though it employs classical equations, this procedure is an excellent approximation for a wide range of materials. Once the system is equilibrated, different equilibrium properties of the system can be measured.

The particle interactions and the potential energies that rule the evolution of the system can be calculated by means of interatomic potentials or molecular mechanics force fields. In the MD simulations performed in this thesis we have made use of *all-atom* force fields, which provide parameters for every type of atom in the system, including hydrogen. In particular, we have considered the OPLS-AA[23,24] and the AMBER[25] force fields with the SPC/E water model[26], because they have proved to be appropriate for modelling thermorresponsive polymers[27,28]. The simulations have been performed by means of the GROMACS package, born in 1991 in the University of Groningen[29]. GROMACS is based on the GROMOS package[30], which was developed to simulate biomolecules in solution.

An infinitely diluted oligomer and a membrane of PNIPAM chains have been simulated using this method in Paper IV. Snapshots of a NIPAM monomer (a) and a PNIPAM chain (b) immersed in water are shown in Figure 3.2. Detailed information about the simulation technique and the characteristics of the models are provided in Paper IV and the references therein.
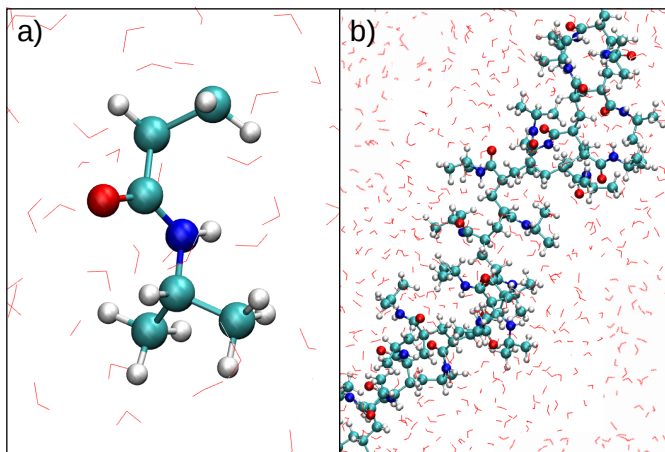

Figure 3.2: Models of NIPAM monomer (a) and a PNIPAM chain (b) immersed in water used in Molecular Dynamics simulations in Paper IV. Images made with VMD[31].

3.3 Experimental methods

3.3.1 Synthesis of microgel particles

Since the preparation of the first microgels, several techniques for the synthesis of microgel particles have been designed with the goal of controlling the size of the resulting particles, the colloidal stability of the suspension, and the distribution of crosslinkers or charged groups inside the polymer network. There are essentially three mechanisms of particle formation[32], namely homogeneous nucleation (e.g., emulsion polymerization[33]), emulsification (e.g., microemulsion polymerization[34]) and polymer complexation (i.e., crosslinking of neighbouring polymer chains[35]).

All the microgels used in this thesis were prepared by *emulsion polymerization*, also named *precipitation polymerization*[36], which is the most widely used technique for microgel syntesis[37]. A general requisite of this strategy is that the polymer must be insoluble under the polymerization conditions[32]. For this reason both PNIPAM and PVCL based microgels are synthesized at high temperature, at which polymers are hydrophobic.

Three different microgel suspensions were considered for the experimental work of this thesis. In Paper III we worked with PNIPAM and PVCL, while in Paper VI a more charged PVCL microgel suspension was used. In Table 3.1 all the chemicals employed in these syntheses are listed. We can observe that, as most of the microgels prepared nowadays, PNIPAM and PVCL were prepared with more than one monomer. In general, the presence of comonomers complicates the process because the components may react differently[32]. For instance, the crosslinker MBA used in PNIPAM synthesis polymerizes considerably faster than NIPAM monomer[38]. Consequently, the resulting microgel has a core-shell structure, in which the inner part of the particle is more crosslinked than the outer shell. The case of PVCL was even more complicated, since three comonomers were reacting. Imaz and Forcada[39] studied different synthesis strategies and developed the optimal method to incorporate acrylic acid (AA) into PVCL microgels with virtually 100% conversion of the three components. This was the strategy employed in the two PVCL microgel suspensions synthesized in this thesis.

As mentioned above, we were interested in microgels bearing electric charge. Although both NIPAM and VCL monomers are neutral, the use of ionic initiators in the syntesis, such as potassium peroxydisulfate (KPS), provides charged microgels through the incorporation of sulfate groups to the polymer network.
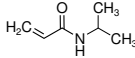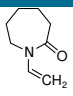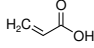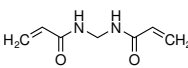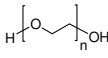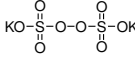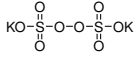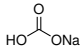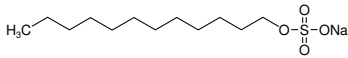
Component	PNIPAM		PVCL	
Monomer	NIPAM		VCL	
Ionic comonomer	—	—	AA	
Crosslinker	MBA		PEGDA	
Initiator	KPS		KPS	
Buffer	—	—	NaHCO$_3$	
Emulsifier	—	—	SDS	

Table 3.1: Chemical structure of reactans used in PNIPAM and PVCL microgel synthesis.

Moreover, in the chase of PVCL microgels, the incorporation of AA enhances microgel bare charge by means of carboxylic groups which are attached to the polymeric chains.

3.3.2 Microgel size and structure

The standard technique for measuring the size of microgel particles is Dynamic Light Scattering (DLS), which works as follows. When a laser beam collides with a small particle, the light is scattered in all directions. Since colloidal particles move randomly in space, describing a Brownian motion, the intensity of the scattered light fluctuates with time. In DLS the characteristic time of these fluctuations is measured and related with the translational diffusion coefficient (D) of the particles. For spherical particles, the hydrodynamic radius R_h can be obtained from the diffusion coefficient (D) by means of the Stokes-Einstein equation[40],

$$D = \frac{k_B T}{6\pi\eta R_h},$$
(3.42)

where k_B is the Boltzmann's constant, η is the solvent viscosity, and T is the absolute temperature. In the case of nonspherical particles, R_h is often taken as the apparent hydrodynamic radius or equivalent sphere radius.

Since measurements are performed in a sample of microgels dispersed in the bulk, DLS is a powerful tool to measure the effect of external stimuli (e.g., temperature, pH, ionic strength) on the swelling behaviour of microgels. However, is important to note that microgel sizes measured by this technique are

sensitive to dangling surface chains and consequently are larger than sizes measured by other techniques such as static light scattering, X-ray scattering or neutron scattering[41].

In this thesis, particle size was measured as a function of temperature by DLS with a Zetasizer Nano ZS system from Malvern Instuments Ltd. An example of the resulting plot is shown in Figure 1.2. In the Nano ZS device the detector position is at 175° from the outgoing not scattered beam, which is known as backscatter detection. This type of detection allows to measure higher concentrations of sample and reduces the effect of multiple scattering and dust in the samples[42].

Figure 3.3 shows two different micrographs of the anionic PNIPAM microgel studied in Paper III. Scanning electron microscopy (SEM), transmission electron microscopy (TEM) and atomic force microscopy (AFM) are different techniques to obtain images which provide a direct estimation of size and shape of colloidal particles in high resolution. However, to obtain accurate quantitative values of microgel size using these techniques requires to count a large number of particles from the images, in order to get good statistical average. The AFM technique allows measurements with and without solvent, while in electron microscopy techniques the solvent of the dispersion always has to be removed. Due to their soft structure, microgel particles may be deformed either because of being spread on a surface in AFM, or due to solvent evaporation, as observed in the SEM micrograph of a PVCL microgel in Figure 1.1. For this reason DLS is used to determine microgel size in bulk, while microscopy images are frequently used to obtain helpful qualitative information about monodispersity and extent of aggregation[32].
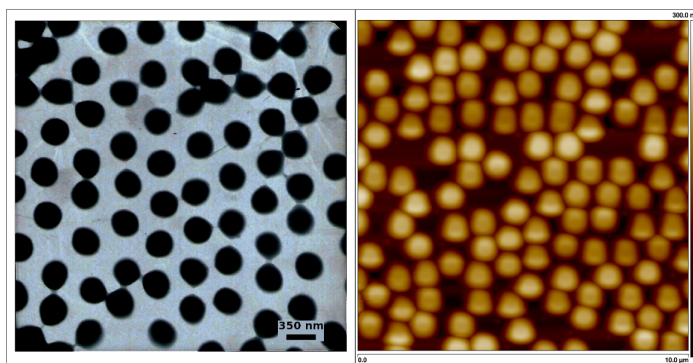
Figure 3.3: Micrographs of anionic PNIPAM microgels obtained with TEM (left) and AFM (right). Images obtained by Pérez-Fuentes[43], used with permission of the author.

3.3.3 Electrophoretic mobility

When an electric field is applied across a sample of charged colloids suspended in an electrolyte solution, the particles move with a constant velocity, called *electrophoretic velocity* (U). This velocity is the result of the balance between the applied electric field and the viscous resistance exerted by the liquid on the particles. If the electric field (E) is weak enough, U is proportional to E. The constant of proportionality is known as *electrophoretic mobility* (μ_e), which is defined as $U = \mu_e E$ [44].

The value of μ_e is obtained by performing an electrophoresis experiment on a microgel suspension and measuring the velocity of the particles using a technique called Laser Doppler Velocimetry (LDV). In this way the sample is located in a cell with electrodes in which a potential is applied. A laser beam is shot into the sample and scattered by the particles that move towards the electrode of opposite charge. The fluctuation of the intensity of the scattered light is proportional to the speed of the particles. Therefore, the characteristic frequencies in the scattered light are extracted by a digital signal processor, which provides the value of μ_e.

The same Zetasizer Nano ZS system used for measuring particle size was employed for the electrophoresis experiments in this thesis. The device employs conventional LDV combined with phase analysis light scattering (PALS). This technique processes the changes in phase of the scattered light signal, instead of its frequency spectrum. [45] The combination of these two techniques allows to measure samples of very low mobility and was patented by Malvern Instuments Ltd. as M3-PALS [42].

Our interest for the electrophoresis measurements lies in that an estimation of microgel charge can be calculated from electrophoretic mobility. However, how these quantities are related is still under discussion, given that the soft and porous structure of microgel particles adds complexity to the problem. An exhaustive discussion about the relationship between electrophoretic mobility and microgel charge is provided section 3 of Paper III.

3.3.4 Langmuir monolayers

The Langmuir film balance is a helpful technique to characterize the interfacial activity of microgels at the air-water interface. This technique allows the measurement of isotherms which relate the surface pressure and the area that microgels occupy at equilibrium [46].

Figure 3.4 shows a picture of the experimental system used in Paper VI of

this thesis. The pressure is measured via the force exerted on a Wilhelmy plate positioned vertically to the interface. Immersed in pure water this plate experiences a force which changes as soon as the microgels are carefully spread on the interface to form a monolayer. Then, the two-dimensional density is varied by moving two side barriers, compressing the monolayer. The force difference measured on the Wilhelmy plate is assumed to be the same as the pressure on the mobile barriers exerted by the microgels[47].
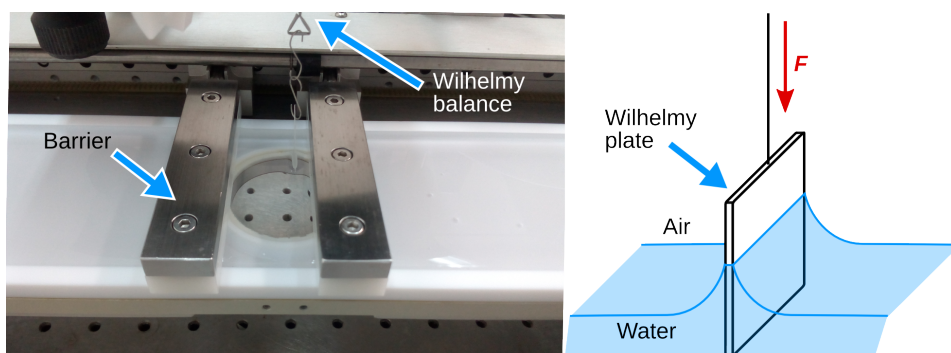
Figure 3.4: Langmuir film balance with the Wilhemy plate immersed in the air-water interface.

By analyzing the resulting isotherms is possible to determine the degree of microgel packing and deformation as the monolayer is compressed. In addition, an effective pair potential may be inferred from the two dimensional behaviour of the particles, although several assumptions have to be considered.

The characterization of the interfacial activity and arrangement of colloids at water/air and water/oil interfaces by means of the Langmuir film balance technique is widely known[46,48–50]. However, little research has been focus on collapsed microgels in the air-water interface.

References

[1] McQuarrie, D. A. *Statistical Mechanics*; University Science Books: Sausalito, 2000.

[2] Hansen, J.-P.; McDonald, I. R. *Theory of Simple Liquids*, 4th ed.; Academic Press: Oxford, 2013; p 619.

[3] Kirkwood, J. G. *The Journal of Chemical Physics* **1935**, *3*, 300–313.

[4] Ornstein, L.; Zernike, F. *Proc. Akad. Sci.(Amsterdam)* **1914**, *XVII*, 793–806.

[5] Rushbrooke, G. S.; Scoins, H. I. *Proc. R. Soc. Lond. A* **1953**, *216,*, 203–218.

[6] Rowlinson, J. S. *Reports on Progress in Physics* **1965**, *28*, 169.

References

[7] Lebowitz, J. L.; Percus, J. K. *Physical Review* **1966**, *144*, 251–258.

[8] Percus, J. K.; Yevick, G. J. *Physical Review* **1958**, *110*, 1–13.

[9] Moncho-Jordá, A. *The Journal of chemical physics* **2013**, *139*, 064906.

[10] Moncho-Jordá, A.; Anta, J. A.; Callejas-Fernández, J. *The Journal of chemical physics* **2013**, *138*, 134902.

[11] Moncho-Jordá, A.; Adroher-Benítez, I. *Soft matter* **2014**, *10*, 5810–5823.

[12] Shah, N. H. *Numerical Methods with C++ Programming*; PHI Learning Pvt. Ltd.: New Delhi, 2009; p 325.

[13] Ohshima, H. *Interface science and technology*; Elsevier Academic Press, 2006; pp xvi, 473 p.

[14] Ohshima, H. *J. Colloid Interface Sci.* **2008**, *323*, 92–97.

[15] Metropolis, N.; Ulam, S. *Journal of the American Statistical Association* **1949**, *44*, 335–341.

[16] Landau, D.; Binder, K. *A guide to Monte Carlo simulations in statistical physics*, 3rd ed.; Cambridge University Press: Cambridge, 2009.

[17] Metropolis, N.; Rosenbluth, A. W.; Rosenbluth, M. N.; Teller, A. H.; Teller, E. *The Journal of Chemical Physics* **1953**, *21*, 1087–1092.

[18] Quesada-Pérez, M.; Martín-Molina, A. *Soft Matter* **2013**, *9*, 7086–7094.

[19] Quesada-Pérez, M.; Ahualli, S. A.; Martín-Molina, A. *The Journal of chemical physics* **2014**, *141*, 124903.

[20] Fermi, E.; Pasta, J.; Ulam, S. *Los Alamos Report LA-1940* **1955**, *978*.

[21] Alder, B. J.; Wainwright, T. E. *The Journal of Chemical Physics* **1959**, *31*, 459–466.

[22] Frenkel, D.; Smit, B. *Understanding molecular simulation*, 2nd ed.; Academic Press: San Diego, 2002; p 638.

[23] Jorgensen, W. L.; Maxwell, D. S.; Tirado-Rives, J. *J. Am. Chem. Soc.* **1996**, *118*, 11225–11236.

[24] Kaminski, G. A.; Friesner, R. A.; Tirado-Rives, J.; Jorgensen, W. L. *J. Phys. Chem. B* **2001**, *105*, 6474–6487.

[25] Lindorff-Larsen, K.; Piana, S.; Palmo, K.; Maragakis, P.; Klepeis, J. L.; Dror, R. O.; Shaw, D. E. *Proteins Struct. Funct. Bioinforma.* **2010**, *78*, 1950–1958.

[26] Berendsen, H. J. C.; Grigera, J. R.; Straatsma, T. P. *The Journal of Physical Chemistry* **1987**, *91*, 6269–6271.

[27] Walter, J.; Ermatchkov, V.; Vrabec, J.; Hasse, H. *Fluid Phase Equilib.* **2010**, *296*, 164–172.

[28] Du, H.; Wickramasinghe, R.; Qian, X. *J. Phys. Chem. B* **2010**, *114*, 16594–16604.

[29] Berendsen, H. J. C.; van der Spoel, D.; van Drunen, R. *Computer Physics Communications* **1995**, *91*, 43–56.

[30] van Gunsteren, W.; Berendsen, H. GROMOS (GROningen MOlecular Simulation

package). 1987.

[31] Humphrey, W.; Dalke, A.; Schulten, K. *Journal of molecular graphics* **1996**, *14*, 33–38.

[32] Pelton, R.; Hoare, T. In *Microgel Suspensions: Fundamentals and Applications*; Fernandez-Nieves, A., Wyss, H. M., Mattsson, J., Weitz, D. A., Eds.; Wiley-VCH Verlag GmbH & Co. KGaA: Weinheim, Germany, 2011; pp 1–32.

[33] Pelton, R.; Chibante, P. *Colloids and Surfaces* **1986**, *20*, 247–256.

[34] Antonietti, M.; Basten, R.; Lohmann, S. *Macromolecular Chemistry and Physics* **1995**, *196*, 441–466.

[35] Denkinger, P.; Rey, A.; Burchard, W. *Die Makromolekulare Chemie, Rapid Communications* **1989**, *10*, 675–681.

[36] Slomkowski, S.; Alemán, J. V.; Gilbert, R. G.; Hess, M.; Horie, K.; Jones, R. G.; Kubisa, P.; Meisel, I.; Mormann, W.; Penczek, S.; Stepto, R. F. T. *Pure and Applied Chemistry* **2011**, *83*, 2229–2259.

[37] Ramos, J.; Forcada, J.; Hidalgo-Álvarez, R. *Chemical Reviews* **2014**, *114*, 367–428.

[38] Wu, X.; Pelton, R. H.; Hamielec, A. E.; Woods, D. R.; McPhee, W. *Colloid & Polymer Science* **1994**, *272*, 467–477.

[39] Imaz, A.; Forcada, J. *Journal of Polymer Science Part A: Polymer Chemistry* **2011**, *49*, 3218–3227.

[40] Hassan, P. A.; Rana, S.; Verma, G. *Langmuir : the ACS journal of surfaces and colloids* **2015**, *31*, 3–12.

[41] Ballauff, M. *Macromolecular Chemistry and Physics* **2003**, *204*, 220–234.

[42] Malvern Instruments, *Malvern Zetasizer SZ User Manual (MAN0485)*, 1st ed.; Malvern Instruments Ltd.: Worcestershire, 2013; p 250.

[43] Pérez-Fuentes, L. Specific effects of organic and inorganic ions in soft interfaces. Ph.D. thesis, Universidad de Granada, 2016.

[44] Ohshima, H. *Encyclopedia of Biocolloid and Biointerface Science 2V Set*; John Wiley & Sons, Inc.: Hoboken, NJ, USA, 2016; Chapter 33, pp 430–438.

[45] Miller, J. F.; Schätzel, K.; Vincent, B. *Journal of Colloid And Interface Science* **1991**, *143*, 532–554.

[46] Kim, J. Y.; Raja, S.; Stellacci, F. *Small* **2011**, *7*, 2526–2532.

[47] Oettel, M.; Dietrich, S. *Langmuir* **2008**, *24*, 1425–41.

[48] Detrich, Á.; Deák, A.; Hild, E.; Kovács, A. L.; Hórvölgyi, Z. *Langmuir* **2010**, *26*, 2694–2699.

[49] Geisel, K.; Isa, L.; Richtering, W. *Angew. Chem.* **2014**, *53*, 4905–4909.

[50] Fernández-Rodríguez, M. Á.; Rodriguez-Valverde, M. A.; Cabrerizo-Vilchez, M. A.; Hidalgo-Alvarez, R. *Advances in Colloid and Interface Science* **2016**, *233*, 240–254.

II
Results and discussion

Role of steric interactions on the ionic permeation inside charged microgels: Theory and simulations

Irene Adroher-Benítez[*], Silvia Ahualli[†], Alberto Martín-Molina[*], Manuel Quesada-Pérez[†], and Arturo Moncho-Jordá[*]

[*]Departamento de Física Aplicada, Facultad de Ciencias, Universidad de Granada, Campus Fuentenueva S/N, 18071 Granada, Spain.
[†]Departamento de Física, Escuela Politécnica Superior de Linares, Universidad de Jaén, 23700 Linares, Jaén, Spain.

Abstract

In this work we study the effect of the steric excluded-volume interactions between counterions and thermo-responsive ionic heterogeneous microgel particles. With this aim, we perform Monte Carlo simulations to calculate the microgel effective net charge and counterion distribution function inside and around the microgel for different degrees of swelling. These results are compared to the ones obtained solving the Ornstein-Zernike integral equations within the HNC approximation. For this purpose, the equilibrium polymer mass and charge distribution inside the microgel resulting from simulations are used as the input for the integral equations. Two different models are considered to quantify microgel-ion steric interaction. The model that considers polymer fibers formed by spheres demonstrates to be a very reliable way to predict counterion permeation in such microgels. Finally, integral equations are solved ignoring the steric interaction as well, in order to determine to what extent this effect is playing a significant role. The comparison between both predictions allows us to conclude that the microgel-ion steric repulsion has relevant effects on the counterion permeation if the polymer volume fraction of the microgel is high enough, and the integral equation theory is a powerful tool to quantitatively predict the local density profiles of ions inside and around the microgel, even in situations where the internal microgel charge and mass density is non-homogeneous.
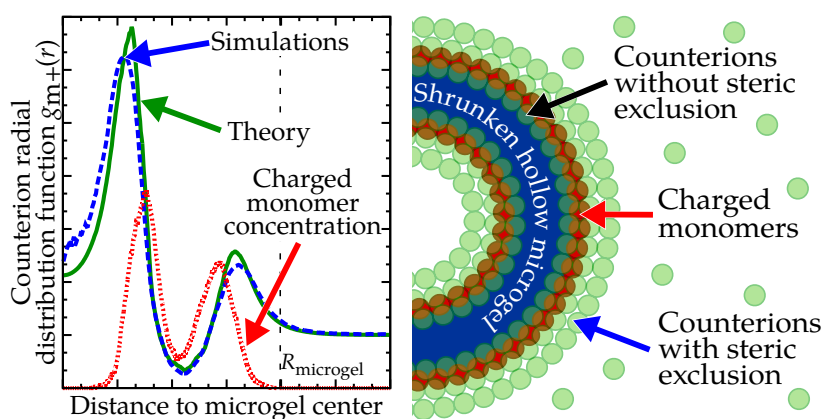
1 Introduction

The term microgel refers to a "colloidal suspension of gel particles"[1]. That is, they are porous particles formed by crosslinked polymer chains dispersed in a solvent. They are also called nanogels, as their diameter usually varies from 10 to 1000 nm. Their main feature is their ability to swell or shrink as a response to a wide variety of parameters such as temperature, pH, solute concentration or solvent nature[2,3]. Microgels respond to external stimuli much faster than macroscopic gels, with a velocity increased by some orders of magnitude[1]. This feature is an advantage for a broad range of biotechnological applications[4]. In particular, the design of new intelligent drug transport and delivery systems is gaining attention in recent years[5–7]. Microgel particles are suitable for this purpose, since a therapeutic molecule can be encapsulated inside the particle and be transported to different parts of the human body, avoiding its degradation before it reaches the place where it has to be released[8]. With this aim, microgels and the interaction with different solutes such as drugs and DNA, are being widely investigated[9–12].

Ionic microgels, formed by crosslinked polyelectrolyte chains, are essential for most of biomedical applications, because drugs and other biomolecules are usually charged solutes dissolved in the medium where microgels are dispersed. For this reason, many authors have developed theoretical studies to analyze the permeation of ions and solutes inside microgels and to estimate the swelling equilibrium state of the particle[13–16]. Most of these works assume that ion permeation inside the microgel is controlled exclusively by the electrostatic interactions. In principle, this is a good approximation for loose, expanded microgel networks, where the pore size between polymer fibers is large enough to guarantee that ions can freely penetrate. However, this may not be the case of denser shrunken microgels, where the large packing fraction of polymer network exerts an additional excluded volume repulsion that might partially hinder the migration of ions or other kind of solutes to the region inside the particle. This repulsive force is usually referred as steric interaction, and its study is the main goal of this work. Although there does not exist a general equation for the steric interaction between a crosslinked microgel and an incoming solute or ion valid for every type of particle, there are some approximated models that assume certain morphologies of the polymer network. These are based on the equilibrium partitioning effect, which states that solute concentration inside a neutral porous medium is smaller than the one in the bulk solution[17].

In this work we focus on the effect that the microgel-ion steric repulsive in-

teraction has on the permeation of counterions inside microgel particles that become heterogeneous as temperature increases. For this purpose, we use a novel hybrid method that blends Ornstein-Zernike integral equations and Monte Carlo simulations. On the one hand, Monte Carlo simulations have been previously used to study volume exclusion effects in gel systems with neutral solutes[18] so they are expected to be appropriate also for microgel particles. Even though this method requires more computational resources than integral equations, it provides accurate predictions of the equilibrium distribution of the cross-linked polymer network and the ionic density profiles. Microgel particles are simulated using a coarse-grained model, the so-called *bead-spring* model. This model has been widely used for both Monte Carlo and Molecular Dynamics simulations of different polyelectrolytes[19–26], gels[27–30], microgels[31–34], and even more complex mesoscopic systems (e.g., viruses[12]). Moreover, it has been successfully employed to compare simulation results with experimental swelling data of microgel particles, not only qualitatively but quantitatively as well[35].

On the other hand, Ornstein-Zernike integral equations with HNC closure relations have demonstrated to be a powerful tool to study the permeation of ions inside microgel particles[36]. We solve these equations for the three-component system microgel-coion-counterion using as input parameters the equilibrium density profiles of charged monomers and the polymer mass distribution obtained from simulations. This method allows the calculation of the pair radial distribution functions and, from them, the density profiles of ions inside and around the microgel particle. These results constitute a novelty in the sense that we are able to predict not only the net permeation of ions inside the microgel, but also to determine the region where they become preferentially adsorbed[36,37]. The integral equations formalism is also especially useful because it takes explicitly ion-ion correlations into account. These correlations, which arise from the finite size of the ions, can be very important at high electrolyte concentration, in regions where they are strongly confined or close to colloidal surfaces[38]. Moreover, non-linear effects resulting from highly charged colloid-ion systems can be studied with this method as well. The combination of simulations and integral equations provide a method to clearly estimate to what extent excluded volume forces influence the ionic permeation inside fibrous microgels.

Two important properties have been obtained using both methods, namely the microgel effective net charge and the counterion and coion radial distribution functions. On the one hand, the effective net charge is defined as the sum of the total charge of the porous particle, considering as well inner ions, with

their respective positive or negative charge. This magnitude strongly depends on the number of counterions that have penetrated inside the microgel particle, and represents an estimate of how efficiently the microgel bare charge has been screened. Its importance may be seen in many aspects. For instance, effective net charge controls the volume phase transition of charged microgel particles under weak screening conditions[39]. Moreover, stability of the suspensions strongly depends on this quantity, because it controls the electrostatic interaction between colloidal particles[36,40]. On the other hand, we also determine the ionic density profiles. They provide detailed information about where ions are preferentially adsorbed inside the microgel particles, which is in general difficult to achieve experimentally. This is really helpful to study the local effects of microgel-ion interaction that arise for highly charged microgels and low ionic strengths. Up to now, most studies regarding interaction of solute with gels and microgels have been performed considering that the polymer packing fraction and the charge distribution inside the microgel are homogeneous[41–43]. However, when solute concentration is low and microgel charge distribution is non-homogeneous, the counterion adsorption inside the microgel becomes highly dependent on the charge and polymer mass distribution. These local effects are expected to have a relevant effect on many microgel applications, in particular in drug transport and delivery.

In addition, by comparing the results given by both integral equations and Monte Carlo simulations we show that electrostatic interactions are not enough to describe the ionic permeation inside the microgel in thermal conditions at which the particle is collapsed. This finding supports the inclusion of an additional steric microgel-ion repulsion in the theoretical model to correctly explain ionic permeation close to the shrunken state. Once this steric effect is taken into account in this work, the comparison between theory and simulations is in general very good.

This paper is organized in the following manner. In the first section we describe the theoretical framework and explain the numerical resolution of Ornstein-Zernike integral equations. Monte Carlo simulations are described in the next section. Then, the results obtained by both methods are shown and discussed, and finally, the conclusions of this work are summarized.

2 Theory

The system under study is a mixture of spherical microgel particles dispersed in water with 1:1 electrolyte. As the solvent is considered a background continuum, the system is formed by a ternary mixture in equilibrium of N_m microgels, N_+ counterions, and N_- coions. Their bare charges are given, respectively, by $-Ze$, $+e$, and $-e$, being e the elementary charge. Hence, to fulfill electroneutrality we get $N_+ = N_- + ZN_m$. Polymer mass distribution and charge distribution inside the microgel network are obtained from the Monte Carlo simulation results.

2.1 Particle interactions

In order to apply the integral equation method is necessary to define the pair interactions between any type of particle of the system (counterions, coions and microgel particles). Ion-ion interaction is assumed to be a combination of a short-range hard-core potential with a long-range Coulombic tail,

$$\beta V_{ij}(r) = \begin{cases} \infty & r \le (\sigma_i + \sigma_j)/2 \\ \dfrac{z_i z_j l_B}{r} & r > (\sigma_i + \sigma_j)/2 \end{cases}, \tag{I.1}$$

where r is the distance between the centers of the ions, σ_i and z_i are, respectively, the diameter and electric charge of particle i, and $\beta \equiv 1/(k_B T)$. l_B is the so-called Bjerrum length, defined as $l_B \equiv e^2/4\pi\epsilon_r\epsilon_0 k_B T$, where ϵ_0 is the vacuum permittivity, k_B is the Boltzmann constant and T the absolute temperature. Bjerrum length also depends on temperature T through the relative permittivity ϵ_r. In this work we assume that the solvent is water, with a permittivity given by the following T-dependence[44]

$$\epsilon_r(T) = 5321\,T^{-1} + 233.76 - 0.9297\,T + 0.1417 \cdot 10^{-2}\,T^2 - 0.8298 \cdot 10^{-6}\,T^3. \tag{I.2}$$

It is important to note that this pair interaction takes the finite size of the ions into account, which can induce relevant correlations at sufficiently large electrolyte concentration.

In order to obtain realistic predictions for ion penetration inside the microgel particle, a suitable model for microgel-ion interaction is required. When ions diffuse through microgel pores, electrostatic interaction may not be the only one that intervenes. There might be also an effective steric repulsion, whose relevance increases as microgel shrinks, that prevents the ion permeation. This

repulsion is present even in the limit of point-like ions, since part of the volume available for the ion is already occupied by the polymer fibers. For ions of finite size, the excluded volume effect becomes logically more important, as ions also have to fit inside the internal pores of the microgel. Here, we assume that the microgel-ion potential can be split into two additive contributions, given by the electrostatic and steric terms, respectively

$$V_{\text{mi}}(r) = V_{\text{mi}}^{\text{elec}}(r) + V_{\text{mi}}^{\text{ster}}(r).$$ (I.3)

This potential only depends on the distance between the ion and the microgel center, r, because microgel particles are considered spherical. The electrostatic contribution can be calculated from the equilibrium spatial distribution of charged monomers. Note that in this work we do not assume any model for the distribution of charged groups inside the microgels, but instead we use the distribution actually obtained from the Monte Carlo simulations. The expression of the electrostatic interaction potential between the microgel and certain ion located outside the microgel at a distance r from the its center can be expressed as

$$\beta V_{\text{mi}}^{\text{elec}}(r) = -\frac{Z\, z_i\, l_{\text{B}}}{r}, \; r > R_{\text{m}}.$$ (I.4)

For $r < R_m$, the electrostatic interaction depends on the specific distribution of charged groups and must be obtained numerically from the electric field generated by the microgel particle, $E(r)$:

$$\beta V_{\text{mi}}^{\text{elec}}(r) = \beta V_{\text{mi}}^{\text{elec}}(R_{\text{m}}) - z_i \int_r^{R_{\text{m}}} E(r)\mathrm{d}r, \; r \leq R_{\text{m}}.$$ (I.5)

From Gauss's law, the electric field is given by

$$E(r) = -\frac{eZ_{\text{in}}(r)}{4\pi\epsilon_{\text{r}}\epsilon_0 r^2},$$ (I.6)

where $Z_{\text{in}}(r)$ is the number of charged monomers enclosed within a sphere of radius r. It is calculated by integration of number density of charged monomers, $\rho_{\text{c}}(r)$, which is directly obtained from the simulations:

$$Z_{\text{in}}(r) = \int_0^r 4\pi r'^2 \rho_{\text{c}}(r')\mathrm{d}r'.$$ (I.7)

The next step involves the deduction of some expression for the steric repulsion that appears when an uncharged solute permeates through the polymeric microgel network and experiences the volume exclusion exerted by the

polymer fibers. This interaction depends on the size of the incoming solute, the size of monomeric units, the polymer packing fraction and, in general, on the internal morphology of the microgel polymer network. In this work we use two different models previously employed by several authors[17,36,45]. In the first one the internal structure of the microgel is approximated by an assembly of randomly placed spherical monomers[46]. The second model (also called the Ogston model[47]) assumes that the internal polymer distribution is given by an assembly of infinitely long cylinders of constant radius, which are randomly distributed and mutually interpenetrable. Both of them may be expressed as the following equation for the steric microgel-ion interaction

$$V_{\mathrm{mi}}^{\mathrm{ster}}(r) = -\ln[1 - \phi(r)]\left(1 + \frac{\sigma_{\mathrm{i}}}{\sigma_{\mathrm{f}}}\right)^n,$$ (I.8)

where $\phi(r)$ is the local polymer volume fraction inside the microgel, σ_{i} is the diameter of the incoming ion, and σ_{f} stands for the typical size of an elementary unit of the polymer network. The exponent n is given by $n = 3$ if we assume that the microgel is formed by an assembly of spherical monomers, and $n = 2$ if we use the Ogston model instead. In the first case, σ_{f} corresponds to the monomer diameter, σ_{mon}. In the second case, the effective diameter of the fiber is given by $\sigma_{\mathrm{f}} = \sqrt{2/3}\sigma_{\mathrm{mon}}$ [18].

It should be emphasized that both analytical expressions for the steric repulsion have been corrected to take the overlapping volume between the polymer fibers into account[48]. As a result of this, both models are consistent with the limiting cases of high and low volume packing fraction. That is, for $\phi(r) \to 0$ there is enough room for ions to penetrate, so $V_{\mathrm{mi}}^{\mathrm{ster}} \to 0$. If the polymer volume fraction is very high, the microgel tends to behave as an impenetrable hard sphere, so $V_{\mathrm{mi}}^{\mathrm{ster}} \to \infty$.

In Figure I.1 both microgel-ion steric potentials are plotted as a function of the polymer packing fraction, using the same parameter values considered in simulations and theoretical calculations. It is observed that the steric interaction is more repulsive for exponent $n = 3$ than for $n = 2$. For $\phi \to 1$ both interactions diverge, so microgel becomes an impenetrable particle.

Finally, the bare microgel-microgel interaction should also be known in order to obtain correct theoretical predictions for suspensions at finite microgel concentration. This interaction is in principle really difficult to determine, specially when microgels are in overlapping configurations, in which elastic forces arise in addition to the electrostatic ones. However, in this work we are only interested in the study of the ionic density profiles around a single microgel in
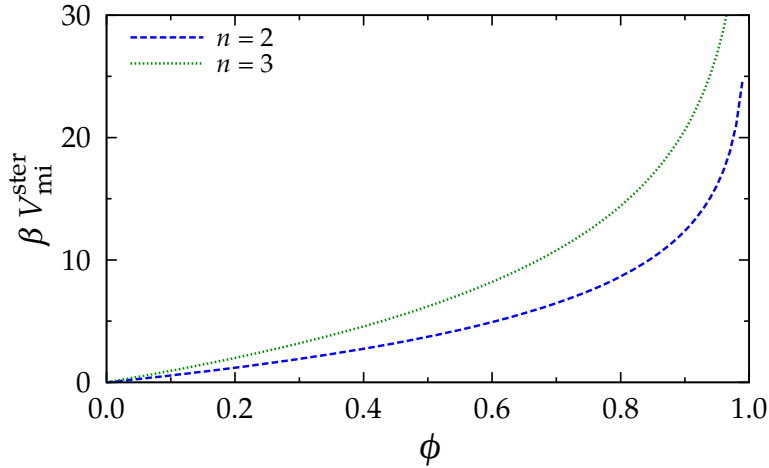
Figure I.1: Microgel-ion steric potential as a function of microgel volume packing fraction. Blue dashed curve corresponds to $n = 2$ (Ogston model), while the green dotted to $n = 3$, in equation (I.8). To calculate $\beta V_{\mathrm{mi}}^{\mathrm{ster}}(r)$ we have used the same values considered in simulations and theoretical calculations, that is, $\sigma_{\mathrm{ion}} = 0.7$ nm, $\sigma_{\mathrm{mon}} = 0.65$ nm, and $\sigma_{\mathrm{f}} = \sqrt{2/3}\sigma_{\mathrm{mon}}$.

the limit of infinite dilution of particles. Hence, there is no need to include this interaction in the theoretical background.

2.2 Ornstein-Zernike integral equations

The equilibrium radial distribution functions of counterions and coions around and inside the microgel particle, $g_{\mathrm{mi}}(r)$, can be obtained by solving Ornstein-Zernike (OZ) integral equations for the microgel (m), counterion (+) and coion (−) mixture. For a three-component mixture, the OZ equations are written in the Fourier space as a set of six algebraic equations,

$$\hat{h}_{\mu\nu}(k) = \hat{c}_{\mu\nu}(k) + \sum_{\lambda=1}^{3} \rho_{0\lambda}\hat{c}_{\mu\lambda}(k)\hat{h}_{\lambda\nu}(k), \qquad \text{(I.9)}$$

where $\hat{h}_{\mu\nu}(k)$ and $\hat{c}_{\mu\nu}(r)$ are the Fourier transforms of the total and direct correlation functions, respectively, and $\rho_{0\lambda}$ stands for the number density of component λ in the bulk. In the limit of very dilute microgel suspension ($\rho_{0\mathrm{m}} \to 0$) the six equations are decoupled into three groups which can be solved in three different steps. In the first step, the ion-ion correlations are calculated. Then, they are used in the second step to determine the microgel-counterion and microgel-coion correlations by solving the following set of two equations. Finally, there

is still remaining a last integral equation which provides the microgel-microgel correlation. This last equation allows the calculation of the effective interaction between microgels particles induced by the presence of electrolyte. However, in this work we are not interested in this property, so we omit this part and focus on the microgel-ion correlations. As this procedure has been already used in previous works [13,36,37], we encourage the reader to dip into them for further details.

In order to solve these equations, it is strictly necessary to complete them with additional closure relations connecting $\hat{h}_{\mu\nu}(r)$ and $\hat{c}_{\mu\nu}(r)$ with the interparticle interaction potentials $V_{\mu\nu}(r)$ (defined in equations (I.1) and (I.3)). In this work, the *Hypernetted-chain approximation* (HNC) [49] is used, due to the fact that it has demonstrated to be a quite precise approximation for the kind of interactions involved in mixtures of ionic microgel suspensions with electrolyte [13,36,37]. It is given by the following equation:

$$h_{\mu\nu}(r) = e^{h_{\mu\nu}(r) - c_{\mu\nu}(r) - \beta V_{\mu\nu}(r)} - 1. \tag{I.10}$$

To solve OZ-HNC equations we make use of Picard method of successive approximation [50]. Once calculated $h_{\mu\nu}(r)$ and $c_{\mu\nu}(r)$, radial distribution functions can be obtained straightforwardly,

$$g_{\mu\nu}(r) = \frac{\rho_{\mu\nu}(r)}{\rho_{\nu 0}} = h_{\mu\nu}(r) + 1. \tag{I.11}$$

Picard method starts with an approximated initial guess for the direct correlation functions, $c_{\mu\nu}^{(0)}$, and after an iteration, a new value $c_{\mu\nu}^{(1)}$ is calculated. The procedure is repeated until convergence of the two last steps of the method is achieved. However, for highly charged microgels, as the one object of this study, Picard method does not converge in just one realization. It is necessary to develop an adaptive method to increase gradually the microgel charge Z which enhances the numerical convergence: the last value of $c_{\mu\nu}^{(i)}$ calculated is used in the next realization of Picard method, in which the microgel charge is increased until the actual charged is achieved Z.

3   Simulations

In the simulation procedure the microgel particle is modeled as a network of crosslinked polymer chains. Monte Carlo simulations are carried out within a coarse-grained model for polyelectrolytes known as the bead-spring model.

In this framework, monomer units of the polymer chain and ions are considered spheres, whereas the solvent is considered as a dielectric continuum[24,30]. Each chain of the microgel consists of a sequence of 8 spherical monomer units (beads) connected by tetrafunctional crosslinkers of the same species than monomers. This number of monomers per chain can be considered typical for highly crosslinked networks.[35] The microgel simulated here is made of 206 chains connected by 133 crosslinkers. The charge of the microgel is conferred by adding beads of each chain with the negative elementary charge, e, as a result of having ionizable groups. In this work, we explore particles with 1 ionized group per chain. The simulation cell also contains ionic species, both cations and anions, as well as excess of cations required to assure an electroneutral system. The ions are also modeled as spheres, whose diameters are $\sigma_{ion} = 0.7$ nm including the corresponding hydration shell.

This hydrated ion size is in agreement with the values experimentally estimated for some monovalent cations and anions by Israelachvili,[51] who compiled data from different techniques. However, for highly concentrated microgel suspensions, the effect of excluded volume interactions could be overestimated using this ion size, since the solvation shell of the ions becomes less relevant in those cases. For that reason, we have also performed simulations considering $\sigma_{ion} = 0.4$ nm, in order to discern whether steric repulsion still plays an important role. In addition, the former diameter used here could be representative for some drugs, such as theophylline or caffeine[52], and may give an approximation of the excluded volume interactions in microgel-drug systems.

Interactions between all particles in the simulation cell are briefly summarized as follows (more details may be found in a previous work[53]). The short-range repulsion between any pair of particles (monomeric units or ions) due to excluded volume effects is modelled by means of the purely repulsive Weeks-Chandler-Andersen (WCA) potential[27,28,54,55]:

$$V_{WCA}(r) = \begin{cases} 4\epsilon_{WCA}\left(\dfrac{\sigma^{12}}{r^{12}} - \dfrac{\sigma^6}{r^6} + \dfrac{1}{4}\right) & r \leq 2^{1/6}\sigma \\ 0 & r > 2^{1/6}\sigma \end{cases} \tag{I.12}$$

where r is the center to center distance between a given pair of particles, $\epsilon_{WCA} = 4.11 \cdot 10^{-21}$ J, and $\sigma = (\sigma_i + \sigma_j)/2$, where σ_i is the particle diameter of component i. The interaction connecting monomer units and crosslinkers with their neighbors is modeled by harmonic bonds,

$$\beta V_{bond}(r) = \frac{k_{bond}}{2k_B T}(r - r_0)^2, \tag{I.13}$$

53

where $k_{\mathrm{bond}} = 0.4$ N/m is the elastic constant and $r_0 = 0.65$ nm is the equilibrium bond length. All the charged species interact through the Coulomb potential,

$$\beta V_{ij}^{\mathrm{elec}}(r) = \frac{z_i z_j l_{\mathrm{B}}}{r},\tag{I.14}$$

where z_i is the valence of species i.

The thermo-responsive character of microgels comes from hydrophobic forces. When non-polar macromolecules are inserted into an aqueous medium, water molecules rearrange their hydrogen bonds and form a structure like a cage, generating a high degree of local order. When temperature increases, the total number of water molecules structured around the hydrophobic solute decreases. To minimize the loss of entropy the number of non-polar molecules exposed to the solvent is reduced aggregating them: the microgel shrinks. In this work, the hydrophobic force is modeled through an interaction potential that consists in a smooth approximation of the square-well potential (previously used by other authors[56,57]) whose depth increases with temperature, given by the following equation:

$$V_{\mathrm{hyd}}(r) = -\frac{\varepsilon_{\mathrm{h}}(T)}{2}\{1 - \tanh[k_{\mathrm{h}}(r - r_{\mathrm{h}})]\},\tag{I.15}$$

where $\varepsilon_{\mathrm{h}}(T) < 0$ is the depth of the potential, r_{h} is its range, and k_{h} is fixed so that $V_{\mathrm{hyd}}(0.9 r_{\mathrm{h}}) = 0.9 \varepsilon_{\mathrm{h}}$. The potential depth obeys an increasing sigmoid function to reproduce the behavior of thermo-shrinking gels[58],

$$\varepsilon_{\mathrm{h}}(T) = -\frac{\varepsilon_{\mathrm{max}}}{2}\{1 + \tanh[k_{\varepsilon/2}(T - T_{\varepsilon/2})]\}.\tag{I.16}$$

$\varepsilon_{\mathrm{max}}$ is the maximum depth of the hydrophobic potential and $k_{\varepsilon/2}$ is proportional to the slope of the function at the point where $\varepsilon_{\mathrm{h}}(T_{\varepsilon/2}) = -\varepsilon_{\mathrm{max}}/2$. The dependence of the interaction parameter ε_h with temperature is shown in the inset of Figure I.2. The behavior of the potential is inspired in physical grounds from the model of hydrophobic interaction developed by Kolomeisky and Widom.[59] However, a previous work showed that this potential leads to unphysical volume fractions at high temperatures.[58] For that reason, a phenomenological potential with a limited depth has been preferred. The values of its parameters were obtained simultaneously matching several experimental data sets on six different microgels with different fraction of charged monomers and temperatures ranging from 10 to 60 ºC.[35] In a subsequent work,[60] it was also checked that these parameters also justified the behavior of a poly(NIPAM)-based gel with a very different crosslinker density. It should be also mentioned that poly(NIPAM) is

considered a model of thermoresponsive polymer, and other polymers with potential applications as drug carriers exhibit similar lower critical solution temperatures[61,62]. Thus realistic simulation results are expected (at least to some extent) if this potential is used. In any case, it should be kept in mind that this hydrophobic potential is operative only for uncharged monomers, since charged groups are considered hydrophilic rather than hydrophobic beads.

Nevertheless, the choice of hydrophobic potential employed in the simulations and, in particular, the dependence of ε_h with T will depend on the specific nature of the polymer fibers of the microgel and the solvent conditions. Therefore, the results predicted in this work may experience some variations when applied to other kind of microgel particles. In spite of this, the predictions deduced in this work represent a good qualitative representation that illustrates the thermal response of real ionic solutions of microgels.

Simulations are performed using the canonical ensemble, in which volume, temperature and number of particles are kept constant. All the simulations are carried out in a cubic box with a length L and periodic boundary conditions. The simulation box is large enough to contain a single microgel particle and a significantly developed electric double layer around it. More specifically, L is calculated as $L \approx 2(R_0 + 4l_D)$, where R_0 is an estimate of the radius of the microgel in the absence of additional electrolyte and l_D is the Debye screening length. For instance, for 1 and 100 mM, the L-values employed are 100 and 34 nm, respectively, much larger than the Debye lengths (9.67 and 0.967 nm at 288 K, respectively). Thus the microgel do not feel significantly the electrostatic repulsion of periodic images. The initial configuration of the microgel and their counterions used in the runs in the presence of salt were obtained from previous simulations in the absence of salt. After this preliminary equilibration, ions coming from the salt were added at random positions and the genuine run in the presence of salt started. Two types of MC moves were employed: i) usual single-particle displacements; ii) rescaling of the positions of all the particles multiplying by a factor to reduce the thermalization time (see reference [33] for further details about this size rescaling). In this way, small changes in the size of the microgel (maximum 1%) were explored. In the single-particle moves, the maximum displacements of monomers and ions were individually adjusted to achieve acceptance ratios of 30-70%. In both equilibration runs, at least 10^8 MC moves were employed. To check that the equilibration had been reached, the evolution of some properties, such as the radius of gyration, was monitored averaging on batches of $5 \cdot 10^4$ steps. At least, $2 \cdot 10^8$ MC moves were employed for averaging. The electrostatic energy was computed through a clas-

sical implementation of Ewald sums, following some practical guidelines given by Linse.[63] The cutoff distance employed in the real space was $L/2$. The calculation of the reciprocal contribution to energy was estimated using sets of integers (n_x, n_y, n_z) that verified $\sqrt{n_x^2 + n_y^2 + n_z^2} \leq 4$ (reciprocal cutoff). The parameter characterizing the width of Gaussian charge distributions was $\alpha = 5/L$ (see review by Linse for notation and further details). The maximum relative error admitted in the real-space contribution to energy was 10^{-3}. Additional information about methods to compute long-range interactions can be found in the work by Arnold and Holm[64].

4 Results and discussion

Monte Carlo simulations were performed at two different concentrations of monovalent salt, 1 mM and 100 mM. We consider this salt to be NaCl, and assume ion sizes given by the corresponding effective hydrated diameters in conditions of high dilution. Their values are shown in Table I.1, together with other properties of the microgel particle, namely the number of charged monomers in the microgel, the size of the composing monomers, and the temperature interval in which our study is performed.

Parameter	Symbol	Value
Monomer diameter	σ_{mon}	0.65 nm
Ion diameter	σ_{ion}	0.70 nm
Microgel charge	Z	206 e
Temperature	T	20-60 °C

Table I.1: Input parameters of Monte Carlo simulations used to generate microgel particles in presence of electrolyte.

Before comparing the simulation results with the theoretical predictions we show some results regarding the thermal response of the simulated microgel particles.

4.1 Thermal response

Due to the fact that attractive hydrophobic interactions between monomers of the microgel are temperature dependent, the microgel becomes a thermoresponsive particle. This means that its internal morphology and the degree of swelling changes with temperature. The equilibrium conformation is a balance

between many contributions, namely the hydrophobic, elastic and electrostatic forces. Therefore, the final equilibrium state not only depends on temperature but also on the electrolyte concentration. In order to determine the thermal response of the microgels we performed a total amount of 9 simulation runs with temperatures ranging from 20 °C to 60 °C for each salt concentration.

Figure I.2 shows microgel effective average radius R_m as a function of temperature. It is defined as $R_m = \sqrt{5/3}R_g$, where R_g is the radius of gyration of the microgel particle. For a spherical microgel with a homogeneous distribution of mass, R_m represents the external radius of the microgel. As observed, the temperature range considered in this work provides different swelling ratios of the microgel particle. For low temperature, microgel particle is swollen, but when temperature is increased it undergoes a volume transition to shrunken states. The transition temperature is about 34 °C, which is consistent with the experimental response of many types of microgel particles.
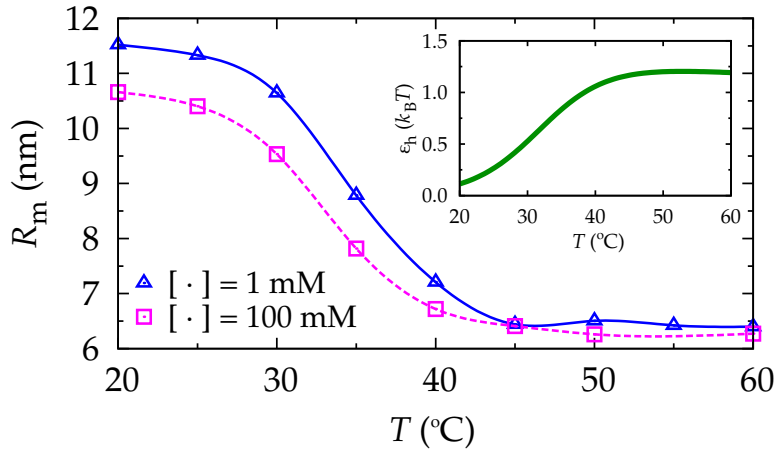
Figure I.2: Average effective radius of the simulated microgel as a function of temperature for two salt concentrations, 1 mM and 100 mM. Error bars are not shown because they are smaller than the size of the symbols. The top x axis shows the values of the deph of the hydrophobic potential for each temperature considered, but note that they are not scaled. In the inset, the depth of the potential ε_h used in the simulations is plotted against the temperature.

With regard to the response with the electrolyte concentration, the shrinking behavior as a function of temperature does not change significantly with the salt concentration. However, at the same temperature, for 100 mM the microgel radius is smaller than for 1 mM. This is a well-known reasonable result, caused by the screening of the microgel charge. In fact, for large electrolyte concentration, repulsive Coulombic interactions between monomers (which enhance

the particle swelling) are more efficiently screened by the counterions. Consequently, the equilibrium swelling state shifts to more shrunken configurations[1]. In addition, the penetration of counterions exerts an osmotic pressure that induces the particle swelling. This pressure difference inside and outside the microgel is roughly inversely proportional to the salt concentration[65], and this is why the swelling observed for 100 mM is less important than for 1 mM. Nevertheless, when microgel is collapsed at high temperature, the swelling state is dominated by monomer-monomer hydrophobic forces, so counterion effects become not very significant, leading to very similar values of R_m for both salt concentrations.

The volume change with the temperature is clearly appreciated in Figure I.3, where the local concentration of polymers and charged monomers are plotted, as well as the snapshots of the microgel, at four different temperatures. As temperature increases, a progressive shrinking in the microgel structure becomes noticeable. In the swollen state, the internal morphology of the particle is consistent of large pores through which ions can penetrate, but as particle shrinks, the size of the pores decreases, even disappearing for high temperature. However, the decrease of the particle size with the temperature is not the only effect that arises. The internal structure is also affected, as shrunken microgels tend to arrange in a non-homegeneous form in the inner region of the particle. This effect has been previously observed in small-sized microgels of few tens of nanometers similar to the ones employed in this work, where the typical length of the interconnected chains is of the same order of magnitude of the size of the particle. As mentioned above, charged monomers are considered hydrophilic (rather than hydrophobic) beads, thus they are not attracted by the uncharged ones. What is more, when uncharged beads collapse due to attractive hydrophobic forces, they would tend to segregate the hydrophilic monomers to minimize the free energy. Consequently, many of the charged beads would be displaced towards the outer and inner surfaces of the monomer clusters, as shown in the Figure for high temperature. In some cases, a few interconnected voids can also be formed in this segregation process instead of a unique hollow[33].

Simulation results not only provide the mass and charge distribution of the microgel network, but also the density profiles of counterions and coions inside and around the particle. In the following sections we discuss these properties. We first analyze the results in terms of a global property such as the effective microgel charge, and then we discuss in more detail the local properties by studying the radial distribution function of counterions. Simulation data are
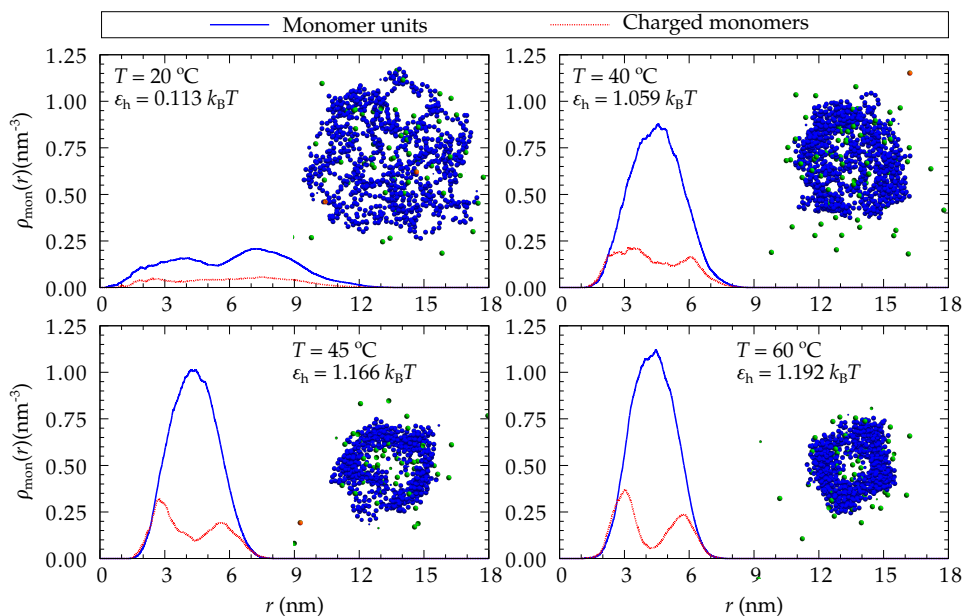
Figure I.3: Polymer (formed by neutral monomers, charged monomers, and crosslinkers) and charged monomer concentration as a function of the distance to microgel center, for different temperatures and hence distinct deph of hydrophobic potential and degree of swelling. For each temperature, a slice of the central part of the simulation box is shown, where cross-sections of the microgel particles can be visualized. Swollen microgels show a more homogeneous structure than the shrunken ones, in which an inner hole is formed. Green spheres represent counterions, while orange ones represent coions.

compared to the theoretical predictions applying the two models for the steric interaction described in equation (I.8). For this purpose, we make use of the local polymer volume fraction, $\phi(r)$, and the local distribution of charged monomers, $\rho_c(r)$ as input parameters to determine the microgel-ion electrostatic and steric interactions (see equations (I.4), (I.5), and (I.8)). Then, these interactions are employed in the Ornstein-Zernike integral equation method to finally obtain the ionic radial distribution functions, $g_{m+}(r)$ and $g_{m-}(r)$. They can be compared to the simulated ones to check whether the theory is able to properly account for the effect of the steric interaction in conditions of charge and mass heterogeneity.

4.2 Effective charge

A very useful way to quantify the global efficiency of the ionic permeation inside a microgel is to study the effective charge of the microgel particle, Z_{eff}. It is straightforwardly calculated from ionic density profiles inside the microgel particle as

$$Z_{eff} = -Z + 4\pi \int_0^{R_m} [\rho_{m+}(r) - \rho_{m-}(r)] r^2 dr, \qquad (I.17)$$

where Z is the number of charged monomers of the microgel. The ionic density profiles $\rho_{m+}(r)$ and $\rho_{m-}(r)$ have been calculated from their radial distribution functions through equation (I.11).

For instance, a small value of Z_{eff} implies a high degree of counterion penetration. If this happens, the microgel bare charge is strongly screened by the the cloud of counterions, reducing the electrostatic repulsion between microgels. This could lead to a colloidal destabilization of the microgel suspension. Indeed, Z_{eff} is very sensitive to swelling and shrinking of microgel particle. For this reason, it is particularly suitable to study the effect of the steric repulsion on the ion permeation[36]. If counterions penetrate inside the microgel, Z_{eff} is expected to decrease owing to screening of the bare charge. On the contrary, if counterions cannot

The effective charge is very helpful to characterize the permeation as a function of the swelling ratio because it is very sensitive to swelling and shrinking of microgel particle. For this reason, it has been previously employed to study the steric interaction[36]. If counterions penetrate inside the microgel, Z_{eff} is expected to decrease owing to screening of the bare charge. On the contrary, if counterions cannot permeate, they accumulate in a external shell around the microgel, leading to a weaker charge screening, and so to a higher value of the effective charge.

In principle, one would expect an increase of the effective charge with temperature. Firstly, because an increase of the temperature leads to a weakening of the electrostatic attraction of counterions to the microgel particle (compared to the thermal energy, $k_B T$), so counterions are less likely to diffuse inside, enhancing the effective charge. Secondly, because the reduction of the microgel size with temperature implies that it is necessary to concentrate the internal counterions in a much smaller volume. Hence, the electrostatic repulsion between pairs of counterions pushes some of them out of the particle, leading to an increase of Z_{eff} too. Finally, the particle shrinking at high temperatures causes an increase of the polymer volume fraction, which enhances the steric repulsion between counterions and the polymer network. As a consequence of

this, counterions are expelled from the interior of the particle in shrunken configurations, which makes charge screening lower than if they did not interact sterically.

Figure I.4 displays the average values of Z_{eff} obtained in the simulations as a function of temperature (symbols) for the two studied electrolyte concentrations, assuming $\sigma_i = 0.7$ nm for the ion diameter (numerical errors below 5% in all cases). The monotonic increase of the effective charge with temperature may be clearly observed for a salt concentration of 100 mM (see top graph of Figure I.4). However, for 1 mM (bottom graph) this increase is weaker and some fluctuations arise. This effect can be attributed to the existence of inhomogeneities in the distribution of the microgel bare charge. As shown above, the charge and mass distribution of the small-sized microgel develop an internal region with low polymer concentration surrounded by a corona of high density. This heterogeneous morphology provides plenty of space in the center of the particle, so counterions are able to better accommodate inside, avoiding counterion-counterion repulsion. The charge heterogeneity induces a decrease of $|Z_{eff}|$, and competes with the effect of the counterion obstruction explained above. The reason why this effect becomes less important at high salt concentration relies simply on the screening of the electrostatic forces.

Figure I.4 also shows the theoretical results obtained under three different approximations. In the first one we neglect the steric repulsion and assume that microgel and ions interact exclusively through electrostatic interactions (dashed line). In the other two situations the steric effect is included using two different exponents in equation (I.8): $n = 2$ and $n = 3$ (dotted and solid lines, respectively).

One of the most remarkable results that we may extract from the comparison between simulations and theory is that the microgel-ion steric repulsion should be considered in the model to account for the counterion permeation in shrunken microgels, at least for ionic sizes comparable to or larger than $\sigma_i = 0.7$ nm, the ones studied here. As can be seen, the curve obtained by solving Ornstein-Zernike equations neglecting volume exclusion effects overestimates the charge screening effect for both salt concentrations at high temperatures (high polymer volume fractions). In other words, in the absence of steric repulsion, the electrostatic interaction alone can sometimes lead to values of Z_{eff} smaller than the ones observed in simulations. However, this Figure also shows that the effect of steric repulsion is not so important for swollen microgels (low temperatures in our case). In fact, Claudio *et al.*[31] succeeded in reproducing the ionic distribution of a microgel in a good solvent using a Poisson-Boltzmann
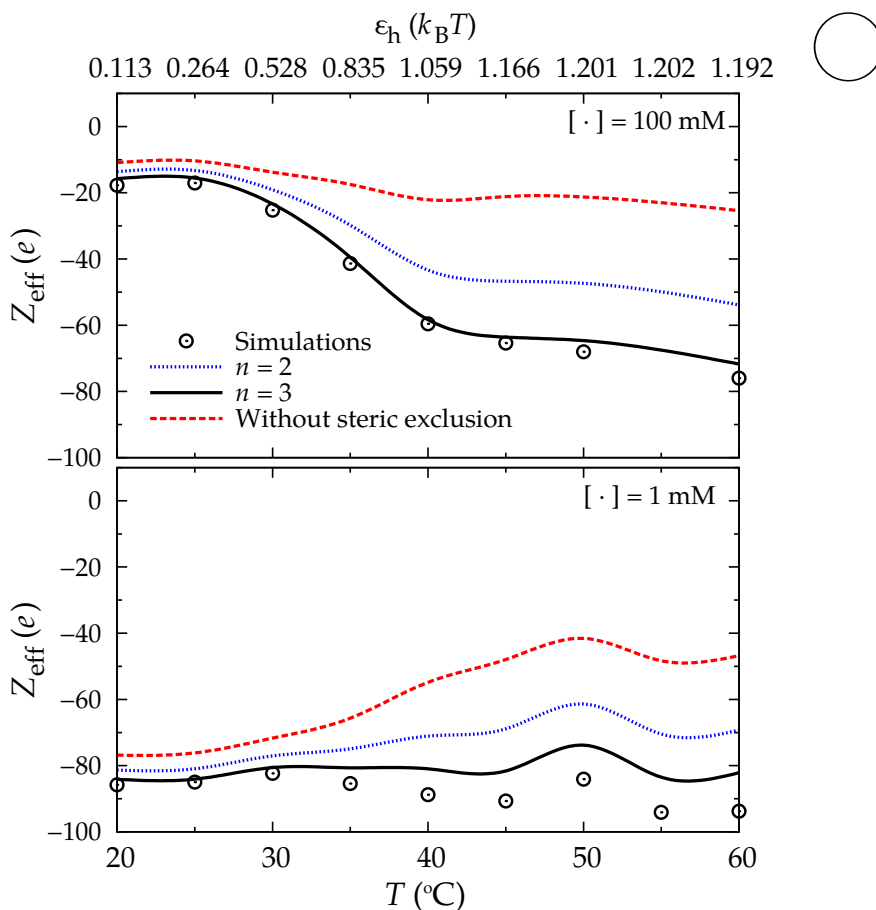
Figure I.4: Microgel effective charge as a function of temperature. Black dots stand for Z_{eff} measured in simulations, while the curves are theoretical predictions calculated by solving Ornstein-Zernike (OZ) equations for three different cases: taking into account $n = 2$ and $n = 3$ in equation (I.8) for steric interaction, and ignoring the steric repulsion, $V_{\text{mi}}^{\text{ster}}(r) = 0$. The top graph has been obtained considering 100 mM of electrolyte concentration, while the bottom one corresponds to 1 mM. Error bars are not shown because they are smaller than the size of the symbols. The top x axis shows the deph of the hydrophobic potential for each temperature considered, but note that the values are not scaled.

model (that does not account for excluded volume effects).

When including the steric effect, we see that the results obtained using $n = 3$ in equation (I.8) provides much better quantitative agreement with simulations than those obtained with the Ogston model ($n = 2$). In fact, the Ogston model underestimates the steric repulsion leading to a smaller values of $|Z_{\text{eff}}|$ com-

pared to simulation data. This means that an assembly of randomly placed spheres provides a more accurate representation of the internal morphology of the microgel than a network of long rigid fibers. This is a quite reasonable conclusion, given that polymer fibers are treated in our simulations as being formed by short interconnected chains with only 8 spherical monomers. However, it should be pointed out that these results do not imply that the use of $n = 3$ in equation (I.8) is always more accurate than the Ogston model for any polymer network in equilibrium with a permeating solute. For instance, previous simulation studies of macroscopic gels show that the permeation of large solutes inside crosslinked polymer networks with very long polymer fibers is better described by the Ogston model[45]. This is because, under such conditions, the chain-like geometry dominates, playing the monomer shape a minor role.

As observed from Figure I.4 the agreement between theoretical predictions with $n = 3$ and simulations is excellent for 100 mM. For 1 mM the model still yields quite good quantitative agreement in the swollen configuration, but over-estimates the counterion permeation about a 10% in the shrunken state. This deviation comes from the very strong density variations of the ionic density profiles arising inside the microgel. Indeed, as will be shown below, at high temperatures and low electrolyte concentration, the internal heterogeneities cause changes of the density of counterions by a factor larger than 100 that the OZ-HNC integral equation theory is not able to completely reproduce.

To confirm whether steric interaction may affect the microgel effective net charge even when there is no hydration shell around the ions, another set of Monte Carlo simulations and Ornstein-Zernike calculations were performed at high concentration (100 mM) using a smaller value for the ion diameter, namely $\sigma_i = 0.4$ nm. These results are compared in Figure I.5 with those obtained for $\sigma_i = 0.7$ nm. It is clearly shown that both simulations and theoretical results follow the same trend for $\sigma_i = 0.4$ nm and $\sigma_i = 0.7$ nm, although the effective charge absolute values in shrunken states are smaller for smaller ions. This is an expected result, since a decrease of the ion size diminishes the steric repulsion between the microgel and the counterions, which leads to larger counterion permeation for $\sigma_i = 0.4$ nm, and hence to an increase of microgel charge screening. However, in swollen states there is no significant difference due to ion diameter, since excluded volume interactions become less relevant for expanded microgels, as mentioned above. In addition, as in Figure I.4, the curve obtained by solving Ornstein-Zernike equations neglecting volume exclusion effects strongly overestimates the charge screening effect for both ion sizes at high packing fractions.
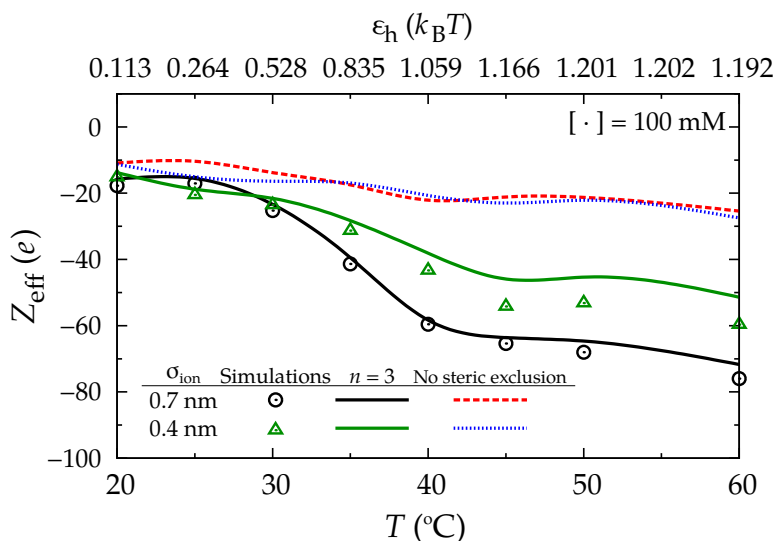
Figure I.5: Microgel effective charge as a function of temperature for 100 mM of electrolyte concentration and two different sizes of ions. Black color is used for $\sigma_i = 0.7$ nm, while green color represents $\sigma_i = 0.4$ nm. Symbols stand for Z_{eff} measured in simulations, while solid lines are theoretical predictions calculated by solving OZ equations, using $n = 3$ in equation (I.8) for steric interaction. Red dashed line and blue dotted line are calculated ignoring the steric repulsion for $\sigma_i = 0.7$ nm and $\sigma_i = 0.4$ nm, respectively.

4.3 Ionic density profiles

Here, we complete the data of effective charge with additional detailed information about the local density profiles of the ions inside and around the microgel particle. Figure I.6 and Figure I.7 show the radial distribution functions of counterions for different temperatures and hence different swollen states. The plots include the simulation results (dashed blue line), and the theoretical predictions with and without considering excluded volume interactions (green and pink solid lines, respectively). Coion density profiles are not shown since they do not contribute with significant insights in the physical interpretation. First, we discuss the simulation results. As it could be observed in both Figures, at low temperature (swollen state), counterions can easily diffuse through microgel pores, so they are homogeneously distributed in the internal region. However, as temperature increases and microgel shrinks, two maxima begin to rise in $g_{m+}(r)$. As mentioned above, the morphology of such small microgel particle becomes heterogeneous for shrunken states, in which charged monomers become reallocated so that they tend to form an inner charged spherical shell

Figure I.6: Radial distribution functions of counterions as a function of the distance to microgel center, for different temperatures and hence distinct deph of hydrophobic potential and degree of swelling. All curves correspond to a salt concentration 100 mM. Dashed line has been obtained directly from simulations, while solid lines represent $g_{m+}(r)$ calculated by solving Ornstein-Zernike integral equations: taking into account steric repulsion from equation (I.8) with $n = 3$ (green) and considering that there is no steric interaction (pink).

and an external one. As a consequence of this, counterions tend to congregate close to both shells, inside the particle (first maximum) or around the microgel (second maximum). An schematic explanation of this phenomenon is drawn in Figure I.8.

Theoretical predictions are also able to reproduce the appearance of these two maxima in the counterion concentration as microgel collapses. In fact, both peaks are observed even in the limit of vanishing steric interactions (see pink solid line), which indicates that this phenomenon is mainly induced by the electrostatic attraction between counterions and the heterogeneous distribution of bare charges inside the microgel. There is, however, a subtle distinction: these maxima are situated closer to the charged shells because counterions are not affected by volume exclusion. As soon as the steric contribution is taken into account (using equation (I.8) with $n = 3$), the internal maximum shifts to smaller r, whereas the external one moves to larger values of r, due to the counterion exclusion exerted by the polymer fibers in the spherical shell.
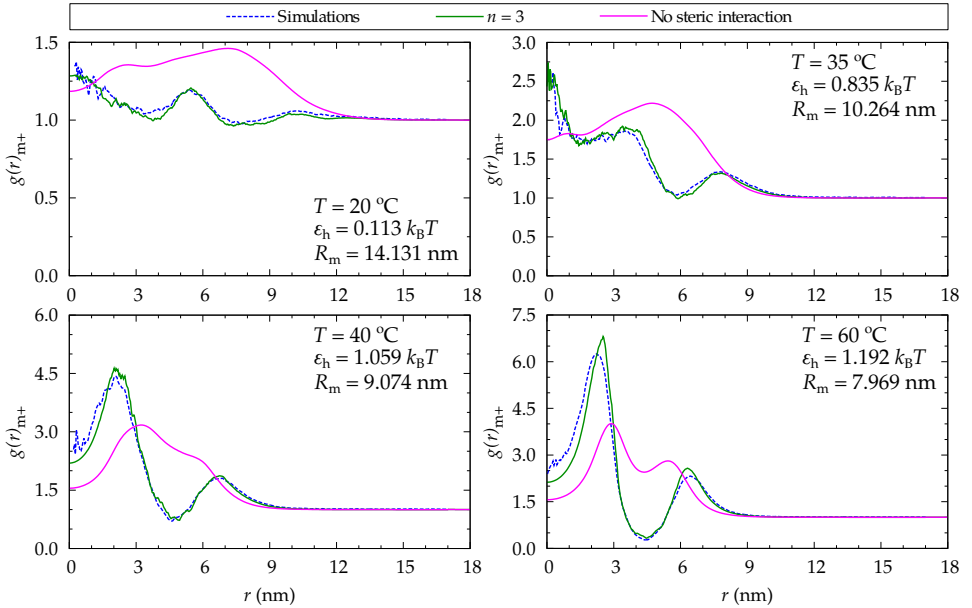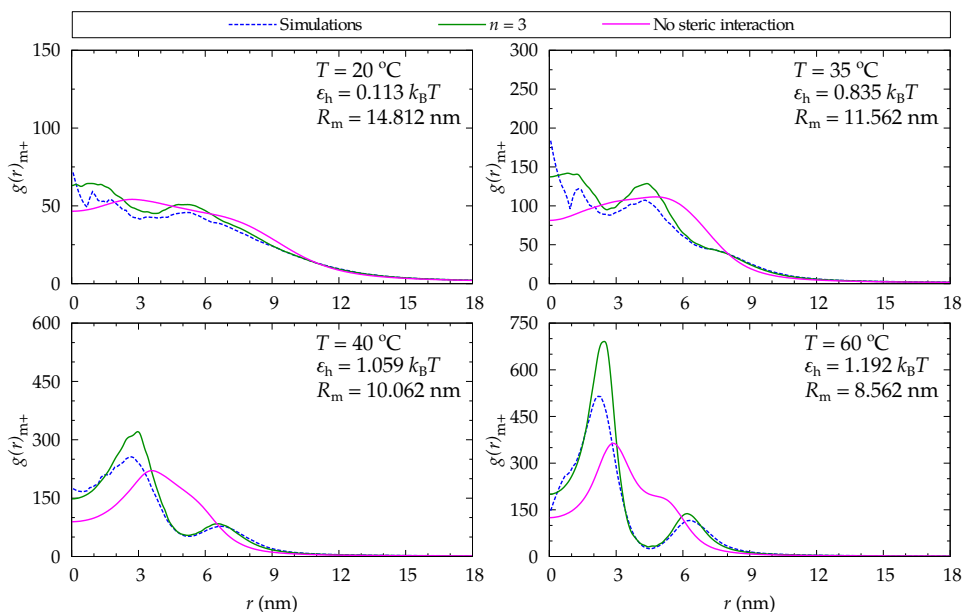
Figure I.7: Radial distribution functions of counterions as a function of the distance to microgel center, for different temperatures and hence distinct deph of hydrophobic potential and degree of swelling. All curves correspond to a salt concentration 1 mM. Dashed line has been obtained directly from simulations, while solid lines represent $g_{m+}(r)$ calculated by solving Ornstein-Zernike integral equations: taking into account steric repulsion from equation (I.8) with $n = 3$ (green) and considering that there is no steric interaction (pink).

The comparison between theory and simulations clearly points out that neglecting the microgel-ion steric interaction may lead to acceptable predictions for the counterion density profiles at 1 mM if microgels are swollen enough, but wrong predictions for shrunken states or high electrolyte concentration. However, when the steric interaction is included in the model, qualitative and even quantitative agreement is achieved for the whole set of swelling states. This agreement is specially good for swollen states, and worsens in the shrunken states for 1 mM, where the model overestimates the concentration of counterions in the internal layer. We attribute these discrepancies to the accuracy of the HNC approximation. This closure works in general very well for the kind of potentials used in this work, but it should be reminded that HNC ignores the so-called bridge function in the potential of mean force, which takes into account strong correlations at short distances[66]. In particular, previous calculations performed in charged colloidal suspensions show that the colloid-ion bridge function contributes with an additional attraction[67,68]. Therefore, it is also expected
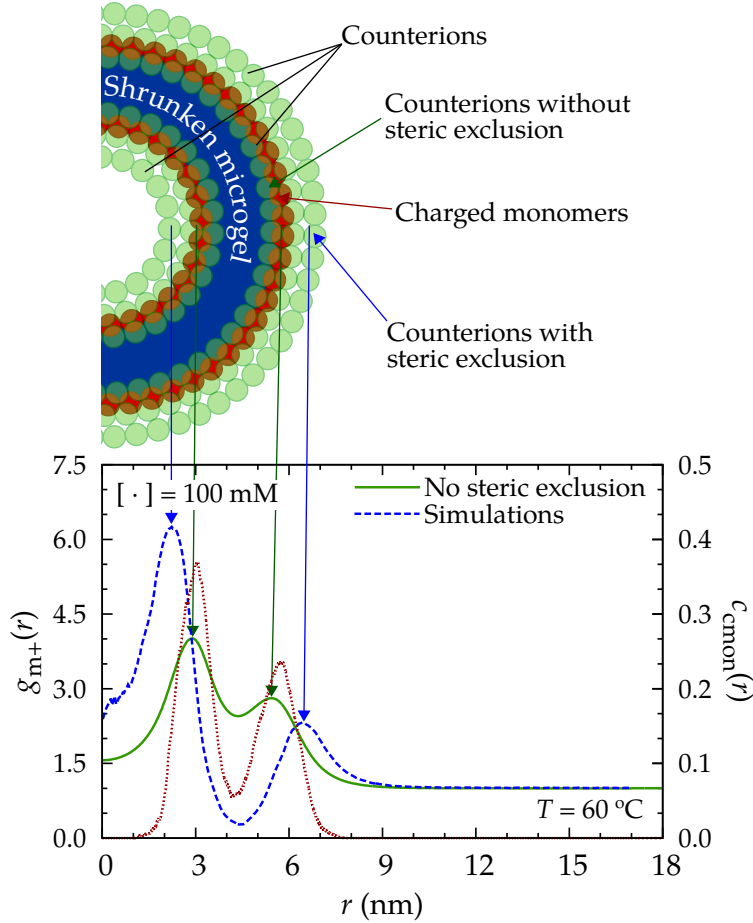
Figure I.8: Explanation of the two maxima observed in radial distribution function of counterions inside and around the shrunken microgel particle. Dashed blue line represents simulation results, while green solid line stands for theoretical results ignoring steric exclusion. In the picture, green circles represent counterions and red circles are the charged monomers allocated in both shells.

that our theory predicts an overestimation of the counterion adsorption at low electrolyte concentration in the shrunken states, since in this case the density charge of the microgel is larger and weakly screened by the counterion cloud. In spite of this, HNC still provide a qualitative agreement in this situation, and has the additional advantage of being very simple to numerically implement, in contrast with other more sophisticated closure relations.

Therefore, we can confirm that the steric microgel-ion interaction plays an important role on the ionic distribution inside the microgel particle, specially close to the collapsed state. Moreover, the model proposed in Equation (I.8) has shown to be accurate enough to correctly described the simulated ionic density profiles, even in the case of non-homogeneous distribution of internal mass and charge of the microgel particle.

5   Conclusions

In this work we study the effect of the steric excluded-volume repulsion exerted by the fibrous polymer network of the microgel on the ionic permeation, for different swelling states and concentrations of monovalent salt. In particular, we focus on the effective charge of the microgel and the local ionic density profiles around and inside the microgel. For this purpose, Monte Carlo simulations are compared to the theoretical predictions assuming that the suspension is a ternary mixture of microgels, counterions and coions, and solving the corresponding OZ integral equations within the HNC approximation.

The results show that splitting the microgel-ion interaction into electrostatic and steric terms is a good approximation. Moreover, the comparison with simulation data also indicates that the internal structure of the microgel crosslinked fibrous structure is better represented by a collection of randomly-placed spherical monomers. An advantage of this model is that the effective steric microgel-ion repulsive interaction can be calculated analytically. This approach for the internal morphology of the microgel works well for the kind of system we are dealing, namely, small highly crosslinked microgel with few monomers per chain permeated by ions with size of the order of the monomer unit. However, it should be emphasized that for larger microgel particles with longer polymer chains between crosslinker nodes may be better represented by a random assembly of cylinders rather than spheres[45].

In conclusion, our work reveals that the steric interaction should be included to correctly account for the ion distributions if the polymer volume fraction of the microgel and ionic sizes are large enough. Under such circumstances, ignoring this contribution could lead to an artificial enhancement of the counterion permeation and so, to a significant decrease of the microgel effective charge. Once this effect is included, the theoretical model is able to correctly describe the response of the effective charge to swelling and shrinking of the microgel particle, and provides a quantitative account for the ionic density profiles, even in situations of heterogeneous charge and mass distributions inside the parti-

cle. Moreover, our predictions could be also interesting to understand the ionic permeation inside non-homogeneous hollow thermoresponsive microgels, like the ones studied by Dubbert *et al.*[69].

Future investigations will focus on the effect of ion specificity on the swelling behavior of the microgel. As shown in previous work[37], hydrophobic ions tend to accumulate in specific locations of the polymer network, leading to new effects that go far beyond charge screening, such as charge inversion and overcharging phenomena. Therefore, it would be interesting to compare simulation and theoretical data also in this situation, given the importance of microgels as carriers of hydrophobic solutes and Biomolecules[9,70].

Acknowledgements

References

[1] Sierra-Martín, B.; Lietor-Santos, J. J.; Fernández-Barbero, A.; Nguyen, T. T.; Fernández-Nieves, A. *Microgel Suspensions: Fundamentals and Applications*; Wiley-VCH Verlag GmbH & Co. KGaA: Weinheim, Germany, 2011; pp 71–116.

[2] Murray, M. J.; Snowden, M. J. *Adv. Colloid Interface Sci.* **1995**, *54*, 73–91.

[3] Saunders, B. R.; Vincent, B. *Adv. Colloid Interface Sci.* **1999**, *80*, 1–25.

[4] Saunders, B. R.; Laajam, N.; Daly, E.; Teow, S.; Hu, X.; Stepto, R. *Adv. Colloid Interface Sci.* **2009**, *147-148*, 251–62.

[5] Lee, S. M.; Nguyen, S. T. *Macromolecules* **2013**, *46*, 9169–9180.

[6] Lee, S. M.; Bae, Y. C. *Macromolecules* **2014**, *47*, 8394–8403.

[7] Du, A. W.; Stenzel, M. H. *Biomacromolecules* **2014**, *15*, 1097–1114.

[8] Vinogradov, S. V. *Nanomedicine* **2010**, *5*, 165–8.

[9] Hoare, T. R.; Pelton, R. *Langmuir* **2008**, *24*, 1005–12.

[10] Malmsten, M.; Bysell, H.; Hansson, P. *Curr. Opin. Colloid Interface Sci.* **2010**, *15*, 435–444.

[11] Ramos, J.; Peláez-Fernández, M. A.; Forcada, J.; Moncho-Jordá, A. In *Soft Nanoparticles for Biomedical Applications*; Callejas-Fernández, J., Estelrich, J., Quesada-Pérez, M., Forcada, J., Eds.; The Royal Society of Chemistry: Cambridge, 2014; Chapter 4, pp 1–37.

[12] Shin, J.; Cherstvy, A. G.; Metzler, R. *Phys. Rev. X* **2014**, *4*, 021002.

[13] Moncho-Jordá, A.; Anta, J. A.; Callejas-Fernández, J. *J. Chem. Phys.* **2013**, *138*, 134902.

[14] Denton, A. R. *Phys. Rev. E* **2003**, *67*, 011804–10. *Erratum–ibid* **2003**, *68*, 049904.

[15] Gottwald, D.; Likos, C. N.; Kahl, G.; Löwen, H. *Phys. Rev. Lett.* **2004**, *92*, 068301.

[16] Colla, T.; Likos, C. N.; Levin, Y. *J. Chem. Phys.* **2014**, *141*, 234902.

[17] Johnson, E. M.; Deen, W. M. *J. Colloid Interface Sci.* **1996**, *178*, 749–756.

[18] Quesada-Pérez, M.; Adroher-Benítez, I.; Maroto-Centeno, J. A. *J. Chem. Phys.* **2014**, *140*, 204910.

[19] Ulrich, S.; Laguecir, A.; Stoll, S. *Macromolecules* **2005**, *38*, 8939–8949.

[20] Reddy, G.; Yethiraj, A. *Macromolecules* **2006**, *39*, 8536–8542.

[21] Chang, R.; Yethiraj, A. *Macromolecules* **2006**, *39*, 821–828.

[22] Jiang, T.; Wu, J. *J. Phys. Chem. B* **2008**, *112*, 7713–7720.

[23] Dias, R. S.; Pais, A. A. C. C. *Adv. Colloid Interface Sci.* **2010**, *158*, 48–62.

[24] Stoll, S. In *Soft Nanoparticles for Biomedical Applications*; Callejas-Fernández, J., Estelrich, J., Quesada-Pérez, M., Forcada, J., Eds.; The Royal Society of Chemistry: Cambridge, 2014; pp 342–371.

[25] Cherstvy, A. G. *J. Phys. Chem. B* **2010**, *114*, 5241–5249.

[26] Ghosh, S. K.; Cherstvy, A. G.; Metzler, R. *J. Chem. Phys.* **2014**, *141*, 074903.

[27] Mann, B. A.; Holm, C.; Kremer, K. *J. Chem. Phys.* **2005**, *122*, 154903–14.

[28] Yin, D. W.; Olvera De La Cruz, M.; De Pablo, J. J. *J. Chem. Phys.* **2009**, *131*, 194907.

[29] Yan, Q.; de Pablo, J. J. *Phys. Rev. Lett.* **2003**, *91*, 018301.

[30] Košovan, P.; Richter, T.; Holm, C. In *Intelligent Hydrogels. Progress in Colloid and Polymer Science*; G., S., W., R., Eds.; Springer International Publishing: Cham, 2013; Vol. 140; pp 205–221.

[31] Claudio, G. C.; Kremer, K.; Holm, C. *J. Chem. Phys.* **2009**, *131*, 094903–9.

[32] Jha, P. K.; Zwanikken, J. W.; Detcheverry, F. A.; de Pablo, J. J.; Olvera de la Cruz, M. *Soft Matter* **2011**, *7*, 5965–5975.

[33] Quesada-Pérez, M.; Martín-Molina, A. *Soft Matter* **2013**, *9*, 7086–7094.

[34] Kobayashi, H.; Winkler, R. G. *Polymers* **2014**, *6*, 1602–1617.

[35] Quesada-Pérez, M.; Ramos, J.; Forcada, J.; Martín-Molina, A. *J. Chem. Phys.* **2012**, *136*, 244903–9.

[36] Moncho-Jordá, A. *J. Chem. Phys.* **2013**, *139*, 064906.

[37] Moncho-Jordá, A.; Adroher-Benítez, I. *Soft Matter* **2014**, *10*, 5810–5823.

[38] Guerrero-García, G. I.; González-Tovar, E.; Lozada-Cassou, M.; de J Guevara-Rodríguez, F. *J. Chem. Phys.* **2005**, *123*, 34703–20.

[39] Fernández-Nieves, A.; Fernández-Barbero, A.; Vincent, B.; de las Nieves, F. J.

Macromolecules **2000**, *33*, 2114–2118.

[40] Belloni, L. *J. Phys.: Condens. Matter* **2000**, *12*, R549–R587.

[41] Sing, C.; Zwanikken, J.; Olvera de la Cruz, M. *Macromolecules* **2013**, *46*, 5053–5065.

[42] Polotsky, A. A.; Plamper, F. A.; Borisov, O. V. *Macromolecules* **2013**, *46*, 8702–8709.

[43] Arndt, M. C.; Sadowski, G. *J. Phys. Chem. B* **2014**, *118*, 10534–10542.

[44] Weast, R. C.; Astle, M. J.; Beyer, W. H.; Others, *CRC handbook of chemistry and physics*; CRC press Boca Raton, FL, 1988; Vol. 69; p 496.

[45] Ahualli, S. A.; Martín-Molina, A.; Quesada-Pérez, M. *Phys. Chem. Chem. Phys.* **2014**, *16*, 25483–25491.

[46] Lazzara, M. J.; Blankschtein, D.; Deen, W. M. *J. Colloid Interface Sci.* **2000**, *226*, 112–122.

[47] Ogston, A. G. *J. Chem. Soc., Faraday Trans.* **1958**, *54*, 1754–1757.

[48] Bosma, J. C.; Wesselingh, J. A. *J. Chromatogr. B* **2000**, *743*, 169–180.

[49] Hansen, J.-P.; McDonald, I. R. *Journal of the American Podiatric Medical Association*, 3rd ed.; Academic Press: Amsterdam, 2006; Vol. 104; p 416.

[50] Shah, N. H. *Numerical Methods with C++ Programming*; PHI Learning Pvt. Ltd.: New Delhi, 2009; p 325.

[51] Israelachvili, J. N. *Intermolecular and surface forces*, third edit ed.; Academic Press: San Diego, 2011; p 674.

[52] Dursch, T. J.; Taylor, N. O.; Liu, D. E.; Wu, R. Y.; Prausnitz, J. M.; Radke, C. J. *Biomaterials* **2014**, *35*, 620–629.

[53] Quesada-Pérez, M.; Ahualli, S. A.; Martín-Molina, A. *J. Chem. Phys.* **2014**, *141*, 124903.

[54] Mann, B. A.; Everaers, R.; Holm, C.; Kremer, K. *Europhys. Lett.* **2004**, *67*, 786–792.

[55] Yin, D. W.; Yan, Q.; De Pablo, J. J. *J. Chem. Phys.* **2005**, *123*, 174909–9.

[56] Escobedo, F.; de Pablo, J. *J. Chem. Phys.* **1996**, *104*, 4788–4801.

[57] Khan, M. O.; Mel'nikov, S. M.; Jönsson, B. *Macromolecules* **1999**, *32*, 8836–8840.

[58] Quesada-Pérez, M.; Ibarra-Armenta, J. G.; Martín-Molina, A. *J. Chem. Phys.* **2011**, *135*, 094109.

[59] Kolomeisky, A. B.; Widom, B. *Faraday Discuss.* **1999**, *112*, 81–89.

[60] Quesada-Pérez, M.; Maroto-Centeno, J. A.; Martín-Molina, A. *Macromolecules* **2012**, *45*, 8872–8879.

[61] Pelton, R. *Adv. Colloid Interface Sci.* **2000**, *85*, 1–33.

[62] Ramos, J.; Imaz, A.; Callejas-Fernández, J.; Barbosa-Barros, L.; Estelrich, J.; Quesada-Pérez, M.; Forcada, J. *Soft Matter* **2011**, *7*, 5067–5082.

[63] Linse, P. In *Advanced Computer Simulation Approaches for Soft Matter Sciences II*; Holm, C., Kremer, K., Eds.; Advances in Polymer Science; Springer Berlin Heidelberg, 2005; Vol. 185; pp 111–162.

References

[64] Arnold, A.; Holm, C. In *Advanced Computer Simulation Approaches for Soft Matter Sciences II*; Holm, C., Kremer, K., Eds.; Advances in Polymer Science; Springer Berlin Heidelberg, 2005; Vol. 185; pp 59–109.

[65] Barrat, J.-L.; Joanny, J.-F.; Pincus, P. *J. Phys. II* **1992**, *2*, 1531–1544.

[66] Iyetomi, H.; Ogata, S.; Ichimaru, S. *Phys. Rev. A* **1992**, *46*, 1051–1058.

[67] Anta, J. A.; Bresme, F.; Lago, S. *J. Phys.: Condens. Matter* **2003**, *15*, S3491–S3507.

[68] Quesada-Pérez, M.; Martín-Molina, A.; Hidalgo-Álvarez, R. *J. Chem. Phys.* **2004**, *121*, 8618–8626.

[69] Dubbert, J.; Honold, T.; Pedersen, J. S.; Radulescu, A.; Drechsler, M.; Karg, M.; Richtering, W. *Macromolecules* **2014**, *47*, 8700–8708.

[70] López-León, T.; Elaïssari, A.; Ortega-Vinuesa, J. L.; Bastos-González, D. *ChemPhysChem* **2007**, *8*, 148–56.

Paper II

Competition between excluded-volume and electrostatic interactions on nanogel swelling: Effect of the counterion valence and nanogel charge

Irene Adroher-Benítez[⋆], Alberto Martín-Molina[⋆], Silvia Ahualli[⋆], Manuel Quesada-Pérez[†], Gerardo Odriozola[‡], and Arturo Moncho-Jordá[⋆][§]

[⋆]Departamento de Física Aplicada, Facultad de Ciencias, Universidad de Granada, Avenida Fuentenueva S/N, 18001 Granada, Spain.

[†]Departamento de Física, Escuela Politécnica Superior de Linares, Universidad de Jaén, 23700 Linares, Jaén, Spain.

[‡]Área de Física de Procesos Irreversibles, División de Ciencias Básicas e Ingeniería, Universidad Autónoma Metropolitana, Av. San Pablo 180 Col. Reynosa, 02200 México CD de México, Mexico.

[§]Instituto de Carlos I de Física Teórica y Computacional, Facultad de Ciencias, Universidad de Granada, Avenida Fuentenueva S/N, 18001 Granada, Spain.

73

Abstract

In this work the equilibrium distribution of ions around a thermo-responsive charged nanogel particle in an electrolyte aqueous suspension is explored using coarse-grained Monte Carlo computer simulations and the Ornstein-Zernike integral equation theory. We explicitly consider the ionic size in both methods and study the interplay between electrostatic and excluded-volume effects for swollen and shrunken nanogels, monovalent and trivalent counterions, and for two different nanogel charges. We find good quantitative agreement between the ionic density profiles obtained in both methods when the excluded repulsive force exerted by the cross-linked polymer network is taken into account. For the shrunken conformation, the electrostatic repulsion between the charged groups provokes a heterogeneous polymer density profile, leading to a nanogel structure with an internal low density hole surrounded by a dense corona. The results show that the excluded-volume repulsion strongly hinders the ion permeation for shrunken nanogels, where volume exclusion is able to significantly reduce the concentration of counterions in the more dense regions of the nanogel. In general, we demonstrate that the thermosensitive behaviour of nanogels, as well as their internal structure, are strongly influenced by the valence of the counterions and also by the charge of the particle. On the one hand, an increase of the counterion valence moves the swelling transition to lower temperatures, and induces a major structuring of the charged monomers into an internal and an external layers around the crown for shrunken nanogels. On the other hand, rising the particle charge shifts the swelling curve to larger values of the effective radius of the nanogel.
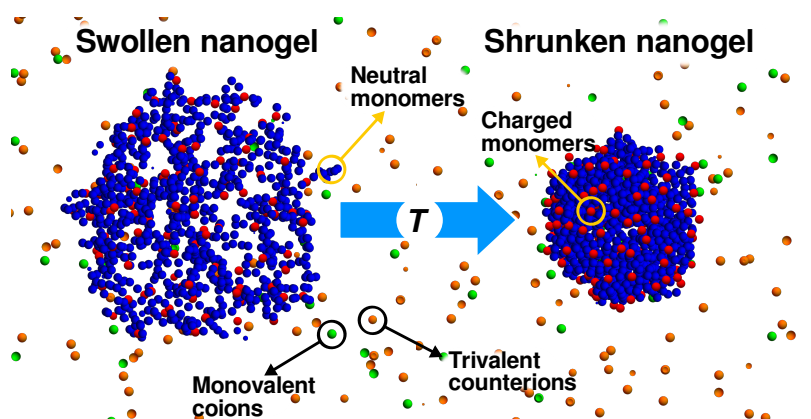
1   Introduction

Nanogels are porous particles of nanometric size formed by cross-linked polymer chains dispersed in a solvent that can reversibly swell or shrink in response to many parameters such as pH, salt concentration, temperature, among others.[1,2] The swelling process occurs by the uptake of large amounts of solvent, but these particles do not dissolve thanks to the constituting structure of the polymeric network, physically or chemically cross-linked. This allows the nanogels to be permeated by ions and other cosolutes, such as small proteins, peptides, biomolecules, drugs or chemical reactants. In addition, the fibrous internal morphology of nanogels maximizes the total exposed surface of polymer to the solvent. All these unique properties, together with the fact that nanogels exhibit a swelling response some orders of magnitude faster than macroscopic gels,[3] make them qualified for a number of biotechnological and medical applications, such as drug nanocarriers or nanoreactors.[4–8]

For the particular case of charged nanogels in aqueous media, the presence of electrolyte in the suspension becomes of fundamental importance. Indeed, mobile ions distribute inside and around the porous nanogel, giving rise to the so-called electric double layer, may determine the degree of swelling of the particle and the efficiency in the cosolute uptake. On the one hand, increasing the bulk salt concentration screens the electrostatic interaction and reduces the effective charge of the particles,[9–11] which in turn induces the shrinking of the nanogel and diminishes the absorption of oppositely charged cosolutes inside it.[12] Moreover, the variation of the local concentration of counter and coions can also affect the swelling response of the charged polymer network, giving rise to internal heterogeneities in the polymer density.[13–15] On the other hand, the transfer of a charged solute from the bulk solution into the charged nanogel involves a change of free energy that arises from the difference in local electrolyte concentration between both locations.[16]

Given the important role that the non-uniform ionic density profiles play on the swelling of the nanogel and on its sorption efficiency of charged cosolutes, it is of capital interest to understand the physical effects involved in the formation of this electric double layer. Outside the nanogel the local density of ions is controlled by the electrostatic potential generated by the charged nanogels. However, in the internal region of the nanogel, the resulting non-uniform ionic density profiles become affected by non-electrostatic forces, such as the excluded-volume (or steric) repulsion that arises due to the finite size of the ions, and the hydrophobic binding for the case of chaotropic ions.[17–19] The

steric repulsion that a single ion experiences when diffusing inside the nanogel has two complementary contributions, namely, the volume exclusion caused by the other ions and the exclusion exerted by the polymer network. This volume exclusion strongly depends on the internal morphology or the polymer network, especially at high polymer volume fractions. Therefore, it is crucial to develop accurate models to account for the structure of the polymer network inside the nanogel.

In this work we combine the Ornstein-Zernike (OZ) integral equation theory with coarse-grain Monte Carlo (MC) simulations to obtain the ionic density profiles and the local polymer mass and charge distributions inside thermo-responsive charged nanogels in equilibrium conditions. We follow a similar scheme used in our previous work, where nanogel swelling in the presence of monovalent salt was addressed,[14] but now extending our calculations to consider the role that the counterion valence and the nanogel charge plays on the competition between electrostatic and excluded-volume forces. The importance of multivalent counterions goes beyond the mere theoretical interest since, as potential therapeutic carriers, nanogels should work at large ionic strengths of electrolyte solutions in which multivalent ions can be present.[20] In this sense, a theory for gels accounting for ion-ion correlations has been recently applied to multivalent electrolytes, finding a first-order transition due to multivalent ions upon inclusion of these correlation effects.[21] Among the multiple models for the internal structure of the nanogel, we assume that the structure of the polymer network is approximated by an assembly of spherical monomeric units randomly distributed within the internal volume of the nanogel. In spite of its simplicity, this model provides good agreement between the ionic density profiles theoretically predicted and simulated, even when applied to ions with different valence. The results show that excluded-volume effects are important, and also that the geometrical properties of the polymer network must be necessarily considered when the polymer packing fraction increases.

This paper is organized as follows. Computer simulations are briefly explained in Section 2. Section 3 describes the ion-ion and ion-nanogel bare interactions and explains the integral equation method. In Section 4 the theoretical predictions for the ionic density profiles are compared to the simulation data. Finally, we highlight the most relevant conclusions in Section 5.

2 Simulations

In order to determine the swelling of a charged nanogel, the charge and mass distribution of the cross-linked polymer network, and the local concentration of counterions and coions, we make use of coarse-grained Monte Carlo (MC) simulations. We simulate a single negatively charged nanogel particle immersed in an electrolyte suspension at a fixed salt concentration. The solvent is not explicitly considered, and instead treated as a continuum of dielectric permittivity, ϵ. On the one hand, counterions and coions are modelled as charged hard spheres with a valence z_+ and z_-, respectively. In both cases the ionic size is assumed to be the same, given by $R_+ = R_- = 0.35$ nm. On the other hand, the nanogel is constructed by an assembly of interconnected spherical monomers of radius $R_{\mathrm{mon}} = 0.325$ nm. In particular, the so-called bead-spring model is used to consider the connectivity of the monomeric units that form the polymer chains. This simple framework has been extensively employed in the study of the collapse and adsorption of polyelectrolytes.[22–28] To correctly account for the real morphology of the cross-linked network, the polymer chains are connected by tetrafunctional cross-linkers. A total amount of 8 monomers are linked to form a single chain, which in turn is connected with the rest of the structure through tetrafunctional cross-linking monomers of the same size. In particular, the nanogel studied in this work has 133 cross-linkers and 206 chains with $f = 1$ or $f = 2$ ionized groups (with one negative elementary charge e) per chain. Accordingly, this system bears a noticeable resemblance to experimental charged nanogels.[29]

The short-range repulsion between any pair of particles (monomers and ions separated a distance r) due to excluded volume effects is modelled by means of a purely repulsive Weeks-Chandler-Andersen (WCA) potential:[30–34]

$$V_{\mathrm{WCA}}(r) = \begin{cases} 4\epsilon_{\mathrm{WCA}} \left(\dfrac{\sigma^{12}}{r^{12}} - \dfrac{\sigma^6}{r^6} + \dfrac{1}{4} \right) & r \le 2^{1/6}\sigma \\ 0 & r > 2^{1/6}\sigma \end{cases}, \tag{II.1}$$

where $\epsilon_{WCA} = 4.11 \cdot 10^{-21}$ J and $\sigma = R_i + R_j$ (i and j run over the three species of particles, namely counterions, coions and monomers). Additionally, all the charged species interact electrostatically through the Coulomb potential $e^2 z_i z_j / (4\pi\epsilon r)$. Since we are interested in thermo-responsive nanogels, it is convenient to consider the temperature dependence of the dielectric permittivity. In this work, we

adopt the following one, which provides a very good estimate of ϵ for water:[35]

$$\begin{aligned} \epsilon(T)/\epsilon_0 = & 5321\,T^{-1} + 233.76 - 0.9297\,T + \\ & + 0.1417 \cdot 10^{-2}\,T^2 - 0.8298 \cdot 10^{-6}\,T^3. \end{aligned} \tag{II.2}$$

The interaction connecting monomer units and cross-linkers with their neighbours along the polymeric chains is approximated by harmonic bonds $V_{\mathrm{bond}}(r) = k_{\mathrm{bond}}(r - r_0)/2$, where k_{bond} is the elastic constant ($k_{\mathrm{bond}} = 0.4$ N/m) and r_0 is the equilibrium bond length, given by the monomer diameter (0.65 nm).[24,36,37]

Finally, it is well known that the thermoresponsive character of nanogels is caused by the shift from enthalpy-ruled to entropy-ruled forces, where hydrogen bonds and water degrees of freedom play key roles. For the particular case of Poly(N-isopropylacrylamide) (PNIPAM), this effect yields an increase of the attractive hydrophobic interaction between the monomeric units when increasing temperature. This interaction, $V_h(r)$, is modelled through a smooth approximation of the square-well potential, which has been extensively used in previous studies.[13,29,38–42]

3 Theory

3.1 Modeling the ion-ion and nanogel ion bare interactions

In the theoretical treatment we make use of the Ornstein-Zernike (OZ) integral equations to determine the ionic density profiles around a single nanogel. We treat our system as a ternary mixture of spherical charged nanogels, counterions and coions. As considered for the simulations, the solvent (water) is assumed to be a mere continuum background with a constant dielectric permittivity, ϵ. In our model, the nanogel can be regarded as a porous macroion with a total charge given by $Z_{\mathrm{m}}e$. This particle can be permeated by the solvent, and by the counterions and coions of the suspension (with charges $z_+ e$ and $z_- e$, respectively). The bulk concentrations for the three species are denoted by $\rho_{0\mathrm{m}}$, ρ_{0+} and ρ_{0-}. In our theoretical model we do not assume that the charge and mass distribution inside the polymer network is uniform or follows a core-shell structure, as it is customary in most theoretical works. Instead, we take the polymer volume fraction $\phi(r)$ and the polymer charge density $\rho_e(r)$ inside the nanogel obtained by means of the MC computer simulations, as they provide a more realistic input of the equilibrium properties of the nanogel.

In order to solve the integral equations, the ion-ion and nanogel-ion bare interactions must be specified. For the ion-ion interaction we use the primi-

tive model (in consistency with the simulations) and consider that ions are hard charged spheres of radius R_i. Accordingly, the ion-ion pair potential is the combination of a Coulomb interaction and a short-range hard sphere repulsion that prevents ion overlapping, i.e.

$$\beta V_{ij}(r) = \begin{cases} \infty & r \le R_i + R_j \\ z_i z_j l_{\mathrm{B}}/r & r > R_i + R_j \end{cases}, \tag{II.3}$$

where r is the distance between the particle centres, $\beta = 1/(k_{\mathrm{B}}T)$ (k_{B} is the Boltzmann constant, and T the absolute temperature) and l_{B} is the Bjerrum length, defined as $l_{\mathrm{B}} = \beta e^2/(4\pi\epsilon)$.

The bare interaction between the nanogel and a single ion has two contributions, the electrostatic and the excluded-volume terms:

$$V_{\mathrm{m}i}(r) = V_{\mathrm{m}i}^{\mathrm{elec}}(r) + V_{\mathrm{m}i}^{\mathrm{exc}}(r). \tag{II.4}$$

The electrostatic term is given by the Coulomb interaction between the incoming ion and the charge distribution inside the nanogel. Hence, it is obtained from the integration of the electric field generated by the nanogel charge distribution

$$V_{\mathrm{m}i}^{\mathrm{elec}}(r) = z_i e \int_r^{\infty} E(r) dr. \tag{II.5}$$

The electric field is given by Gauss's law, $\beta e E(r) = l_{\mathrm{B}} Z(r)/r^2$, where $Z(r)$ is the polymer charge enclosed within an sphere of radius r,

$$Z(r) = \begin{cases} \dfrac{4\pi}{e} \displaystyle\int_0^r r'^2 \rho_e(r') dr' & r \le R_{\mathrm{m}} \\ Z_{\mathrm{m}} & r > R_{\mathrm{m}} \end{cases}, \tag{II.6}$$

where R_{m} represents the external radius of the nanogel.

The next step is to figure out an analytical expression for the excluded-volume term, $V_{\mathrm{m}i}^{\mathrm{exc}}(r)$, as a function of the distance r between the nanogel centre and the ion. In accordance with the simulation framework, the polymer network can be thought of as being composed of spherical monomers, represented by spheres of radius R_{mon}. By definition, $V_{\mathrm{m}i}^{\mathrm{exc}}(r)$ is the effective repulsive interaction that the nanogel exerts onto a single spherical ion of radius R_i due exclusively to the volume restriction caused by the monomeric units that form the polymer network. Due to the finite size of the ions, they cannot approach to any monomer a distance smaller than $R_{\mathrm{mon}} + R_i$, so the exclusion volume is always larger than the volume occupied by the monomers. In fact, the total excluded volume is

given by the volume filled by the monomers plus the volume of the depletion region around them.

Defining the partition coefficient as the ratio between the local ion density inside the nanogel and in the bulk suspension in the limit of infinite dilution, $K_i = \lim_{\rho_{0i} \to 0} \rho_i^{\text{in}}(r)/\rho_{0i}$, it can be shown that the excluded-volume repulsion can be written as [17]

$$\beta V_{\text{m}i}^{\text{exc}}(r) = \begin{cases} -\ln K_i(r) & r \leq R_{\text{m}} \\ 0 & r > R_{\text{m}} \end{cases}, \quad i = +, -. \tag{II.7}$$

The relation between $K_i(r)$ and the local polymer volume fraction $\phi(r)$ is not obvious since the volume excluded in the depletion regions around the monomers depends on the geometric details of the internal morphology of the nanogel. In this work we assume one of the simplest non-trivial description for the polymer network structure, and comsider that the spherical monomers are randomly distributed (uncorrelated) inside the polymer network, which means that monomers can freely overlap each other without any energy cost. In this particular case, the partition coefficient can be analytically calculated, and the resulting effective excluded-volume pair potential is [43]

$$\beta V_{\text{m}i}^{\text{exc}}(r) = -\frac{1}{\lambda_i^3} \ln(1 - \phi(r)) \tag{II.8}$$

where $\lambda_i = R_{\text{mon}}/(R_{\text{mon}} + R_i)$.

More details about the derivation of expression II.8 may be found in the Appendix. In the limit of very low polymer volume fraction the excluded-volume repulsion tends to

$$\beta V_{\text{m}i}^{\text{exc}}(r) \approx -\ln\left(1 - \phi(r)/\lambda_i^3\right). \tag{II.9}$$

Although the last equation represents an acceptable estimate of the steric interaction for loosely bounded nanogels in the swollen state, it rapidly leads to nonphysical predictions when the polymer network approaches the more concentrated deswollen state.

3.2 Ornstein-Zernike integral equations

Once the ion-ion and ion-nanogel pair interaction potentials are specified, the mass and charge distribution of the polymer network inside the nanogel can be used to determine the ionic density profiles inside and outside the particle by solving the Ornstein-Zernike integral equations. This methodology has been

successfully employed to describe the ionic permeation and the particle swelling state in nanogel suspension.[11,19,21,44] In the limit of infinite dilution of nanogel particles ($\rho_{0m} \to 0$) these equations split into two separated set of equations, three for the ion-ion correlations

$$\hat{h}_{ij}(q) = \hat{c}_{ij}(q) + \sum_{k=+,-} \rho_{0k} \hat{c}_{ik}(q) \hat{h}_{kj}(q), \quad i = +, -; \tag{II.10}$$

and two for the nanogel-ion correlations

$$\hat{h}_{mi}(q) = \hat{c}_{mi}(q) + \sum_{k=+,-} \rho_{0k} \hat{c}_{mk}(q) \hat{h}_{ki}(q), \quad i = +, -; \tag{II.11}$$

where $\hat{h}_{ij}(q)$ and $\hat{c}_{ij}(q)$ are the Fourier transforms of the total and direct correlation functions, respectively. Five additional closure relations are required to solve the previous set of equations. Here, we use the well-known Hypernetted-Chain-Closure (HNC), which has proved to be reasonably good for the kind interactions while still maintaining the simplicity[11,45]

$$h_{ij}(r) = \exp\left[-\beta V_{ij}(r) + h_{ij}(r) - c_{ij}(r)\right] - 1. \tag{II.12}$$

The integral equations are solved following a simple Picard iterative procedure of successive approximation with the help of Fast Fourier Transforms until convergence of the total correlation functions is attained. More details about the numerical implementation of the numerical method may be found elsewhere.[11,14] As a final output, the ionic concentration at a distance r from the nanogel centre is calculated from the total correlation functions as

$$\rho_i(r) = \rho_{0i}[h_{mi}(r) + 1], \quad i = +, -. \tag{II.13}$$

The comparison between these theoretical predicted $\rho_+(r)$ and $\rho_-(r)$ and the simulated ones will show if electrostatic and excluded-volume effects are properly accounted for in the model.

4   Results and discussion

Monte Carlo simulations were performed for two types of electrolytes with different counterion valences, namely 3:1 and 1:1. Analogously, we also studied the effect of the nanogel charge considering tho different values, $Z_m = -206e$ and $-412e$ (corresponding to $f = 1$ and $f = 2$, respectively). The salt concentration for 1:1 salt was 100 mM, whereas the concentration for 3:1 electrolyte

was 16.7 mM. This choice allows to compare the result between monovalent and trivalent counterions at a common ionic strength of $I = \rho_{0+}z_+^2 + \rho_{0-}z_-^2 = 100$ mM. In order to reach the equilibrium distribution of the nanogel and the surrounding ions, at least 10^8 MC moves were employed for equilibration and 2×10^8 MC for statistics. The radius of gyration was monitored averaging on batches of 10^5 MC steps.
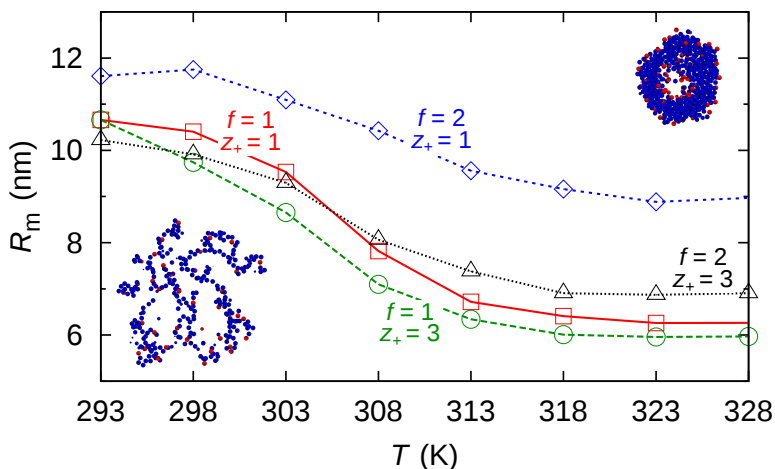
Figure II.1: Nanogel radius resulting from Monte Carlo simulations as a function of temperature for two different values of charge ($Z_m = -206e$ and $-412e$) and counterion valence ($z_+ = 1$ and $z_+ = 3$). Two snapshots of the nanogel at low and high temperature are included to illustrate the changes in the internal structure of the particle. Blue and red spheres represent neutral and charged monomers, respectively.

Before analysing the ionic distribution, we first start with the description of the swelling response of the particle with temperature for the studied conditions of counterion valences and nanogel charge. Fig. II.1 shows the effective radius of the nanogel, defined as $R_m = \sqrt{5/3}R_g$, where R_g is the radius of gyration of the nanogel, obtained as an average throughout many configurations after having reached the thermal equilibrium.

All simulated curves show the typical swelling behaviour, going from the expanded hydrophilic state for $T < T_\Theta$, to the collapsed hydrophobic state for $T > T_\Theta$. The phase transition between these two morphologies occurs at T_Θ, the so-called lower critical solution temperature (LCST). The value of T_Θ changes in response to the features of the solvent medium and the nanogel particle. In our case, T_Θ is close to 305 K, the typical value for Poly(N-isopropylacrylamide) (PNIPAM) nanogels.

Figure II.2: Blue solid line: simulated density profile of charged monomers as a function of the distance to the nanogel centre.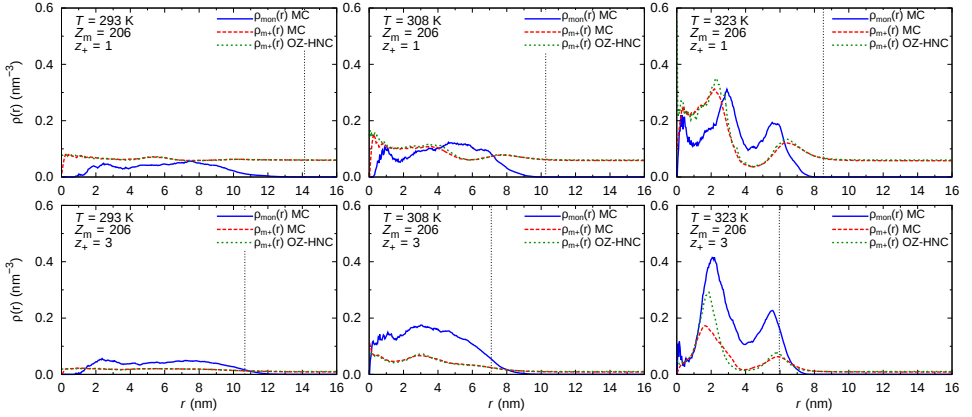 Red dashed line: simulated density profile of counterions. Green dotted line: density profile of counterions predicted from integral equations within the HNC approximation. The different plots show the results for monovalent and trivalent counterions at three different swelling states, for $Z_m = -206e$ ($f = 1$). The dashed vertical line represents the external radius of the nanogel.

Although all curves exhibit a common functional dependence with T, there are significant differences between them. On the one hand, the nanogel swelling is clearly affected by the counterion valence. Indeed, an increase from $z_+ = 1$ to $z_+ = 3$ (at a fixed ionic strength) yields a decrease of the nanogel size and a shift of the transition temperature, T_Θ, to lower values. This means that increasing z_+ leads to a more efficient screening of the electrostatic repulsion. The explanation of this effect relies on the interplay between electrostatic and steric forces. Indeed, the number of trivalent counterions that permeate inside the nanogel to compensate the nanogel charge is about three times smaller (compared to monovalent counterions), and so the volume exclusion that they experience is smaller. In addition, trivalent ions tend lo strongly bind to more than one charged groups, so polymer chains deform to wrap the trivalent counterions, thus enhancing the nanogel shrinking. On the other hand, rising the particle charge shifts the swelling curve to larger values of R_m. This effect is due to the electrostatic repulsion between the charged beads within the nanogel, which causes an enhanced stretching or the polymer chains. This charged-induced stretching is less pronounced for the case of trivalent counterions, which is consistent with the reinforced screening effect induced by multivalent ions.

Along with the changes of the average size, the particle shrinking also carries the appearance of inhomogeneities in the polymer mass and charge distribu-

tion inside the particle. Two snapshots of the simulated nanogel in the swollen and shrunken states are depicted in Fig. II.1 to illustrate this effect. In the expanded state, the distribution of charge and mass is rather uniform in the major part of the nanogel, and gradually goes to zero in the external shell. However, in the collapsed state, the internal structure is clearly not homogeneous, as it develops a hollow core where the crosslinker chains are stretched. The size of the central low-density region is of the order of the distance betwee two neighbouring cross-linkers (about 2 nm). Surrounding this low density region, there is a peripheric spherical shell where the polymer concentration is very high. Moreover, the charged monomeric units tend to accumulate preferentially at the internal and external sides of the dense crown. We obtain this kind of structure in the collapsed state in all cases, regardless the values of the nanogel charge and counterion valence. This result agrees with previous simulation and theoretical predictions that prove that this particular morphology minimizes the free energy of the system formed by the nanogels and the surrounding ions.[13–15]. Indeed, the total free energy of the system may be split in a sum of ideal, elastic, solvation and electrostatic contributions $F_{tot} = F_{id} + F_{elas} + F_{solv} + F_{elec}$. F_{id} is the ideal free energy of the ions. The elastic term, F_{elas}, is usually approximated by the rubber elasticity model.[2] The solvation free energy is controlled the temperature-dependent monomer-monomer hydrophobic attraction, and can be written in first approximation as $F_{solv} = k_B T \int B_2(T) \rho_{\mathrm{mon}}(r)^2 dr^3$, where $B_2(T)$ is the second virial coefficient of the monomer-monomer pair potential and $\rho_{\mathrm{mon}}(r)$ is the local number density of monomers inside the nanogel. Finally, F_{elec} accounts for the electrostatic interactions between charged monomers and ions, and can be calculated in consistency with the HNC intergral equation framework.[19]. For neutral or weakly charged nanogels, the elastic and solvent contribution dominate, leading to homogeneous swelling. However, for strongly charged nanogeles (as the ones considered in our work) the electrostatic free energy is able to dominated over the elastic contribution and provoke the appearance of such kind of heterogeneous morphology when approacing the collapsed state.

At this point, it should be noticed that nanogels can adopt very different conformations as a function of the number of beads per chain changes. This aspect has been previously observed by explicit coarse-grained Monte Carlo simulations of thermo-responsive nanogels in salt-free solutions.[13,46] In this sense, Claudio *et al.* have demonstrated that gel immersed in salt-free solutions in the micrometer range, it is permissible to assume full charge compensation inside the gel. However, for gels smaller than 250 nm, counterions can leak out of the

gel.[47] On the other hand, Mozuelos have recently shown that interaction be-
tween charged microgels immersed in a simple electrolyte can be influenced by
their size.[44]

In order to analyse the internal structure of the different nanogels studied in
this work, in Fig. II.2 we plot the distribution of charged monomers and coun-
terions as a function to the distance to the nanogel centre, for nanogels with 1
monomer charged per chain ($f = 1$). To this end, three temperatures (293 K,
308 K and 323 K), which resemble representative states of our thermosensitive
nanogels (expanded, transition and collapse states, respectively), are explored.
Also, the effect of the counterion valence is discussed ($z_+ = 1$ and $z_+ = 3$ for
up and down panels of Fig. II.2, respectively). First, we will focus on the distri-
bution of charged monomers obtained from simulations (blue lines), that will
be used as inputs in the theory. As can be seen, similar qualitative behaviour
is observed for $z_+ = 1$ and $z_+ = 3$. As the temperature increases (left to right),
charged monomers tend to change from approximate homogeneous distribu-
tions, to form clear structures with two peaks in the case of collapsed confor-
mations. Uncharged beads collapse due to attractive hydrophobic forces and
they would tend to segregate the hydrophilic charged monomers to minimize
the free energy. Consequently, many of the charged beads would be displaced
toward the outer and inner surfaces of the monomer clusters, which would give
rise to the appearance of the peaks. These peaks are more noticeable for the
case of $z_+ = 3$. Hence one can infer that, for collapsed nanogels, an increase of
the counterion valence induces a major structuting of charged monomers into
internal and external layers, which is intimately related to the strong binding
between multivalent ions and the charged beads. This is in agreement with the
swelling curves shown in Fig. II.1 and with previous computer simulation results
obtained for thermo-responsive nanogels in salt-free suspensions.[41] Therein it
was shown that the thermo-shrinking response of these systems shifts to lower
temperatures when monovalent counterions are replaced by multivalent ones.
As mentioned, this effect was justified in terms of the reduction of the number
of counterions required to neutralize the particle bare charge.

We shall now centre on the counterion distributions obtained from the-
ory and simulations (green and red dashed lines, respectively) also included in
Fig. II.2. In most of the cases, the agreement between theory and simulations is
excellent. In the swollen state, the internal morphology of the particle consists
of large pores through which ions can penetrate, but as particle shrinks, the size
of the pores decreases. Collapsed states, however, exhibit a non-homogeneous
morphology in the inner region of the particle characterized by two peaks. Log-
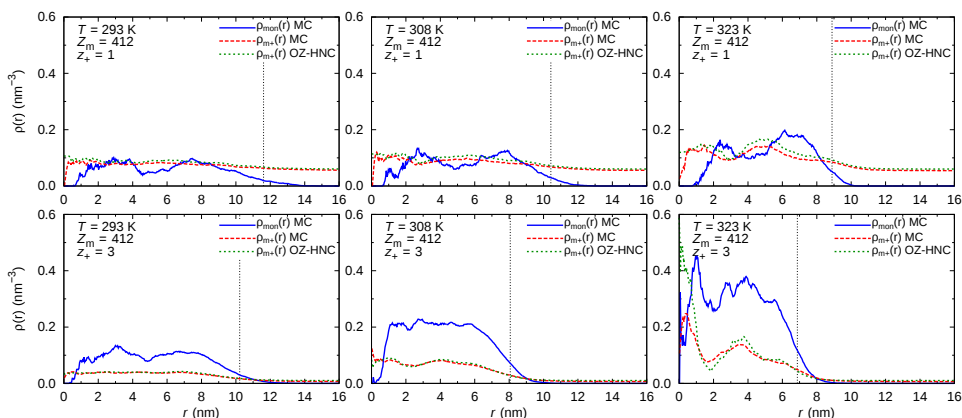
Figure II.3: Blue solid line: simulated density profile of charged monomers as a function of the distance to the nanogel centre. Red dashed line: simulated density profile of counterions. Green dotted line: density profile of counterions predicted from integral equations within the HNC approximation. The different plots show the results for monovalent and trivalent counterions at three different swelling states, for $Z_m = -402e$ ($f = 2$). The dashed vertical line represents the external radius of the nanogel.

ically, counterions tend to be placed in the vicinity of charged beads. Indeed, it is well known that when the polymer is strongly charged, the electrostatic potential on the chain is large and some of the counterions remain bound to the chain. This counterion condensation is referred as Manning condensation.[48] Therefore, a parallelism between charged monomer and counterion distributions is expected. Nonetheless, the coincidence of the position of the peaks of both, charged beads and counterions, is more patent in the case of $z_+ = 3$. This feature can be due to the fact that a larger amount of monovalent counterions are required to neutralize the monomer charges than in the case of trivalent cations. Accordingly, many non-punctual monovalent counterions are necessary structured in different layers around the charged beads. Concerning the height of the peaks of counterion distribution, this is quite similar to that found for the charged monomer for $z_+ = 1$, in which the valence of counterions coincides with the valence of charged monomers in absolute value. For $z_+ = 3$, the height of the counterions distributions is logically less than the one for the charged monomers. However, a disagreement is observed in this particular case, as the theoretical predictions overestimate the heigth of main peak of the counterion density profile. This finding can be explained if one considers that integral equation theories within the HNC approximation tend to overestimate the ionic short-range correlation effects.[49] Such overestimation is expected to

be more strengthened when ionic short-correlations are promoted: collapsed nanogels in the presence of multivalent counterions.

Having arrived at this point, we can ask ourselves a question: how can the charge of the polyelectrolyte affect the distribution curves previously shown? In order to answer this query, charges per chains have been doubled ($f = 2$) and the corresponding results have been plotted in Fig. II.3. As can be seen, significant differences with respect to the case of $f = 1$ (Fig. II.2) are observable. Now, for the case of $z_+ = 1$, the appearance of two comparable peaks in the charged monomer distribution is discernible for the three temperatures studied. As the nanogel collapses, the height of the peaks increases. Moreover, it seems that in this case, a larger amount of charged beads are displaced towards the outer surface of the monomer clusters, previously commented. Notwithstanding, this tendency in collapsed nanogels disappears when $z_+ = 3$. Under this scenario, two dissimilar peaks are observed again, although their shape is less well-defined that in the case of $f = 1$. This feature is consistent with the fact that trivalent counterions are able to neutralize several charged beads and diverse structures can be adopted by collapsed nanogels. Regarding the counterion distributions, a similar behaviour than in the case of $f = 1$ is in general observed. In this case, the position of the counterions peaks in collapsed nanogels and $z_+ = 3$ does not fit with the distance at which the charged beads exhibit the peaks. These results can be related to the fact that, now, there is a larger uncertainty in the position of the charged monomers when $f = 2$. Whatever the case, the inner structure of the nanogels significantly change when the charge per chain increases. This agrees with previous simulations in which the charge of the polyelectrolytes decisive influence on thermo-sensitive behaviour of nanogels.[42] Therein it was proved that the increase of the number of ionized monomers per chain results in a reduction of thermosensitivity.

It is important to remark that the ionic strength fixed in our calculations is relatively high (100 mM) for the two studied electrolytes. This means that the screening of the monomeric charges within the nanogel attained at such electrolyte concentration is quite significant due to the small value of the Debye screening length $\lambda_D = \kappa^{-1}$. Under these conditions, the neutralization of the nanogel charge is expected to occur locally almost at every point of the particle. With the aim to corroborate this, we plotted in Fig. II.4 the net charge density $\rho_e(r)$ as a function of the distance to the nanogel centre for both salts and for $f = 1$. As mentioned in Section 2, the charged monomers of the nanogel and the monovalent coions are negatively charged, while the counterions have positive electric charge. Hence, in those regions of space where nanogel charge is
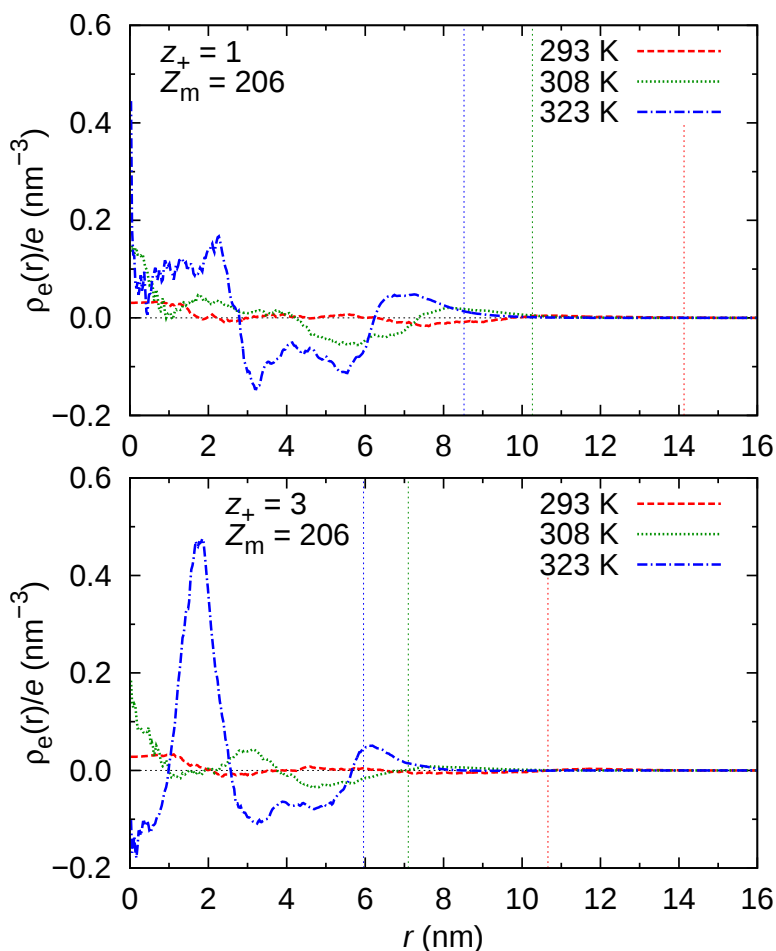
Figure II.4: Net charge density as a function of the distance to the nanogel centre for three swelling states and for 1:1 (top pannel) and 3:1 (bottom pannel) electrolytes. In all cases $f = 1$. Vertical dashed lines represent the external radius of the microgel for each swelling state.

not neutralized $\rho_e(r)$ is locally negative, while if there is a large concentration of counterions the total net charge density becomes positive. As observed in Fig. II.4, for nanogels in the swollen state and around the transition temperature electroneutrality is practically fulfilled, with only few fluctuations appearing mostly close to the nanogel centre. This is especially true for the trivalent salt, where the screening effect is emphasized by the valence of the counterions. However, in the collapsed state, the large fluctuations that arise due to the bimodal charge distribution and the steric exclusion exerted by the denser corona

lead to the appearance of regions where local electroneutrality is disrupted.

Finally, it is interesting to include some general comments on the reliability of the model employed for the excluded-volume interaction between the polymer network and the in-diffusing finite-size ions (see equation II.8). As observed from the comparison between theory and simulations, this model works surprisingly well in spite of the crude approximation that it involves. Indeed, this excluded-volume interaction is deduced from the assumption that the internal structure of the nanogel can be modelled by an array of randomly located overlapping spherical monomers, which is a very rough approximation of the real structure. A possible way to correct this effect is to consider the penetrable-concentric shell model (PCS), which was originally introduced by Torquato.[50] Within this improved model, the monomers are again randomly distributed, but monomer overlap is forbidden. An analytical formula that provides a very good estimate of the steric repulsion for this case is (see the Appendix for further details)[51–53]

$$\beta V_{\mathrm{m}i}^{\mathrm{exc}}(r) = -\ln(1 - \phi(r)) + \frac{1 - \lambda_i^3}{\lambda_i^3} \frac{\phi(r)}{1 - \phi(r)} +$$
$$+ \frac{3\phi(r)^2}{2\lambda_i^3(1 - \phi(r))^3} \left[2 - 3\lambda_i + \lambda_i^3 - (3\lambda_i - 6\lambda_i^2 + 3\lambda_i^3)\phi(r) \right], \tag{II.14}$$

where, again, $\lambda_i = R_{\mathrm{mon}}/(R_{\mathrm{mon}} + R_i)$.

In principle, the PCS approximation should provide a more realistic representation of the internal structure of the nanogel, as it corrects for the monomer impenetrability at the time that allows the overlap of the depletion regions. However, when this model is applied to calculate the ionic density profiles, it systematically overestimates the steric exclusion (not shown). The disagreement provided by the PCS model is especially important when considering collapsed nanogels, at it emphasizes the depletion of ions in the region inside the dense crown. Clearly, this result indicates that the real morphology of the polymer network is not well captured by a naive model based on an assembly of randomly placed hard monomers. Indeed, the monomeric units are in fact inter-connected to form cross-linked chains. This chain-like structure leads to larger pores that, in turn, provides extra free volume inside the nanogel, and so reduces the steric exclusion. In addition, the pores inside the nanogel are not permanent, but they are the result of the temporary spacings between the flexible and mobile polymer chains, which may deform when ions passes through them. This polymer flexibility facilitates the ionic in-diffusion in comparison to the permeation though a rigid network. Therefore, the reason why the model

based on random overlapping monomers (eqn II.8) works so well seems to be a compensation of allowing monomer overlaps, which decreases excluded volume, with assuming randomly placed beads, which increases it. Nevertheless, a more detailed theoretical description of the internal conformation of the polymer network should be addressed in future studies.

5   Conclusions

The good agreement between the simulated density profiles and the theoretical predictions provide us the following feedback. First, integral equation theory within the HNC closure represents a reliable method for predicting the distribution of ions inside porous thermo-responsive nanogels, even for large nanogel charges, multivalent ionic species, and in conditions of strong confinement. Second, splitting the nanogel-ion effective interaction into electrostatic and excluded-volume additive terms is in general a good approximation. Third, modeling the internal structure of the nanogel by an assembly of random overlapping spherical monomers works surprisingly well even though it represents a strong approximation of the real morphology of the nanogel.

The results show that the valence of counterions affects the internal structure of the nanogel. Moreover, trivalent counterions neutralize the nanogel charge more efficiently than monovalent ones, inducing a shift of volume transition at lower temperatures. Moreover, as the nanogel charge increases, the effect of the valence of counterions is more noticeable. In fact, an enhanced nanogel shrinking is achieved for the case of highly charged nanogels in the presence of trivalent counterions. Nevertheless, it must be taken into account that the primitive model used here is too rudimentary to rationalize the real behaviour of such soft nanoparticles. Therefore, more complex interactions between the charged monomers and the ions (for instance, those depending on their chemical nature) are required for a complete description of this kind of systems.

Appendix: Partition coefficient of arrays of random spheres

In this Section we derive the equilibrium partition coefficient of a spherical solute that permeates inside a polymeric matrix. For this purpose, we consider a bulk suspension of a certain solute molecule in equilibrium with a porous polymer network. If the polymer-solute interactions are negligible, the concentration of solute inside and outside are identical. However, the existence of attractive or repulsive solute-polymer interactions establishes a concentration difference between the porous and bulk media. The partition coefficient is defined as

$$K = \frac{\rho_{\text{in}}}{\rho_{\text{bulk}}} \tag{II.15}$$

If the solute permeation is hindered exclusively by excluded-volume interactions, then in the limit of very low solute concentration the partition coefficient is given by

$$K = \frac{v_{\text{free}}}{v} = \phi_{\text{free}} \tag{II.16}$$

where v is the volume of the polymer network, v_{free} is the free volume left by the polymer chains, and ϕ_{free} is the free volume fraction (or porosity) inside the polymer network. We consider that our porous medium is homogeneous, defined by a constant polymer volume fraction, ϕ (the generalization to the non-homogeneous case will be done at the end of the section). We also assume that the solute is spherical and neutral, with a radius R_{s}. The polymer network can be thought of as being composed by a collection of spherical monomers, each one represented by a sphere of radius R_{mon}.

In the limit of point-like solute ($R_{\text{s}} = 0$), the free volume is simply given by $\phi_{\text{free}} = 1 - \phi$. However, for finite-size solutes the relation between ϕ_{free} and ϕ is not so obvious. The main difficulty arises from the fact that, in dense polymer networks, the volume-exclusion effect not only depends on ϕ, but also on the geometric details of the internal morphology of the porous medium, that is, on the location of the spherical monomers. Indeed, as we increase the monomer packing fraction the overlap between the depletion regions of two or more monomers increases in a non-linear fashion and becomes very difficult to calculate (see Fig. II.5).

Therefore, the problem to tackle is the calculation of free volume fraction, ϕ_{free}, left by a collection of N spheres that can mutually overlap. In order to
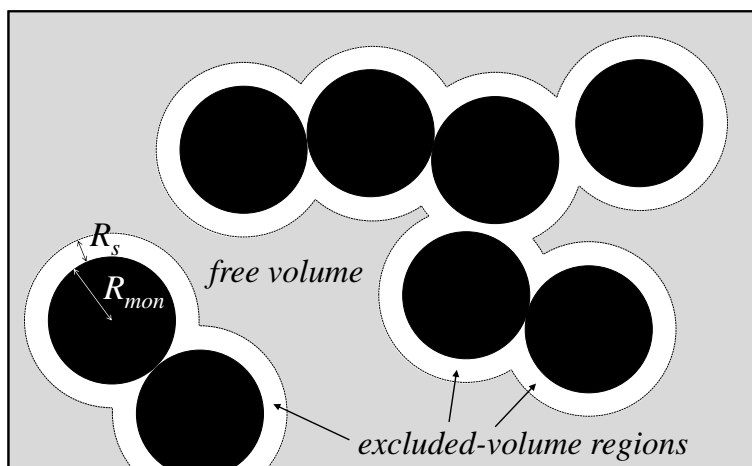
Figure II.5: Schematic view of the internal volume of a nanogel. Black spheres represent the spherical monomeric units, of radius R_{mon}. The excluded-volume regions around the monomers are depicted in white. The total volume occupied by the monomers is the union of spheres of radius $R_{\mathrm{mon}} + R_{\mathrm{s}}$. The free volume left by the monomers is shown in grey.

simplify more the notation, we define a as the radius of the spheres and ρ its number density. The position of the N spheres are specified by their coordinates $\{\vec{r}_1, \vec{r}_2, \cdots, \vec{r}_N\} \equiv \{\vec{r}_i\}$. In order to identify the positions of the particles we make use of the indicator function, firstly introduced by Torquato and Stell[54]

$$m(\vec{x}, \vec{r}_i) = \begin{cases} 1 & |\vec{x} - \vec{r}_i| < a \\ 0 & |\vec{x} - \vec{r}_i| \geq a \end{cases} \tag{II.17}$$

where $\vec{r}_i$ is the position of the centre of the ith sphere. Analogously, we define the statistical variable $I(\vec{x}, \{\vec{r}_i\})$, so that $I(\vec{x}, \{\vec{r}_i\}) = 0$ if $\vec{x}$ lies inside any of the spheres and $I(\vec{x}, \{\vec{r}_i\}) = 1$ if $\vec{x}$ does not belong to any sphere

$$I(\vec{x}, \{\vec{r}_i\}) = \begin{cases} 1 & \text{if } |\vec{x} - \vec{r}_i| < a \quad \forall i = 1, \cdots, N \\ 0 & \text{otherwise} \end{cases} \tag{II.18}$$

We can write $I(\vec{x}, \{\vec{r}_i\})$ in terms of the indicator functions

$$I(\vec{x}, \{\vec{r}_i\}) = \prod_{i=1}^{N} (1 - m(\vec{x}, \vec{r}_i)) \tag{II.19}$$

The free volume ϕ_{free} is nothing but the the statistical canonical average of $I(\vec{x}, \{\vec{r}_i\})$ performed over all possible positions of the N spheres[54]

$$\phi_{\mathrm{free}} = \langle I(\vec{x}, \{\vec{r}_i\}) \rangle = \int I(\vec{x}, \{\vec{r}_i\}) P_N(\{\vec{r}_i\}) d\vec{r}_1 \cdots \vec{r}_N \tag{II.20}$$

where $P_N(\{\vec{r}_i\}) = Z_N^{-1} \exp(-\beta U_N)$. U_N is the total interaction energy of the N spheres, and Z_N is the configuration integral, defined as $Z_N = \int \exp(-\beta U_N) d\vec{r}_1 \cdots d\vec{r}_N$. From P_N we can calculate the n–point correlation functions, defined as

$$g^{(n)}(\vec{r}_1, \cdots, \vec{r}_n) = \frac{N!}{\rho^n (N-n)!} \int P_N d\vec{r}_{n+1} \cdots \vec{r}_N \tag{II.21}$$

Expanding the products in equation II.19 and gathering the multiple identical terms we find that

$$\phi_{\text{free}} = \int P_N d\vec{r}_1 \cdots d\vec{r}_N - N \int m(\vec{x}, \vec{r}_1) P_N d\vec{r}_1 \cdots d\vec{r}_N +$$
$$+ \frac{N(N-1)}{2} \int m(\vec{x}, \vec{r}_1) m(\vec{x}, \vec{r}_2) P_N d\vec{r}_1 \cdots d\vec{r}_N - \cdots = \tag{II.22}$$
$$= 1 + \sum_{n=1}^{N} \frac{(-1)^n N!}{n!(N-n)!} \int \prod_{i=1}^{n} m(\vec{x}, \vec{r}_i) P_N d\vec{r}_1 \cdots d\vec{r}_N$$

Using the correlation functions given by equation II.21 and taking the thermodynamic limit $N \to \infty$

$$\phi_{\text{free}} = 1 + \sum_{n=1}^{\infty} \frac{(-1)^n}{n!} \rho^n \int \prod_{i=1}^{n} m(\vec{x}, \vec{r}_i) g^{(n)}(\vec{r}^n) d\vec{r}_1 \cdots d\vec{r}_n \tag{II.23}$$

Equation II.23 provides the free volume as an expansion in the correlation functions. Retaining the first n terms of the sum provides an approximation that improves as the number density of spheres becomes smaller. For instance, for very low number density the terms with $n > 3$ in the sum could be neglected. Unfortunately, the knowledge of $g^{(n)}(\vec{r}^n)$ is in general difficult for an arbitrary interaction energy U_N. At this point, it is necessary to make some approximations. Here, we present the two approximations used in this paper

5.1   Model 1: Random overlapping monomers

This model supposes that the location of the monomer centres inside the polymer matrix is completely random. It involves a very tough approximation: the correlation functions of the spheres are $g^{(n)}(\vec{r}^n) = 1$, which means that they behave as an ideal gas. In spite of its simplicity, this model has two important advantages: first, it takes the overlap between depletion regions into account and so, the model can be applied even for dense media. Second, the free volume can be analytically determined.

In this case, the n integrals in expression II.23 are decoupled and can be independently solved, each integral being the volume of the sphere, $v_1 = (4/3)\pi a^3$:

$$
\begin{aligned}
\phi_{\text{free}} &= 1 + \sum_{n=1}^{\infty} \frac{(-1)^n}{n!} \rho^n \left[\int m(\vec{x}, \vec{r}_1) d\vec{r}_1 \right]^n \\
&= \sum_{n=0}^{\infty} \frac{(-\rho v_1)^n}{n!} = \exp(-4\pi \rho a^3/3).
\end{aligned}
\tag{II.24}
$$

Now, we consider again our original problem, i.e. the calculation of the free volume for a solute of radius R_{s} that diffuses inside a polymer network with a volume fraction ϕ, formed by a collection of monomers of size R_{mon} each one surrounded by a depletion layer of radius $R_{\text{mon}} + R_{\text{s}}$. If equation II.24 is applied with $a = R_{\text{mon}}$ we get

$$
1 - \phi = \exp(-4\pi \rho R_{\text{mon}}^3/3)
\tag{II.25}
$$

In a similar way, if we consider the excluded volume for the solute (spheres with radius $a = R_{\text{mon}} + R_{\text{s}}$), the total free volume available for the solute is

$$
\phi_{\text{free}} = \exp(-4\pi \rho (R_{\text{mon}} + R_{\text{s}})^3/3)
\tag{II.26}
$$

Both expressions can be combined to express ϕ_{free} in terms of ϕ:

$$
\phi_{\text{free}} = (1 - \phi)^{(1 + \frac{R_{\text{s}}}{R_{\text{mon}}})^3}
\tag{II.27}
$$

If the polymer network is not homogeneous but exhibits dependence with the distance (as occurs in a nanogel), we can apply a local field approximation and assume that the free volume calculated for an homogeneous network can also be used in the case of an r-dependent polymer volume fraction, $\phi(r)$. This approximation is expected to work well as long as the length scale of the heterogeneities is larger than R_{s}.

5.2 Model 2: Random non-overlapping spheres

In the previous section we wrote down the equation for the fraction of free volume inside a system formed by a random collection of spheres of radius a with a number density ρ. It was given by $\phi_{\text{free}} = \exp(-4\pi \rho a^3/3)$. As it was already mentioned, this equation is exact for totally penetrable (uncorrelated) spheres. In the opposite limit, when the assembly is made of impenetrable hard spheres, the fraction of free volume left by the spheres is $\phi_{\text{free}} = 1 - 4\pi \rho a^3/3$. Both models can be considered as limiting cases of a more general situation, the so-called

penetrable-concentric-shell model (PCS).[50] Within this more general approximation, each sphere of radius a is composed of an impenetrable hard core of radius λa surrounded by a fully permeable concentric shell of thickness $(1-\lambda)a$. λ represents an scaling factor between the core and the particle radius. The extreme limits $\lambda = 0$ and 1 correspond, respectively, to the cases of perfectly penetrable (i.e., randomly centred) and totally impenetrable monomers.

Within the PCS model, the depletion regions around the hard monomers may intersect, but the monomers are still impenetrable. Although the exact calculation of ϕ_{free} for any λ-value has not been performed yet, we still can make use of an approximated analytical expression for the PCS model obtained by Rikvold and Stell using the scaled-particle framework[52,53]. Their model compares really well with computer simulation results of random media composed of spheres distributed with an arbitrary degree of permeability[51]. According to their theoretical prediction, the free volume in the PCS as a function of the packing fraction of the impenetrable cores, $\phi = 4\pi\rho(\lambda a)^3/3$, is given by

$$\phi_{\text{free}} = (1-\phi)\exp\left[-\frac{1-\lambda^3}{\lambda^3}\frac{\phi}{1-\phi}\right]F_3(\lambda,\phi) \tag{II.28}$$

where

$$F_3(\lambda,\phi) = \exp\left\{-\frac{3\phi^2}{2\lambda^3(1-\phi)^3}\left[2-3\lambda+\lambda^3-(3\lambda-6\lambda^2+3\lambda^3)\phi\right]\right\} \tag{II.29}$$

On the one hand, for $\lambda = 1$ the previous equation reduces to $\phi_{\text{free}} = 1-\phi = 1-4\pi\rho a^3/3$. On the other hand, for $\lambda \to 0$ we must take the limit carefully, as $\phi \to 0$ but keeping constant $\phi/\lambda^3 = 4\pi\rho a^3/3$. In this limit, we recover the exact result $\phi_{\text{free}} = \exp(-4\pi\rho a^3/3)$, consistent with equation II.24.

In order to apply this expression to calculate the free volume inside the nanogel, we take R_{mon} as the radius of the core, whereas the radius of the penetrable sphere is $R_{\text{mon}} + R_{\text{s}}$ (excluded region). Therefore, in our particular case the scaling factor is $\lambda = R_{\text{mon}}/(R_{\text{mon}} + R_{\text{s}})$. Again, eqn II.28 may be extended to study the solute permeation inside a non-homogeneous nanogel by including the local dependence of the volume fraction $\phi(r)$.

References

[1] Saunders, B. R.; Vincent, B. *Adv. Colloid Interface Sci.* **1999**, *80*, 1–25.

[2] Fernandez-Nieves, A.; Wyss, H. M.; Mattsson, J.; Weitz, D. A. In *Microgel Suspensions: Fundamentals and Applications*; Fernandez-Nieves, A., Wyss, H., Mattsson, J., Weitz, D., Eds.; Wiley-VCH: Weinheim, 2011; p 461.

[3] Tanaka, T.; Fillmore, D. J. *J. Chem. Phys.* **1979**, *70*, 1214–1218.

[4] Blackburn, W. H.; Dickerson, E. B.; Smith, M. H.; McDonald, J. F.; Lyon, L. A. *Bioconjugate Chem.* **2009**, *20*, 960–968.

[5] Ghugare, S. V.; Mozetic, P.; Paradossi, G. *Biomacromolecules* **2009**, *10*, 1589–1596.

[6] Ramos, J.; Imaz, A.; Callejas-Fernández, J.; Barbosa-Barros, L.; Estelrich, J.; Quesada-Pérez, M.; Forcada, J. *Soft Matter* **2011**, *7*, 5067–5082.

[7] Smith, M. H.; Lyon, L. A. *Acc. Chem. Res.* **2012**, *45*, 985–993.

[8] Lu, Y.; Welsch, N.; Dzubiella, J.; Ballauff, M. In *Intelligent Hydrogels*; Sadowski, G., Richtering, W., Eds.; Springer International Publishing: Cham, 2013; pp 113–130.

[9] Denton, A. R. *Phys. Rev. E* **2003**, *67*, 011804–10. *Erratum–ibid* **2003**, *68*, 049904.

[10] Gottwald, D.; Likos, C. N.; Kahl, G.; Löwen, H. *Phys. Rev. Lett.* **2004**, *92*, 068301.

[11] Moncho-Jordá, A.; Anta, J. A.; Callejas-Fernández, J. *J. Chem. Phys.* **2013**, *138*, 134902.

[12] Colla, T.; Likos, C. N.; Levin, Y. *J. Chem. Phys.* **2014**, *141*, 234902.

[13] Quesada-Pérez, M.; Martín-Molina, A. *Soft Matter* **2013**, *9*, 7086–7094.

[14] Adroher-Benítez, I.; Ahualli, S. A.; Martín-Molina, A.; Quesada-Pérez, M.; Moncho-Jordá, A. *Macromolecules* **2015**, *48*, 4645–4656.

[15] Rumyantsev, A. M.; Rudov, A. A.; Potemkin, I. I. *J. Chem. Phys.* **2015**, *142*, 171105–5.

[16] Yigit, C.; Welsch, N.; Ballauff, M.; Dzubiella, J. *Langmuir* **2012**, *28*, 14373–14385.

[17] Moncho-Jordá, A. *J. Chem. Phys.* **2013**, *139*, 064906.

[18] Moncho-Jordá, A.; Adroher-Benítez, I. *Soft Matter* **2014**, *10*, 5810–5823.

[19] Moncho-Jordá, A.; Dzubiella, J. *Phys. Chem. Chem. Phys.* **2016**, *18*, 5372–5385.

[20] Topuz, F.; Henke, A.; Richtering, W.; Groll, J. *Soft Matter* **2012**, *8*, 4877–4881.

[21] Sing, C.; Zwanikken, J.; Olvera de la Cruz, M. *Macromolecules* **2013**, *46*, 5053–5065.

[22] Ulrich, S.; Seijo, M.; Stoll, S. *Curr. Opin. Colloid Interface Sci.* **2006**, *11*, 268–272.

[23] Dobrynin, A. V. *Curr. Opin. Colloid Interface Sci.* **2008**, *13*, 376–388.

[24] Dias, R. S.; Pais, A. A. C. C. *Adv. Colloid Interface Sci.* **2010**, *158*, 48–62.

[25] de Carvalho, S. J.; Metzler, R.; Cherstvy, A. G. *Phys. Chem. Chem. Phys.* **2014**, *16*, 15539–15550.

[26] de Carvalho, S. J.; Metzler, R.; Cherstvy, A. G. *Soft Matter* **2015**, *11*, 4430–4443.

[27] Clavier, A.; Seijo, M.; Carnal, F.; Stoll, S. *Phys. Chem. Chem. Phys.* **2015**, *17*, 4346–4353.

[28] Uhlík, F.; Košovan, P.; Zhulina, E. B.; Borisov, O. V. *Soft Matter* **2016**, *12*, 4846–4852.

[29] Quesada-Pérez, M.; Ramos, J.; Forcada, J.; Martín-Molina, A. *J. Chem. Phys.* **2012**, *136*, 244903–9.

[30] Mann, B. A.; Everaers, R.; Holm, C.; Kremer, K. *Europhys. Lett.* **2004**, *67*, 786–792.

[31] Mann, B. A.; Holm, C.; Kremer, K. *J. Chem. Phys.* **2005**, *122*, 154903–14.

[32] Yin, D. W.; Yan, Q.; De Pablo, J. J. *J. Chem. Phys.* **2005**, *123*, 174909–9.

[33] Yin, D. W.; Olvera De La Cruz, M.; De Pablo, J. J. *J. Chem. Phys.* **2009**, *131*, 194907.

[34] Košovan, P.; Richter, T.; Holm, C. *Macromolecules* **2015**, 151005144031005.

[35] Weast, R. C.; Astle, M. J.; Beyer, W. H.; Others, *CRC handbook of chemistry and physics*; CRC press Boca Raton, FL, 1988; Vol. 69; p 496.

[36] Schneider, S.; Linse, P. *J. Phys. Chem. B* **2003**, *107*, 8030–8040.

[37] Ghosh, S. K.; Cherstvy, A. G.; Metzler, R. *J. Chem. Phys.* **2014**, *141*, 074903.

[38] Escobedo, F.; de Pablo, J. *J. Chem. Phys.* **1996**, *104*, 4788–4801.

[39] Khan, M. O.; Mel'nikov, S. M.; Jönsson, B. *Macromolecules* **1999**, *32*, 8836–8840.

[40] Schneider, S.; Linse, P. *Macromolecules* **2004**, *37*, 3850–3856.

[41] Quesada-Pérez, M.; Maroto-Centeno, J. A.; Martín-Molina, A. *Macromolecules* **2012**, *45*, 8872–8879.

[42] Quesada-Pérez, M.; Ahualli, S. A.; Martín-Molina, A. *J. Chem. Phys.* **2014**, *141*, 124903.

[43] Chiew, Y.; Glandt, E. *J. Colloid Interface Sci.* **1984**, *99*, 86–96.

[44] González-Mozuelos, P. *J. Chem. Phys.* **2016**, *144*, 054902.

[45] Karanikas, S.; Dzubiella, J.; Moncho-Jordá, A.; Louis, A. A. *J. Chem. Phys.* **2008**, *128*, 204704.

[46] Rizzi, L. G.; Levin, Y. *J. Chem. Phys.* **2016**, *144*, 114903.

[47] Claudio, G. C.; Kremer, K.; Holm, C. *J. Chem. Phys.* **2009**, *131*, 094903–9.

[48] Manning, G. S. *J. Chem. Phys.* **1969**, *51*, 924–933.

[49] Quesada-Pérez, M.; Martín-Molina, A.; Hidalgo-Álvarez, R. *J. Chem. Phys.* **2004**, *121*, 8618–8626.

[50] Torquato, S. *J. Chem. Phys.* **1984**, *81*, 5079.

[51] Lee, S. B.; Torquato, S. *J. Chem. Phys.* **1988**, *89*, 3258.

[52] Rikvold, P. A.; Stell, G. *J. Chem. Phys.* **1985**, *82*, 1014–1020.

[53] Rikvold, P. A.; Stell, G. *J. Colloid Interface Sci.* **1985**, *108*, 158–173.

[54] Torquato, S.; Stell, G. *J. Chem. Phys.* **1982**, *77*, 2071.

The effect of electrosteric interactions on the effective charge of thermoresponsive ionic microgels: Theory and experiments

Irene Adroher-Benítez[⋆], Silvia Ahualli[⋆], Delfi Bastos-González[⋆], José Ramos[†], Jacqueline Forcada[†], and Arturo Moncho-Jordá[⋆‡]

[⋆]Departamento de Física Aplicada, Facultad de Ciencias, Universidad de Granada, Campus Fuentenueva S/N, 18071 Granada, Spain
[†]Grupo de Ingeniería Química, Facultad de Ciencias Químicas, Universidad del País Vasco/EHU, 20080 San Sebastián, Spain
[‡]Instituto Carlos I de Física Teórica y Computacional, Universidad de Granada, Campus Fuentenueva S/N, 18071 Granada, Spain

99

Abstract

In this work the influence of counterion valence and salt concentration on the effective charge of two types of thermoresponsive ionic microgel particles has been studied. The effective charge of the microgel at different swelling states has been experimentally determined from electrophoretic mobility measurements by solving the electrokinetic equations of the solvent for a single polyelectrolyte brush in the presence of an electric field, taking into account the friction of the solvent inside the polymer network. The experimental results have been compared to those obtained by means of the Ornstein-Zernike integral formalism within the HNC relation. Results show that microgel bare charge is screened by the combined effect of counterion condensation and permeation inside the microgel particle. In addition to the electrostatic interaction, the steric exclusion exerted by the polymer plays an important role on the local ionic concentrations, especially for shrunken configurations. This steric term is responsible for the strong increase of the microgel effective charge experimentally observed when particles shrink for temperatures above the lower critical solution temperature. We also observe that, in the internal region of the microgel, charge electroneutrality is fulfilled, so the effective charge mainly arises from the region close to the microgel surface.
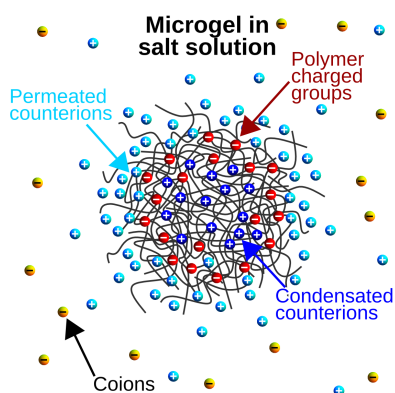
1   Introduction

Microgels are soft materials formed by a cross-linked polymer matrix that is subject to be permeated by the solvent, ions or other kinds of small macromolecules such as proteins or peptides[1]. In addition, microgels can reversibly swell or shrink in response to many external parameters as pH, ionic strength, temperature, light, or through external fields[2–7]. The combined capabilities of responsive swelling and solvent uptake have motivated their use in biomedical applications such as transport and delivery of drugs or other substances in a controlled fashion[8–13]. Even though the microgel softness allows the particles to be deformed and compressed, which has important implications on the fluid-solid phase coexistence in concentrated suspensions,[14] they still keep the entity of particle. That is, two microgel particles can not totally overlap due to the excluded-volume repulsion exerted by the cross-linked polymer chains[15].

Particles carrying charged monomeric units inserted into the internal polymer chains are usually refereed as ionic microgels. When an ionic microgel is immersed into an aqueous electrolyte solution, counterions and coions are able to diffuse through the inter-chain pores. The equilibrium swelling state of these microgels is the result of the balance among electrostatic, elastic and solvent-induced interactions,[4] which depend on many parameters. For instance, a decrease in the solvent affinity of the polymer chains provokes the microgel shrinking. This volume change is usually induced by raising the temperature above the so-called lower critical solution temperature (LCST), due to the fact that polymer chains become more hydrophobic in such case. Analogously, an increase of the cross-linker concentration contributes to enhance the particle stiffness, which narrows the degree of swelling. In addition, if microgel bare charge is increased, particle swelling is prompted by the enhanced electrostatic repulsion. Finally, the equilibrium swelling may be also strongly affected by the electrolyte concentration and the valence of the ions present in the solution[16–18].

An ionic microgel has a structural (or bare) charge, Z_{bare}, due exclusively to the polyelectrolytes that compound the microgel network. However, the degree of ionic permeation and the overall screening induced by the presence of electrolyte is usually characterized by the so-called effective charge, Z_{eff}[19]. In this work, it is defined as the net charge of the microgel particles, taking into account the contribution of the charged monomeric units and *all* the ions that have diffused inside the microgel, which partially screen Z_{bare}.

This effective charge provides a global estimate of the *real* charge that any other microgel or incoming ion experiences when approaching the particle from

outside[20,21]. Consequently, Z_{eff} is one of the most important parameters controlling the stability of the suspension.

The effective charge is also responsible for the electrostatic repulsive interaction between the inner charged polymer chains, so it also plays a crucial role on the swelling state of the particle. Indeed, large values of the effective charge promote the appearance of more expanded conformations of the microgel polymer network. Z_{eff} may be affected by many parameters, as the electrolyte concentration, the ion valence and the microgel swelling. In this respect, Z_{eff} is expected to decrease with the electrolyte concentration and the valence of the counterion due to the screening of the particle structural charge. In addition, if ion specificity is involved in the ionic adsorption, charge inversion and overcharging effects may arise, which cannot be explained only in terms of electrostatics[22–24]. Inversely, by shrinking the microgel, larger values of Z_{eff} are observed, since the microgel-ion excluded-volume repulsion together with the electrostatic repulsion between counterions inside the particle enhance the counterion exclusion from the volume inside the microgel[20,25].

In this work, the influence of the salt concentration and the counterion valence on the effective charge of thermoresponsive microgels have been analyzed. In order to confirm that the conclusions drawn from our study do not depend on the specific nature of the microgels, we have made use of two different microgels, PNIPAM and PVCL, based on N-isopropylacrylamide and N-vinylcaprolactam polymers, respectively.

On the one hand, PNIPAM-based cross-linked particles have been extensively investigated, and nowadays represent a model system in the field of polymer science[17,18,26]. However, their biotechnological applications have been limited because NIPAM monomers have been found to be toxic for living organisms[27,28]. On the other hand, PVCL-based microgels have shown higher biocompatibility,[28] so recent work have been done to develop biotechnological systems using these microgels, especially for drug delivery[29–32].

These microgels have been studied in presence of three different electrolytes with increasing counterion valence, namely NaCl, MgCl$_2$ and LaCl$_3$. The effective charge has been obtained in both experimental and theoretical ways. Firstly, experimental effective charge has been determined by measuring the electrophoretic mobility (μ_{e}) of very diluted microgel suspensions at different temperatures (i.e. swelling states), given that electrophoresis is the most common technique of microgel characterization[16,33]. For this purpose, the hydrodynamic equations of the solvent flowing through and around a single polyelectrolyte brush in the presence of an electric field have been solved, with ex-

plicit consideration of the internal friction exerted by the solvent inside the microgel polymer network[34]. Then, the experimental effective charge has been compared with the theoretical predictions obtained by solving the Ornstein-Zernike (OZ) integral equations for a three- component microgel-counterion-coion mixture.

In our model, not only the electrostatic interaction, but also the excluded-volume (steric) repulsion between the porous microgel and the permeating ions has been considered[20,22,35]. This procedure allows to determine the equilibrium density profiles of the ions inside and outside the microgel particle, and from direct integration, to calculate the effective charge of the particle. OZ equations are solved with the help of the well-known Hypernetted-Chain Closure relation (HNC) for all (microgel-ion and ion-ion) pair interactions. This approximation has been shown to perform very well for the kind of soft potentials employed in this study, regardless if they are attractive or repulsive,[36] leading to very good agreement with predictions obtained for swollen microgels by means of linear response theory[35,37,38].

We find good qualitative agreement between experiments and theory, and observe that the effective microgel charge increases as the particles de-swell toward more shrunken states. Theoretical predictions are able to fit the values of Z_{eff} at different swelling states, and interpret the changes in terms of the electrostatic and steric interactions between the incoming ions and the microgel. In addition, ionic condensation has been detected from the comparison between experiments and theory. This phenomenon has been previously observed in electrophoresis measurements[39] and widely studied by several authors,[19,40–44] given the significant consequences that is has on the electrostatic properties of colloidal suspensions. In this work, the condensation of counterions has been observed for PNIPAM microgels in presence of multivalent electrolytes. In such cases, the microgel bare charge is screened by means of two different mechanisms, namely counterion diffusion through microgel pores and counterion condensation inside the microgel. Consequently, an intermediate microgel charge has been defined, the apparent charge Z_{app}, which stands for the the net charge of the microgels screened by counterion condensation exclusively, so that $|Z_{\text{bare}}| > |Z_{\text{app}}| > |Z_{\text{eff}}|$.

This paper is organized as follows. First, the synthesis of the two microgels and the experimental techniques employed in their characterization are briefly described in Section 2. Then, Section 3 explains the method used to convert the measured electrophoretic mobility into effective charge. Section 4 shows the model for particle interactions and the theoretical framework employed to de-

termine the ionic density profiles and the microgel effective charge. The experimental results are presented and compared with our theoretical data in Section 5. Finally, in Section 6 the most relevant conclusions of this work are summarized.

2 Experimental

2.1 Chemicals

All the products employed in this work were of analytical grade and used as received. For each synthesis and salt solution, double deionized (DDI) water was used (Milli-Q). For PNIPAM microgels, the polymer N-isopropylacrylamide (NIPAM) and the cross-linking agent N,N'-methylenebis(acrylamide) (MBA) were obtained from Acros, while the iniciator potassium peroxydisulfate (KPS) was purchased from Sigma-Aldrich and Scharlau. Por PVCL microgels, the polymer N-vinylcaprolactam (VCL), the buffer sodium bicarbonate (NaHCO$_3$), the emulsifier sodium dodecyl sulfate (SDS), the iniciator potassium peroxydisulfate (KPS) and the acrylic acid (AA) used to provide the electric charge were purchased from Sigma-Aldrich, while the cross-linker poly(ethylene glycol) diacrylate (PEGDA) was obtained from Polysciences, Inc.

Salt solutions were prepared with sodium chloride (NaCl), magnesium chloride (MgCl$_2$) hexahydrate, and lanthanum chloride (LaCl$_3$) heptahydrate from Sigma-Aldrich.

2.2 Preparation of microgels

Both PNIPAM and PVCL microgels were synthesized by emulsion polymerization in a batch reactor. A detailed description of the synthesis procedure and cleaning process of the PNIPAM is given by Pérez-Fuentes *et al.*[45]. The PVCL microgel suspension was synthesized following the protocol developed by Imaz and Forcada[46] (the PVCL microgel corresponds to AA4st2 in their nomenclature). In Table III.1 the amounts of every chemical employed in its synthesis are shown. After the synthesis, the PVCL microgel was cleaned by dialysis, until the conductivity of the dialysate was similar to that of the DDI water.

Reactant	VCL	NaHCO$_3$	SDS	PEGDA	H$_2$O DDI	KPS	AA
Mass (g)	2.04	0.0203	0.0804	0.0804	200.12	0.0201	0.08

Table III.1: Quantities of reactants used in PVCL microgel synthesis

Even though both NIPAM and VCL are neutral monomers, charged groups have been incorporated to the microgels during the syntheses in order to obtain ionic particles. In both cases, sulfate groups come from the initiator KPS. In addition, PVCL-based microgels have carboxylic groups provided by the acrylic acid.

2.3   Diameter and electrophoretic mobility measurements

Measurements were performed with a Zetasizer Nano ZS system from Malvern Instruments. Particle size was determined by means of Dynamic Light Scattering (DLS) technique, while electrophoretic mobility was measured by using the laser Doppler micro-electrophoresis technique.

Temperature ranged from 20 °C to 52 °C, taking measurements every 2 °C, in order to study the whole range of volume states of the microgel. The sample was equilibrated during two minutes at the desired temperature to ensure a stable temperature. Three measurements at each temperature were taken, with a maximum standard deviation of 3.71% for size measurements. For the electrophoretic mobility, the standard deviation of the measurements is shown in Figure III.3.

3   Converting the electrophoretic mobility into effective charge

The question about how the measured electrophoretic mobility is related to the charge of the microgel is not trivial. Since the pioneering works of Helmholtz and Smoluchowski[47] to more recent analytical or semi-analytical models,[48] the developed theories have provided successful results in a broad range of particle sizes of different shapes (mostly spherical), arbitrary ionic compositions of the medium, high or low particle charges, etc. Nevertheless, the consideration of particles coated with a polymeric layer, or "soft particles" is more recent,[49] and the model elaboration becomes complicated by the fact that typical electrokinetic quantities, specifically zeta potential,[50] lose their meaning. Indeed, for a microgel particle the bare charge is spatially distributed in the volume occupied by the microgel rather than on the surface.

Electrophoresis is a complex problem because it involves several phenomena coupled to each other. A complete treatment like the one elaborated by O'Brien and White,[51] offers a good opportunity to understand the different mechanisms taking place. Under the action of an external electric field, both the

charged particle and the ions surrounding it move while being subjected to gradients of electric potential, pressure and concentration, and to viscous drag. A steady state is reached in which the particle moves with the electrophoretic velocity **U** with respect to the laboratory frame. Then, the problem can be divided into two parts. One is purely hydrodynamic, and regards the motion of a spherical particle in a viscous fluid subjected to an applied external force. The second part involves the electro-osmotic fluid motion around the particle due to the action of the applied electric field on the ions in the electrical double layer.

It is possible to numerically solve the problem if the microgel particle is considered not as a set of monomers interacting between them, but as a particle with a net charge homogeneously distributed in its volume and permeable to both the fluid and the ions, that is, a soft particle. For simplicity, and as a reasonable hypothesis for the system described, we consider that the microgel has spherical symmetry, with a radius given by R_{m}. Since these microgels are thermoresponsive particles, R_{m} depends on temperature. The polymer mass distribution inside the particle is assumed to be uniform, so it can be characterized by a constant polymer packing fraction, ϕ. Analogously, the charge density inside the microgel, ρ_{m} is also considered uniform (see Figure III.1). We use a reference system anchored in the centre of particle in such a way that the fluid velocity at very large distance from the core is $-\mathbf{U}$.

The set of equations to be solved[34,52] includes first of all the Navier-Stokes equation for the fluid velocity together with the continuity equation, assuming that the fluid is Newtonian and incompressible, with viscosity η:

$$\begin{cases} -\nabla P + \eta \nabla^2 \mathbf{u} - \sum_{j=1}^{N} e z_j n_j \nabla \Psi - \gamma \mathbf{u} = 0 & \text{if } r < R_{\mathrm{m}} \\ -\nabla P + \eta \nabla^2 \mathbf{u} - \sum_{j=1}^{N} e z_j n_j \nabla \Psi = 0 & \text{if } r > R_{\mathrm{m}} \end{cases} , \qquad \text{(III.1)}$$

where P is the pressure, γ is the Stokes coefficient, η is the solvent viscosity and **u** is the local fluid velocity, which fulfills the continuity equation for steady-state conditions, $\nabla \cdot \mathbf{u} = 0$.

The third addend occurring in equation (III.1) refers to the external force arising from the local gradient of the electrostatic potential (Ψ) in a medium consisting of an electrolyte solution composed of $N(j = 1, \ldots, N)$ ionic mobile species of valence z_j, distributed in the fluid with a concentration (number density) n_j. In the region occupied by the polymer, $r < R_{\mathrm{m}}$, the fluid suffers an extra hydrodynamic drag force proportional to the fluid velocity due to the presence of the polymeric chains, defined as $\mathbf{F}_{\mathrm{drag}} = -\gamma \mathbf{u}$. The mathematical
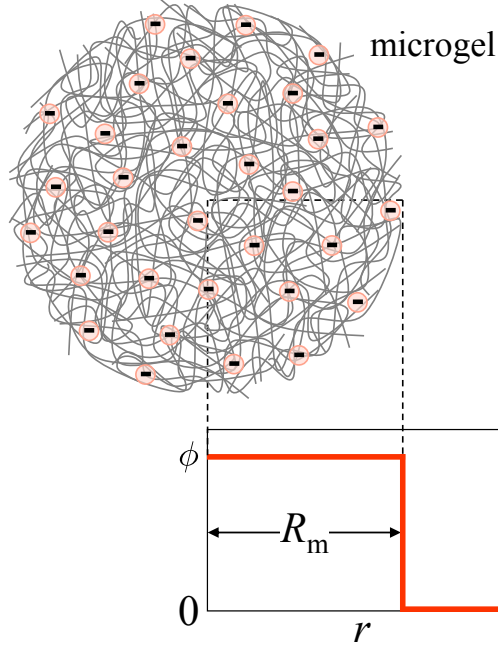
Figure III.1: Scheme of a microgel particle of radius R_m. The polymer volume fraction and the density of charged groups are assumed to be uniform.

form of this force (Darcy force), assuming that the chains behave as a homogeneous group of spherical resistance centres acting on the interstitial fluid,[53] is $\mathbf{F}_{drag} = n_{mon}\mathbf{F}_{mon}$. According to the Bueche model,[54] it is expressed as the product of n_{mon}, the number of resistance centres (monomers) per unit volume, and $\mathbf{F}_{mon}$, the drag force on a single monomer that, except for the presence of the factor f, is the Stokes force. Hence, if σ_{mon} is the diameter of the resistance centre,

$$\mathbf{F}_{drag} = -n_{mon}3\pi\eta\sigma_{mon}f\mathbf{u} \tag{III.2}$$

Consequently, the coefficient γ depends on the properties of the polymer chains (size and density of monomers), in the following way:

$$\gamma = n_{mon}3\pi\eta\sigma_{mon}f. \tag{III.3}$$

The volume packing fraction of the microgel can be calculated as

$$\phi = \frac{N_{mon}V_{mon}}{V_m} = n_{mon}V_{mon} = n_{mon}\frac{4}{3}\pi\left(\frac{\sigma_{mon}}{2}\right)^3, \tag{III.4}$$

107

which can be related to equation (III.3), so that:

$$\frac{\gamma}{\eta} = \frac{18f}{\sigma_{\text{mon}}^2}\phi \equiv \lambda^2. \tag{III.5}$$

λ is a parameter that characterizes the friction exerted by the solvent on the polymer network inside the microgel, and so it depends on the swelling state of the microgel. From equation (III.5) it can be understood that it is possible to use as fitting parameter λ_0, that is, the value of λ corresponding to the shrunken microgel of radius R_{m0} and volume packing fraction ϕ_0. Hence, λ can be calculated for any expanded configuration as

$$\lambda^2 = \lambda_0^2 \left(\phi/\phi_0\right). \tag{III.6}$$

This equation can be written in terms of microgel radius as well, given that:

$$\phi/\phi_0 = (R_{\text{m0}}/R_{\text{m}})^3. \tag{III.7}$$

The electrophoresis is not entirely an hydrodynamic problem because, as the equation (III.1) shows, the ionic distribution and hence the fluid motion is affected by the electric field. The equation governing the electric potential is the Poisson's equation, where the charge density is given by the ionic charge density, n_j, and, only for the region occupied by the polymer charged chains, also the uniform polymeric charge density has to be considered, ρ_{m}

$$\nabla^2\Psi = \begin{cases} -\displaystyle\sum_{j=1}^{N} \frac{ez_j n_j}{\varepsilon_{\text{r}}\varepsilon_0} - \frac{\rho_{\text{m}}}{\varepsilon_{\text{r}}\varepsilon_0} & \text{if } r < R_{\text{m}} \\[4mm] -\displaystyle\sum_{j=1}^{N} \frac{ez_j n_j}{\varepsilon_{\text{r}}\varepsilon_0} & \text{if } r > R_{\text{m}} \end{cases}, \tag{III.8}$$

Hence, the electric potential is the one resulting from the charge density of the microgel itself (ρ_{m}), the ionic distribution and the external electric field. ε_0 is the vacuum permittivity and ε_{r} is the relative permittivity of the medium, assumed to be water, calculated as a function of the absolute temperature, T[55]

$$\begin{aligned} \varepsilon_{\text{r}}(T) \ = \ & 5321\,T^{-1} + 233.76 - 0.9297\,T \\ & + 0.1417 \cdot 10^{-2}\,T^2 - 0.8298 \cdot 10^{-6}\,T^3. \end{aligned} \tag{III.9}$$

The ionic velocities fulfill the continuity equation in any place of the space, $\nabla \cdot [n_j \mathbf{v}_j] = 0$, where $\mathbf{v}_j$ is the velocity of the jth ionic species. This velocity may be split in two additive parts

$$\mathbf{v}_j = \mathbf{u} + \frac{D_j}{kT}\nabla\mu_j, \tag{III.10}$$

where **u** is the convective contribution and the second term is the diffusive and electric field contributions, represented by the electrochemical potential $\mu_j = -z_j e \Phi_j = \mu_j^\infty + e z_j \Psi + k_B T \ln n_j$.

The solution of these system of equations under spherical symmetry allows the determination of $\psi(r)$, $n_j(r)$ and $\mathbf{u}(r)$, where r is the distance to the microgel center. For this purpose, Ψ, Φ_j, P and **u** are expressed in terms of their equilibrium value plus a first-order perturbation linear with the applied electric field. Different kinds of boundary conditions are required, namely, the continuity of the potentials, pressure and velocity field at the particle interface ($r = R_m$), the charge electroneutrality in the entire system, the absence of perturbation far from the particle ($r \rightarrow \infty$), and the condition of zero net force balance on the microgel particle and the surrounding electrical double layer. Finally, the electrophoresis velocity is given by $\mathbf{U} = -\mathbf{u}(r \rightarrow \infty)$. Further details about the resolution of the problem may be found elsewhere.[34,52]

4 Ornstein-Zernike integral equations

With the help of the Ornstein-Zernike equations, the equilibrium density profiles of all ionic species around and inside the microgel particle can be calculated. For this purpose, we consider our system as a ternary mixture formed by microgels, counterions and coions (indexes m, + and −, respectively) immersed in a homogeneous solvent. The solvent degrees of freedom are integrated out and only contribute through the electric permittivity, which in this case is the one for water (see eq. III.9). Counterions (coions) are assumed to be modeled by charged hard spheres of diameter σ_+ (σ_-) and valence z_+ (z_-). This allows their mutual interpenetrability to be accounted for. As it was already mentioned, microgels are represented by permeable spheres of radius R_m with a uniform mass and charge distribution. At this point, it should be noted that multivalent counterions are very likely to be condensated inside the microgel due to the strong electrostatic coupling or due to specific sortion. As already pointed out by previous experimental studies, specific condensation is a very important phenomenon for ions such as Mg^{2+} or La^{3+}, as it may induce charge inversion and overcharging effects[56]. These condensed ions do not diffuse. Instead, they are attached to the polymer chains, so that the electrophoretic mobility of the microgel is the one corresponding to the apparent charge defined in the introduction, where the condensed charge is subtracted to the bare charge, $Z_{app} = Z_{bare} - Z_{cond}$. In order to compare the effective charge obtained with this OZ integral equations to the experimental one, we must take into account

this correction, and consider that the microgel holds an apparent charge, Z_{app}, homogeneously distributed within a sphere of radius R_m.

To determine the equilibrium ionic density profiles inside and around the microgel particle we need to know the explicit form of the particle interactions. The dimensionless pair interaction potentials between ions are given by

$$\beta V_{ij}(r) = \begin{cases} \infty & r \le (\sigma_i + \sigma_j)/2 \\ z_i z_j l_B / r & r > (\sigma_i + \sigma_j)/2 \end{cases}, \qquad \text{(III.11)}$$

where r is the distance between the centres of both ions; $i, j = +, -$, and l_B is the Bjerrum length, defined as $l_B = e^2/(4\pi\varepsilon_0\varepsilon_r k_B T)$, where k_B is the Boltzmann constant, and $\beta = 1/(k_B T)$. The pair interaction between ions and a microgel particle is split into two additive contributions[20]

$$V_{mi}(r) = V_{mi}^{elec}(r) + V_{mi}^{ster}(r), \qquad i = +, -. \qquad \text{(III.12)}$$

The first term of equation (III.12) corresponds to the electrostatic potential energy between an ion and a microgel, represented by an uniformly charged sphere of radius R_m. Using the Gauss's law for a homogeneous charge distribution and integrating the electric field leads to the following expression

$$\beta V_{mi}^{elec}(r) = \begin{cases} \dfrac{Z_{app} z_i l_B}{2R_m}\left(3 - \dfrac{r^2}{R_m^2}\right) & r \le R_m \\ \dfrac{Z_{app} z_i l_B}{r} & r > R_m \end{cases}, \qquad \text{(III.13)}$$

where r is here the distance between the microgel and ion centers. The second term accounts for the excluded-volume repulsion that an incoming ion experiences when diffuses through the internal polymer network of the microgel. For point-like ions this interaction is only dependent on the free volume left by the polymer chains:

$$\beta V_{mi}^{ster}(r) = \begin{cases} -\ln(1 - \phi) & r \le R_m \\ 0 & r > R_m \end{cases}. \qquad \text{(III.14)}$$

However, for ions with finite size, this steric repulsion becomes more complicated as it also depends on the size of the monomeric units (σ_{mon}), the ionic size and on the internal morphology of the cross-linker polymer network. Here, we assume that the polymer network may be modeled by an assembly of randomly placed spherical monomers. This approximation has been successfully

employed to predict the ionic density profiles inside and outside a single microgel and the permeation of neutral and charged solutes with Monte Carlo computer simulations[25,57]. In this case, the ion-microgel steric repulsion may be analytically calculated[25,58]

$$\beta V_{\mathrm{m}i}^{\mathrm{ster}}(r) = \begin{cases} -\ln\left(1-\phi\right)(1+\sigma_i/\sigma_{\mathrm{mon}})^3 & r \le R_{\mathrm{m}} \\ 0 & r > R_{\mathrm{m}} \end{cases}. \tag{III.15}$$

The number density of counterions and coions at a distance r from the microgel centre ($\rho_{\mathrm{m}+}(r)$ and $\rho_{\mathrm{m}-}(r)$, respectively) are calculated by integration of the Ornstein-Zernike equations,[59,60]

$$h_{ij}(r) = c_{ij}(r) + \sum_{k=+,-} \int \rho_k^{\mathrm{b}} c_{ik}(|\vec{r}-\vec{r}'|) h_{kj}(r') d\vec{r}', \tag{III.16}$$

where ρ_+^{b} and ρ_-^{b} are the number density of counterions and coions in the bulk, far away from the perturbation of the microgel particle. Please note that these equations consider the particular case of a single microgel particle, and so they correspond to infinite diluted suspensions ($\rho_{\mathrm{m}}^{\mathrm{b}} \to 0$). The study of the ionic density profiles for concentrated colloidal suspensions necessarily requires the knowledge of the microgel-microgel interaction potential. $h_{ij}(r)$ and $c_{ij}(q)$ are the so-called total and direct correlation functions. In order to solve these equations, six additional closure relations are required to couple both functions. In this work, the Hypernetted-Chain Closure (HNC) is used for all particle correlations, as it has demonstrate to represent a quite accurate approximation for ionic microgel suspensions[20,35]

$$h_{ij}(r) = \mathrm{e}^{h_{ij}(r)-c_{ij}(r)-\beta V_{ij}(r)} - 1. \tag{III.17}$$

Using the bulk ionic concentration and the pair interaction potentials (see equations III.11, III.12, III.13, III.15) as input parameters, both set of equations are successively iterated starting from an initial guess until convergence is finally achieved. More details about the numerical integration of the OZ equations may be found elsewhere.[35] The sought ionic density profiles are finally given by

$$\rho_{\mathrm{m}i}(r) = \rho_i^{\mathrm{b}}[h_{\mathrm{m}i}(r) + 1], \qquad i = +, -. \tag{III.18}$$

Integrating these ionic density profiles over the volume of the microgel yields the effective charge of the particle:

$$Z_{\mathrm{eff}} = Z_{\mathrm{app}} + 4\pi \int_0^{R_{\mathrm{m}}} \left[z_+ \rho_{\mathrm{m}+}(r) + z_- \rho_{\mathrm{m}-}(r) \right] r^2 \mathrm{d}r. \tag{III.19}$$

As explained above, we have solved the OZ-HNC equations for different systems, all of them involving a type of microgel (PNIPAM or PVCL), counterion (Na$^+$, Mg^{2+}, or La^{3+}) and coion (Cl$^-$). In Table III.2 the ionic and monomer diameters used as input parameters are shown. [61] In order to obtain the effective charge that best fits the experimental data, there are only two fitting parameters for every microgel: the reference volume fraction of the shrunken state (ϕ_0) and the microgel apparent charge (Z_{app}). ϕ_0 is fixed for a given microgel, so that the volume fraction in every different swelling state can be calculated from equation (III.7), using the experimental microgel radius (Figure III.2). In this work, $\phi_0 = 0.864$ for PNIPAM-based microgels and $\phi_0 = 0.923$ for PVCL-based microgels. On the other hand, Z_{app} may change with counterion valence due to counterion condensation, as will be shown further on.

Ion size (nm)	Hydrated	Dehydrated
Cl$^-$	0.664	0.40
Na$^+$	0.716	0.40
Mg^{2+}	0.856	0.43
La^{3+}	0.904	0.44
Monomer size (nm)		
NIPAM	0.9	
VCL	0.7	

Table III.2: Diameter of ions and monomers used to solve the OZ equations.

5 Results and discussion

As mentioned above, we intend to investigate how the presence of multivalent ions and the salt concentration affect the effective charge of the microgel particles at different swelling states, from swollen to shrunken conformations. On one hand, the effect of the counterion valence has been studied using PNIPAM microgel suspension at three different salt solutions, namely NaCl, MgCl$_2$ and LaCl$_3$, at the same ionic strength, I, defined as

$$I = \frac{1}{2} \sum_{i=1}^{n} c_i z_i^2,$$ (III.20)

where c_i is the molar concentration of the ion i and z_i its valence. In this work, $I = 1$ mM, which implies an electrolyte concentration of NaCl 1 mM, MgCl$_2$

0.3 mM, and LaCl$_3$ 0.17 mM. On the other hand, the effect of salt concentration has been studied by means of PVCL microgel particles in NaCl solution at two different concentrations, 1 mM and 0.1 mM.
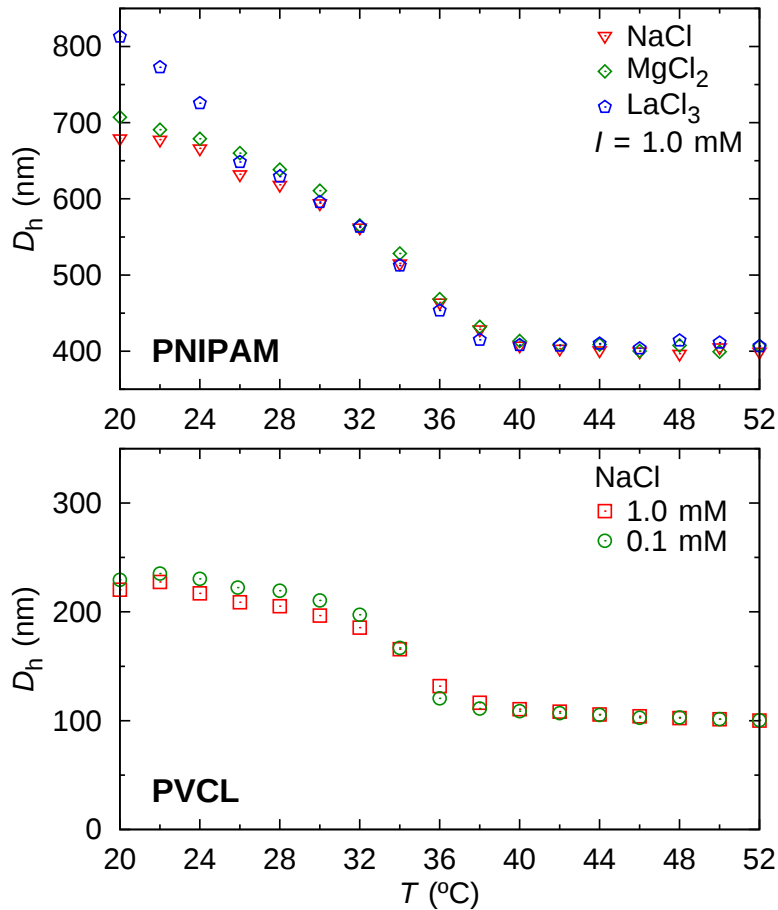
5.1   Hydrodynamic diameter

Figure III.2: Microgel experimental hydrodynamic diameter as a function of temperature, measured by dynamic light scattering (DLS). The top graph corresponds to PNIPAM microgel in three different salt solutions at 1 mM of ionic strength: NaCl ($\triangledown$), MgCl$_2$ ($\diamond$) and LaCl$_3$ ($\circ$) solutions. The bottom graph corresponds to PVCL microgel in NaCl solution at two different concentration: 1 mM ($\square$) and 0.1 mM ($\circ$). Error bars are not shown because they are smaller than the size of the symbols.

To begin with, we have measured the microgel hydrodynamic diameter in

the mentioned conditions, as shown in Figure III.2. It can be observed that both PNIPAM and PVCL are thermoresponsive microgels that remain swollen at low temperatures and shrinks as temperature increases, though they cover different size range: PNIPAM are bigger particles than PVCL. It is also clear that the PNIPAM diameter does not depend on the valence of the counterions present in the solutions, and that PVCL does not depend on salt concentration, at least for the range of salt concentrations studied here. There is only a deviation of these results for PNIPAM in LaCl$_3$ solution, where an increase of the swollen diameter is observed at low temperature. This effect could be attributed to an experimental error, but it also may be due to the existence of an specific attraction between polymer chains and lanthanum counterion. Indeed, given its large diameter, La^{3+} may deform the network structure to get in through the pores, hence increasing microgel size.

The fact that using multivalent ions does not affect the transition temperature (top graph of Figure III.2) seems to be in contradiction with previous simulation studies, which indicate that the LCST shifts to lower temperatures when monovalent counterions are substituted by multivalent ones at a fixed salt concentration.[62] This occurs because a less number of counterions are found inside the microgel, which reduces the entropic and electrostatic contributions to the osmotic pressure.[4,63] However, it should be noticed that those simulation data were obtained using mono- and multivalent counterions at a fixed salt concentration, whereas our experiments are performed at a lower salt concentration in order to fix the ionic strength. Therefore, the decrease of the salt concentration induces a smaller charge screening effect, which yields an increase of both the electrostatic contribution and the osmotic pressure. Therefore, entropic and electrostatic terms become compensated in our experiments so that the location of the LCST remain roughly insensitive to the counterion valence.

The LCST also remains unaffected with the change in concentration of monovalent salt (bottom graph of Figure III.2). This result is not surprising given the low values of salt concentrations explored in this work, which scarcely contribute to the free energy of the system. However, for large amounts of salt, the LCST transition is expected to shift to lower temperatures[64,65]. This is due again to two combined effects that favors the particle shrinking: the screening of the microgel bare charge and the increase of the osmotic pressure over the microgel surface exerted by the ions from outside.
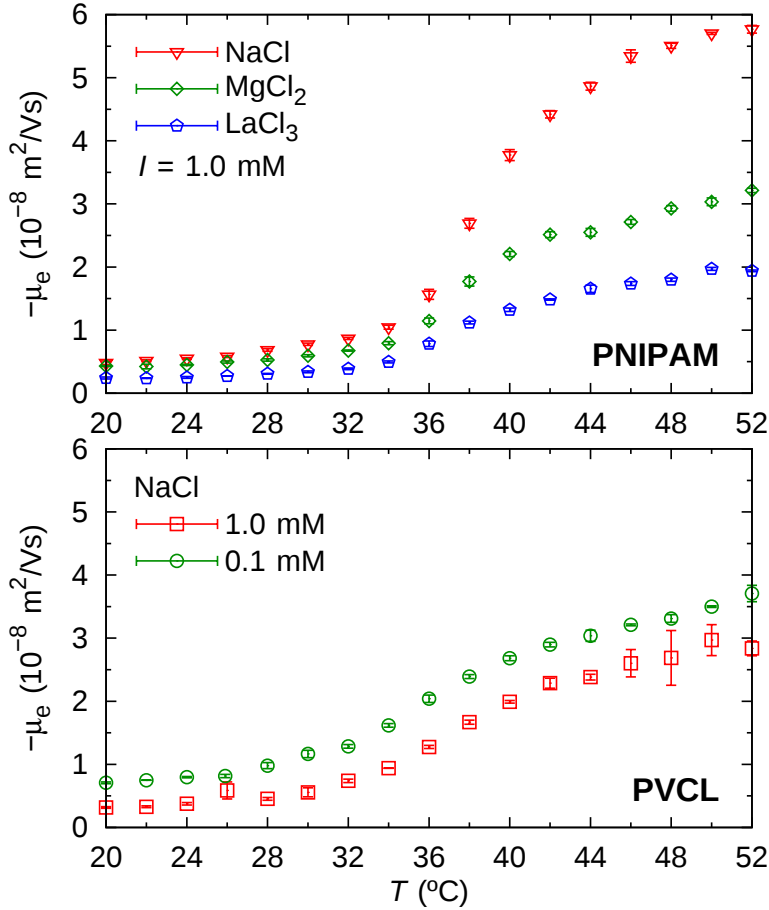
Figure III.3: Experimental electrophoretic mobility of the microgels as a function of temperature, measured by using laser the Doppler micro-electrophoresis technique. The top graph corresponds to PNIPAM microgel suspensions at three different salt solutions at 1 mM of ionic strength: NaCl ($\triangledown$), MgCl$_2$ ($\diamond$) and LaCl$_3$ ($\circ$) solutions. The bottom graph corresponds to PVCL microgels in NaCl solution at two different concentrations: 1 mM ($\square$) and 0.1 mM ($\circ$).

5.2   Electrophoretic mobility and effective charge

The electrophoretic mobility of both kinds of microgels particles has also been experimentally determined for the set of salt concentrations and counterion valences mentioned above. The experimental results are shown in Figure III.3, where the negative value of μ_e indicates that both PNIPAM and PVCL are negatively charged, so Na$^+$, Mg^{2+} and La^{3+} act as counterions, while Cl$^-$ is the only

coion present in the systems under study. One of the more relevant feature of these plots is the fact that μ_e always increases with temperature. Moreover, the curves show a transition at a temperature close to the the LCST. Although the values of the PNIPAM mobility are different from the ones for PVCL (as well as the size of the gap from the minimum to the maximum values), the general behavior is common to all studied salt concentrations, counterion valences and for both microgel particles. The increase of μ_e is in some cases very important, leading to electrophoretic mobilities at high temperatures up to 10 times larger than the ones obtained at low temperature. Regarding the effect of the counterion valence and salt concentration, it is worth to point out that, although the swelling curve does not depend on both properties, this is not the case of the electrophoretic mobility. As observed, increasing the counterion valence and the electrolyte concentration leads to a reduction of μ_e. This effect becomes especially significant for shrunken states.

In order to understand these general trends, we must perform a very careful interpretation of the results, since μ_e do not depend on just one quantity, but on a complex combination of parameters. Indeed, raising the temperature also provokes a decrease in the microgel size (D_h), and an increase of both the net charge density inside the microgel (ρ_e) and the resistance of the particle in the fluid environment (which is quantified by the drag coefficient, λ). All these parameters are involved in the value of μ_e, so we need to deduce which one is playing the dominant role. With this aim, a theoretical analysis has been undertaken to determine the dependence of μ_e with these four parameters: D_h, T, ρ_e, and λ. In Figure III.4 the electrophoretic mobility has been theoretically calculated as described in Section 3, varying one of the mentioned parameters and keeping constant the other three. It is clear that, although μ_e increases with temperature and microgel diameter, charge density and drag coefficient are the ones that feel a stronger influence. For the input parameters used in this work, electrophoretic mobility shows a linear growth with the charge density (although it is known that this behavior is valid only for weakly charged particles). In contrast, the electrophoretic mobility decreases with the drag coefficient, as it represents a measure of the resistance of the particle inside the fluid.[34,49] The resulting mobility is the result of the competition between these two opposing effects. Since μ_e increases when the microgel shrinks, this means that the increase of the microgel charge density dominates over the effect of the friction. Moreover, this result suggests that the decrease of μ_e with the counterion valence and salt concentration for shrunken states must be necessarily linked to a decrease in ρ_e (since the other three parameters do not depend on the ionic properties).
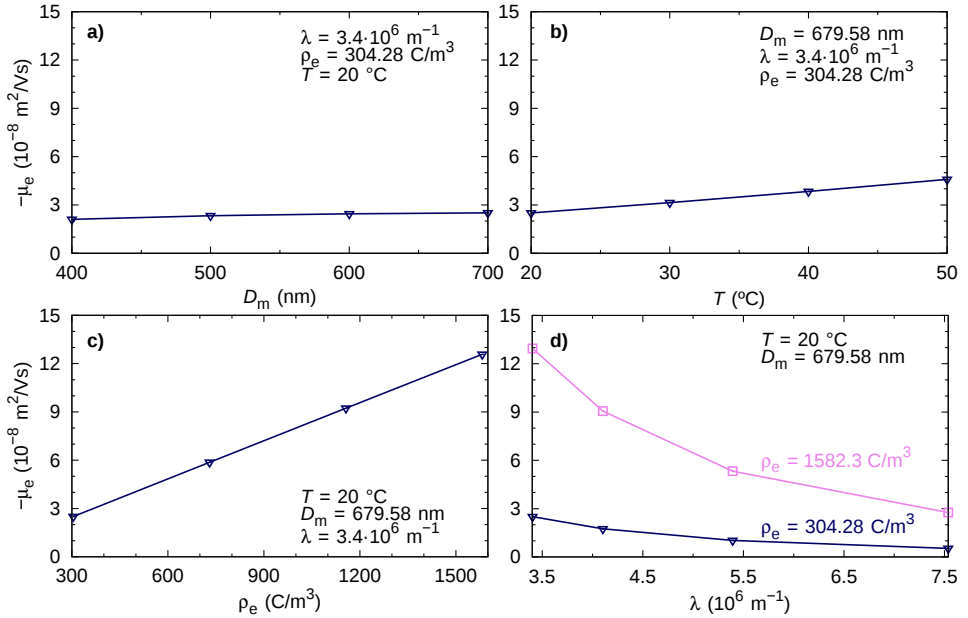
Figure III.4: Variation of the microgel electrophoretic mobility as a function of microgel diameter (a), temperature (b), charge density (c) and drag coefficient (d). μ_e has been theoretically calculated following the method described in Section 3.

Although the experimental results clearly indicate that the increase of ρ_e is the most important factor controlling the increase of the electrophoretic mobility above the LCST, we still lack a deep understanding of the physical effects involved behind this effect. In order to tackle this question we calculated the effective charge of the microgel particles from the electrophoretic mobility measurements (see Section 3), and compared to the theoretical predictions deduced by solving the OZ-HNC equations. In Figure III.5 and Figure III.6 the effective charge obtained from the experiments is plotted as a function of temperature for PNIPAM and PVCL, respectively (open symbols). Given the definition of the effective charge, if counterions penetrate inside the microgel, the effective charge is expected to decrease, because the positive charge of the counterions partially screens the negative bare charge of the microgel. The trend observed for Z_{eff} is the same as for μ_e, namely, it increases as the microgel shrinks. Now let us focus on Figure III.5, where the effect of the counterion valence on the PNIPAM effective charge can be appreciated. These results show that the charge screening is enhanced by increasing the counterion valence: the screening induced by La^{3+} is stronger than the one caused by Mg^{2+}, and so Na^+, especially

117

for shrunken states. This is reflected in smaller values of Z_{eff} for higher counterion valences. But to be sure that charge screening is due to counterion permeation, the reader should bear in mind that the ionic strength is the same for the three different counterions, and hence, the Debye length. Consequently, if microgel was a solid sphere, charge screening caused by all the counterions would be the same, no matter their valence. However, as microgel is a porous particle, if a La^{3+} counterion permeates inside, we observe that it screens the microgel bare charge three times more than a Na^+ counterion does.
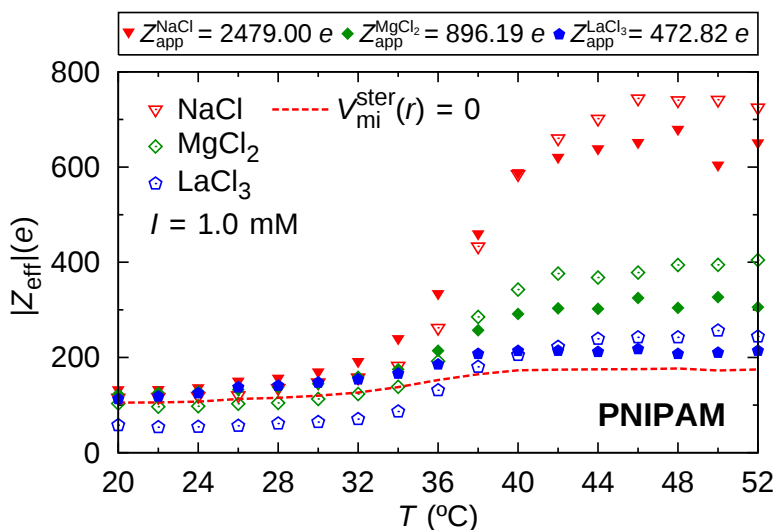

Figure III.5: PNIPAM microgel effective charge as a function of temperature, for three different salt solutions at 1 mM of ionic strength. Red symbols stand for NaCl solution, green symbols for $MgCl_2$ solution and blue symbols for $LaCl_3$ solution. Open symbols correspond to the effective charge obtained from experimental data, while filled symbols correspond to theoretical predictions of effective charge obtained from OZ-HNC integral equations. The microgel apparent charge fitted for each salt solution is shown in the top label. Error bars are not shown in the graph because they are smaller than the size of the symbols.

The experimental Z_{eff} values are compared with the theoretical predictions calculated by solving the OZ-HNC equations using the microgel-ion electrosteric potential given by eqs III.12, III.13 and III.15. The results are represented by filled symbols in Figure III.5. For this purpose, Z_{app} has been used as fitting parameter. It must be reminded that Z_{app} represents the charge of the microgels when the conunterions condensed inside the microgel are taken into account. These counterions are stuck to polymer chains so that they do not move with the fluid when applying an electric field. This phenomenon is known as counterion

condensation and neutralizes the microgel bare charge so that we obtain a lower effective charge than the expected from mobility results [19,42–44]. In other words, Z_{bare} is the charge due exclusively to the polyelectrolytes that compound the microgel network, Z_{app} represents the charge neutralized only by counterion condensation and Z_{eff} is the charge that takes into account *all* the counterions that have passed through microgel pores, both in repose or in movement. Since few monovalent counterions as Na$^+$ are expected to condensate inside the microgel, for PNIPAM microgel we may approximate $Z_{bare} \approx Z_{app}^{NaCl}$ in Figure III.5. However, our results reveal that the strong electrostatic and ion-specific attraction between multivalent counterions and the charged groups emphasizes the counterion condensation leading to lower values of Z_{app}, as already pointed out by other authors [43,56]. In particular, ionic condensation reduces the bare charge by a factor of the order of 3 for Mg^{2+} and 5 for La^{3+}. For the PVCL microgel, La^{3+} sorption is so important that causes the particle aggregation by increasing the temperature (not shown in the paper). The specific condensation effect is sensitive to many paremeters, such as the nature of the particle, the salt concentration, and the type of ion. Therefore, very different results for the electrophoretic mobility (different inversion points, effective charges,...) are obtained depending on the particular conditions. For instance, specific adsorption of Mg^{2+} and La^{3+} ions is able to induce the charge inversion of hard colloids [56]. For the case of microgel particles, this condensation effect is expected to be even stronger, since the total surface of polymer exposed to the solvent is much greater than for hard colloids. In this regard, the results obtained for Z_{app} in our paper are reasonable, and lie inside the values observed in the literature for this kind of systems. As observed, when the ionic condensation effect is accounted for, the theoretical fitting leads to effective charges that are in good qualitative and even quantitative agreement with the experimental data.

The increase of Z_{eff} as the microgel shrinks may be attributed to two cooperative effects. First, the microgel de-swelling induces an increase of the polymer packing fraction, which enhances the steric repulsion between the counterions and the microgel. As a consequence, counterions are expelled from the interior of the particle, which makes charge screening less efficient. Second, a decrease of the microgel size forces the counterions to accumulate within a smaller volume inside the particle. The counterion-counterion repulsion also contributes to the counterion exclusion, and so to the increase of the effective charge. In order to separate both effects we performed calculations of the effective charge for the PNIPAM microgel in NaCl 1 mM solution making use of the same parameters, but turning off the steric repulsive barrier (see red dashed

line on Figure III.5). As observed, the enhanced electrostatic repulsion between counterions arising in shrunken states is able to induce an increase of Z_{eff} even in the absence of the steric exclusion effect. However, this increase is much less important than the one observed if the steric exclusion of the ions is also taken into account. This result is totally consistent with the experimental observation, and explains why μ_e is always larger above the LCST.
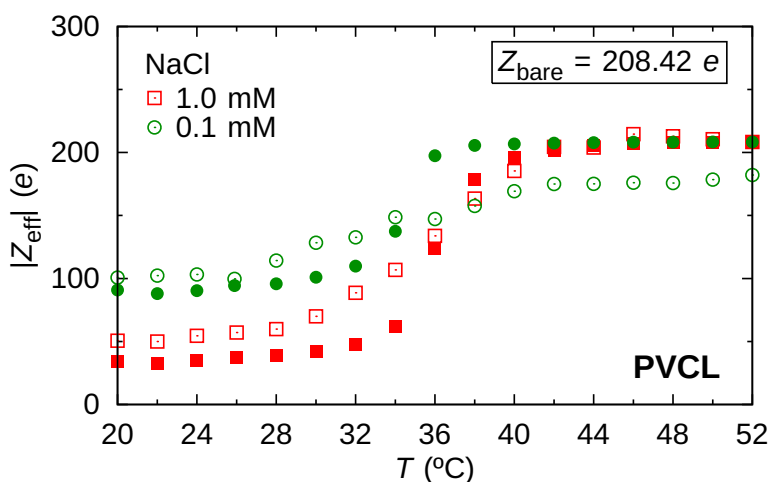

Figure III.6: PVCL microgel effective charge as a function of temperature, in NaCl solution at two different concentrations. Red squares stand for 1 mM solution, green circles for 0.1 mM. Open symbols correspond to the effective charge obtained from experimental data, while filled symbols correspond to theoretical predictions of effective charge obtained from OZ-HNC integral equations. The microgel apparent charge fitted for both cases is shown in the top right label. Error bars are not shown because they are smaller than the size of the symbols.

Now let us regard the effect of the salt concentration, which has been investigated using the PVCL microgels. Looking back on the bottom graph of Figure III.3 we can observe that electrophoretic mobility measurements for NaCl electrolyte follow the same trend for 1 mM and 0.1 mM concentration, though higher concentration leads to slightly lower values of μ_e in the whole range of temperatures. This result was expected, since the the difference in μ_e depends exclusively on ionic strength: the more concentration, the more charge screening. The same conclusion may be extracted from Figure III.6, where both the experimental and theoretical microgel effective charge are plotted, for the two studied salt concentrations. In this case only one common value of Z_{app} has been used to fit the experimental Z_{eff}, because even if there were condensed counterions inside the microgel, it is known that this phenomenon does not de-

pend on salt concentration[66]. But analogously to PNIPAM, for PVCL microgel is also a good approximation to assume $Z_{bare} \approx Z_{app}^{NaCl}$. Hence, the Z_{eff} observed in the figure accounts for approximately the whole charge screening caused by counterion permeation. The screening of the microgel bare charge increases for low temperature, that is, for swollen states of the microgel, since counterions permeate through the polymer network. In those expanded states we also observe higher differences with electrolyte concentration. However, as microgel shrinks and counterion permeation is hindered by the steric exclusion, electrolyte concentration becomes less relevant and Z_{eff} increases to similar values than the fitted Z_{app}.

Finally, it is interesting to wonder whether the microgel effective charge is homogeneously distributed inside the microgel or, on the contrary, the charge is localized in some specific regions of the particle. This study can be done analyzing the net charge density density predicted by the OZ-HNC equations as a function of the distance to microgel center,

$$\rho_e(r) = [z_{mon}\rho_{mon}(r) + z_+\rho_+(r) + z_-\rho_-(r)]e, \qquad \text{(III.21)}$$

where $\rho_{mon}(r)$, $\rho_+(r)$ and $\rho_-(r)$ are the number densities of monomers, counterions and coions, respectively. We can consider the PNIPAM in presence of NaCl 1 mM electrolyte as an example, represented in Figure III.7. As observed, the density profiles become flat inside the microgel particle, what means that electroneutrality is fulfilled in this region. However, as we get close to the particle interface, a sharp increase of the charge is observed. This feature implies that the microgel effective charge is mainly located at the surface of the particle, not homogeneously distributed, as has been reported in previous work.[67] We can also appreciate the effect of the swelling state of the particle, since two different temperatures have been considered in Figure III.7. As can be also deduced from our previous results, the net charge density in swollen microgels is lower than in shrunken states, since they have a lower effective charge distributed in a higher volume. In addition, at low temperature, the perturbation provoked by the leap in the bare charge density and the steric barrier at the microgel interface are less pronounced, so the electroneutrality is fulfilled in almost the whole space inside the particle. However, as the microgel shrinks with temperature, charge density increases and the interfacial effects tend to disrupt electroneutrality.
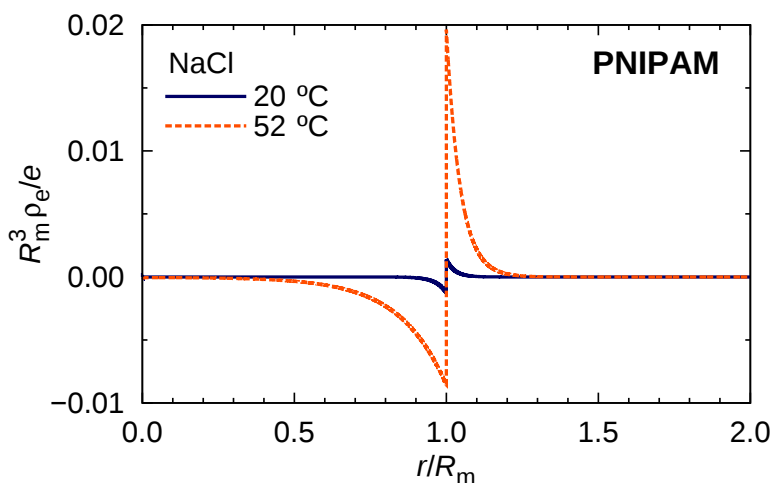
Figure III.7: PNIPAM microgel density charge, in presence of NaCl 1 mM electrolyte, as a function of the distance to microgel centre, in normalized units. Two different temperatures, and hence, two different swelling states, are considered. Solid blue line stands for $T = 20$ °C (swollen state), while dashed orange line represents $T = 54$ °C (shrunken state).

6   Conclusions

In this work the swelling behavior and the electrophoretic mobility of two different thermoresponsive charged microgel suspensions have been studied. We have specially focused on the effect that the counterion valence and salt concentration of the suspension have on the effective charge of the particles. The experimental results have been interpreted in terms of the theoretical predictions obtained by solving the Ornstein-Zernike integral equation within the HNC approximaxion. For this purpose we have made use of electrosteric interactions between the ions and the charged polymer network of the microgel. The comparison between theory and experiments shows that the ionic condensation inside the microgel plays an important role when multivalent counterions are present in the suspension. Indeed, the immobile condensed counterions strongly contribute to neutralize the microgel charge, leading to smaller values of the electrophoretic mobility. Moreover, the important increase of the experimental effective charge observed when microgel shrinks can not be exclusively attributed to electrostatic forces: excluded-volume repulsive interactions need to be considered too. This steric contribution, although very weak in swollen conformations, becomes very relevant for highly dense shrunken states, and it is able to push out counterions from the internal volume of the microgel, giving

raise to an enhanced augment of the effective charge.

Theoretical predictions also show that, deep inside the microgel particle (far from the interface) the ionic density profiles are homogeneous and charge electroneutrality is satisfied. This means that a number density of counter- and coions are located in this region to exactly compensate the bare charge density regardless the swelling state of the particle. However, as soon as we get close to the microgel interface charge electroneutrality is violated. This implies that the effective charge of the microgel particles meanly comes from the region close to the surface.

As future research, it would be worth to include the elastic and solvent-induced free energy contributions in the model in order to theoretically predict not only the ionic density profiles and the microgel effective charge, but also the swelling state of the particle. Those contributions could be adjusted to reproduce the complete swelling curve, from the swollen to the shrunken conformation. In addition, the model could be extended to consider the inhomogeneous swelling of the microgel, caused by the electrostatic repulsion between the charged groups. This could be done by means of a local free energy for the microgel that includes a position-dependent mass and charge distribution of the polymer network, in a similar way as the work by Rumyantsev *et al.*[68] More challenges arise if we aim to investigate the swelling behavior and effective charge of microgel particles in solution of chaotropic counter- or coions, or to study the sorption of more complex solutes such as charged surfactants or proteins[23,69]. In all these cases, ion or solute specificity would also play and important role on determining the equilibrium value of Z_{eff}, leading to charge inversion and overcharging phenomena. The comparison between theory and experiments could provide quantitative information about the strength of the polymer-ion and polymer-solute specific effective interaction in terms of the swelling state.

References

[1] Hodge, R. M.; Simon, G. P.; Whittaker, M. R.; Hill, D. J. T.; Whittaker, A. K. *J. Polym. Sci. Part B Polym. Phys.* **1998**, *36*, 463–471.

[2] Murray, M. J.; Snowden, M. J. *Adv. Colloid Interface Sci.* **1995**, *54*, 73–91.

[3] Saunders, B. R.; Vincent, B. *Adv. Colloid Interface Sci.* **1999**, *80*, 1–25.

[4] Pelton, R.; Hoare, T. In *Microgel Suspensions: Fundamentals and Applications*; Fernández-Nieves, A., Wyss, H. M., Mattsson, J., Weitz, D. A., Eds.; Wiley-VCH Verlag GmbH & Co. KGaA: Weinheim, Germany, 2011; pp 1–32.

[5] Ramos, J.; Imaz, A.; Callejas-Fernández, J.; Barbosa-Barros, L.; Estelrich, J.; Quesada-Pérez, M.; Forcada, J. *Soft Matter* **2011**, *7*, 5067–5082.

[6] Ramos, J.; Imaz, A.; Forcada, J. *Polym. Chem.* **2012**, *3*, 852.

[7] Naficy, S.; Razal, J. M.; Whitten, P. G.; Wallace, G. G.; Spinks, G. M. *J. Polym. Sci. Part B Polym. Phys.* **2012**, *50*, 423–430.

[8] Imaz, A.; Forcada, J. *J. Polym. Sci. A Polym. Chem.* **2010**, *48*, 1173–1181.

[9] Lü, S.; Liu, M.; Ni, B.; Gao, C. *J. Polym. Sci. Part B Polym. Phys.* **2010**, *48*, 1749–1756.

[10] Lee, S. M.; Nguyen, S. T. *Macromolecules* **2013**, *46*, 9169–9180.

[11] Ramos, J.; Forcada, J.; Hidalgo-Álvarez, R. *Chem. Rev.* **2014**, *114*, 367–428.

[12] Lee, S. M.; Bae, Y. C. *Macromolecules* **2014**, *47*, 8394–8403.

[13] Du, A. W.; Stenzel, M. H. *Biomacromolecules* **2014**, *15*, 1097–1114.

[14] Peláez-Fernández, M.; Souslov, A.; Lyon, L. A.; Goldbart, P. M.; Fernández-Nieves, A. *Phys. Rev. Lett.* **2015**, *114*, 098303–5.

[15] Lyon, L. A.; Serpe, M. J. In *Hydrogel Micro and Nanoparticles*; Lyon, L. A., Serpe, M. J., Eds.; Wiley-VCH, 2012; p 406.

[16] Pelton, R. H.; Pelton, H. M.; Morphesis, A.; Rowell, R. L. *Langmuir* **1989**, *5*, 816–818.

[17] Daly, E.; Saunders, B. R. *Phys. Chem. Chem. Phys.* **2000**, *2*, 3187–3193.

[18] Daly, E.; Saunders, B. R. *Langmuir* **2000**, *16*, 5546–5552.

[19] Belloni, L. *Colloids Surf., A* **1998**, *140*, 227–243.

[20] Moncho-Jordá, A. *J. Chem. Phys.* **2013**, *139*, 064906.

[21] Gottwald, D.; Likos, C. N.; Kahl, G.; Löwen, H. *J. Chem. Phys.* **2005**, *122*, 074903–11.

[22] Moncho-Jordá, A.; Adroher-Benítez, I. *Soft Matter* **2014**, *10*, 5810–5823.

[23] Rumyantsev, A. M.; Santer, S.; Kramarenko, E. Y. *Macromolecules* **2014**, *47*, 5388–5399.

[24] López-León, T.; Elaïssari, A.; Ortega-Vinuesa, J. L.; Bastos-González, D. *ChemPhysChem* **2007**, *8*, 148–56.

[25] Adroher-Benítez, I.; Ahualli, S. A.; Martín-Molina, A.; Quesada-Pérez, M.; Moncho-Jordá, A. *Macromolecules* **2015**, *48*, 4645–4656.

[26] Saunders, B. R.; Laajam, N.; Daly, E.; Teow, S.; Hu, X.; Stepto, R. *Adv. Colloid Inter-*

face Sci. **2009**, *147-148*, 251–62.

[27] Hideji, T.; Kazuo, H. *Toxicol. Lett.* **1991**, *58*, 209–213.

[28] Vihola, H.; Laukkanen, A.; Valtola, L.; Tenhu, H.; Hirvonen, J. *Biomaterials* **2005**, *26*, 3055–3064.

[29] Peng, S.; Wu, C. *Macromol. Symp.* **2000**, *159*, 179–186.

[30] Imaz, A.; Forcada, J. *Macromol. Symp.* **2009**, *281*, 85–88.

[31] Tsai, H.-C.; Tsai, C.-H.; Lin, S.-Y.; Jhang, C.-R.; Chiang, Y.-S.; Hsiue, G.-H. *Biomaterials* **2012**, *33*, 1827–1837.

[32] Luk, B. T.; Zhang, L. *ACS Appl. Mater. Interfaces* **2014**, *6*, 21859–21873.

[33] Fernández-Nieves, A.; Fernández-Barbero, A.; de las Nieves, F. J.; Vincent, B. *J. Phys.: Condens. Matter* **2000**, *12*, 3605–3614.

[34] Ahualli, S. A.; Jiménez, M. L.; Carrique, F.; Delgado, Á. V. *Langmuir* **2009**, *25*, 1986–1997.

[35] Moncho-Jordá, A.; Anta, J. A.; Callejas-Fernández, J. *J. Chem. Phys.* **2013**, *138*, 134902.

[36] Karanikas, S.; Dzubiella, J.; Moncho-Jordá, A.; Louis, A. A. *J. Chem. Phys.* **2008**, *128*, 204704.

[37] Denton, A. R. *Physical Review E* **2003**, *67*, 011804–10. *Erratum–ibid* **2003**, *68*, 049904.

[38] Gottwald, D.; Likos, C. N.; Kahl, G.; Löwen, H. *Phys. Rev. Lett.* **2004**, *92*, 068301.

[39] Klein, J. W.; Ware, B. R. *J. Chem. Phys.* **1984**, *80*, 1334–1339.

[40] Philippova, O. E.; Khokhlov, A. R. *Macromol. Symp.* **1999**, *3*, 207–213.

[41] Mologin, D. A.; Khalatur, P. G.; Khokhlov, A. R.; Reineker, P. *New J. Phys.* **2004**, *6*, 133.

[42] Manning, G. S. *J. Phys. Chem. B* **2007**, *111*, 8554–8559.

[43] Hoffmann, M.; Jusufi, A.; Schneider, C.; Ballauff, M. *J. Colloid Interface Sci.* **2009**, *338*, 566–72.

[44] Gillespie, D. A. J.; Hallett, J. E.; Elujoba, O.; Che Hamzah, A. F.; Richardson, R. M.; Bartlett, P. *Soft Matter* **2014**, *10*, 566–577.

[45] Pérez-Fuentes, L.; Drummond, C.; Faraudo, J.; Bastos-González, D. *Soft Matter* **2015**, *11*, 5077–5086.

[46] Imaz, A.; Forcada, J. *J. Polym. Sci. A Polym. Chem.* **2011**, *49*, 3218–3227.

[47] Wall, S. *Curr. Opin. Colloid Interface Sci.* **2010**, *15*, 119–124.

[48] Delgado, Á. V.; González-Caballero, F.; Hunter, R. J.; Koopal, L. K.; Lyklema, J. *J. Colloid Interface Sci.* **2007**, *309*, 194–224.

[49] Ohshima, H. *Adv. Colloid Interface Sci.* **1995**, *62*, 189–235.

[50] Hunter, R. J. *Introduction to modern colloid science*; Oxford University Press: Oxford, 1993; p 338.

References

[51] O'Brien, R. W.; White, L. R. *J. Chem. Soc. Faraday Trans. II* **1978**, *74*, 1607–1626.

[52] Ahualli, S. A.; Ballauff, M.; Arroyo, F. J.; Delgado, Á. V.; Jiménez, M. L. *Langmuir* **2012**, *28*, 16372–16381.

[53] Hill, R. J.; Saville, D.; Russel, W. *J. Colloid Interface Sci.* **2003**, *258*, 56–74.

[54] Debye, P.; Bueche, A. M. *J. Chem. Phys.* **1948**, *16*, 573–579.

[55] Weast, R. C.; Astle, M. J.; Beyer, W. H.; Others, *CRC handbook of chemistry and physics*; CRC press Boca Raton, FL, 1988; Vol. 69; p 496.

[56] Jiménez, M. L.; Delgado, Á. V.; Lyklema, J. *Langmuir* **2012**, *28*, 6786–6793.

[57] Ahualli, S. A.; Martín-Molina, A.; Quesada-Pérez, M. *Phys. Chem. Chem. Phys.* **2014**, *16*, 25483–25491.

[58] Lazzara, M. J.; Blankschtein, D.; Deen, W. M. *J. Colloid Interface Sci.* **2000**, *226*, 112–122.

[59] Hansen, J.-P.; McDonald, I. R. *Theory of simple liquids*, 3rd ed.; Academic Press: Amsterdam, 2006; Vol. 104; p 416.

[60] Caccamo, C. *Phys. Rep.* **1996**, *274*, 1–105.

[61] Nightingale Jr., E. *J. Phys. Chem.* **1959**, *63*, 1381–1387.

[62] Quesada-Pérez, M.; Maroto-Centeno, J. A.; Martín-Molina, A. *Macromolecules* **2012**, *45*, 8872–8879.

[63] Fernández-Nieves, A.; Fernández-Barbero, A.; Vincent, B.; de las Nieves, F. J. *Macromolecules* **2000**, *33*, 2114–2118.

[64] Quesada-Pérez, M.; Ahualli, S. A.; Martín-Molina, A. *J. Polym. Sci. Part B Polym. Phys.* **2014**, *52*, 1403–1411.

[65] Heyda, J.; Soll, S.; Yuan, J.; Dzubiella, J. *Macromolecules* **2014**, *47*, 2096–2102.

[66] Mohanty, U.; Ninham, B. W.; Oppenheim, I. *Proc. Natl. Acad. Sci. U.S.A.* **1996**, *93*, 4342–4.

[67] Moncho-Jordá, A.; Dzubiella, J. *Phys. Chem. Chem. Phys.* **2016**, *18*, 5372–5385.

[68] Rumyantsev, A. M.; Rudov, A. A.; Potemkin, I. I. *J. Chem. Phys.* **2015**, *142*, 171105–5.

[69] Yigit, C.; Welsch, N.; Ballauff, M.; Dzubiella, J. *Langmuir* **2012**, *28*, 14373–85.

Conformation change of a poly(N-isopropylacrylamide) membrane: molecular dynamics

Irene Adroher-Benítez[⋆], Arturo Moncho-Jordá[⋆][†], and Gerardo Odriozola[‡]

[⋆]Departamento de Física Aplicada, Facultad de Ciencias, Universidad de Granada, Avenida Fuentenueva 2, 18001, Granada, Spain
[†]Instituto Carlos I de Física Teórica y Computacional, Universidad de Granada, Avenida Fuentenueva 2, 18001, Granada, Spain
[‡]Área de Física de Procesos Irreversibles, División de Ciencias Básicas e Ingeniería, Universidad Autónoma Metropolitana, Av. San Pablo 180 Col. Reynosa, 02200 CD de México, Mexico

Abstract

In this work a thermoresponsive polymer, poly(N-isopropylacrylami-de) (PNIPAM), in neat water and in electrolyte solutions is studied by means of molecular dynamics simulations. This is done for an infinitely diluted oligomer and for an assembly of several PNIPAM chains arranged into a planar membrane configuration with a core-shell morphology. We employed two different force fields, AMBER and OPLS-AA in combination with SPC/E water. Our estimations for the coil to globule transition temperature are $T_\Theta = (308 \pm 5)$ K and $T_\Theta = (303 \pm 5)$ K, respectively. The membrane configuration allows to include chain-chain interactions, to follow density profiles of water, polymer, and solutes, and accessing the water-polymer surface tension. Results show the shrinking and swelling of the membrane by switching temperature above and below T_Θ, as well as the increase and decrease of the surface tension. Finally, concentration profiles for 1 M NaCl and 1 M NaI electrolytes are shown, depicting a strong salting-out effect for NaCl and a much lighter effect for NaI, in good qualitative agreement with experiments.

1 Introduction

Poly(N-isopropylacrylamide) (PNIPAM) is a polymer that, when suspended in water, yields a coil to globule transition at the temperature $T_\Theta = 303$ K[1], where coil refers to the state where the gyration radii scales with chain length following a 0.6-power law, and the globule state is characterized by a (1/3)-power relationship with chain length[2]. When the expanded coil chains are cross-linked forming a three-dimensional network, the resulting structure is a swollen microgel (or hydrogel). On the other hand, the globule chains lead to a shrunken dehydrated state of the hydrogel, where most water content is expelled out from the particles. The underlying mechanism for this transition relies on a shift from an enthalpy ruled coil-state, mostly by polymer-water hydrogen bonding, to an entropy ruled globule state, where water molecules gain degrees of freedom, as temperature is raised above T_Θ. The coil to globule transition is common in other polymeric systems such as proteins and DNA molecules, and so understanding its behavior is important for biological sciences. Indeed, PNIPAM shares the amide group with proteins, although this group is part of the side chains of PNIPAM and forms the backbone of proteins. For this reason, in certain cases PNIPAM can be regarded as a protein simile, for instance, when dealing with protein stability in the presence of different electrolyte solutions. Also, as PNIPAM releases its water content at a temperature close to that of the human body, it has been proposed for biotechnological applications such as controlled drug delivery[3–5] and tissue engineering[6–8].

Driven by the possible impact of these biotechnological applications, there has been recent considerable effort in developing theoretical models and studies to disentangle the interaction of different electrolytes with hydrogel particles[9–14]. As a first approximation, most works assume ions to interact with the hydrogel network solely by means of a Coulombic interaction in both states, swollen and shrunken. This could be a good approximation in the first case, but clearly poor in the second, where repulsive polymer-ion excluded volume interactions turn important. Although this excluded-volume effect has been, at least partially, accounted for[15–17], many other important contributions, which depend on the nature of the ion and not only on its valence and size[13], are in general not completely taken into account. For instance, a recent work dealing with charge-inversion on hydrogels includes a direct hydrophobic ion-chain attraction but neglects the possibility of ions interacting with several chains at a time, which again, can be expected in the shrunken state[18]. In addition, this direct hydrophobic ion-chain attraction can be seen as an effective (properly

weighted average) potential, including loosing (gaining) water molecules when attaching (detaching) to the polymer surface, but cannot adjust to each particular configuration. These nature-dependent effects of ions are so important up to the point of producing large or tiny shifts of T_Θ when changing the ion nature while keeping constant its valence and concentration. For example, T_Θ decreases from 303 K to 298 K when replacing pure water by 1 M NaCl solution, whereas there is a barely noticeable decrease for 1 M NaI[1,13]. In the list of effects that should be taken into account lies the ion-water interaction, the ion-polymer interaction, and the difference of the entropy of solvation of ions in water and in the hydrated-polymer phase. A natural way of accounting for all these entangled effects together is by means of all-atom molecular simulations, with the price of strongly decreasing timescale and system size. This has been done mostly by considering an infinitely diluted oligomer chain in water for several force-fields[13,19–24], and for different electrolyte solutions[20]. In particular, Tucker et al. have studied the T_Θ dependence with oligomer length for an isotactic chain, concluding that the large chain limit of T_Θ is achieved with 30-mers. On the other hand, Walter et al. end Du et al. report[19,20] that the AMBER and OPLSS-AA forcefields, both in combination with SPC/E water, are good combinations for capturing T_Θ. Unfortunately, they do not specify the tacticity of their oligomer, making their study ambiguous. Indeed, it has been shown that this property affect the oligomer behavior[23,25].

In this work, we further study the swelling behavior of PNIPAM immersed in water and electrolyte solutions in the region close to the transition temperature, T_Θ by means of all-atom molecular simulations. As Walter et al. and Du et al.[19,20], we employ both, AMBER and OPLSS-AA, in combination with SPC/E water, but considering well-defined isotactic chains. We first focus on an infinitely diluted 30-mer in pure water, and confirm T_Θ is reasonably captured in both cases, in qualitative agreement with previous works[19,20]. Our results suggest that Du et al. have set an isotactic chain while Walter et. al a syndiotactic one. Following, we assemble several PNIPAM chains to form a planar membrane-like arrangement in order to investigate the chain-chain interactions and the thermal response of the whole structure. For the assembled structure we show a less pronounced change with temperature of the individual properties of the chains, as found in arrangements of polymer brushes for coarse-grained models with implicit solvent[26]. Nonetheless, the obtained T_Θ for both forcefields do not significantly shift from those obtained for the single chain cases. Finally, we immerse the membrane in 1 M NaCl and NaI solutions, to get the ionic profiles below and above T_Θ. We observe the so-called salting-

out effect[27], namely a decrease of polymer solubility accompanied by a poor electrolyte adsorption, for both electrolytes, although the effect is much more pronounced for NaCl, in agreement with experiments[1]. In addition, and despite the fact of having very different Lennard Jones parameters defining cations and anions, we find that the electroneutrality condition holds for all considered cases, meaning that cationic and anionic normalized profiles are practically the same. In this last case, the obtained polymer profiles could be used as inputs for integral-equation theories for scaleup results from nano to mesoscopic scales, whereas the ionic profiles can be used to test the theoretical output[11,16].

The paper is structured as follows. After this brief introduction, we present the methods and models employed to carry out the study. More details on the building of the model and on the employed parameters are given as supporting information. A following section shows the results. This section is split in three; infinitely diluted single chain, the hydrated-membrane, and electrolyte profiles in the hydrated-membrane system. Finally, some remarks are drawn at the conclusions section.

2 Methods and models

We are employing the GROMACS package[28–30] and a leap frog algorithm for integrating the classical equations of motion. Version 5.12 is used for single chain NPT simulations and version 2016 for semi-isobaric $NP_{zz}T$ simulations of membranes. For all cases we are setting a time step of 0.001 ps, periodic boundary conditions for all directions, treating electrostatic contributions through the particle mesh Ewald scheme with a minimum cutoff for the real contribution of 1.2 nm and a grid Fourier-spacing around 0.12 nm, a van der Waals cutoff of 1.2 nm, and considering long-range dispersion corrections for energy and pressure. The v-rescale algorithm is employed for coupling the system with a reservoir at temperature T with a coupling time constant of $\tau_t = 0.1$ ps. In case of single chain simulations, we fix an isotropic pressure letting the cell vary its size for all orthogonal directions in the same amount. We perform 50 ns runs for these simulations and discard the first 10 ns. For membranes, red the x and y sides of the simulation box are fixed to 5.0 nm, whereas the z side can vary its length. This is done by employing a semi-isobaric coupling, fixing the zz component of the pressure tensor as 1.0 bar, and setting a compressibility of 4.5×10^{-5} bar^{-1} for the z direction, and 0.0 bar^{-1} for the x and y directions. For these simulations we cover 100 ns, and the first 50 ns are discarded for sampling.

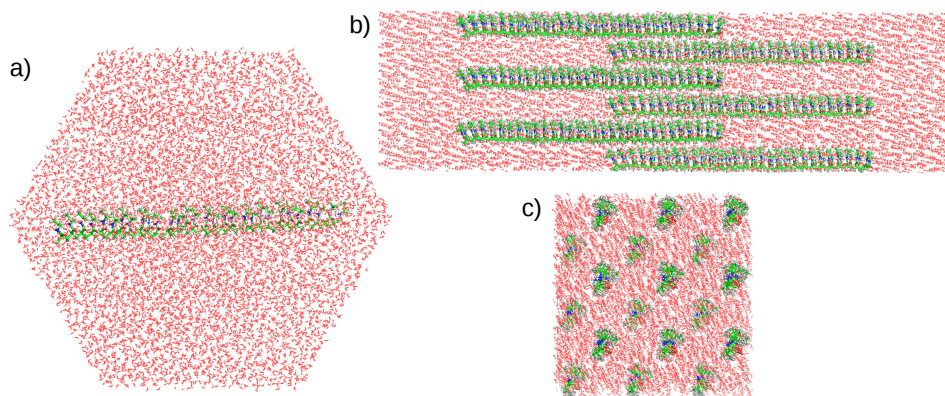The model is setup by employing the tool pdb2gmx of the GROMACS pack-

Figure IV.1: Snapshots of non-relaxed initial configurations for: a) a single 30-mere in a do-decahedron water box and b) a membrane-like configuration composed of 18 single chains in a prism-shaped simulation cell. Panel c) shows a front view of the same membrane-like configuration.

age, and by considering the OPLS-AA[31,32] and the AMBER[33] force fields. In both cases we are employing the SPC/E water, since it was observed that combining OPLS-AA[19] and AMBER[20] with SPC/E yields a good approach to the coil-globule transition temperature, T_Θ (for an OPLS-AA with TIP3P study - TIP3P is the recommended water model for OPLS-AA - see reference [34]). `pdb2gmx` needs atom positions, residue definitions, and a hydrogen database containing information on how to connect hydrogen atoms to existing atoms. We build the atom positions by producing a NIPAM monomer with the Avogadro program[35]. Then, we align the growing direction with the z axis of our cell, and connect 30 monomers to produce an isotactic oligomer. The isotactic conformer is employed since, for small oligomers, it seems to not strongly change the coil to globule transition temperature, while it may aid to fasten the collapse from an extended conformation[24]. Nonetheless, other properties, such as the gyration radius, are clearly affected by tacticity[23,25]. On the other hand, according to Walter et. al, a 30-mer is long enough to properly capture the coil to globule transition, while being reasonably small to allow a short computation time[19]. For shorter chains the transition temperature strongly depends on the oligomer size[19,21]. The building of the oligomer is performed with a simple home made code, which produces a pdb-formated file of the oligomer without most hydrogen atoms (`oligomer.pdb`). In case of a membrane, the code also replicates the oligomer in a square xy and 3x3 lattice to form one side of the membrane, which

is then replicated, mirrored, and shifted to partially fit in the interstices of the first layer, as shown in panels b) and c) of Figure IV.1. In this way, we get an initial configuration of a membrane having a dense central region and half the central density at their sides. This is done to somehow mimic the structure of a spherical hydrogel colloidal particle, which has a dense hard core and a light crown for $T < T_\Theta$. In addition to the `oligomer.pdb` file, the code generates an additional file with the membrane-like structure. See the Supplemental Material for further details.

The output of `pdb2gmx` is the topology and a gro-formated file containing the oligomer (or membrane) coordinates. Both systems, the oligomer and the membrane, are then solvated in SPC/E water. In case of the single oligomer chain, this is done by considering a sufficiently large dodecahedric-shaped cell to completely fit the stretched oligomer and avoid self-interactions, i. e., interactions with its own image, (see panel a) of Figure IV.1). The dodecahedric-shaped cell is simply employed to decrease around 30% the number of water molecules to be used. This cell is initially set with an image distance of 7.68 nm and contains 10175 SPC/E molecules. On the other hand, the membrane is embedded in a prismatic cell with dimensions $L_x = L_y = 5.0$ nm and $L_z = 18.0$ nm, containing 11424 SPC/E molecules. Note that the ratio between the number of polymer and water molecules increases substantially when considering the membrane. This should give rise to better averaging of the polymer properties. These non-relaxed initial configurations are shown in panels a) and b) of Figure IV.1 for the oligomer and membrane, respectively. We performed a 20ns low temperature (280 K) simulation to relax the oligomer previous to formal simulations, and a longer 50 ns run with the same temperature for the membrane. This is done since the membrane needs longer runs to reach a steady state. The starting configuration for all membrane runs is shown in Figure IV.2.

3   Results and Discussion

3.1   Infinitely diluted 30-mer

We start this section by comparing results from OPLS-AA and AMBER force fields as obtained with a single 30-mer chain in SPC/E water. For this purpose we produce 50 ns runs, from which the first 10 ns are discarded. During these runs several properties are followed. These are: the end-to-end distance, given from one of the ending carbones of the first isopropyl towards one of the ending hydrogens of the last backbone methyl (GROMACS `polystat` tool), the radius of
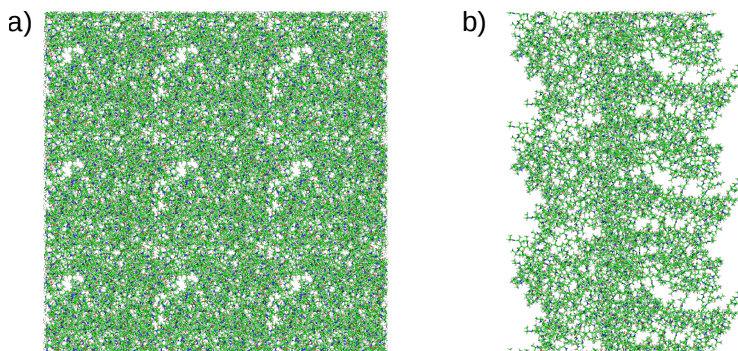
Figure IV.2: Snapshot of the membrane initial configuration for all runs. a) Front view. b) Side view. Water molecules are not shown and the simulation cell is replicated three times in the x and y directions.

gyration (GROMACS `gyrate` tool), $R_g = (\sum_i m_i |\vec{r}_i|^2 / \sum_i m_i)^{1/2}$ running i over all massive sites and being m_i and $\vec{r}_i$ their mass and position respect to the polymer center of mass, the solvent accessible surface area (SASA)[36] (GROMACS `sasa` tool), making use of the Van der Waals radii given by Bondi[37], and the number of hydrogen bonds among the oligomer and the SPC/E water molecules. For this last quantity we are employing a cutoff angle for the hydrogen-donor-acceptor of 30 degrees and a cutoff donor-acceptor distance of 0.35 nm (default values of the GROMACS `hbond` tool). These properties are expected to show certain degree of correlation. That is, as the oligomer transits from a coil to a globule structure all these properties should decrease. Results for the AMBER force field evaluated at temperatures 290 K, 300 K, 310 K, and 325 K are given in Figure IV.3. These temperatures are around the experimental T_Θ thus we expect to observe some signature of it.

In general, the oligomer reaches a steady state in less than 10 ns when starting from the relaxed configuration. Note that this steady state does not mean the system is at equilibrium. In fact, 30-mers starting from a tight globule configuration do not re-hydrate under any temperature for the OPLS-AA with TIP4P/2005 water molecules and for very long runs[24]. We have observed a similar behavior for our system, although using a much smaller time window. This means that, in general, all properties here reported correspond to metastable states. Moreover, previously reported properties should also correspond to metastable states[19,20]. Kang et. al. results also suggest that metastable states associated to loose globule configurations and coil configurations have shallower local free-energy minima than those corresponding to tight globule configurations. Hence, by start-
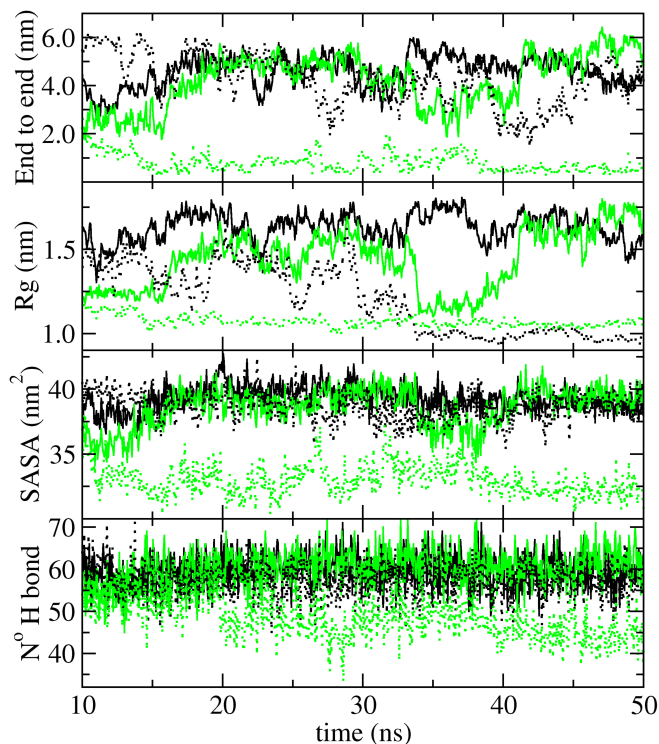
Figure IV.3: End to end distance, radius of gyration, solvent accessible surface area (SASA), and number of H bonds among polymer and SPC/E water, as a function of time, from top to bottom. The dark (black) solid, light (green) solid, dark (black) dashed, and light (green) dashed curves correspond to 290 K, 300 K, 310 K, and 325 K, respectively.

ing from an hydrated state one captures a hydrated-dehydrated configuration change, which seems to be reproducible. After this non-steady state stage, properties fluctuate around their corresponding average values. Fluctuations increase for a temperature close to T_Θ. For $T = 290$ K, the largest average values for the end-to-end distance and R_g are attained, which in turn translates into large solvent accessible surface area and number of oligomer-water hydrogen bonds. Conversely, for $T = 325$ K, we observe a smaller average end-to-end distance, R_g, SASA, and number of oligomer-water hydrogen bonds. However, mixed results for T=300 K, and 310 K are found. For $T = 300$ K in the range of 35-40 ns and for $T = 310$ K and times above 35 ns, we get large end-to-end distances, SASA and number of oligomer-water H bonds, but a not so large R_g average value. Indeed, R_g seems to strongly fluctuate between the values corresponding to $T = 290$ K

and $T = 325$ K. In order to obtain better averages of the properties one should capture several of these crossings from high to low values and vice-versa. Note that the time spent in each state is large compared to the time window we are employing. In addition, these long time-scale and strong fluctuations may also be present for temperatures away from T_Θ [24]. A low R_g and a large SASA suggest the formation of a relatively compact coil hydrated structure. A true globule structure should exhibit not only low R_g values, but also low SASA and number of oligomer-water hydrogen bonds, such as the ones obtained for $T = 325$ K.
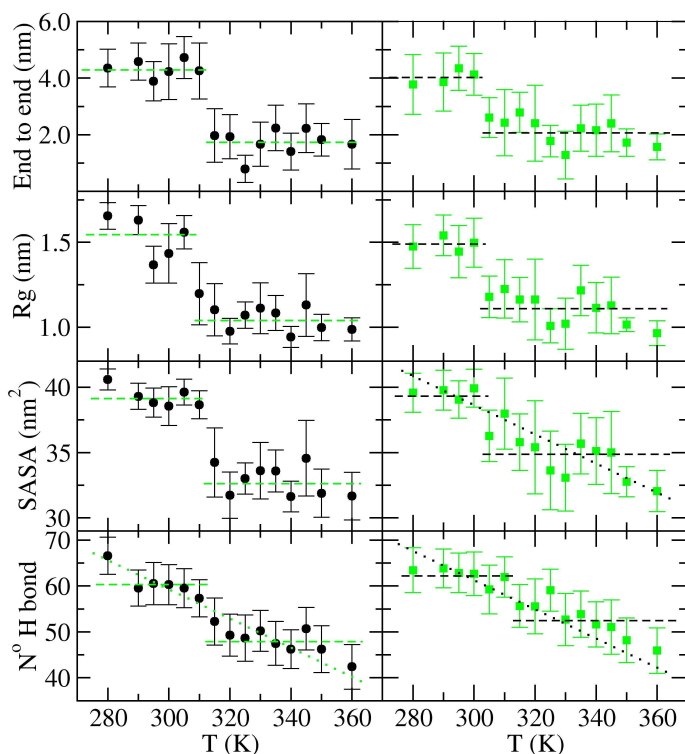

Figure IV.4: Equilibrium properties of a single chain oligomer in SPC/E water. Left, AMBER force field. Right, OPLS-AA force field. End to end distance, radius of gyration, solvent accessible surface area, and number of H bonds among polymer and SPC/E water, from top to bottom. Dashed and dotted lines are guides to the eye.

The averages and fluctuations of the time dependent curves shown in Figure IV.3 are displayed in Figure IV.4. Left panels show AMBER results, and right panels OPLS-AA results, both by considering SPC/E water. Left panels define, in general, step functions, which are depicted as dashed lines to guide the eye. This

seems to be clear for all studied properties except for the number of polymer-water hydrogen bonds, where a general decreasing trend is overlapped to a more steep decrease close to T_Θ. This general decreasing trend is expected since the number of hydrogen bonds monotonously decreases with temperature even for pure water in the same temperature interval. This sharp drop occurs at temperatures comprised between 310 and 315 K for all curves except for R_g, which arises in-between 305 K and 310 K. As remarked in the previous paragraph, there are some configurations with low R_g while keeping large SASA, end-to-end distances, and number of oligomer-water hydrogen bonds. From our R_g data we estimate the transition at $T = (308 \pm 5)$ K. This value can be compared with the 295 - 310 K temperature interval given for a similar system by Du. et. al[20]. This agreement suggests that the 30-mer set by Du et al. is isotactic.

A similar picture arises when considering the OPLS-AA force field instead of AMBER (see right panels of Figure IV.4). There are, however, some slight differences. On the one hand, the height of the steps of the curves seems to be smaller than that obtained with AMBER. That is, in general, the low temperature values are a little smaller and the high temperature values are slightly higher than those for AMBER. This produces a less clear definition of the transition temperature. In fact, a linear trend cannot be discarded for SASA and the number of oligomer-water hydrogen bonds with temperature. This finding is in line with results for OPLS-AA and TIP3P water[34]. On the other hand, for all properties except the number of hydrogen bonds, the transition temperature appears in the interval 300 - 305 K. Our estimate is $T = (303 \pm 5)$ K, in good agreement with the experimental value. We should also mention that our T_Θ estimate is smaller than the one obtained in reference [19] for a similar system ($T_\Theta \approx 320$ K). This shift of T_Θ suggests that Walter et al. 30-mer is syndiotactic, since sysdiotactic oligomers are more water soluble[23].

3.2 Membrane in pure water

In this Section we go beyond the isolated single-chain and study the collective and single chain properties of an oligomer formed by an assembly of 18 chains, as described in Section II. For this purpose, we start the simulation with a membrane-like initial configuration, such as the one depicted in Figure IV.2. This starting configuration is obtained letting the system relax at a fixed temperature of $T =280$ K. After a 100 ns run at $T =325$ K, the membrane looks like the one shown in Figure IV.5. As can be seen, the side view exhibits a more compact structure, although somehow heterogeneous. The front view, in turn, shows the existence of pores along the membrane. This is a consequence of the folding of
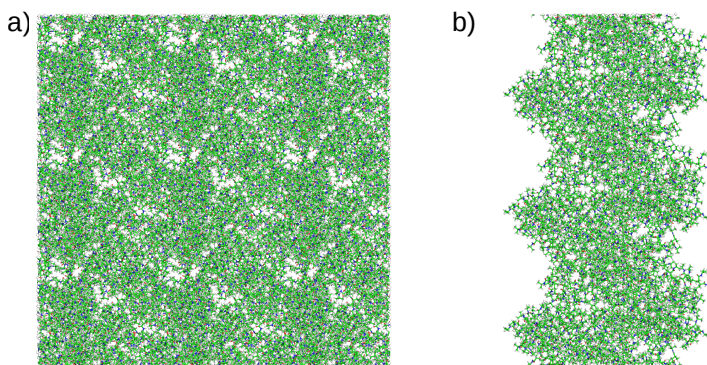
Figure IV.5: Snapshot of the membrane final configuration for T=325 K. a) Frontal view. b) Side view. Water molecules are not shown and the simulation cell is replicated three times in the x and y directions.

the oligomers into denser structures, as expected. To confirm the existence of a single-chain transition from an extended coil to a shrunken dense structure, we have traced the time averages of the same properties analyzed in the previous Section.

Figure IV.6 shows time averages of the end-to-end distance, R_g, SASA, and total number of H bonds among oligomers and water, for the 18 single-chains that define the polymeric membrane. In general, the results obtained for the membrane confirm the same trends than the ones already obtained for an infinitely diluted single chain, at least for the end-to-end distance and R_g. That is, we observe a sudden drop of these quantities for a temperature close to T_Θ, for both force fields. The drop is, notwithstanding, smaller than for the single-oligomer case. We get an 8-9 % drop for the end-to-end distance which can be compared with the corresponding 50 - 60 % drop for the single-chain case. For the particular case of R_g, the membrane drop is close to 11-13 %, to be compared with a 26 - 33 % of the single oligomer. This is not an unexpected result since chains are confined into a parallel arrangement for the membrane, restricting their motion to some extent. As a consequence, their average end-to-end and R_g distance are always larger than for the infinitely diluted case, being the difference between these cases larger at high temperatures. This feature is consistent with results of polymer brushes, where increasing brush grafting density and/or decreasing temperature leads to an increase of the end-to-end distance [26]. Thus, in the membrane configuration we should avoid referring to the more compact structure as globule, although much longer chains should lead to such structure. On the other hand, the fact of averaging on several
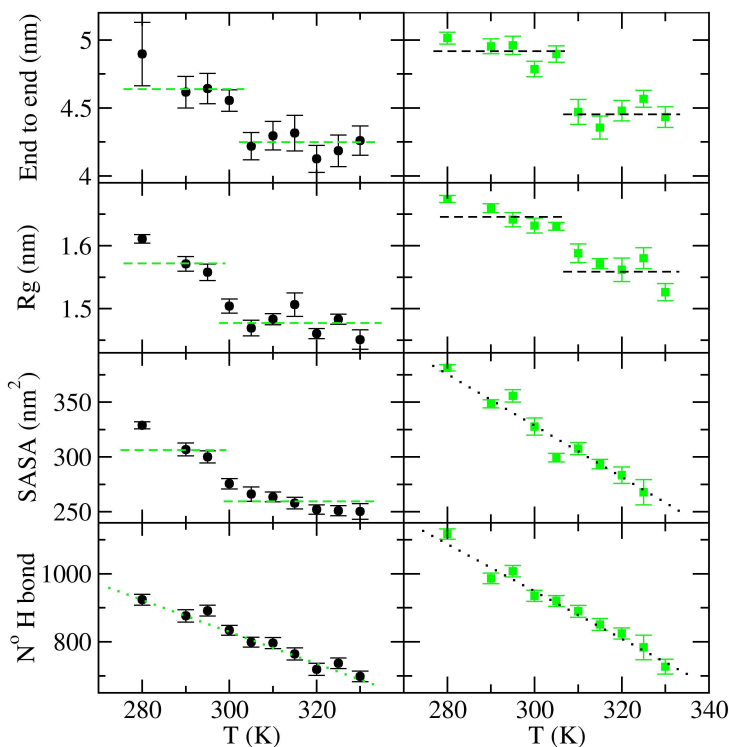
Figure IV.6: Time and number average properties of a PNIPAM membrane in SPC/E water. Left, AMBER force field. Right, OPLS-AA force field. We are showing, from top to bottom, the end to end distance, radius of gyration, solvent accessible surface area, and number of H bonds among polymer and SPC/E water. Dashed and dotted lines are guides to the eye.

molecules reduces the uncertainty, making possible the detection of smaller drops. Note that for $T > T_\Theta$, and as for the single-chain case, we are getting larger values of the end-to-end distance and R_g for the OPLS-AA force field than for the AMBER, suggesting a somewhat softer nature of the chains in the last case.

We should note that the coil to globule transition for the AMBER force field seems to occur at smaller temperatures from the membrane results than for the diluted case. Results from OPLS-AA force field are more consistent with those shown in the previous section. We have also noted that the collective motion is much slower for the membrane configuration than for the single chain. Thus, particular membrane configurations live, on average, longer times than single-chain ones, which also impacts on results for relatively short runs (tens

to hundreds of nanoseconds). In this regard, we feel that 100 ns is not enough to capture several membrane disjoint configurations in configuration space, as it would be desirable to guaranty a proper sampling. This, in turn, may explain the displacement of the transition temperature for the AMBER force field when comparing both, membrane and infinite diluted results.

For membranes, in contrast to the single chain case, SASA and the number of hydrogen bonds between water and oligomers are linked to the self and collective chain-chain interaction among polymer molecules. This is simply because a small chain-chain distance reduces the exposed polymer surface area to the solvent molecules, as it also decreases the probability of producing water-polymer hydrogen bonds. We find a drop percentage of the SASA at the transition temperature for the AMBER force field close to 16 %, which is very similar to the one found for the single molecule case. For the membrane, the drop is less sharp, though. We did not find a SASA drop for OPLS-AA. Also, as in the previous section, the number of hydrogen bonds among water and polymer chains does not show a clear jump close to the coil to globule transition, but a gradual decreasing trend. This is in line with a gradual reduction in the number of water molecules in the first solvation shell[38] and dehydration starting at T_Θ, as experimentally found elsewhere[39].
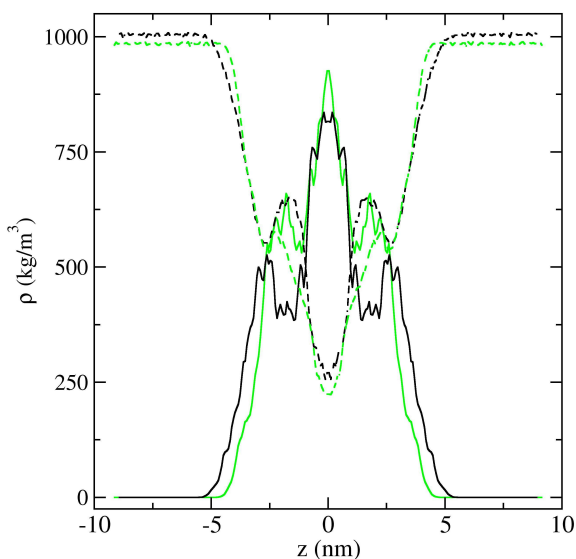

Figure IV.7: Density profiles for polymer (solid lines) and water (dashed lines) at $T = 290$ K (dark lines) and $T = 325$ K (light lines). They correspond to the AMBER force field.

The membrane configuration allows to study the polymer density profiles as a function of the distance from the vertical z axis. In Figure IV.7 we show the average profile for $T = 290$ K (dark lines) and $T = 325$ K (light lines). We are also including the corresponding water profiles as dashed lines. The sum of both, water and polymer profiles, gives rise to an almost constant density profile, though the membrane region is a little bit denser. Thus, the water profile can be seen as complementary of the membrane to yield a constant value, which is close to 1000 kg/m^3 for $T = 290$ K and 980 kg/m^3 for $T = 325$ K. We can see from both profiles a denser central region (with density ρ_c), which is a consequence of the initial arrangement into a core-shell morphology (see Figure IV.1). We observe that the density of the central region increases as compared to the less dense initial configuration for all T. This is unexpected for the $T = 280$ K case. Note that there is nothing impeding the disassembling of the membrane, which one should expect for a sufficiently large run at low temperature. This does not happen even for a slab of trimmers in water (not shown), for both considered force fields, which is in agreement with simulations from several forcefields[22]. The polymer regions at both sides of the central core (having half of the central density at the initial configuration) shrink along the run to produce larger densities (ρ_s), and thiner profiles (with width w). This shrinking process leads to the secondary maxima placed at the borders of the membrane, which are a consequence of the bending of the oligomer tips towards the central plane. As expected, shrinking is more pronounced at higher temperatures, as well as the increase of the central, ρ_c, and side, ρ_s, densities.

We have measured the membrane width, w, as the z-distance at which the profiles cut the $\rho = 300$ kg/m^3 horizontal line, and both densities ρ_c and ρ_s as a function of temperature, with the purpose of observing jumps close to the coil to globule transition temperature. Results are shown in Figure IV.8, where the increasing density and decreasing width trends with temperature are clearly captured with both force fields. However, sudden changes close to the transition temperature are not so clear. Something similar occurs with the surface tension (not shown). This property fluctuates around 300±100 and 500±100 bar nm for temperatures below and above the transition, respectively. Letting aside the possible existence of hysteresis cycles which would brake the ergodic hypothesis and which are certainly present for large and crosslinked polymer molecules[40], we think that these collective properties cannot be precisely determined with 100 ns runs, where sampling is not performed from disjoint phase-space configurations. An obvious way to improve this issue would be enlarging the sampling time (probably by a factor above ten). Another possibility would
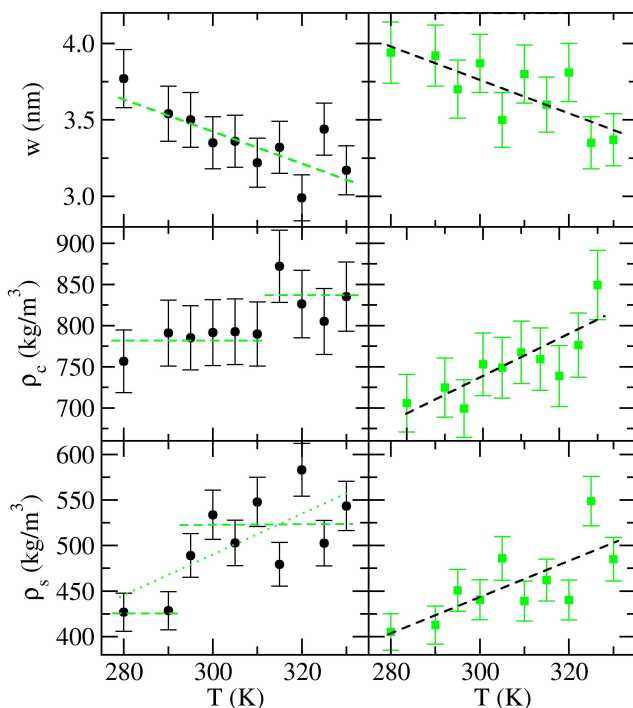
Figure IV.8: Membrane width (w), central region density (ρ_c), and side density (ρ_s), as taken from profiles.

be to consider a replica exchange molecular dynamics (REMD) sampling, with a temperature expansion of the NPT ensemble. In the first case one should count with a much larger computational power than we actually do. In the second case, one may use similar computational resources but concentrated in a single cluster. This is not our case either. It is worth mentioning that GROMACS allows easily implementing REMD simulations (see for instance [41]).

3.3   Membrane in water and electrolyte

Once the behavior of the membrane structure with temperature is well characterized in the presence of pure water, one can study how a certain solute interacts with it. In this section, we are focusing on the distribution profiles of NaCl and NaI electrolytes for temperatures below ($T = 290$ K) and above ($T = 320$ K) the transition temperature. We are comparing NaCl with NaI results since I^- exhibits a less hydrophilic (more hydrophobic) behavior than Cl^-. In other words, I^- is at the right of Cl^- in the Hofmeister series [42,43]. This is frequently explained
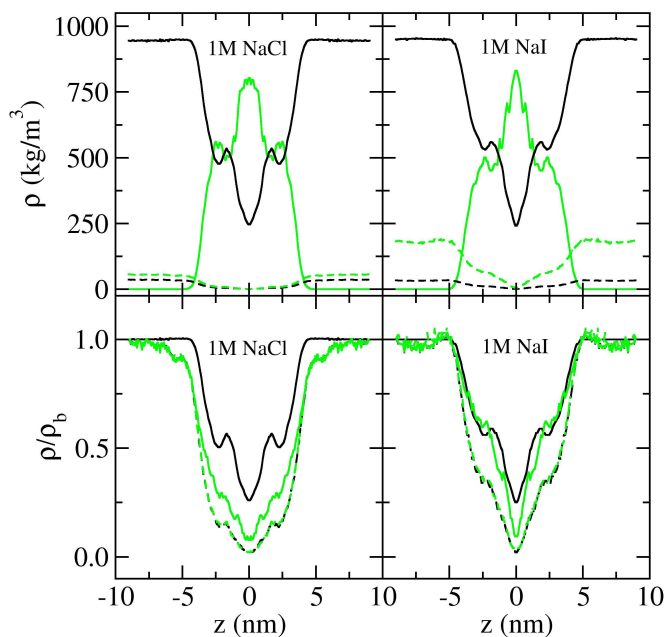
Figure IV.9: Density profiles at $T = 320$ K. Top panels) Density profiles for water (dark solid lines), polymer (light solid lines), cation (dark dashed lines) and anion (light dashed lines). Bottom panels) The corresponding normalized density profiles (taking bulk as reference). Polymer normalized density is not shown, instead, light solid lines correspond to the ratio between cation and water normalized profiles. Left and right panels correspond to 1 molar NaCl and NaI electrolytes, respectively. Results are obtained with the AMBER force field.

in terms of the more chaotropic (less kosmotropic) nature of I$^-$ in comparison with Cl$^-$, which is a smaller anion. In this view the iodide ion would produce more structural chaos (less ordering) than chloride, and so it would induce a stronger disruption of the water structure in its surroundings, lowering further the average number of hydrogen bonds, and leading to a less favorable solvation energy[44,45]. Nonetheless, recent experimental studies point out that ions are only able to perturb the first hydration shells[46,47], making this argument weak. In addition to this chaotropic-kosmotropic effect, a smaller ion yields a larger Coulombic interaction favoring solvation. We should also mention that, due to its finite size, any solute produces a larger decrease of possible solvent configurations in bulk than when located over an interface. This last mechanism lowers entropy, and the effect is more pronounced for larger solutes. Due to all these reasons, and others which rely on the ion-polymer interactions[13,43], I$^-$ is expected to be more adsorbed by the polymeric membrane than Cl$^-$. The

larger affinity of electrolyte by water than for the polymer rich phase gives rise to the so-called salting-out effect, whereby the polymer chains tend to collapse to minimize the area exposed to the solvent, showing an impact on T_Θ[27]. As expected, this effect is much more pronounced for NaCl (12 K for 1 M concentration) than for NaI (solely 2 K for 1 M concentration)[1,13]. Indeed, NaI shows a nonlinear shift of T_Θ with salt concentration, leading to a maximum close to [NaI]=0.3 M. That is, NaI shows salting-in at low concentrations followed by salting-out as concentration increases above 0.3 M[1]. The salting-in is explained in terms of the large affinity of I$^-$ for the PNIPAM chains, promoting, in turn, the entering of water molecules[13]. The maxima would appear as a consequence of a saturation of the PNIPAM sites where I$^-$ can be linked to, and so, larger electrolyte concentrations would promote a positive concentration difference from the outside to the inside (salting-out)[13]. This positive concentration difference causes a decrease of the water activity at the bulk solution, and so the hydrogel particle reacts shrinking to deliver water.

The profiles for $T = 320$ K are shown in Figure IV.9. In the top panels, in addition to the polymer and water densities, we are showing the cationic and anionic profiles. As for the case without electrolyte, the total density is close to a constant, but now somewhat above 1000 kg/m^3, due to the salt addition. In both top panels we observe a bulk concentration (close to 1 M), which corresponds to the flat ionic profiles far from the membrane. The mass concentration of anions is larger than that of cations due to their larger molar mass. This is more evident in the top right panel, since iodide has more than five times the sodium mass. When profiles are presented normalized with their bulk concentration, the differences between cationic and anionic profiles vanish, as shown in the bottom panels of Figure IV.9. Hence, the membrane remains uncharged for the cases here reported. This total absence of charge is somewhat unexpected given the large asymmetry of the anion and cation potentials. This situation may change for not so large electrolyte concentrations or when considering more asymmetric salts (for instance, including different valences). We also observe that the ratio between ions and water molecules decreases as entering the membrane. This is shown as light solid lines for the bottom panels of Figure IV.9. In fact, this ratio decreases as entering the membrane becoming almost zero at the membrane midplane. In other words, for large electrolyte concentrations (1M), ions are more comfortable surrounded by pure water than by hydrated-polymer chains. We also observe some differences between NaCl and NaI for the dehydrated membrane. On the one hand, NaI leads to a larger amount of water inside the membrane, which in turn makes the membrane a

little bit wider. Also, the amount of ions (both, cations and anions) entering inside the membrane and the cation-water ratio are larger in the case of NaI than for NaCl (see bottom panels of Figure IV.9). As mentioned in the previous paragraph, this behavior is expected for a less hydrophilic anion such as I^- as compared to Cl^-. Nonetheless, one may also expect a larger adsorption of I^- to be compensated with the outcome of a similar amount of water, in such a way to keep the membrane volume invariant. As mentioned this is not the case, the larger I^- adsorption enhances both, water and Na^+ income. We think cation income increases driven by the need of fulfilling the local electroneutrality condition (although this condition is not strong and could be broken) which in turn, carries binded water in the process.
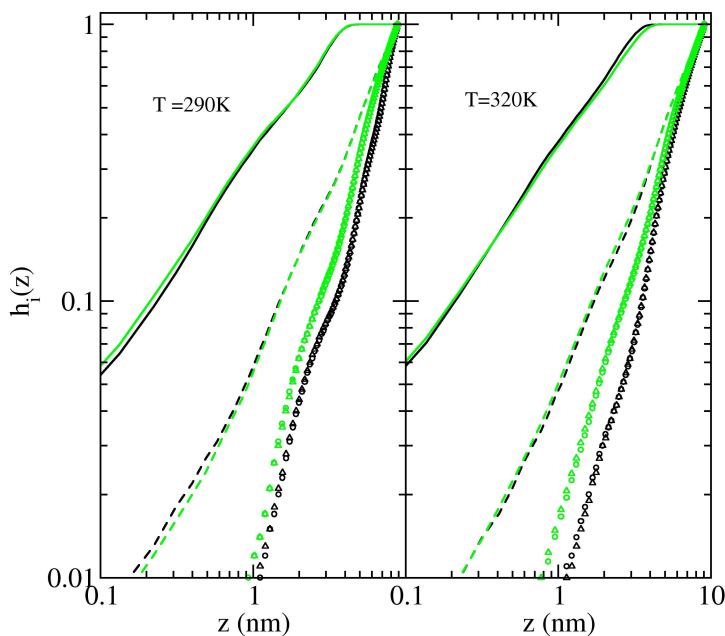

Figure IV.10: Normalized number of molecules of species i inside a slab of width z ($h_i(z)$), as a function of z. Solid lines, dashed lines, circles and triangles correspond to polymer, water, cation, and anion, respectively. Dark lines and symbols are employed for NaCl, whereas light lines and symbols for NaI. Left and right panels correspond to $T = 290$ K and 320 K, respectively.

From the simulated density profiles we can obtain the function $h_i(z) = \frac{2AN_A}{N_i M_i} \int_0^z \rho_i(z) dz$, where A is the transversal area of the prismatic simulation cell, N_A is the Avogadro constant, and N_i, M_i, and $\rho_i(z)$ are the total number of molecules in the cell, the molar mass, and the mass profile of species i, respectively. $h_i(z)$ repre-

sents the number of molecules of species i inside a slab of width $2z$, centered in the membrane, normalized by the total number of molecules of species i. It is shown in Figure IV.10 for $T = 290$ K (left panel) and for $T = 320$ K (right panel). For the low temperature chart we can observe that 77% of the polymer mass is inside a 6 nm width slab ($z = 3$nm) for both electrolytes, 23% of water molecules, 11% of electrolyte in case of NaI, and 8% in case of NaCl. That is, water and polymer do not show large differences of profiles, but ions are more adsorbed by the membrane in the case of NaI. The situation changes for $T = 320$ K, where we can observe some differences on the water and polymer profiles when considering NaI instead of NaCl. In this case we observe a drop from 88% of the polymer mass inside the 6 nm slab to 81%, a slight increase of water from 19% to 20%, and an important increase of electrolyte from 6% to 11%. Hence, the membrane is slightly more expanded for NaI than NaCl at $T = 320$ K. When comparing the electrolyte adsorption at $T = 290$ K with that at $T = 320$ K we observe a similar adsorption of NaI (11%) and a reduction of NaCl from 8% to 6%. This reduction is consistent with the enhanced hydrophobic nature of the polymer at high temperatures, and with the decrease of T_Θ with NaCl[13]. The similar adsorption of NaI for 1 M on the coil and on the globule phases is also consistent with the practically null shift of T_Θ from pure water to 1 M NaI electrolyte solution. Finally, one should note that the cation/anion ratio is always close to one for all z and all cases, implying an always neutral slab.

Electrolyte	$T = 290$ K	$T = 320$ K
None	300 ± 80	520 ± 60
1 M NaI	340 ± 60	590 ± 80
1 M NaCl	400 ± 80	580 ± 50

Table IV.1: Surface tension (given in bar nm) for some cases of the membrane configuration here studied. Surface tension should increase from left to right, and from top to bottom. Errors are taken from time fluctuations of the obtained trajectories.

Finally, we present Table IV.1 where the surface tension is shown for six cases, namely with no added electrolyte, 1 M NaI, and 1 M NaCl, for both temperatures, $T = 290$ K and $T = 300$ K. The calculation follows the virial route, as implemented by the GROMACS tool *gmx energy*. We should note that virial fluctuations are very large so wide errors ranges are expected to be found in these calculations. Much longer runs would be necessary to obtain meaningful results. Nonetheless, the surface tension seems to increase with temperature, which is the expected behavior. That is, by trespassing the coil to globule transition one should get a more defined interface, leading to a larger surface tension.

On the other hand, adding NaCl also promotes a sharper water-polymer interface, whereas the polymer turns more hydrophobic (the so-called salting-out process for protein precipitation). In case of NaI, salting-out is less pronounced, since, as mentioned, I^- ions tend to promote a larger ionic membrane adsorption which is not very sensitive to the polymer structure. These results are in line with those given elsewhere when considering a single oligomer chain[20], where radial distribution functions are shown. There it is reported a large increase of the height of the O(C=O)-Na^+ main peak when considering NaI instead of NaCl for T =288 K. Something similar occurs for the C(C=0)-Na^+ and N(N-H)-Na^+ peaks, pointing to an enhanced Na^+-membrane binding when replacing chloride by iodide. It also shows an enhanced anion-membrane interaction for several membrane atoms, although they weakly interact in all cases. For the membrane we observe the same trends (not shown). However, both Na^+-membrane and anion-membrane radial distribution function main peaks strongly diminish their heights due to the presence of the other polymeric chains as compared with the infinitely diluted chain case. In brief, it seems that small changes in this weak, unlocalized anion-membrane interaction with all membrane groups is sufficient to produce remarkable changes in the interaction between cations and the amide groups of the membrane, driven by the fact that the electroneutrality condition is not locally broken in the cases here studied.

4 Conclusions

This work presents molecular dynamics simulations of a thermoresponsive polymer in water and in electrolyte solutions. We have split the results into three sections. The first deals with an infinitely diluted 30-mer in water. The second focused on the structure and collective properties of a membrane-like slab of 18 30-mers in water. Finally, we have replaced pure water with a 1 M NaCl and 1 M NaI water solutions to study the membrane adsorption. Most of the first subsection confirms the findings reported in references [19, 20], where both, AMBER/OPLS-AA force fields in combination with SPC/E water are shown to capture the coil to globule transition temperature in qualitative good agreement with experiments. We have determined a coil to globule transition temperature of ($T_\Theta = 308 \pm 5$) K and ($T_\Theta = 303 \pm 5$) K for the AMBER and OPLS-AA force fields, respectively. These values suggest that Du et al. have set an isotactic 30-mer while Walter et. al a syndiotactic one.

   In the second section we have shown that the transition can be also captured with a membrane-like setup, with some advantages and disadvantages.

Disadvantages are that a larger number of molecules per simulation cell are necessary, and that larger simulation runs are needed to allow for a proper equilibrium sampling. This last issue is related with larger relaxation times of the whole membrane structure. An advantage is that a larger polymer/water ratio is implemented, improving statistics on the polymeric part of the system, which is the subject of study. A second one is that the slab configuration allows to follow properties related with interfaces such as profiles and surface tension. In addition, there is the possibility of including the interaction among different polymer chains and not only the self-interaction. Despite this fact, results from this section show no significant difference of T_Θ with those obtained for 30-mers, suggesting that polymer-polymer interactions are not a key ingredient for the T_Θ determination. Finally, it could provide valuable information on the interaction between the membrane and solutes as electrolytes, leading to density profiles which can then be considered in theoretical approaches, such as integral equation theories, to scaleup results to study microgel-microgel interactions in mesoscopic scales. As an example of membrane-electrolyte interaction, the final section present results on the salting-out effect that occurs in the presence of electrolyte by considering 1 M NaCl and 1 M NaI. We find no breaking of the electroneutrality condition for all considered cases, i. e., both normalized ionic profiles are indistinguishable. Finally, the salting out effect is much less pronounced for NaI than for NaCl, in good agreement with experiments.

References

[1] Zhang, Y.; Furyk, S.; Bergbreiter, D. E.; Cremer, P. S. *J. Am. Chem. Soc.* **2005**, *127*, 14505–14510.

[2] Rissanou, A. N.; Anastasiadis, S. H.; Bitsanis, I. A. *J. Polym. Sci. Part B Polym. Phys.* **2006**, *44*, 3651–3666.

[3] Chung, J. E.; Yokoyama, M.; Yamato, M.; Aoyagi, T.; Sakurai, Y.; Okano, T. *J. Control. Release* **1999**, *62*, 115–127.

[4] Yan, H.; Tsujii, K. *Colloids Surf., B* **2005**, *46*, 142–146.

[5] Wei, H.; Cheng, S. X.; Zhang, X. Z.; Zhuo, R. X. *Prog. Polym. Sci.* **2009**, *34*, 893–910.

[6] von Recum, H.; Kikuchi, A.; Okuhara, M.; Sakurai, Y.; Okano, T.; Kim, S. W. *J. Biomater. Sci. Ed.* **1998**, *9*, 1241–1253.

[7] Von Recum, H.; Okano, T.; Kim, S. W. *J. Control. Release* **1998**, *55*, 121–130.

[8] Ohya, S.; Nakayama, Y.; Matsuda, T. *Biomacromolecules* **2001**, *2*, 856–863.

[9] Denton, A. R. *Phys. Rev. E* **2003**, *67*, 011804.

[10] Gottwald, D.; Likos, C. N.; Kahl, G.; Löwen, H. *Phys. Rev. Lett.* **2004**, *92*, 068301.

[11] Moncho-Jordá, A.; Anta, J. A.; Callejas-Fernández, J. *J. Chem. Phys.* **2013**, *138*.

[12] Colla, T.; Likos, C. N.; Levin, Y. *J. Chem. Phys.* **2014**, *141*.

[13] Heyda, J.; Dzubiella, J. *J. Phys. Chem. B* **2014**, *118*, 10979–10988.

[14] Heyda, J.; Soll, S.; Yuan, J.; Dzubiella, J. *Macromolecules* **2014**, *47*, 2096–2102.

[15] Moncho-Jordá, A. *J. Chem. Phys.* **2013**, *139*.

[16] Adroher-Benítez, I.; Ahualli, S. A.; Martín-Molina, A.; Quesada-Pérez, M.; Moncho-Jordá, A. *Macromolecules* **2015**, *48*, 4645–4656.

[17] Moncho-Jorda, A.; Dzubiella, J. *Phys. Chem. Chem. Phys.* **2016**, *18*, 5372–5385.

[18] Moncho-Jordá, A.; Adroher-Benítez, I. *Soft Matter* **2014**, *10*, 5810–5823.

[19] Walter, J.; Ermatchkov, V.; Vrabec, J.; Hasse, H. *Fluid Phase Equilib.* **2010**, *296*, 164–172.

[20] Du, H.; Wickramasinghe, R.; Qian, X. *J. Phys. Chem. B* **2010**, *114*, 16594–16604.

[21] Tucker, A. K.; Stevens, M. J. *Macromolecules* **2012**, *45*, 6697–6703.

[22] Botan, V.; Ustach, V.; Faller, R.; Leonhard, K. *J. Phys. Chem. B* **2016**, *120*, 3434–3440.

[23] Chiessi, E.; Paradossi, G. *J. Phys. Chem. B* **2016**, *120*, 3765–3776.

[24] Kang, Y.; Joo, H.; Kim, J. S. *J. Phys. Chem. B* **2016**, acs.jpcb.6b09165.

[25] Autieri, E.; Chiessi, E.; Lonardi, A.; Paradossi, G.; Sega, M. *J. Phys. Chem. B* **2011**, *115*, 5827–5839.

[26] Léonforte, F.; Müller, M. *ACS Appl. Mater. Interfaces* **2015**, *7*, 12450–12462.

[27] Algaer, E. A.; Van Der Vegt, N. F. A. *J. Phys. Chem. B* **2011**, *115*, 13781–13787.

[28] Berendsen, H. J. C.; van der Spoel, D.; van Drunen, R. *Comput. Phys. Commun.* **1995**, *91*, 43–56.

[29] Van der Spoel, D.; Lindahl, E.; Hess, B.; Groenhof, G.; Mark, A. E.; Berendsen, H. J. C. *J. Comput. Chem.* **2005**, *26*, 1701–1718.

[30] Pronk, S.; Páll, S.; Schulz, R.; Larsson, P.; Bjelkmar, P.; Apostolov, R.; Shirts, M. R.; Smith, J. C.; Kasson, P. M.; Van Der Spoel, D.; Hess, B.; Lindahl, E. *Bioinformatics* **2013**, *29*, 845–854.

[31] Jorgensen, W. L.; Maxwell, D. S.; Tirado-Rives, J. *J. Am. Chem. Soc.* **1996**, *118*, 11225–11236.

[32] Kaminski, G. A.; Friesner, R. A.; Tirado-Rives, J.; Jorgensen, W. L. *J. Phys. Chem. B* **2001**, *105*, 6474–6487.

References

[33] Lindorff-Larsen, K.; Piana, S.; Palmo, K.; Maragakis, P.; Klepeis, J. L.; Dror, R. O.; Shaw, D. E. *Proteins Struct. Funct. Bioinforma.* **2010**, *78*, 1950–1958.

[34] Alaghemandi, M.; Spohr, E. *Macromol. Theory Simulations* **2012**, *21*, 106–112.

[35] Hanwell, M. D.; Curtis, D. E.; Lonie, D. C.; Vandermeerschd, T.; Zurek, E.; Hutchison, G. R. *J. Cheminform.* **2012**, *4*, 1–17.

[36] Eisenhaber, F.; Lijnzaad, P.; Argos, P.; Sander, C.; Scharf, M. *J. Comput. Chem.* **1995**, *16*, 273–284.

[37] Bondi, A. *J. Phys. Chem.* **1964**, *68*, 441–451.

[38] Kamath, G.; Deshmukh, S. A.; Baker, G. A.; Mancini, D. C.; Sankaranarayanan, S. K. *Phys. Chem. Chem. Phys.* **2013**, *15*, 12667–73.

[39] Shiraga, K.; Naito, H.; Suzuki, T.; Kondo, N.; Ogawa, Y. *J. Phys. Chem. B* **2015**, *119*, 5576–5587.

[40] Wang, X.; Qiu, X.; Wu, C. *Macromolecules* **1998**, *31*, 2972–2976.

[41] Orea, P.; Odriozola, G. *J. Chem. Phys.* **2013**, *138*.

[42] Hofmeister, F. *Arch. Exp. Pathol. Pharmakol.* **1888**, *24*, 247–260.

[43] Zhang, Y.; Cremer, P. S. *Curr. Opin. Chem. Biol.* **2006**, *10*, 658–663.

[44] Marcus, Y. *Chem. Rev.* **2009**, *109*, 1346–1370.

[45] Ball, P.; Hallsworth, J. E. *Phys. Chem. Chem. Phys.* **2015**, *17*, 8297–8305.

[46] Omta, A. W.; Kropman, M. F.; Woutersen, S.; Bakker, H. J. *Science* **2003**, *301*, 347–9.

[47] Batchelor, J. D.; Olteanu, A.; Tripathy, A.; Pielak, G. J. *J. Am. Chem. Soc.* **2004**, *126*, 1958–1961.

Sorption and spatial distribution of protein globules in charged hydrogel particles

Irene Adroher-Benítez[*], Arturo Moncho-Jordá[*][†], and Joachim Dzubiella[‡][§][¶]

[*]Departamento de Física Aplicada, Facultad de Ciencias, Universidad de Granada, Avenida Fuentenueva 2, 18001, Granada, Spain

[†]Instituto Carlos I de Física Teórica y Computacional, Universidad de Granada, Avenida Fuentenueva 2, 18001, Granada, Spain

[‡]Institut für Physik, Humboldt-Universität zu Berlin, Newtonstrasse 15, D-12489 Berlin, Germany

[§]Institut für Weiche Materie and Funktionale Materialen, Helmholtz-Zentrum Berlin, Hahn-Meitner Platz 1, D-14109 Berlin, Germany

[¶]Multifunctional Langmuir for Medicine, Helmholtz Virtual Institute, 14513 Teltow, Germany

Abstract

We have theoretically studied the uptake of a non-uniformly charged biomolecule, suitable to represent a globular protein or a drug, by a charged hydrogel carrier in the presence of a 1:1 electrolyte. Based on the analysis of a physical interaction Hamiltonian including leading order electrostatic contributions, we have identified five different sorption states of the system, from complete repulsion of the molecule to its full sorption deep inside the hydrogel, going through meta- and stable surface adsorption states. The results are summarized in state diagrams that also explore the effects of varying the electrolyte concentration, excluded-volume contributions as well as the hydrophobic interaction between protein and hydrogel. We show that the dipole moment of the biomolecule is a key parameter controlling the spatial distribution of the globules. In particular, biomolecules with a large dipole moment tend to be adsorbed at the external surface of the hydrogel, even if like-charged, whereas uniformly charged biomolecules tend to partition towards the internal core of an oppositely charged hydrogel. Our results establish a guidance for the spatial partitioning of proteins and drugs in hydrogel carriers, tuneable by hydrogel charge, pH and salt concentration.
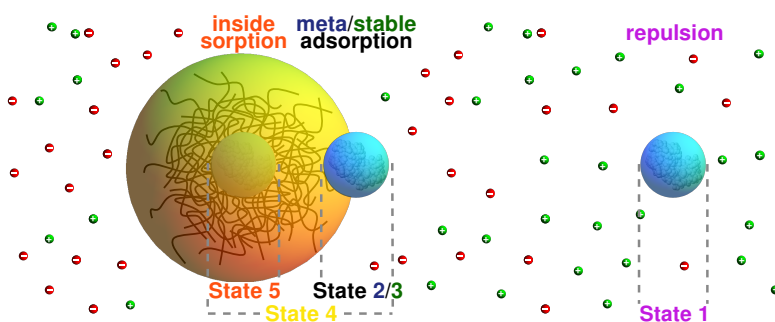
1 Introduction

Hydrogels are soft colloidal particles of nanometric size formed by cross-linked polymer chains dispersed in water. They have received considerable attention during the last decades due to their exceptional physicochemical properties[1]. Firstly, hydrogels can be considered as multi-responsive nanomaterials because they are able to reversible swell and shrink in a useful and reproducible manner in response to various stimuli from their surroundings, such as variations of the the solvent quality, temperature, salt concentration, pH, or external electric/magnetic fields[2–4]. In addition, since the swelling kinetics roughly scales with the square of the particle size, the swelling response is several orders of magnitude faster than the one observed in macroscopic gels[5,6].

In the swollen state, hydrogels are hydrophilic and incorporate a large amount of water, leading to very open porous structures that allow the permeation of ions and other kind of cosolutes, such as proteins, peptides, lipids, enzymes, genetic material, drugs and chemical reactants. Oppositely, in the shrunken state, the particles partially expel their content due to the collapse of the cross-linked network induced by the enhanced hydrophobic attractions between the polymers. Moreover, hydrogels can be designed to be biocompatible, biodegradable and, due to the large water content allow the incorporation of biomacromolecules with relatively small changes in the native structure. This preserves the drug's biological activity and conformation state, reducing the toxicity and enhancing its protection from chemical and enzymatic degradation[7–11].

Due to the combination of all these features, hydrogels have been proposed as excellent candidates for transport and delivery systems of biomacromolecules and drugs[12], e.g., in anti-cancer and gene therapy, permitting a high payload capacity. The release of the entrapped molecule can be triggered externally in a controlled fashion[13–16]. Furthermore, they can be selectively surface-functionalized to enable tumour-specific targeting[17].

The uptake of biomolecules is mediated by the underlying physical interactions between the biomolecule and the polymer network[18,19]. These interactions not only determine the net degree of uptake but also the preferential location of the biomolecule in the hydrogel volume. In this respect, it must be emphasized that the properties of the hydrogel-biomolecule complex strongly depend on whether the molecule is superficially adsorbed at the external shell of the hydrogel or internally absorbed deep inside the polymer network. Protein surface adsorption leads to a protein 'corona' that largely defines the biological identity of the particle[20]. In some practical situations, surface adsorption is

unwanted. An example would be the surface deposition of lysozyme proteins on contact lenses, which can cause adverse responses and shortens the time that lenses can be worn[21]. Analogously, the use of hydrogels as nanocarriers requires in some cases the complete encapsulation of the therapeutic agent in the internal matrix of the particle. In this way the biomolecule is not able to interact with the biological environment, thus avoiding the enzymatic breakdown before reaching the site of action in the body[22]. In some other circumstances surface adsorption is desirable. For instance, the exposure of certain protein domains located at the hydrogel surface (corona) can be used to activate specific recognition pathways for cellular uptake[23–25]. Clearly, the details of local interactions and spatial partitioning of the drugs in hydrogels will also affect their time-dependent uptake[26] and release kinetics[12].

Therefore, it is of fundamental importance to know the hydrogel-biomolecule interactions implied in the uptake process in order to understand how drugs partition in the hydrogel carrier. In general, this interaction depends on many parameters that involve solvent properties (such as temperature, electrolyte concentration, pH), hydrogel features (e.g., charge distribution, network morphology, hydrophobicity) and properties of the biomacromolecule (e.g., size, shape and charge distribution). In particular, the electrostatic interaction is shown to be one of the most relevant contributions in biomolecule uptake, as, e.g., shown in experiments performed with different types of peptides in the presence of oppositely charged poly(acrylic acid) or poly(acrylamidopropyltriethylammoniumchloride) hydrogels[27–29]. Here, the incorporation is enhanced simply by increasing the peptide charge. Similarly, the encapsulation of Cytochrome C proteins inside oppositely charged hydrogels is also electrostatically driven, leading to a uniform distribution of proteins within the structure[30]. Naturally, salt concentration and pH become then additional factors affecting the uptake process. On the one hand, lowering the electrolyte concentration enhances both the electrostatic interactions and the osmotic repulsion induced by the *free* counterions confined within the hydrogel[18,31]. On the other hand, pH controls the sign (and actually also the distribution) of the charge of the biomacromolecule. Close to the isoelectric point of the latter, for instance, charge regulation can even lead to charge inversion of the protein[32,33].

Additional experimental studies evidence that charged proteins can significantly partition into planar and spherical polyelectrolyte brushes even when they hold the same net charge, at pH conditions far away from the isoelectric point[34–36]. This adsorption 'on the wrong side' is surprising in the sense that, intuitively, proteins are expected to be repelled by electrostatic and excluded-

volume forces. Recent theoretical studies and simulations have shown that this phenomenon can be attributed to the superposition of several interactions. First, proteins and other biomacromolecules usually carry patches of opposite charge sign. The non-uniform, 'multipolar' charge distribution generates an effective dipole moment that interacts asymmetrically with the polyelectrolyte, leading to an attraction that can overcome the electrostatic repulsion[31,37]. Second, due to the larger electrolyte concentration found inside the brush compared to the bulk concentration, there is an attractive Born (self-)electrostatic energy that arises upon insertion into the charged brush[18,31]. Finally, there can be additional attraction related to the release of the condensed counterions in the case of highly charged polyelectrolyte chains: when the protein patches of opposite charge come into contact with the chains, the release of the counterions leads to a large increase of the translational entropy in the system[19,31,35,38]. All these effects are also expected to be present at some extent in the sorption of biomacromolecules to charged hydrogels.

In addition to electrostatic forces, the spatial partitioning of the biomolecule inside the hydrogel will be influenced by other sorts of interactions, such as steric repulsion effects or hydrophobic attractions. Excluded-volume effects, for instance, have been observed in the encapsulation of proteins and peptides when the mean network mesh size is smaller than the size of the biomolecule[21,39]. Hence, the biomolecules are precluded to enter the hydrogel and may tend to adsorb at the surface as the molecular weight of the biomolecule is raised, the cross-linker concentration within the hydrogel increases, or the hydrogel de-swells. Otherwise, the hydrophobic attraction between the incoming biomolecule and the hydrogel can be a very important driving force for some specific macromolecules or drugs. Indeed, increasing both the biomolecule and hydrogel hydrophobicity significantly enhances the sorption to the hydrogel, where the preferential location of the binding depends on the swelling state of the nanoparticle[19,40–44].

The aim of this work is to explore theoretically the conditions that guarantee stable and metastable uptake of biomolecules and, in particular, how the latter spatially partition within the hydrogel (e.g., surface adsorption versus sorption deep inside).

Our analysis is based on a well-defined interaction Hamiltonian[18,26] extended to include dipolar contributions[31] between a non-uniformly charged biomolecule and the charged hydrogel particle. This allows to consider many different types of biomolecules attending to their net charge and dipole moment (charge asymmetry), both controllable by pH. The potential of mean force ex-

erted by the hydrogel as a function to the distance (i.e., the effective interaction Hamiltonian) is determined for different combinations of net charge, dipole moment, bulk salt concentration, and hydrophobic/steric effects. The calculations include the effect of the local variation of the electrolyte concentration from the bulk reservoir to the internal volume of the hydrogel, which has important implications especially for low salt concentrations. We finally summarize in state diagrams where the biomacromolecule uptake is more likely to occur, i.e., classify the results in five different states, namely repulsion (no adsorption), metastable surface adsorption, stable surface adsorption, and partial and full inside sorption.

2   Models and Methods

2.1   Model of the hydrogel and globular biomolecule

The system under study consists of a charged hydrogel particle and a single charged dipolar biomolecule in an aqueous suspension in presence of 1:1 electrolyte at a given bulk concentration c_s^{bulk}. The hydrogel particle is modelled in the swollen configuration as a porous sphere of radius R_h. While several configurations of hydrogel and charge structure may be considered[45–47], as a start, we have kept the problem as simple as possible and we have considered that both neutral monomers and charged groups follow a uniform distribution inside the hydrogel particle, which decreases to zero at the hydrogel interface.

Figure V.1 shows the hydrogel charge distribution for the two salt concentrations studied in this work. Two limiting cases of electrolyte concentration have been considered, namely 'low' and 'high' salt concentration. These regimes are distinguished by the Debye screening length, λ_D, and the intrinsic hydrogel-water interface width, σ. In the low salt limit $\sigma \ll \lambda_D$, so the hydrogel-water interface can be modelled by a sharp edge. On the other hand, in the high salt limit the interface width is large and smoothly decaying. For this we approximate the charge distribution as a error function, so that

$$c_h(r) = \frac{c_h^0}{2} \left[1 - \mathrm{erf}\left(\frac{r - R_h}{\sqrt{2}\,\sigma} \right) \right],\ 0 < r < +\infty. \tag{V.1}$$

The high salt limit will be the relevant one for physiological applications where we will study sorption for the $c_s^{bulk} = 100$ mM case.

The biomolecule is also modelled as a spherical particle of radius R_b, representing for instance a protein globule.
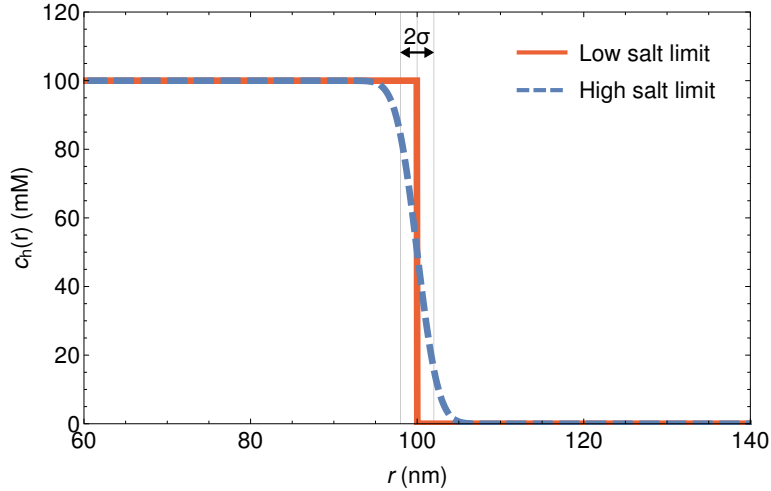
Figure V.1: Model of hydrogel charge distribution in the low and high electrolyte concentration limit for $c_h^0 = 100$ mM and $R_h = 100$ nm.

It is important to notice that charged groups in proteins, peptides and other biomolecules are not usually located in the particle centre and they are not homogeneously distributed either. On the contrary, these discrete charges are often asymmetrically distributed on and inside the molecules, leading to multipolar contributions to the electrostatic potential. To include the multipolar effect, in this work we have modelled the biomolecule as a particle with net charge q_b and an electric dipole moment μ_b that accounts for the heterogeneous charge distribution in leading order. We also assume that the biomolecules are at infinite dilution, that is, we neglect the collective effects that arise from the interaction between biomolecules. Therefore, this study focuses on the sorption and distribution of a single globule.

2.2 Effective interaction Hamiltonian

To calculate the potential of mean force (PMF), i.e., the effective interaction Hamiltonian, between the hydrogel and the dipolar biomolecule, we split the pair interaction in three different phenomenological contributions[18,26,48],

$$V_{total}(r) = V_{elec}(r) + V_{osm}(r) + V_{spec}(r). \tag{V.2}$$

The electrostatic interaction is in turn split into three additive terms, $V_{elec}(r) = V_{mono}(r) + V_{dip}(r) + V_{Born}(r)$. The first one, $V_{mono}(r)$, represents the classical

electrostatic monopole attraction or repulsion due to the net charge of both the hydrogel and the biomolecule. The second term, $V_{\text{dip}}(r)$, accounts for the non-uniformly charge distribution of the biomolecule. We considered the next leading term of the multipolar expansion to get the dipolar contribution. Explicitly, the classical electrostatic interaction up to the dipolar term is given by[49]

$$V_{\text{mono}}(r) + V_{\text{dip}}(r) = z_b y(r) - k_B T \ln \left\{ \frac{\sinh[\widetilde{\mu}_b Y(r)]}{\widetilde{\mu}_b Y(r)} \right\} \tag{V.3}$$

where k_B is Boltzmann constant, T is the absolute temperature of the system, $z_b \equiv q_b/e$ is the biomolecule valency, $y(r) \equiv ze\psi(r)$ is the reduced electrostatic potential calculated by means of the linear Poisson-Boltzmann approximation, $\widetilde{\mu}_b \equiv \mu_b/e$ is the electric dipole moment of the solute and $Y(r) \equiv zeE(r)/k_B T$ is the reduced electric field generated by the charged hydrogel. The electrostatic dipolar term is always attractive because the heterogeneously-charged biomolecule tends to align its dipole with the electrostatic field generated by the charged hydrogel. The third contribution, $V_{\text{Born}}(r)$, is the Born (self-) interaction that characterizes the difference in charging (or solvation) energy when the biomolecule is charged in the bulk or inside the polyelectrolyte network, which contains an effectively larger salt concentration. It is defined as the difference between the solvation energy at r and the solvation energy at bulk, $\Delta V_{\text{Born}}(r) = V_{\text{Born}}(r) - V_{\text{Born}}(r \to \infty)$, being[31,50]

$$V_{\text{Born}}(r) = k_B T \left\{ \frac{\lambda_B z_b^2}{2R_b[R_b\kappa(r) + 1]} + \frac{3\lambda_B \widetilde{\mu}_b^2}{2R_b^3} \frac{[R_b\kappa(r) + 1][(R_b\kappa(r))^2 + 2R_b\kappa(r) + 2]}{[(R_b\kappa(r))^2 + 3R_b\kappa(r) + 3]^2} \right\}, \tag{V.4}$$

where z_b and R_b are the valence and radius of the biomolecule, respectively, $\lambda_B \equiv e^2/4\pi\varepsilon_0\varepsilon_r k_B T$ is the Bjerrum length and $\kappa(r) = \sqrt{4\pi\lambda_B z^2[c_+(r) + c_-(r)]}$ is the local inverse screening length[18]. The first term of equation (V.4) is the classical monopolar result of a sphere in an electrolyte suspension in the Debye-Hückel approximation[50]. The second term is the dipolar expansion for a dipole moment $\widetilde{\mu}_b$ centered in a sphere of radius R_b. Charging the particle inside the hydrogel is always an energy-favorable process due to the larger ionic concentration there, so the difference in Born solvation energy contributes to an attractive hydrogel-biomolecule interaction. Counterion-release effects are neglected in our study.

The second term of the right-hand side of equation (V.2) stands for the ef-

fects of the osmotic pressure due to the confined ions inside the hydrogel,

$$V_{\text{osm}}(r) = k_B T[c_+(r) + c_-(r) - 2c_s^{\text{bulk}}]V_b, \tag{V.5}$$

which depends on the biomolecule volume V_b and on the difference between local number density of free ions ($c_+ + c_-$) inside the polymer network and within the bulk ($2c_s^{\text{bulk}}$). The osmotic pressure always exerts a repulsion on the incoming solute and decreases with electrolyte bulk concentration, given that the biomolecule sorption is hindered by the excess of counterions.

Lastly, with the third term of equation (V.2) we have defined a phenomenological specific potential that accounts for the steric effects and the hydrophobic character of the biomolecule. On the one hand, the partitioning of particles within the hydrogel is always obstructed due to the volume-exclusion exerted by the polyelectrolyte chains of the network. This effect is naturally small for swollen hydrogels and small globules (i.e., nanometer size) but becomes very important when shrinking the hydrogel or increasing the size of the biomolecule. However, this repulsion may be overcome by the attractive interaction that results from the hydrophobic character of the molecule. Indeed, many of the molecules employed in biotechnological applications are significantly hydrophobic and show preferential binding for the polyelectrolyte network rather than the aqueous environment. Both steric and hydrophobic effects are considered in the following mean-field potential

$$V_{\text{spec}}(r) = -k_B T \ln[1 - 2c_p(r)\mathscr{B}_2], \tag{V.6}$$

where $c_p(r)$ is the monomer density of the network and $\mathscr{B}_2$ is the second virial coefficient (or 'interaction' parameter) of the local two-body interaction between a biomolecule and a monomer. This potential can be derived by expanding the corresponding partitioning coefficient $K = \exp(-\beta V_{\rho_m spec}) \simeq 1 + c_p\Gamma$ in powers of the polymer density. The parameter $\Gamma = -2\mathscr{B}_2$ represents the protein-polymer adsorption in the limit of infinite dilution of protein[51]. If the hydrophobicity of the particle is more relevant than the excluded-volume effects, then $V_{\text{spec}}(r) < 0$ and the specific potential will be attractive. Otherwise, if the system exhibits strong excluded-volume effects, the overall specific interaction will be repulsive.

To make an exhaustive discussion of the results we should recall the main features of every potential that contributes to the total PMF and their dependence on q_b and μ_b. First, the electrostatic monopolar contribution is attractive if the hydrogel and the biomolecule are oppositely-charged, repulsive otherwise, and does not depend on the electric dipole moment. Since this contribution is proportional to the electrostatic potential, it reaches its maximum

(absolute) value inside the hydrogel and quickly decreases in the bulk. The electrostatic dipolar term is always attractive and it is coupled to the local electric field. Hence, it becomes especially relevant at the hydrogel surface, where the electrostatic field reaches its maximum value. Since $V_{\text{dip}}(r)$ is the result of the inhomogeneous charge distribution of the biomolecule, it is independent of q_{b} and increases with μ_{b}. Considering the monopolar and dipolar part of Born solvation energy together, their contribution is always attractive and increases with q_{b} and μ_{b}. On the other hand, the osmotic pressure always exerts a repulsive force and does not depend on q_{b} and μ_{b}, but increases as the salt concentration drops.

Lastly, as mentioned above, the specific contribution may be attractive, null or repulsive.

3   Results and discussion

3.1   PMF features and the definition of sorption states

From the shape of the PMF curves is possible to determine the sorption degree and predict where the biomolecule will be preferentially partition. In this work we have distinguished five different sorption states: (1) no adsorption, (2) metastable surface adsorption, (3) stable surface adsorption, and (4) partial and (5) full inside sorption. As an example, in Figure V.2 one PMF is plotted for each state of the system.

- **State 1** corresponds to those cases in which the total PMF is completely repulsive, avoiding any permeation of the molecule within the polyelectrolyte network.

- In **state 2** a local minimum in the repulsive potential located at the hydrogel interface arises. This potential well allows an accumulation of biomolecules, leading to a metastable adsorption onto the hydrogel surface.

- In **state 3** the PMF is repulsive inside the hydrogel, but the local minimum is deep enough to become attractive, the adsorption of the biomolecule in the hydrogel surface is stable.

- In **state 4** the hydrogel-biomolecule interaction potential is also attractive inside the microgel, partitioning of the globules will also significantly happen inside the hydrogel network.

- Finally, in **state 5** no surface adsorption takes place but full inside sorption.
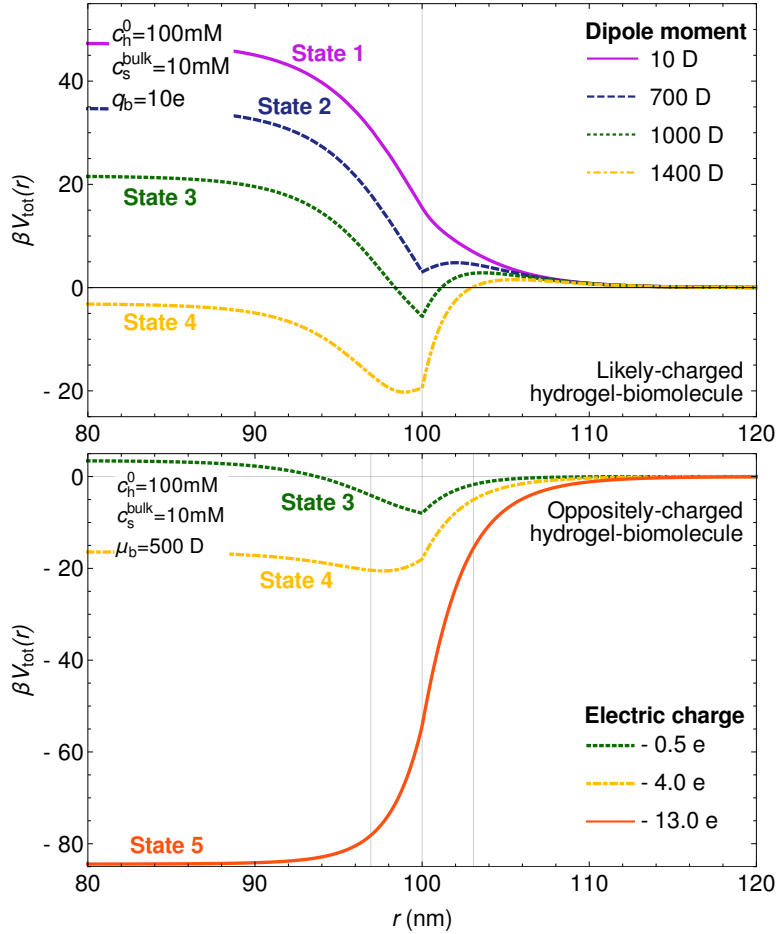
Figure V.2: Potential of mean force in the low salt regime ($c_s^{\text{bulk}} = 10$ mM). Top graph corresponds to a likely-charged biomolecule ($q_b = 10e$) and different values of electric dipole moment μ_b (in Debye units), while bottom graph represents the case of a biomolecule with electric dipole moment $\mu_b = 500$ D and different values of electric charge q_b opposite to that of the hydrogel. These five states are observed in the bottom diagrams of Figure V.3.

3.2   Parameter range

We have studied the sorption states of the system for a large interval of (positive and negative) net charge and electric dipole moment.

From the early experimental works[52], to more recent computational tools working on data of the Protein Data Bank[53,54], we have determined the range of possible values of (μ_b, q_b). In fact, the biomolecule net charge can reach values up to $20e$ (elementary charge units), whereas the dipole moment up to 2000 D (Debye units).

Every sorption state resulting from each combination of (μ_b, q_b) has been plotted in state diagrams.

As mentioned above, the electrolyte concentration has also a determinant effect on the hydrogel-molecule interaction. Therefore, two limiting cases of low and high 1:1 electrolyte concentration have been considered.

In the low salt regime we studied the system at $c_s^{bulk} = 1$ mM and $c_s^{bulk} = 10$ mM, but we observed that in the lowest case the osmotic pressure was so high that no sorption state was achieved in any case. Therefore, in this work we have focused at $c_s^{bulk} = 10$ mM for the low salt regime, while in the high salt limit we have considered $c_s^{bulk} = 100$ mM. In this way, the study of the PMF of oppositely- and likely-charged biomolecules at two salt concentrations leads to four state diagrams. Note that the high salt limit is the relevant one for physiological applications.

In addition, the hydrophobicity of the biomolecules and the volume exclusion exerted by the hydrogel (entering through $V_{spec}(r)$) can also determine the uptake into the polyelectrolyte network. In order to investigate both effects, three different hypothetical frameworks have been analyzed: a system where both the hydrogel exclusion-volume and the biomolecule hydrophobicity are negligible ($V_{spec}(r) = 0$), a system in which the biomolecule hydrophobicity dominates the specific interaction ($V_{spec}(r) < 0$), and a system with high excluded-volume effects ($V_{spec}(r) > 0$). As a result, four state diagrams have been plotted for each one of the three systems in Figures V.3, V.4 and V.5, respectively. A summary of all the other system features is listed in Table V.1.

3.3   Discussion of state diagrams

To begin with, we discuss the general trends of the state diagrams for $V_{spec}(r) = 0$, that is, a system where the hydrogel exclusion-volume is negligible and the biomolecule does not show hydrophobic character (Figure V.3). In these cases, the stable sorption states 4 and 5 are resulting from almost any combination of

Variable	Symbol	Value
Absolute temperature	T	298 K
Hydrogel radius	R_h	100 nm
Hydrogel charge concentration at $r = 0$	c_h^0	100 mM
Width of the hydrogel charge distribution (100 mM)	σ	2 nm
Valence of hydrogel charged groups	Z	1
Valence of ions	z	1
Radius of the biomolecule	R_b	1.5 nm

Table V.1: Summary of the values of the variables in the hydrogel-electrolyte-biomolecule system.

(μ_b, q_b), with the exception of very small values of charge and dipole moment. This is a predictable result, since if the biomolecule electric charge is opposite to that of the hydrogel, all contributions to the total PMF but the osmotic interaction are attractive. Therefore, the repulsion exerted by the osmotic pressure is only relevant when μ_b and q_b are small enough to make the other interactions less dominant. For the lower salt concentration the osmotic pressure is higher because of the larger difference between the neutralizing counterions inside the hydrogel and the counterions in the bulk.

On the other hand, in the case of likely-charged particles, the biomolecule sorption states are more dependent on electrolyte concentration. The osmotic pressure decreases as the ionic bulk concentration increases, so it has a negligible effect on the total PMF at $c_s^{bulk} = 100$ mM. In addition, at this salt concentration the difference in the Born energy is also irrelevant for small values of (μ_b, q_b), although it increases with both variables. Consequently, the sorption state of the biomolecule at high electrolyte concentration is mainly the result of the competition between the electrostatic monopolar repulsion (directly proportional to q_b) and the dipolar attraction (which increases with μ_b). Hence, if the biomolecule net charge is high enough, monopolar repulsion will hinder its permeation deeply into the carrier independently of the electric dipole moment. However, as q_b decreases and μ_b increases, dipolar attraction becomes more relevant, raising the chance of (meta- and stable) interfacial adsorption of the biomolecule, leading to sorption states 2 and 3. In this way, the sorption of the molecule inside the hydrogel (state 4) will be possible when μ_b is high enough to enhance the attraction produced by the difference in Born solvation energy.

Regarding the low electrolyte concentration regime for likely-charged par-

ticles, the sorption state diagram shows less dependence on the electrostatic monopolar repulsion than in the high salt regime. The main reason of this change is that the relevance of both the osmotic pressure and the Born solvation energy in the total PMF increases for low electrolyte concentrations. For instance, at $\mu_b = 1000$ D and $q_b = 10e$, the osmotic contribution in the origin is $V_{osm}^0 \sim 0.25 V_{mono}^0$ and the Born contribution is $\Delta V_{Born}^0 \sim -0.82 V_{mono}^0$ for a salt concentration $c_s^{bulk} = 10$ mM, while in the high salt regime, both contributions are only $V_{osm}^0 \sim 0.04 V_{mono}^0$ and $\Delta V_{Born}^0 \sim -0.27 V_{mono}^0$ at $c_s^{bulk} = 100$ mM. Therefore, although the increase in osmotic pressure enhances the repulsion already dominated by the electrostatic monopolar interaction, the sorption state of the system becomes strongly dependent on the electric dipole moment of the biomolecule by means of both the dipolar and Born attractive interactions. Hence, for small values of μ_b the total PMF is repulsive and no molecule adsorption takes place in the system, with the exception of extreme values of q_b. In the case of very low molecule net charge, the monopolar and osmotic repulsion are not strong enough to prevent stable surface adsorption due to the dipolar attraction and, to a lesser extent, the Born solvation energy contribution. On the other hand, for the highest values of q_b the system exhibits metastable adsorption as a result of the competition between the repulsive monopolar interaction and the attractive Born contribution, given that the electrostatic dipolar interaction does not depend on the biomolecule net charge. Indeed, at high values of q_b the difference in charging energy dramatically increases and can overcome the effect of monopolar repulsion at the hydrogel surface. As the biomolecule electric dipole moment increases, the repulsion due to the electrostatic monopolar interaction and the osmotic pressure remains constant for a given q_b. Therefore, the increase of the dipolar interaction with μ_b at the hydrogel surface and the Born contribution inside the hydrogel network lessen the total PMF, leading first to metastable surface adsorption of the biomolecule, then to stable adsorption, and finally to the partial sorption of the particle inside the hydrogel for the highest values of dipole moment.

Let us now focus on the influence of specific hydrophobic-steric effects. In Figure V.4 we show the state diagrams for likely- and oppositely-charged biomolecules at high and low salt concentrations for a system in which the hydrophobic attraction dominates the specific interaction. In this case, $V_{spec}^0 = -5 k_B T$, in addition to the other contributions discussed above. Therefore, it is expected that the biomolecule sorption is enhanced with respect to the system described in Figure V.3. In fact, we can see that there is always some kind of sorption in the four state diagrams of the hydrophobic system, while the state 1 of no-
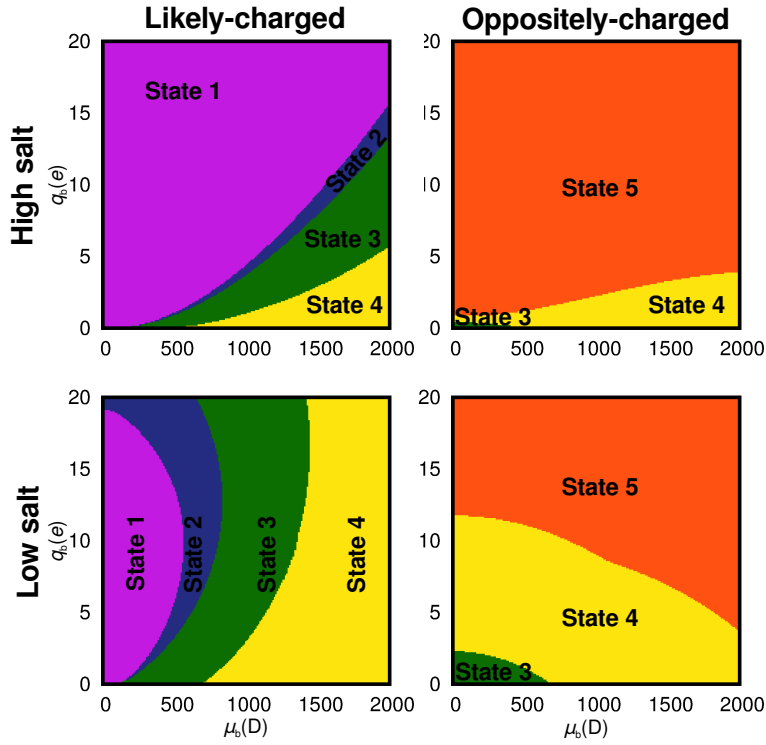
Figure V.3: Phase diagrams in the high and low salt concentration limits and for like-charged (left panels) and oppositely-charged (right panels) hydrogel and biomolecule in a system where steric repulsion is compensated with hydrophobic attraction ($V_{\mathrm{spec}}(r) = 0$).

adsorption never takes place. In particular, for oppositely charged particles, the biomolecule is always sorbed, given that it is highly attracted to the hydrogel. Only for very small values of net charge and dipole moment at low salt concentrations the osmotic pressure is relevant enough to avoid the permeation inside the polyelectrolyte network, leading to a stable adsorption of the biomolecule onto the hydrogel surface.

On the other hand, when the electric charge of the hydrogel and the biomolecule share the same sign, it has been mentioned that the sorption state at high electrolyte concentration is resulting from the interplay between the electrostatic monopolar repulsion and the dipolar attraction. However, in the case of hydrophobic molecules, the monopolar repulsion is overcome by this effective attraction due to the tendency of the particles to exclude water molecules. Hence, the resulting state diagram is highly dominated by the sorption state, although when the biomolecule net charge is high enough, the electrostatic re-

pulsion restricts its sorption to the hydrogel surface, leading to state 3. Similar changes affect the state diagram of likely-charged particles in the low salt concentration regime: the repulsion due to the electrostatic monopolar interaction and the osmotic pressure is not enough to prevent the sorption of the hydrophobic biomolecule. Hence, even for small values of electric dipole moment the molecule experiences a metastable surface adsorption. As μ_b increases, the attraction due to the dipolar interaction at hydrogel surface and the difference in Born solvation energy increases, leading to stable surface adsorption at mid-values of dipole moment and to the inside sorption of the particle for higher values of μ_b.
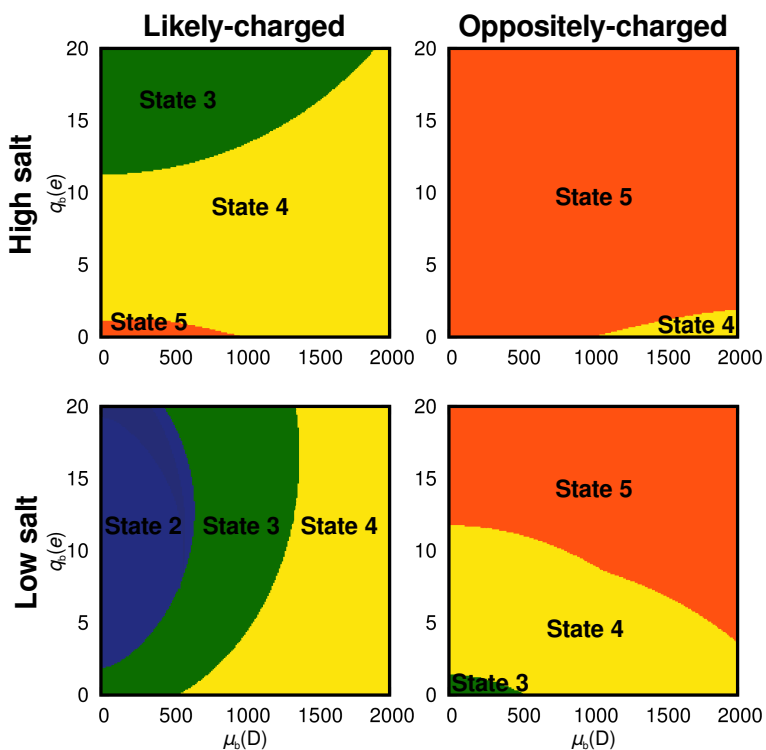

Figure V.4: Phase diagrams in the high and low salt concentration limits and for like-charged (left panels) and oppositely-charged (right panels) hydrogel and biomolecule in a system in which biomolecule hydrophobicity dominates the specific interaction ($V_{spec}(r) < 0$).

Let us finally consider the least favorable case for the biomolecule sorption, that is, a hydrogel with high excluded-volume effects. To represent such a system we have considered a repulsive specific potential with $V_{spec}^0 = 5k_B T$. The

corresponding state diagrams are plotted in Figure V.5, where we can easily see the opposite trend to the one observed in Figure V.4. That is, while in the hydrophobic case the inside sorption states were dominant in most cases, in this situation it looses ground in favour of other hydrogel-biomolecule configurations. Actually, at first sight the four state diagrams are quite similar to those of Figure V.3, with subtle differences. Regarding the oppositely-charged systems, we can see that higher values of net charge are needed to attain the biomolecule sorption inside the polyelectrolyte network. This effect is more remarkable at high electrolyte concentration, where the sorption state of the biomolecule is the result of the competition between electrostatic attraction and steric repulsion. Moreover, for small enough values of net charge and dipole moment, the excluded-volume effects dominate the total hydrogel-biomolecule interaction, avoiding any permeation of the molecule (state 1).

The same tendency is observed for likely-charged biomolecules, especially in the high electrolyte concentration limit, where the total PMF is mainly repulsive due to the joint effect of electrostatic monopolar interaction and steric exclusion. Only for small values of the net charge and high values of the dipole moment, the electrostatic dipolar attraction becomes strong enough to allow meta- and stable surface adsorptions of the biomolecule. In the low salt concentration regime, however, the excluded-volume effects seem to be less relevant in the sorption state diagram of the system, taking into account that it is quite similar to the corresponding diagram at $V_{\mathrm{spec}}^0 = 0$. This is a reasonable result because, in contrast to the high salt regime, when the electrolyte concentration is low the total PMF has a magnitude of tens of $k_{\mathrm{B}}T$. Consequently, a steric repulsion of $V_{\mathrm{spec}}^0 = 5 k_{\mathrm{B}}T$ has little effect on the total interaction potential.

4   Conclusions

The aim of this work was to understand the different mechanisms that are involved in the sorption and spatial distribution of a multipolar biomolecule to a hydrogel particle in presence of a 1:1 electrolyte.

To construct the total potential of mean force (PMF) between the hydrogel and the dipolar biomolecule, different phenomenological contributions were considered, namely electrostatic interaction and Born solvation energy up to the dipolar term of the multipolar expansion, the osmotic pressure contribution, and a specific steric-hydrophobic interaction. From the study of the PMF five sorption states of the system were determined, namely no adsorption, metastable surface adsorption, stable surface adsorption and partial and full inside sorp-
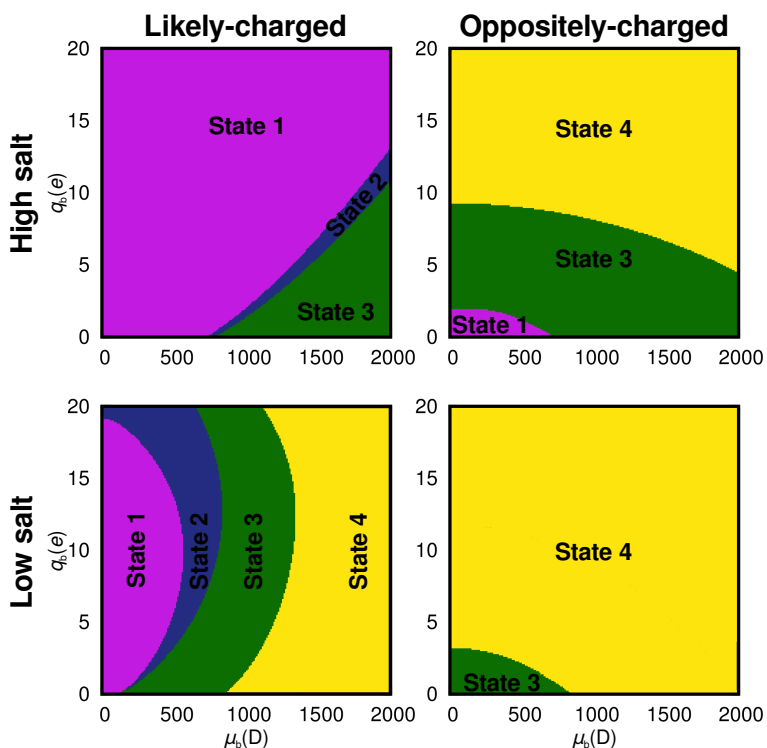
Figure V.5: Phase diagrams in the high and low salt concentration limits and for like-charged (left panels) and oppositely-charged (right panels) hydrogel and biomolecule in a system with high excluded-volume effects ($V_{\text{spec}}(r) > 0$).

tion. The resulting sorption states were compiled in state diagrams as a function of net charge and electric dipole moment, for different electrolyte concentrations and specific hydrogel-biomolecule interactions.

Results show that for oppositely-charged particles, the biomolecule was sorbed inside the polyelectrolyte network for almost every combination of net charge and dipole moment at both high and low salt concentration limits, with the exception of very small values of (μ_b, q_b) and high excluded-volume effects. In those less favorable situations the biomolecule experienced a stable surface adsorption or, just in case of really high steric repulsion, it was not adsorbed.

For likely-charged hydrogel-biomolecule, however, the electrolyte concentration had a determinant effect on the overall configuration of the state diagrams, which showed more variability. At high electrolyte concentration the sorption state of the biomolecule was mainly the result of the interplay between

the electrostatic monopolar repulsion and the dipolar attraction. Consequently, in most cases the biomolecule is precluded by the hydrogel network, except for hydrophobic particles. In the rest of cases high values of the electric dipole moment where needed to achieve some kind of sorption of the molecule. On the other hand, in the low salt regime the adsorption of the biomolecule was subject to a multiple competing interaction mechanisms, being the electric dipole moment the driving variable that leads the system to all the different sorption states, from complete repulsion to full inside sorption.

From this study we can conclude that the electrostatic interaction has a determinant role in the uptake and spatial distribution of charged molecules inside hydrogels, as has been suggested by several authors[27–30]. Although biomolecules of the opposite charge of the hydrogel are more likely to be adsorbed, we have seen that different sorption states can be achieved even for likely-charged biomolecules. *Importantly, the non-uniform charge distribution of the biomolecule leading to large dipoles is a determining factor to take into account, especially when surface adsorption is a focus.* We emphasize again that the protein charge distribution is tuneable by pH. Further, the hydrophobicity of the particle clearly enhances the biomolecule uptake inside the polyelectrolyte network.

In summary, there is no a unique variable which controls the sorption of molecules inside the hydrogel, but a wide range of factors are to consider. The total hydrogel-biomolecule interaction potential is the result of a complex combination of mechanisms that depend on the molecule net charge and electric dipole moment, electrolyte bulk concentration, hydrogel charge, monomer distribution, volume, and hydrophobic character of the particles, among others. Although the complexity of the problem may seem discouraging, we have demonstrated that it is possible to predict the qualitative behaviour of such systems with the help of a relatively simple theoretical framework. Not only discerning whether the molecule is taken up by the hydrogel or not, but determining the place where the particle is located within the carrier particle is crucial for both the encapsulation and release kinetics of the biomolecule and hence hydrogel carrier functionality. Therefore, our work should serve as a useful guide in the development of hydrogel-based carrier systems for biotechnological applications due to its simplicity and effectiveness.

References

[1] Stuart, M. A. C.; Huck, W. T. S.; Genzer, J.; Müller, M.; Ober, C.; Stamm, M.; Sukhorukov, G. B.; Szleifer, I.; Tsukruk, V. V.; Urban, M.; Winnik, F.; Zauscher, S.; Luzinov, I.; Minko, S. *Nat. Mater.* **2010**, *9*, 101–113.

[2] Murray, M.; Snowden, M. *Adv. Colloid Interface Sci.* **1995**, *54*, 73–91.

[3] Saunders, B. R.; Laajam, N.; Daly, E.; Teow, S.; Hu, X.; Stepto, R. *Adv. Colloid Interface Sci.* **2009**, *147-148*, 251–62.

[4] Fernandez-Nieves, A.; Wyss, H. M.; Mattsson, J.; Weitz, D. A. *Microgel Suspensions: Fundamentals and Applications*; Wiley-VCH: Weinheim, 2011; p 461.

[5] Tanaka, T.; Fillmore, D. J. *J. Chem. Phys.* **1979**, *70*, 1214–1218.

[6] Longo, G. S.; Olvera de la Cruz, M.; Szleifer, I. *J. Chem. Phys.* **2014**, *141*, 124909–10.

[7] Frokjaer, S.; Otzen, D. E. *Nat Rev Drug Discov* **2005**, *4*, 298–306.

[8] Malmsten, M. *Soft Matter* **2006**, *2*, 760–769.

[9] Ghugare, S. V.; Mozetic, P.; Paradossi, G. *Biomacromolecules* **2009**, *10*, 1589–1596.

[10] Vinogradov, S. V. *Nanomedicine* **2010**, *5*, 165–8.

[11] Bae, K. H.; Wang, L.-S.; Kurisawa, M. *J. Mater. Chem. B* **2013**, *1*, 5371–5388.

[12] Kim, S. W.; Bae, Y. H.; Okano, T. *Pharm. Res.* **1992**, *9*, 283–290.

[13] Malmsten, M.; Bysell, H.; Hansson, P. *Curr. Opin. Colloid Interface Sci.* **2010**, *15*, 435–444.

[14] Ramos, J.; Imaz, A.; Callejas-Fernández, J.; Barbosa-Barros, L.; Estelrich, J.; Quesada-Pérez, M.; Forcada, J. *Soft Matter* **2011**, *7*, 5067–5082.

[15] Ramos, J.; Forcada, J.; Hidalgo-Alvarez, R. *Chem. Rev.* **2014**, *114*, 367–428.

[16] Lesher-Perez, S. C.; Segura, T.; Moraes, C. *Integr. Biol.* **2016**, *8*, 8–11.

[17] Blackburn, W. H.; Dickerson, E. B.; Smith, M. H.; McDonald, J. F.; Lyon, L. A. *Bioconjugate Chem.* **2009**, *20*, 960–968.

[18] Yigit, C.; Welsch, N.; Ballauff, M.; Dzubiella, J. *Langmuir* **2012**, *28*, 14373–14385.

[19] Welsch, N.; Lu, Y.; Dzubiella, J.; Ballauff, M. *Polymer* **2013**, *54*, 2835–2849.

[20] Cedervall, T.; Lynch, I.; Lindman, S.; Berggard, T.; Thulin, E.; Nilsson, H.; Dawson, K. A.; Linse, S. *Proc. Natl. Acad. Sci. U.S.A.* **2007**, *104*, 2050–2055.

[21] Garrett, Q.; Chatelier, R. C.; Griesser, H. J.; Milthorpe, B. K. *Biomaterials* **1998**, *19*, 2175–86.

[22] Johansson, C.; Gernandt, J.; Bradley, M.; Vincent, B.; Hansson, P. *J. Colloid Interface Sci.* **2010**, *347*, 241–51.

[23] Giudice, M. C. L.; Herda, L. M.; Polo, E.; Dawson, K. A. *Nat. Commun.* **2016**, *7*, 13475.

[24] Shaw, C. A.; Mortimer, G. M.; Deng, Z. J.; Carter, E. S.; Connell, S. P.; Miller, M. R.; Duffin, R.; Newby, D. E.; Hadoke, P. W.; Minchin, R. F. *Nanotoxicology* **2016**, *10*, 981–991.

[25] Schöttler, S.; Becker, G.; Winzen, S.; Steinbach, T.; Mohr, K.; Landfester, K.; Mailänder, V.; Wurm, F. R. *Nat. Nanotechnol.* **2016**, *11*, 1–6.

[26] Angioletti-Uberti, S.; Ballauff, M.; Dzubiella, J. *Soft Matter* **2014**, *10*, 7932–45.

[27] Bysell, H.; Schmidtchen, A.; Malmsten, M. *Biomacromolecules* **2009**, *10*, 2162–2168.

[28] Bysell, H.; Malmsten, M. *Langmuir* **2009**, *25*, 522–8.

[29] Hansson, P.; Bysell, H.; Månsson, R.; Malmsten, M. *J. Phys. Chem. B* **2012**, *116*, 10964–10975.

[30] Smith, M. H.; Lyon, L. A. *Macromolecules* **2011**, *44*, 8154–8160.

[31] Yigit, C.; Kanduc, M.; Ballauff, M.; Dzubiella, J. *Langmuir* **2017**, *33*, 417–427.

[32] Biesheuvel, P. M.; Wittemann, A. *J. Phys. Chem. B* **2005**, *109*, 4209–4214.

[33] Lund, M.; Jo, B. *Langmuir* **2005**, *21*, 8385–8388.

[34] Wittemann, A.; Haupt, B.; Ballauff, M. *Phys. Chem. Chem. Phys.* **2003**, *5*, 1671–1677.

[35] Wittemann, A.; Ballauff, M. *Phys. Chem. Chem. Phys.* **2006**, *8*, 5269–5275.

[36] Ballauff, M.; Borisov, O. *Curr. Opin. Colloid Interface Sci.* **2006**, *11*, 316–323.

[37] Hu, Y.; Cao, D. *Langmuir* **2009**, *25*, 4965–4972.

[38] Leermakers, F. A. M.; Ballauff, M.; Borisov, O. V. *Langmuir* **2007**, *23*, 3937–3946.

[39] Bysell, H.; Malmsten, M. *Langmuir* **2006**, *22*, 5476–5484.

[40] Kawaguchi, H.; Fujimoto, K.; Mizuhara, Y.; Science, P. *Colloid Polym. Sci.* **1992**, *270*, 53–57.

[41] Lord, M. S.; Stenzel, M. H.; Simmons, A.; Milthorpe, B. K. *Biomaterials* **2006**, *27*, 1341–1345.

[42] Lord, M. S.; Stenzel, M. H.; Simmons, A.; Milthorpe, B. K. *Biomaterials* **2006**, *27*, 567–575.

[43] Bysell, H.; Hansson, P.; Malmsten, M. *J. Phys. Chem. B* **2010**, *114*, 7207–7215.

[44] Bysell, H.; Hansson, P.; Schmidtchen, A.; Malmsten, M. *J. Phys. Chem. B* **2010**, *114*, 1307–1313.

[45] Daly, E.; Saunders, B. R. *Langmuir* **2000**, *16*, 5546–5552.

[46] López-León, T.; Ortega-Vinuesa, J. L.; Bastos-González, D.; Elaïssari, A. *J. Phys. Chem. B* **2006**, *110*, 4629–36.

[47] Geisel, K.; Rudov, A. A.; Potemkin, I. I.; Richtering, W. *Langmuir* **2015**, *31*, 13145–

54.

[48] Yigit, C.; Kanduc, M.; Ballauff, M.; Dzubiella, J. *Langmuir* **2016**, *33*, 417–427.

[49] Hill, T. L. *Introduction to Statistical Thermodynamics*; Dover: New York, 1986; p 461.

[50] McQuarrie, D. A. *Statistical Mechanics*; Harper & Row: New York, 1976.

[51] Shulgin, I. L.; Ruckenstein, E. *J. Phys. Chem. B* **2008**, *112*, 1465–1467.

[52] Oncley, J. L. *Chem. Rev.* **1942**, *30*, 433–450.

[53] Felder, C. E.; Prilusky, J.; Silman, I.; Sussman, J. L. *Nucleic Acids Res.* **2007**, *35*, W512–21.

[54] Berman, H. M.; Westbrook, J.; Feng, Z.; Gilliland, G.; Bhat, T. N.; Weissig, H.; Shindyalov, I. N.; Bourne, P. E. *Nucleic Acids Res.* **2000**, *28*, 235–242.

Thermoresponsive microgels at the air-water interface: impact of swelling state on interfacial conformation

J. Maldonado-Valderrama[*], T. del Castillo-Santaella[*], I. Adroher-Benítez[*],
A. Moncho-Jordá[*†], and A. Martín-Molina[*]

[*]Departamento de Física Aplicada, Facultad de Ciencias, Universidad de Granada, Avenida Fuentenueva 2, 18001, Granada, Spain
[†]Instituto Carlos I de Física Teórica y Computacional, Universidad de Granada, Avenida Fuentenueva 2, 18001, Granada, Spain

Abstract

Poly(N-vinylcaprolactam) (PVCL) is a new temperature-responsive type of polymer microgel with improved biocompatibility as compared to more commonly used poly(N-isopropylacrylamide) (PNIPAM). Both polymers swell at low temperatures and collapse at high ones, showing a Volume Phase Transition Temperature (VPTT) around the physiological temperature. Exploring the interfacial characteristics of thermoresponsive microgels is important due to their potential application in emulsions based systems with tailored stability and controlled degradation profile. In this work, we study the properties of charged PVCL particles at the air-water interface by combination of adsorption, dilatational rheology and Langmuir monolayers. Although PVCL particles adsorb spontaneously at the air-water interface in both, swollen and collapsed conformations, the interfacial properties show significant differences depending on the swelling state. In particular, the total amount of adsorbed microgels and the rigidity of the monolayer increase as the temperature raises above the VPTT, which is connected to the more compact morphology of the microgels in this regime. Dilatational rheology data shows the formation a very loose adsorbed layer with low cohesivity. In addition, collapsed microgels yield a continuous increase of the surface pressure, whereas swollen microgels show a phase transition at intermediate compressions caused by the deformation of the loose external polymer shell of the particles. We also provide a qualitative interpretation for the surface pressure behavior in terms of microgel-microgel effective pair potentials, and correlate our experimental findings to recent rescaling models that take into account the importance of the internal polymer degrees of freedom in the rearrangement of the conformation of the microgel particles at the interface.
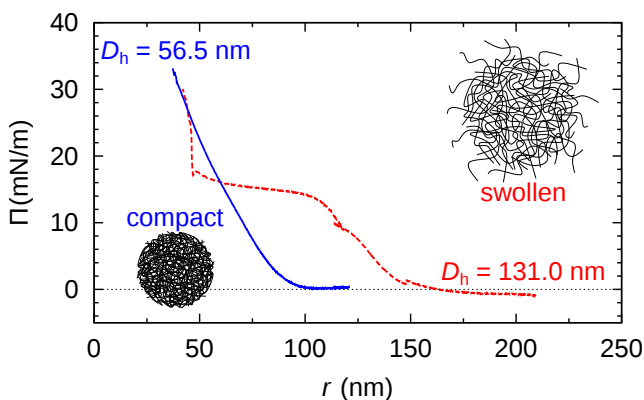
1 Introduction

Polymer gels are among the most attractive and versatile soft materials. They are present in many everyday products including food and pharmaceutical industry. Polymer gels typically contain large amounts of liquid confined within a flexible network of polymer chains or colloidal particles.[1] Among the different types of gels, all with different properties and applications, microgels are sub-micrometer sized cross-linked polymer particles that can carry or incorporate macromolecules in their network structure. This property, coupled with their "soft" character and the ability to introduce stimuli-responsive characteristics, means that they have many attractive applications, including drug delivery.[2,3] The choice of stimuli depends on the application, being thermoresponsive microgels the most frequently investigated since their small size enables them to develop a rapid kinetic response to temperature changes.[4] In particular, thermoresponsive microgels showing a volume phase transition temperature (VPTT) near physiological temperature, have been investigated lately. Microgels based on biocompatible and temperature-sensitive polymers having a lower critical solution temperature (LCST) around 32°C in aqueous solutions swell at low temperatures and collapse at high ones.

Since 1986 there have been many publications describing the preparation, characterization and application of temperature sensitive microgels from an experimental point of view[3,5–10] as well as their physical properties by theories and simulations.[8,9,11–21] Amongst all the temperature-sensitive polymer microgel systems the ones based on Poly-N-Isopropylacrylamide (PNIPAM), are the most widely studied. PNIPAM microgels are considered to be "smart" or "switchable" materials having the VPTT close to physiological temperature. This means that they have the potential as an intelligent drug delivery vehicle where the release of an active agent or drug can be triggered by changes in temperature. This can be used by simple contact, for example, in transdermal delivery systems via our skin.[22] In addition to their ability to change conformation with temperature, PNIPAM microgels adsorb onto fluid/fluid interfaces due to their surface activity (i.e. lower the surface tension of water).[22–36] In general, the adsorption and self-assembly of microgel particles at fluid interfaces has been a topic of study for many researchers for the past few years providing many interesting challenges (see[37–39] and references cited therein). The behaviour of polymeric particles lies in between that of colloidal particles and soft polymers while the adsorbed state provides an anisotropic media which affects their morphology and interactions. These facts, in addition to their temperature responsive na-

ture, make of these soft particles potential candidates as Pickering stabilizers for emulsions with tunable stability.[30] Therefore, understanding the adsorption behavior of soft PNIPAM microgels onto fluid interfaces has become increasingly important both in terms of fundamental science and applications of microgels as multi-stimuli responsive emulsion stabilizers.[23] However, despite the increasing number of studies on adsorbed layers of PNIPAM-based microgels reported in the literature, the properties of the adsorbed state and the link with emulsion stability is still not well understood yet.[35]

Recently, Geisel and coworkers have found differences between Gibbs monolayers, where particles spontaneously adsorb in the presence of excess in the bulk, and Langmuir monolayers, where a fixed amount of particles is spread at the interface. Although both routes offer in principle the possibility to tune the microstructure of the interface, they demonstrate that Langmuir monolayer is much more effective technique for the fabrication of 2D ordered microgel arrays, where the interparticle separation can be easily tuned by changing the surface pressure.[32,33] Pinaud and coworkers have related interfacial properties of PNIPAM microgels to their conformation and packing at a model oil-water interface.[35] Therein, the authors propose a model for the microgel deformation and packing at the interface during compression comprised by various packing states in the Langmuir film for PNIPAM microgels. For their part, Zielińska and coworkers, have recently provided valuable information concerning the structure of the adsorbed microgel layer by neutron reflectivity. They prove that PNIPAM microgels form more complex structures at the interface, which have to date not been resolved.[22] The specific impact of temperature (swelling state) on the surface conformation has also been addressed is some detail by various authors.[23,27,40,41] However, a systematic interfacial study including kinetics, adsorption isotherms, dilatational rheology and Lanmguir films has not been actually performed so far.

Another issue is that the use of PNIPAM as a biomaterial may be limited because of its high cytotoxicity and its low cell viability. In this sense, temperature-sensitive polymer microgel based on poly(N-vinylcaprolactam (PVCL) appears as an alternative to PNIPAM-based microgels.[6] PVCL polymers are especially interesting due their stability against hydrolysis and biocompatibility. In fact, it has been recently shown that PVCL-based microgels are more biocompatible than traditional microgels based on PNIPAM and therefore, more suitable for bio-applications.[6] The development of PVLC requires a better understanding of the complex dynamic structure of such micromaterials and currently there is a lack of experimental data about how these materials actually behave at inter-

faces. With the exception of Wu and coworkers who focus on the properties of mixed PVCL and PNIPAM at the interface. [40]

In this work we have used PVCL based charged microgel and carried out a complete surface characterisation including kinetics, adsorption isotherms, dilatational rheology and Langmuir monolayers. Such a complete interfacial study has not been attempted before on PVCL and we hence show for the first time the conformational changes undergone at the air-water interface. We evaluate the synergism with the temperature deformation and provide important new aspects on the interfacial properties of PVCL. Understanding the behaviour of microgels at interfaces will enable the rational design of emulsion based systems for targeted delivery of drug administration.

2 Experimental

2.1 Materials

Poly(N-vinylcaprolactam)-based microgel (PVCL) was synthesized by emulsion polymerization in a batch reactor. The original protocol was developed by Imaz and Forcada. [42] The monomer N-vinylcaprolactam (VCL, Sigma-Aldrich); the crosslinker, poly(ethylene glycol) diacrylate (PEGDA 200, Polysciences); the anionic initiator, potassium persulfate (KPS, Sigma-Aldrich); the buffer, sodium bicarbonate (NaHCO$_3$, Sigma-Aldrich), and the emulsifier, sodium dodecyl sulfate (SDS, Sigma-Aldrich) were used as supplied with concentrations in Table VI.1. An the ionic comonomer, acrylic acid (AA, Sigma-Aldrich), was used to confer charge to the resulting microgel particles. The reaction mixture was heated at 70°C, stirred at 300 rpm agitation rate, and purged with nitrogen for 1 h before starting the polymerization. After adding the initiator, the reaction was allowed to continue under nitrogen atmosphere while stirring and a shot of AA was added in the reaction medium after 30 min of reaction. Once the reaction was finished (5 h) the reaction mixture was subsequently cooled to 25°C, whilst maintaining the stirring and nitrogen flow to prevent possible aggregation. The final dispersion was filtered through glass wool, and cleaned by dialysis (Spectra/Por Dialysis Membrane. Molecular weight cut off: 12,000–14,000 Da) at room temperature. The water was exchanged every 12 h and dialysis was allowed to run until the dialysate reached a conductivity and surface tension values close to those of pure water (2 μS/cm and 70 mN/m) The concentration of the final PVLC microgel suspension was 0.662% (w/w).

Dispersions of microgels were prepared by dilution in ultrapure water fol-

Function	Compound	% w/w
Monomer	VCL	1.0126
Ionic comonomer	AA	0.0798
Crosslinker	PEGDA	0.0400
Initiator	KPS	0.0100
Buffer	$NaHCO_3$	0.0103
Emulsifier	SDS	0.0400

Table VI.1: Concentration of reactants used in PVCL microgel synthesis

lowed by mixture of the solution in vortex for 1 min. All measurements were made in ultrapure water at different temperatures. For the preparation of buffer solutions, the cleaning is carried out by dialysis against deionized water (Milli-Q Academic, Millipore, France). All glassware was washed with 10% Micro-90 cleaning solution and exhaustively rinsed with tap water, isopropanol, deionized water, and ultrapure water in this sequence. All other chemicals used were of analytical grade and used as received.

2.2 Methods

The hydrodynamic diameter (D_h) of the microgel in solution was measured by means of Dynamic Light Scattering (DLS) technique with Zetasizer Nano ZS system from Malvern Instruments. The hydrodynamic diameters were calculated from the diffusion coefficient using the Stokes-Einstein equation. The self-optimization routine and correlogram analysis provided by the software was used for all measurements. Samples were diluted 1:20 in ultrapure water. Measurements were taken every 2°C, ranging from 20°C to 54°C, in order to consider the whole range of sizes of the microgels. At each temperature, we waited two minutes to equilibrate each sample and then we took three measurements. The deviation was found to be less than 2% and final values are plotted as mean values of replicates, with standard deviations obtained according to statistical analysis tools.

Adsorption/desorption and dilatational rheology measurements were made in the OCTOPUS (WO2012080536-A1). This is a Pendant Drop Surface Film balance implemented with subphase multi exchange device.[43] The OCTOPUS is fully automated by computer software DINATEN® and CONTACTO®. The detection and calculation of surface area and surface tension are based on axisymmetric drop shape analysis (ADSA). The pendant drop is placed on a three-axis micropositioner and is immersed in a glass cuvette (Hellma®) which is kept in

an externally thermostated cell, which was varied from 20°C–55°C during the experiments. The adsorption/desorption curves comprised three steps: adsorption, dilatational rheology and desorption. A microgel solution droplet is formed at the tip of the double capillary and the surface tension is recorded at constant surface area. Then, we measure the dilatational rheology of the surface by applying an oscillatory perturbation to the surface, by injecting and extracting volume into the pendant drop. The system records the response of the surface tension to this area deformation, and the dilatational modulus (E) of the interfacial layer is calculated from this response. In a general case, the dilatational modulus is a complex quantity that contains a real and an imaginary part

$$E = E' + iE'' = \epsilon + i\nu\eta \qquad (VI.1)$$

E' is the storage modulus that accounts for the elasticity of the interfacial layer (ϵ), E'' is the loss modulus that accounts for the viscosity (η) of the interfacial layer, and $\nu = 0.1$ Hz is the angular frequency of the applied oscillation. In this work, the applied oscillations in interfacial area were maintained at amplitude values lower than 5%, to avoid excessive perturbation of the interfacial layer. After re-equilibration of the surface, we measure the desorption profile. This is done exchanging the bulk subphase by that of pure water at least 50 times the volume of the drop. We record the evolution of the surface tension while the subphase exchange proceeds until the surface tension is not affected by further subphase exchanges and a new steady state is reached.[43]. Finally, we monitor the surface tension at constant surface area (20 mm^2) for 1 h. The pendant drop volume and surface area is preserved during the whole desorption profile. Adsorption/desorption curves were carried out in triplicate at temperatures: 20, 30, 37, 45, 50 and 55°C and a fixed concentration of 0.02% (w/w). The deviation was found to be less than 2% and final values are plotted as mean values of replicates, with standard deviations according to statistical analysis tools.

Langmuir monolayers were measured using a Langmuir Film balance equipped with paper Wilhelmy plate pressure measuring system (KSV) with a sensitivity of 0.1 mN/m and total area 244.5 cm^2. The whole setup is located in a transparent Plexiglas case to avoid air streams and dust deposition connected to a thermostat. The system records the evolution of the surface pressure (Π) as the available surface is compressed. The surface pressure is defined as $\Pi = \gamma_0 - \gamma$, being γ_0 the surface tension of the pure water surface. The absence of surface active contaminants was verified by compressing the bare water subphase, obtaining values of $\Pi < 0.2$ mN/m within the whole compression cycle. The Π-A isotherms were recorded at two temperatures well below and above the tran-

sition temperature of the microgels, namely 20°C and 45°C respectively. The samples were incubated at the required temperature for 15 min before spreading. Then, the microgel solution (0.5 g/l in pure water) was carefully spread on the subphase by means of a microsyringe (Hamilton®). After an equilibration time of 15 min, we record the surface pressure-area (Π-A) isotherm upon symmetric uniaxial compression at a constant rate of 5 mm/min. Various amounts of solution (50–200 μl) were spread in different experiments to cover the whole compression isotherm at 20°C while 300 μl were spread to obtain the isotherm at 45°C. The number of measurements needed was determined depending on the variability of the results and standard deviations obtained. In particular, 3 replicates were needed for the measurements at 45°C, where deviation was found to be less than 2%, whereas 6 repetitions were needed at 20°C, where deviations ranged from 2 to 8%.

3   Results and discussion

3.1   Swelling behavior

The PVCL charged microgels were first characterized by dynamic light scattering (DLS) to determine their average size, the temperature dependence of the hydrodynamic diameter (D_h), the temperature range of the volume phase transition (VPTT) and the swelling ratio. Fig. VI.1 depicts the average hydrodynamic diameter of the microgels as a function of temperature. The polydispersity has been calculated by light scattering and the results shown as error bars. As observed, D_h remains constant at temperatures below 20°C and above 40°C. The VPTT lies around 32°C in close agreement with literature values.[42] The hydrodynamic diameter of the microgels decreases from 131±3 nm to 56.5±0.5 nm, when the temperature increases from 20°C to 40°C, indicating that the internal volume fraction of the microgels increases with raising temperature. The values are in agreement with those reported in the literature[40,42], and fall within the nanometric scale. The swelling ratio depends fundamentally on the amount of crosslinker used in the synthesis and despite the differences in size the swelling ratio obtained for PVLC based microgels is similar to that reported for PNIPAM based microgels with the same amount of crosslinker.[6,40] The variation of temperature induces a change in the hydrophilic/hydrophobic balance of microgels, which leads to a variation in size. The collapse of microgel particles is due to the destruction of hydrogen bonds in the structure of the microgel as the temperature rises above the VPTT. This induces the increase of hydropho-

bic attractions between polymer chains, leading to the exclusion of water and consequently, to the shrinking of the microgels.[13] The PVCL microgel synthesized and used in this work also contains a significant amount of AA (Table VI.1) which provides the microgel with surface charge.[42] Most of the studies in the literature deal with neutral PNIPAM microgels, and this also will possibly make a difference in the characterization.[6]
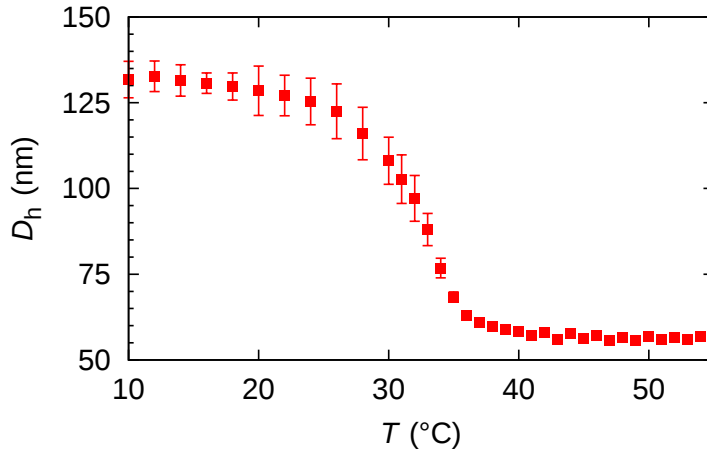

Figure VI.1: Hydrodynamic diameter of PVCL microgels as a function of temperature.

Fig. VI.2 illustrates the SEM images of the PVLC microgels. As observed, particles are approximately circular in appearance. The SEM images illustrate the diameter of the dehydrated particle. The values obtained for the diameter in the SEM images practically coincide with those obtained for the compact microgel in Fig. VI.1, corresponding to dehydrated particle.

3.2 Gibbs monolayer: dynamics, adsorption and surface rheology

Fig. VI.3 shows the dynamic adsorption curves of the microgel solution at a fixed concentration of 0.02% w/w recorded at different temperatures below and above the VPTT. In all cases the surface tension decreases with time and eventually attains a plateau. The adsorption of microgels at the air-water interface involves two process: diffusion of particles towards the interface followed by a much slower reconfiguration of the microgels at the surface.[24,34,40] In Fig. VI.3 we observe clearly these two distinct adsorption regimes, similar to the adsorption of concentrated solutions of surfactants and proteins.[44] The dynamic curves comprise a first stage with a sharp decline of the surface tension followed by
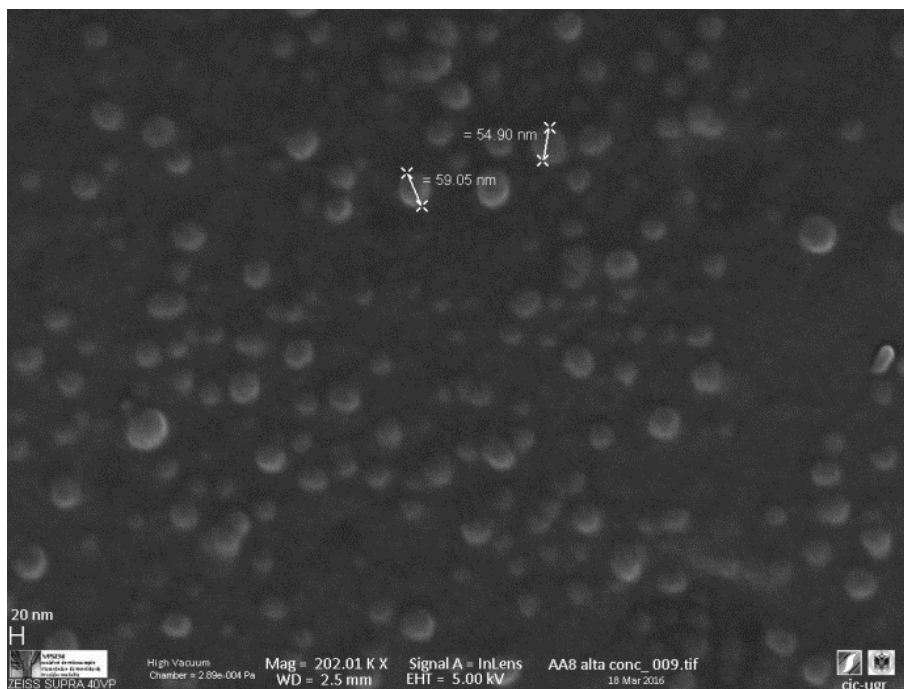
Figure VI.2: Images obtained with a Zeiss SUPRA 40VP Field Emission Scanning Electron Microscope (SEM).

a second stage in which the variation is much less pronounced. The first adsorption stage is in general size dependant and the decreasing slope illustrates the diffusion of particles onto the air-water interface.[24] The second stage is the result of balancing the hydrophobic and hydrophilic moieties to minimize the free energy at the surface (unfolding of polymer chains to optimal conformation). These general trends agree with the dynamic adsorption curves of PNIPAM based microgel solutions published elsewhere.[24,34,40] There are however, no reported results of dynamic adsorption of PVCL microgel solutions in the literature.

The adsorption kinetics of PVLC based microgels in Fig. VI.3 show similar slopes in the first regime, indicating similar diffusion rates below and above the VPTT. Instead, the impact of temperature appears more evident in the final surface tension attained after the sharp decline, which is higher above the VPTT. Accordingly, this is an indication of a higher number of particles reaching the surface at a rather similar rate as the temperature increases in the sys-
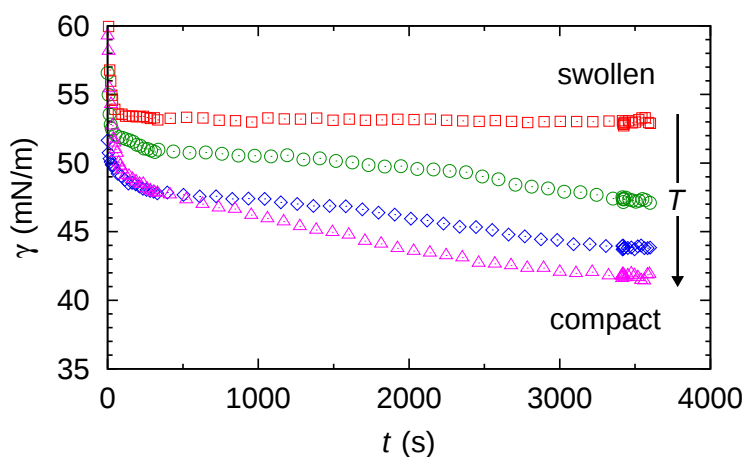
Figure VI.3: Dynamic surface tension of 0.02% w/w PVLC microgel adsorption onto the air-water interface. Squares: 20°C, rhomboids: 30°C, triangles: 45°C, circles: 55°C.

tem; namely, as the microgel particles are more compact. This correlates with Zielińska and coworkers data, who reported that the amount of particles adsorbed at the air-water interface increases for more crosslinked microgels.[22] Hence, the more compact structure of the microgels above the VPTT allows accommodation of a higher number of particles and a more efficient packing at the interface. The quasi-equilibrium regime shows that the surface tension reduces slightly over time accounting for surface deformation of the microgels upon adsorption. However, it is difficult to assess the differences between swollen and collapsed states as the high concentration of the surface layer counteracts the different deformability of the nanoparticles below and above the VPTT. This will be analyzed in more detail later on in this paper. Also, the structural changes induced in the particles by surface conformational changes will be addressed specifically in the monolayer study.

After adsorption at constant surface for 1 h and once a stationary state is clearly reached (Fig. VI.3), we replaced the bulk subphase with pure water by using the subphase exchange accessory. We observed no change of surface tension during, or after, the subphase exchange (results not shown). Thus, we can conclude that microgels do not spontaneously desorb from the air-water interface after adsorption. Similar results were obtained by Pinaud and coworkers for PNIPAM microgels at the dodecane-water interface.[35] These are important findings supporting the conformational change undergone by microgels upon adsorption and the stability of the adsorbed layers. Moreover, the formation

of stable layers at the air-water interface also allows the use of Langmuir Film Balance to study the monolayers of PVLC microgels.
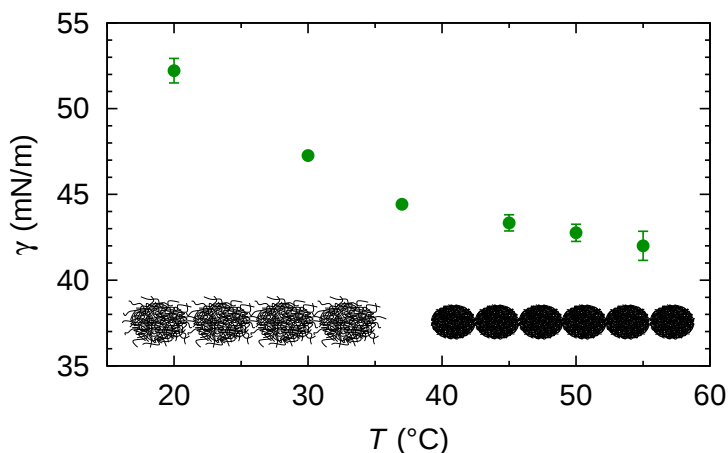

Figure VI.4: Variation of the quasi-equilibrium surface tension with temperature (1 h adsorption) for PVLC microgels adsorbed layers at the air-water interface (0.02% w/w).

Fig. VI.4 shows the quasi-equilibrium surface tension values obtained for PVLC microgels as a function of temperature. As predicted from the dynamic curves in Fig. VI.3, the final surface tension, after 1 hour adsorption at constant surface area, decreases with temperature. Specifically, below the VPTT, the values decrease significantly while reach a quasi-plateau after the VPTT. Wu and coworkers found a similar plateau for PVLC particles at the toluene-water interface.[40] At T < VPTT, the swollen microgel particles are very deformable and reorient the hydrophobic moieties towards the air phase so as to cover the interface as much as possible. Recent neutron reflectivity experiments clearly show that swollen microgels confined at the air-water interface adopt a core-shell structure, with a highly crosslinked central region surrounded by a more diluted shell of polymer chains that spread out at the interface and towards the bulk solution.[22] These morphological changes of the particles at the surface, lead then to connections between adjacent particles forming a loose surface layer.[26] Conversely, at T > VPTT, the collapsed microgel particles are less deformable and more rigid. Accordingly, the maximum coverage of the surface is achieved at a higher number of particles and a closer packing density, resulting in a more compact surface layer. This agrees with findings from ellipsometry[41] and neutron reflectivity[22] for PNIPAM based microgels, showing the increase in adsorption density as the microgel collapses. Moreover, this explains the lower

surface tension reached above the VPTT in Fig- VI.4. The morphology of the adsorbed layers is illustrated schematically in Fig- VI.4. Namely, a loosely packed layer composed of swollen microgel particles is formed bellow the VPTT and a more condensed layer with higher density is formed above the VPTT.

The interfacial behavior of PVLC microgel particles differs from that of PNIPAM microgel particles reported in the literature. PNIPAM particles present a minimum value of interfacial tension around the VPTT rather than the plateau shown for PVLC particles.[27,40] The increase interfacial tension for temperatures above the VPTT is attributed in the literature to the formation of loose aggregates[27], the possible existence of a surface gel[41] or the formation of a loosely packed microgel[35]. Anyhow, this increase at high temperatures accounts for the lower stability of PNIPAM emulsions above the VPTT. These differences between PNIPAM and PVCL adsorbed layers have been also reported by Wu and coworkers at the toluene/water interface[40], but these authors do not provide an explanation for this different behavior. Nonetheless, the constant value of surface tension above the VPTT for PVLC microparticles suggests the formation of a more stable surface layer on emulsified systems than PNIPAM. On the one hand, this stability could be attributed to the enhanced electrostatic repulsion between the immerse parts of the microgels, which arises when the microgel shrinks. Indeed, charged microgels show a larger effective charge in the shrunken state due to the steric exclusion of the excess counterions from the internal region exerted by the crosslinked polymer network.[45,46] On the other hand, the higher condensing ratio of PVLC microgels[6] could result in a better packing at the surface resulting in a more stable conformation, resistant to aggregation above the VPTT. Brugger et al., concluded that the presence of charges strongly influences the behavior of charged PNIPAM-co-MAA microgels at oil-water interfaces.[26] In particular, the authors showed how the deprotonation of the MAA moieties leads to local amphiphilicity that affects the chain conformation. Moreover, the comparison between the compression isotherms of charged and uncharged microgels indicate that increasing the number of charges in the microgel does not lead to emphasized electrostatic repulsion. Instead, it causes a significant reduction of the surface pressure, which has been attributed to the highest softness of the charged microgels.[32] In this sense, some authors points out that the unexpected influence of charges on the compression behaviour of microgel-covered oil-water interfaces has not been explained in detail yet.[35] Accordingly, this is an important issue that can have implications for emulsion development and will be explored in a future work.

In order to further explore the characteristics of adsorbed layers of micro-
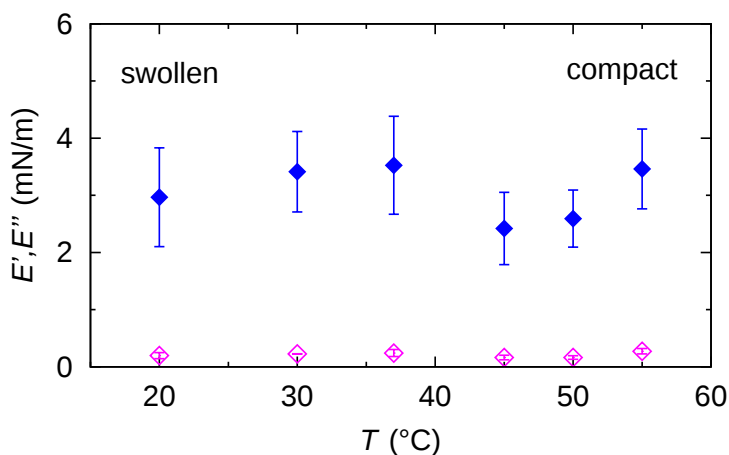
Figure VI.5: Dilatational rheology: storage (E′) and loss (E″) moduli of adsorbed layers of PVLC microgel (0.02%) at the air-water interface as a function of temperature. Solid symbols: E′, hollow symbols: E″.

gels we measured the dilatational rheology after adsorption for 1 h at constant surface area.[47,48] There is little work published on the dilatational rheology of microgels at fluid interfaces, and among it, there is a large variability in the published results of dilatational rheology of adsorbed layers of microgels at fluid interfaces.[34,35] This is possibly because this magnitude is strongly influenced by the molecular structure and hence small variations in composition (crosslinker, charge,...) of the microgel can affect severely the obtained parameters.[47] In particular, we have found no studies of the dilatational rheology of PVLC based microgel at fluid interface to date.

Fig. VI.5 shows the response of the surface layers, characterized in Figs. VI.3 and VI.4, to an imposed deformation. This response is characterized by the elastic (E′) and loss (E″) moduli of the microgel covered interface at various temperatures. In the entire temperature range, E′ is larger than E″, indicative of solid-like behavior.[34] The elastic moduli obtained for PVLC adsorbed layers range between 2–4 mN/m for all temperatures, which is just significantly higher than the residual elasticity of the pure air-water interface. However, these results are of the same order as other reported works on PNIPAM based particles adsorbed at fluid interfaces[26,29,34] and one order of magnitude lower than those reported by Pinaud and coworkers.[35] E′ is a measure of the response of the surface layers to surface tension gradients and is sensitive to the diffusion of molecules between the bulk solution and the interface.[49] For interfaces covered with irre-

versibly adsorbed species such as polymers, the dilatational modulus is a complex balance between inter and intramolecular interactions within the adsorbed layers, including intrinsic mechanical properties of the adsorbed material. Data in Fig. VI.5 show that E' is very low in the whole range of surface coverage, below and above VPTT. This indicates the formation a very loose adsorbed layer with low cohesivity between polymer chains.

3.3 Langmuir monolayer

The properties of surface layers of microgels build up upon adsorption onto a fluid interface are weakly influenced by the temperature as demonstrated in Figs. VI.3–VI.5 and in agreement with literature works.[26,27,29,35] An additional complication in adsorption experiments is that the surface coverage is not constant. Further adsorption from bulk solution can take place as the size of particles decreases with temperature. Hence, this can counteract the surface deformation caused by the microgel particles.[35] To gain a more comprehensive understanding of the temperature effect on surface conformation of microgels we have used Langmuir monolayers. In these experiments, the number of particles at the interface is constant over the whole range of surface coverage, i.e. compression range. Hence, the picture provided by these experiments can importantly complement the findings obtained from adsorption layers.
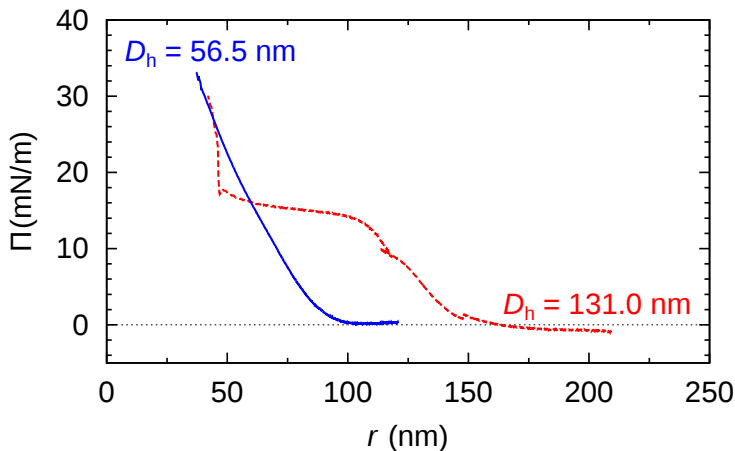

Figure VI.6: Compression isotherms of PVLC microgels obtained above and below the VPTT. The surface pressure is plotted versus the inter-particle distance (r) assuming disc-shape. Solid line: 45°C (collapsed state), dashed line: 20°C (swollen state). The arrows indicate the hydrodynamic diameters obtained for the collapsed and swollen microgel conformations in Fig. VI.1.

Fig. VI.6 shows the compression isotherms of PVLC microgels below and above the VPTT. The isotherms are normalized to the number of particles at the surface and then represented versus the inter-particle distance, r. This distance is obtained assuming that the particles homogeneously distribute as flat disks at the air-water interface. The number of particles has been calculated considering that, in the collapsed state, the internal polymer volume fraction of the microgels is composed of 70 wt% polymer and 30 wt% water. From the hydrodynamic diameter measured in the collapsed state and the density of the polymer 1.029 g/ml we obtain the volume per particle and hence the mass of the polymer particle. This representation allows for an interpretation of the microgel deformation and the packing at the surface upon compression. It can be seen that the shape of the compression isotherm is strongly influenced by the temperature obtaining a clear difference between the swollen and the collapsed states (Fig. VI.6). The shape of the swollen microgels is similar to results published for PNIPAM microgels below the VPTT.[32,33,35] We have found much less literature concerning monolayers in the collapsed state. Hence, to our knowledge, this study is the first to provide comparative compression isotherms of microgels in the collapsed and swollen state.

From Fig. VI.6 we may distinguish various compression regimes for the microgel in the swollen state. In the first regime, microgels behave as a gas of non-interacting particles leading to the absence of surface pressure. This corresponds to an inter-particle distance larger than the diameter of the swollen particle in bulk according to Fig. VI.1 ($r >$150 nm). The second regime shows a continuous increase of the surface pressure. In this regime, the inter-particle distance is of the order of the diameter of the swollen particles, namely 100 nm $< r <$ 150 nm (Fig. VI.1). Experimental results obtained by Rey and coworkers clearly show that, within this compression regime, microgels are already structured into a 2D hexagonal lattice, with their external shells partially overlapped. Hence, this increase corresponds to the repulsion exerted by the microgel shells when they are mutually interpenetrated.[50] The high deformability of the particle in the swollen state means that the structure can deform and reorient the hydrophobic residues onto the air-water interface. Upon further compression, in fact, the surface pressure rises steeply and the work done onto the system goes into compressing the particle coronas, resulting into a continuous change in the lattice constant of the 2D hexagonal packing.

In a third regime, the surface pressure becomes constant as the inter-particle distance is decreased. Classically for lipids, this plateau is described as the coexistence between expanded and condensed phase.[51] In the case of microgel par-

ticles, this plateau indicates that two packing states coexist at the surface while the density of polymeric chain at the surface is constant. The two coexisting states would correspond to highly compressed microgels with an inter-particle distance equals the D_h at 45°C(compact) and less compressed microgels with inter-particle distance equal to the D_h at 20°C (swollen). Another possibility is that within this regime, all particles remain in a swollen conformation and, as the compression proceeds, some segments are forced into the subphase to maintain the surface density. Both hypothesis imply that microgels are soft and deformable particles in this plateau as also suggested by Pinaud and coworkers.[35] This plateau maintains until reaching inter-particle distances equal to the diameter of the compact particles: 55 nm (Fig. VI.1). Then, a second increase of surface pressure arises. This increase appears very sharp and maintains at inter-particle distances of approximately 50 nm. At this stage it becomes difficult to compress the microgels further. This fourth regime corresponds to the condensed phase and we assume that the particles are in a contracted state similar to the collapsed state after the VPTT.

The compression isotherm recorded for the microgels in the collapsed state, above VPTT (45°C) shows a different distribution of compression regimes (Fig. VI.6). The first regime, comprised of non-interacting particles leading to the absence of surface pressure maintains now until much inter-particle much lower and already within the transition state in Fig. VI.1 ($r < 100$ nm). The monolayer enters then into a second regime in which the surface pressure increases continuously until collapse. For inter-particle distances larger than the microgel diameter, the electrostatic repulsion plays the dominant role. However, for $r < D_h \approx 55$ nm, the free energy arising from the deformation of the polymer network is expected to be more relevant. The fact that collapsed microgels do not show any transition region suggests that the interaction is now occurring directly between the core of the particles through an elastic repulsive pair potential. Hence, this regime would directly correspond to a condensed state in which microgels are compressed in a collapsed state at the surface. Furthermore, compression isotherms recorded in the swollen and collapsed state overlap at inter-particle distance of the order of magnitude of dehydrated (or collapsed) microgels (Fig. VI.6). This suggests that the compression of swollen PVLC microgels at the surface leads to dehydration of the structure and promotes a transition between swollen and collapsed state. Also, it proves that soft PVLC particles present some common features with proteins, which are able to adapt their conformation to the interfacial environment by surface denaturation.[35]

From the compression isotherms we can also have a guess of how the microgel-

microgel effective pair potential, $u(r)$, looks like, at least qualitatively. For the particular case of swollen microgels (20°C), as the particles get closer during the compression of the monolayer and the external shells overlap, the increase of the surface pressure implies the existence of a repulsive interaction. In principle, this interaction should have two contributions: an electrostatic term and a soft elastic repulsion caused by the loss of entropy of the polymer chains when overlap. However, the fact that upon further compression the surface pressure becomes roughly constant for a range of inter-particle distances means that an additional overlap does not involve a significant free energy cost. In other words, once the particles are forced to reach some degree of overlap, the microgel pair potential can be modelled by a penetrable potential with a constant repulsion, $u(r) \approx \epsilon > 0$ for $0.4D_h < r < 0.8D_h$. This implies that the microgel shell deforms without compressing the polymer network, as already suggested by Peláez and coworkers in dense microgel bulk suspensions.[52] This penetrable potential leads, in bulk solutions, to broad phase coexistence regions where the particles join together to form clusters.[53] Therefore, although bulk and interface are indeed very different geometries, the fact that the equation of state shows a phase transition at large packing fractions means that the deformation of the shell without compression is a common feature in both situations. Our experimental observations and direct visualizations performed by Rey and coworkers show that these clusters are formed by microgels with their mutual cores touching each other, where the number of particles per cluster increases with the monolayer compression.[50] As already discussed, additional monolayer compression leads to the overlap of the microgel cores, which brings another increase of the surface pressure. In this case, the crosslinked polymer network of the particles is compressed, and the effective repulsion becomes dominated by the elastic free energy, which is strongly dependent of the inter-particle separation. In this case, an Hertzian model would be able to capture the physics for these inter-particle distances, $u(r) = u_0(r_0 - r)^{5/2}$ for $r < r_0$, where $u_0 > 0$ and r_0 is of the order of the core diameter.[52]

It should be emphasized that this picture based on effective potentials is not enough to correctly estimate the surface pressure obtained experimentally. Indeed, the surface pressure calculated from this approximation scales as $\Pi \sim k_B T / D_h^2$, which leads to values of the order of μN/m, whereas experimental results provide values about 10 mN/m, i.e. 4 orders of magnitud larger. This huge difference between theoretical and experimental data has been attributed to the internal degrees of freedom of the polymer network inside the microgel particle, which also contributes to the pressure.[54] For this kind of soft nanoparticles, the

pressure scales as $\Pi \sim k_B T / d_{cross}^2$, where d_{cross} is the size of the correlated domains inside the particle, typically given by the separation between two neighbouring crosslinkers.[31] In our particular case, for collapsed microgels we estimated a value of $d_{cross} \approx$ 3–4 nm, so the surface pressure deduced theoretically from the effective interactions must be rescaled by a factor of $(D_h / d_{cross})^2 \sim 10^4$, which leads to values of the order of the experimental results. Nevertheless, future research should focus on supporting this rescaling argument with more accurate theoretical models. This will provide a deeper understanding of the role that the polymer chain fluctuations play on the surface pressure of adsorbed microgels.

4 Conclusions

We have carried out a complete surface characterization of a new type of ionic microgels, based on PVCL, considered to have better biocompatibility than more commonly used PNIPAM. The D_h of PVCL microgel decreases from 131 nm to 56.5 nm, when the temperature increases from 20°C to 40°C. The dynamic surface tension plot shows two adsorption regimes, similar to the classic kinetics of protein adsorption. The results clearly indicate that a higher number of particles reach the surface above the VPTT while the diffusion coefficient remains unchanged. We evaluate also the influence of swelling state in the quasi-equilibrium surface tension values, obtaining that the surface tension decreases below the VPTT while it maintains above the VPTT. This behavior indicates that the surface accommodates a higher number of particles and a closer packing density as the microgel collapses, resulting in a more compact surface layer. The plateau above the VPTT contrasts with a well reported minimum for PNIPAM around the VPTT and suggests a more efficient packing at the surface resulting in a more stable conformation, resistant to aggregation above the VPTT. Dilatational rheology data shows the formation a very loose adsorbed layer with low cohesivity within the whole range of surface coverage.

The PVCL microgels confined onto a 2D monolayer under forced compression show two different behaviors depending on whether the system is above or below the VPTT. On the one hand, the elastic and electrostatic repulsion between collapsed microgels lead to a continuous increase of the surface pressure. On the other hand, swollen microgels display a phase transition at intermediate surface pressures similar to soft polymers, which is attributed to the displacement of the polymer chains in the external shell of the particles, induced by the shell overlapping. In other words, the loose external polymer chains are forced

into the subphase by keeping the free energy of the system constant. Therefore, the evolution of the surface pressure allows identifying the interaction of the shells and cores as the inter-particle distance decreases in the monolayer by comparison with the D_h of the microgels. New insights arise from calculations of the surface pressure of the particles alone, obtaining values four orders of magnitude larger than the theoretical predictions obtained using effective pair potentials. This effect points out the importance of the internal degrees of freedom within the particles. All these results represent important findings for the rational use of microgels in emulsified systems.

References

[1] Noro, A.; Hayashi, M.; Matsushita, Y. *Soft Matter* **2012**, *8*, 6416.

[2] Pelton, R.; Hoare, T. *Microgel Suspensions*; Wiley-VCH Verlag GmbH & Co. KGaA, 2011; pp 1–32.

[3] Ramos, J.; Imaz, A.; Callejas-Fernández, J.; Barbosa-Barros, L.; Estelrich, J.; Quesada-Pérez, M.; Forcada, J. *Soft Matter* **2011**, *7*, 5067–5082.

[4] Alexander, C. *Nat. Mater.* **2008**, *7*, 767–768.

[5] Pelton, R. *Adv. Colloid Interface Sci.* **2000**, *85*, 1–33.

[6] Ramos, J.; Imaz, A.; Forcada, J. *Polym. Chem.* **2012**, *3*, 852.

[7] Ledesma-Motolinía, M.; Braibanti, M.; Rojas-Ochoa, L. F.; Haro-Pérez, C. *Colloids Surf., A* **2015**, *482*, 724–727.

[8] Quesada-Pérez, M.; Ramos, J.; Forcada, J.; Martín-Molina, A. *J. Chem. Phys.* **2012**, *136*, 244903.

[9] Lee, C. H.; Bae, Y. C. *Macromolecules* **2015**, *48*, 4063–4072.

[10] Jung, S. C.; Oh, S. Y.; Chan Bae, Y. *Polymer* **2009**, *50*, 3370–3377.

[11] Quesada-Pérez, M.; Maroto-Centeno, J. A.; Forcada, J.; Hidalgo-Alvarez, R. *Soft Matter* **2011**, *7*, 10536.

[12] Hertle, Y.; Zeiser, M.; Hasenöhrl, C.; Busch, P.; Hellweg, T. *Colloid Polym. Sci.* **2010**, *288*, 1047–1059.

[13] Sierra-Martin, B.; Lietor-Santos, J. J.; Fernandez-Barbero, A.; Nguyen, T. T.; Fernandez-Nieves, A. *Microgel Suspensions*; Wiley-VCH Verlag GmbH & Co. KGaA, 2011; pp 73–116.

[14] Quesada-Pérez, M.; Ibarra-Armenta, J. G.; Martín-Molina, A. *J. Chem. Phys.* **2011**, *135*, 094109.

[15] Quesada-Pérez, M.; Maroto-Centeno, J. A.; Martín-Molina, A. *Macromolecules* **2012**, *45*, 8872–8879.

[16] Quesada-Pérez, M.; Martín-Molina, A. *Soft Matter* **2013**, *9*, 7086–7094.

[17] Lee, S. M.; Bae, Y. C. *Macromolecules* **2014**, *47*, 8394–8403.

[18] Quesada-Pérez, M.; Ahualli, S.; Martín-Molina, A. *J. Polym. Sci. Part B: Polym. Phys.* **2014**, *52*, 1403–1411.

[19] Quesada-Pérez, M.; Ahualli, S.; Martín-Molina, A. *J. Chem. Phys.* **2014**, *141*, 124903.

[20] Adroher-Benítez, I.; Ahualli, S.; Martín-Molina, A.; Quesada-Pérez, M.; Moncho-Jordá, A. *Macromolecules* **2015**,

[21] González-Mozuelos, P. *J. Chem. Phys.* **2016**, *144*, 54902.

[22] Zielińska, K.; Sun, H.; Campbell, R. A.; Zarbakhsh, A.; Resmini, M. *Nanoscale* **2016**, *8*, 4951–4960.

[23] Li, Z.; Geisel, K.; Richtering, W.; Ngai, T. *Soft Matter* **2013**, *9*, 9939.

[24] Zhang, J.; Pelton, R. *Langmuir* **1999**, *15*, 8032–8036.

[25] Nerapusri, V.; Keddie, J. L.; Vincent, B.; Bushnak, I. A. *Langmuir* **2006**, *22*, 5036–5041.

[26] Brugger, B.; Rütten, S.; Phan, K. H.; Moller, M.; Richtering, W. *Angew. Chem.* **2009**, *48*, 3978–3981.

[27] Monteux, C.; Marliere, C.; Paris, P.; Pantoustier, N.; Sanson, N.; Perrin, P. *Langmuir* **2010**, *26*, 13839–13846.

[28] Geisel, K.; Isa, L.; Richtering, W. *Langmuir* **2012**, *28*, 15770–6.

[29] Cohin, Y.; Fisson, M.; Jourde, K.; Fuller, G. G.; Sanson, N.; Talini, L.; Monteux, C. *Rheol. Acta* **2013**, *52*, 445–454.

[30] Deshmukh, O. S.; van den Ende, D.; Stuart, M. C.; Mugele, F.; Duits, M. H. G. *Adv. Colloid Interface Sci.* **2014**, *222*, 215–227.

[31] Deshmukh, O. S.; Maestro, A.; Duits, M. H.; van den Ende, D.; Cohen-Stuart, M. a.; Mugele, F. *Soft Matter* **2014**, *9*, 2731–2738.

[32] Geisel, K.; Isa, L.; Richtering, W. *Angew. Chem.* **2014**, *53*, 4905–4909.

[33] Geisel, K.; Richtering, W.; Isa, L. *Soft Matter* **2014**, *10*, 7968.

[34] Li, Z.; Richtering, W.; Ngai, T. *Soft Matter* **2014**, *10*, 6182–6191.

[35] Pinaud, F.; Geisel, K.; Massé, P.; Catargi, B.; Isa, L.; Richtering, W.; Ravaine, V.;

Schmitt, V. *Soft Matter* **2014**, *10*, 6963–6974.

[36] Geisel, K.; Rudov, A. A.; Potemkin, I. I.; Richtering, W. *Langmuir* **2015**, *31*, 13145–13154.

[37] Li, Z.; Ngai, T. *Nanoscale* **2013**, *5*, 1399–410.

[38] Mehrabian, H.; Harting, J.; Snoeijer, J. H. *Soft Matter* **2015**, *12*, 1–17.

[39] Style, R. W.; Dufresne, E. R. *Soft Matter* **2015**, *11*, 1–8.

[40] Wu, Y.; Wiese, S.; Balaceanu, A.; Richtering, W.; Pich, A. *Langmuir* **2014**, *30*, 7660–7669.

[41] Lee, L. T.; Jean, B.; Menelle, a. *Langmuir* **1999**, *15*, 3267–3272.

[42] Imaz, A.; Forcada, J. *J. Polym. Sci. Part A: Polym. Chem.* **2011**, *49*, 3218–3227.

[43] Maldonado-Valderrama, J.; Torcello-Gómez, A.; del Castillo-Santaella, T.; Holgado-Terriza, J. A.; Cabrerizo-Vílchez, M. A. *Adv. Colloid Interface Sci.* **2015**, *222*, 488–501.

[44] Maldonado-Valderrama, J.; Fainerman, V. B.; Aksenenko, E.; Jose Gálvez-Ruiz, M.; Cabrerizo-Vílchez, M. a.; Miller, R. *Colloids Surf., A* **2005**, *261*, 85–92.

[45] Moncho Jordá, A.; Dzubiella, J. *Phys. Chem. Chem. Phys.* **2016**, *18*, 5372–5385.

[46] Moncho-Jordá, A. *J. Chem. Phys.* **2013**, *139*, 064906.

[47] Maldonado-Valderrama, J.; Patino, J. M. R. *Curr. Opin. Colloid Interface Sci.* **2010**, *15*, 271–282.

[48] Maldonado-Valderrama, J.; Martín-Rodriguez, A.; Gálvez-Ruiz, M. J.; Miller, R.; Langevin, D.; Cabrerizo-Vílchez, M. a. *Colloids Surf., A* **2008**, *323*, 116–122.

[49] Langevin, D. *Adv. Colloid Interface Sci.* **2000**, *88*, 209–222.

[50] Rey, M.; Fernández-Rodríguez, M. Á.; Steinacher, M.; Scheidegger, L.; Geisel, K.; Richtering, W.; Squires, T. M.; Isa, L. *Soft Matter* **2016**, *12*, 3545–3557.

[51] Luque-Caballero, G.; Martín-Molina, A.; Sánchez-Treviño, A. Y.; Rodríguez-Valverde, M. a.; Cabrerizo-Vílchez, M. a.; Maldonado-Valderrama, J. *Soft Matter* **2014**, *10*, 2805–15.

[52] Peláez-Fernández, M.; Souslov, A.; Lyon, L. A.; Goldbart, P. M.; Fernández-Nieves, A. *Phys. Rev. Lett.* **2015**, *114*, 1–5.

[53] Likos, C. N.; Watzlawek, M.; Löwen, H. *Phys. Rev. E* **1998**, *58*, 16.

[54] Groot, R. D.; Stoyanov, S. D. *Soft Matter* **2010**, *6*, 1682.

Conclusions and summary

1

Conclusions

The aim of this chapter is to remark the most relevant results obtained in this research. In the first part of this dissertation the interactions involved in the permeation of ions inside thermoresponsive ionic microgel particles in the limit of very diluted microgel suspensions have been studied from theoretical, computational and experimental approaches. The main conclusions that can be drawn from this work are listed below.

1) When ions diffuse through microgel pores, not only the electrostatic interaction, but also the excluded-volume effects may determine the degree of permeation and ionic distribution inside and around the microgel particle. This steric effects are responsible for the important increase of the microgel effective charge observed experimentally in microgel deswelling. It has been also demonstrated that it is necessary to include this microgel-ion steric interaction in the theoretical models to accurately reproduce the ionic density profiles obtained in Monte Carlo simulations.

2) The Ornstein-Zernike integral formalism within the HNC closure relation is a reliable method which allows to predict the radial distribution functions of ions inside and around microgel particles, even for highly charged particles, multivalent ionic species, and in conditions of strong confinement. Within this theoretical framework, splitting the microgel-ion ef-

fective interaction into electrostatic and excluded-volume additive terms leads to satisfactory results. To calculate the steric interaction, the internal fibrous structure of the microgel must be modelled. It has been observed that the polymer network is surprisingly well represented by assembly of random overlapping spherical monomers, even though it represents a strong approximation of the real morphology of the nanogel.

3) The valence of the counterions that permeate inside the microgel plays an important role in several aspects. First, multivalent counterions neutralize microgel charge more efficiently than monovalent ones, leading to lower values of the microgel effective charge. Consequently, microgel volume transition shifts to lower temperatures. This effect is more noticeable for highly charged microgels. In addition, the valence also enhances counterion condensation inside the microgel network, which has a striking impact in electrophoretic mobility experiments.

4) Deep inside the polymer network the ionic density profiles are homogeneous and charge electroneutrality is satisfied, but close to the microgel-water interface electroneutrality is violated. Therefore, microgel effective charge mainly comes from the microgel surface.

5) Molecular Dynamics simulations of an oligomer and a PNIPAM membrane in water confirm that both AMBER and OPLS-AA force fields in combination with SPC/E water capture the coil to globule transition temperature in qualitative good agreement with experiments. This result suggests that polymer-polymer interactions are not a key ingredient for the determination of the transition temperature. For a membrane in presence of electrolyte a salting out effect has been observed. The phenomenon is more pronounced for NaCl electrolyte than for NaI, in good agreement with experiments.

The second part of this thesis has been focused on the theoretical study of the interactions involved in the sorption of a non-uniformly charged biomolecule inside an ionic microgel. From this work we can conclude:

6) The total microgel-biomolecule interaction is the consequence of a complex interplay between several phenomena. Among them, the electrostatic interaction has a determinant role in the uptake and spatial distribution of the molecule inside the microgel. In addition, the heterogeneous charge distribution of the biomolecule that leads to large electric dipoles is a determining factor to take into account, especially when

adsorption at microgel surface is sought. This work demonstrates that, despite the wide range of factors that intervene in biomolecule sorption inside microgels, it is possible to predict the qualitative behaviour of such systems by means of a relatively simple theoretical framework.

Finally, from the study of the behaviour of thermoresponsive ionic microgels at the air-water interface, two main results have been obtained.

7) Above the volume phase transition temperature (VPTT) a higher number of microgels reach the interface. In this regime the surface accommodates more particles and a closer packing density as the microgel collapses, which results in a more stable conformation, resistant to aggregation than below the VPTT.

8) The analysis of the Langmuir monolayers provides useful information about the internal structure of microgel particles. Indeed, by decreasing the inter-particle distance and studying the microgel-microgel interactions is possible to estimate the size of the particle core and shell by comparison with the hydrodynamic diameter measured by dynamic light scattering.

2

Resumen

2.1 Introducción

Hablamos de *microgel* para referirnos a una "suspensión coloidal de partículas de gel"[1]. Es decir, son partículas porosas formadas por cadenas de polímero entrecruzadas dispersas en un disolvente. Es frecuente denominarlas también *nanogeles*[2], pues su diámetro oscila entre los 10 y los 1000 nm, o *hydrogeles,* cuando se encuentran dispersas en agua.

La principal característica de los microgeles es que pueden absorber grandes cantidades de disolvente, provocando drásticos cambios en su tamaño, en respuesta a un gran número de estímulos tales como temperatura, pH, concentración salina, luz, campos externos o solutos específicos como glucosa u otras biomoléculas[3–8]. Gracias a esta versatilidad se dice que los microgeles son materiales "inteligentes". La capacidad para responder a estímulos externos unida a su tamaño coloidal les permite formar diferentes estructuras con numerosas aplicaciones. Por ejemplo, el estudio de monocapas de microgeles en la interfase aire-agua[9], aceite-agua[10,11] y otras interfases[12] ha ganado interés en los últimos años. De la misma forma, otras estructuras tridimensionales, tales como cristales[13,14], láminas delgadas y multicapas[15,16] han sido investigadas por diferentes autores.

En los últimos años está creciendo enormemente el interés por desarrol-

lar nuevos sistemas de transporte y encapsulación de fármacos [17-20]. Los microgeles resultan prometedores para este cometido, pues el espacio disponible en el interior de la red polimérica permite la encapsulación de diferentes solutos tales como ADN, proteínas, péptidos y otras biomoléculas [21-25], tanto hidrófilas como hidrófobas, lo que permite mejorar su solubilidad y evitar su degradación en el organismo [26]. Asimismo, la capacidad de los microgeles para expandirse y compactarse puede aprovecharse para absorber y liberar fármacos de manera controlada. Por estos motivos, un gran número de aplicaciones médicas y biotecnológicas para los microgeles están siendo ampliamente investigadas [27-30].

Los tipos de microgeles que más interés atraen son los microgeles sensibles a la temperatura y/o el pH. Por un lado, los microgeles termosensibles cuya temperatura de transición de volumen (VPTT) está próxima a la temperatura del cuerpo humano pueden resultar muy útiles en el campo de la medicina, mientras que para microgeles sensibles al pH la liberación y el transporte de biomoléculas se puede controlar mediante las interacciones electrostáticas [31].

Los microgeles basados en N-isopropilacrilamida, conocidos como PNIPAM, son los que más se han estudiado a lo largo de los años. Desde que fueron sintetizados por primera vez en los años 80 [32], se han publicado una gran cantidad de trabajos sobre diferentes estrategias de síntesis y caracterización [33-37]. De hecho, actualmente se considera el PNIPAM como un microgel modelo para la ciencia de polímeros en general, lo cual resulta especialmente útil para desarrollar y probar modelos teóricos y computacionales de microgeles [38-40]. Otro tipo interesante de microgel recientemente desarrollado es el PVCL, basado en N-vinilcaprolactama [41]. El potencial de estas partículas reside en su biocompatibilidad, que los hace muy apropiados para aplicaciones biomédicas. Esto supone una ventaja respecto a los microgeles de PNIPAM, en los que se ha observado una alta citotoxicidad [42,43].

La mayoría de microgeles diseñados con aplicaciones biotecnológicas son microgeles iónicos, es decir, poseen carga eléctrica debido a los polielectrolitos que forman la red polimérica. Cuando estos microgeles cargados se encuentran inmersos en una solución de electrolito, los iones móviles de la sal penetran a través de los poros de las partículas y se distribuyen en torno a los microgeles, creando una doble capa eléctrica. Tanto la estructura interna como la respuesta en tamaño de estos microgeles está fuertemente ligada a la concentración de electrolito y a la valencia de los contraiones presentes en el medio [33,44-46].

La presencia de electrolito también determina la interacción efectiva entre los microgeles y otras partículas presentes en la dispersión coloidal como

biomoléculas. Esto se debe al apantallamiento de la carga del microgel provocado por los contraiones que penetran a través de sus poros, los cuales pueden encontrarse en libre movimiento o bien condensados en el interior de la red de polímeros[47]. Dicho apantallamiento suele caracterizarse mediante la llamada carga efectiva del microgel, que proporciona una estimación de la carga electrostática que otra partícula del medio percibe cuando se aproxima al microgel[40,48,49]. Asimismo, si los iones disueltos en el medio presentan especificidad iónica (efectos Hofmeister), el microgel puede verse afectado por fenómenos de inversión de carga o sobrecarga[50–52].

Dado el importante papel que la presencia de electrolito juega en los cambios de volumen del microgel y en las interacciones de microgeles con otras moléculas del medio, es indispensable entender los fenómenos físicos involucrados en la distribución de iones en el interior y en torno a los microgeles. Sabemos que para solutos dispersos en el medio es la interacción coulombiana que surge a consecuencia de la carga efectiva del microgel la que controla los perfiles de densidad iónicos en torno al microgel. Sin embargo, cuando un ion intenta penetrar a través de los poros de un microgel, no sólo sufre el efecto de la interacción electrostática, sino que experimenta una exclusión de volumen debido a que las fibras de polímero ocupan un espacio que el ion no puede atravesar. Esta interacción repulsiva se conoce como interacción estérica, depende de la morfología interna de la red de polímeros y es especialmente relevante cuando el microgel se encuentra en estado compactado[40,50].

Desde que los primeros microgeles fueron sintetizados, se ha publicado un gran número de trabajos relativos a la síntesis, caracterización, modelado y aplicaciones de estas partículas. Sin embargo, sólo una pequeña fracción de ellos tienen el objetivo de estudiar desde un punto de vista teórico el comportamiento de estas partículas en presencia de otros solutos cargados. Profundizar en el conocimiento de los fenómenos físicos involucrados en la respuesta de los microgeles a los cambios en el medio y de las interacciones entre microgeles y otras partículas puede estimular el desarrollo de nuevas aplicaciones, abrir nuevas líneas de investigación y en general contribuir al avance de la ciencia de materiales en general.

2.2 Procedimiento

La investigación desarrollada en esta tesis doctoral puede dividirse en tres partes diferenciadas. A continuación describimos brevemente los trabajos realizados en cada una de ellas.

2.2.1 Microgeles en disoluciones de electrolito

El objetivo de los artículos I, II, III y IV consiste en el estudio de las interacciones que intervienen en la permeación de iones en el interior de microgeles iónicos termosensibles, en el límite de dispersiones de microgeles muy diluidas. Para ello se ha hecho uso del formalismo de las ecuaciones integrales de Ornstein-Zernike, de simulaciones Monte Carlo y de Dinámica Molecular, así como de trabajos experimentales de síntesis y caracterización.

El punto de partida de esta tesis ha sido el estudio del efecto de la interacción estérica en la permeación de contraiones monovalentes en el interior de microgeles, recogido en el artículo I. Con este objetivo hemos desarrollado un método que combina las ecuaciones integrales de Ornstein-Zernike con simulaciones Monte Carlo y hemos comparado los perfiles de densidad iónica y la carga efectiva del microgel obtenidos mediante ambos métodos para distintos estados de compactación del microgel. Este análisis nos ha permitido probar dos modelos diferentes para la repulsión estérica microgel-ion y determinar cuál de ellos es más apropiado para cuantificar los efectos de exclusión de volumen en estos sistemas. También hemos estudiado la distribución de carga del microgel, la concentración de electrolito y el tamaño iónico.

Continuando con la idea del trabajo anterior, en el artículo II la técnica combinada de simulaciones Monte Carlo y ecuaciones de Ornstein-Zernike se ha usado para estudiar el hinchado y desinchado de los microgeles en respuesta a dos variables concretas. Por una parte, se ha estudiado el efecto de la valencia de los contraiones mediante el estudio de microgeles en disoluciones de electrolito 1:1 y 1:3. Por otra parte, hemos considerado dos microgeles diferentes para analizar el efecto de la carga bruta de los mismos en las transiciones de volumen y la permeación de contraiones. Para modelar la interacción estérica hemos utilizado el modelo que resultó más satisfactorio en el trabajo anterior y lo hemos comparado con otro modelo diferente.

La fiabilidad del formalismo teórico de Ornstein-Zernike ha sido confirmado en la publicación III, en el cual hemos interpretado los resultados experimentales obtenidos para dos microgeles iónicos termosensibles distintos mediante dichas ecuaciones integrales. En este trabajo hemos medido el diámetro hidrod-

inámico y la movilidad electroforética de dos microgeles basados en PNIPAM y PVCL para diferentes valencias y concentraciones de electrolito. Hemos obtenido una carga efectiva experimental a partir de las medidas de movilidad y la hemos comparado con la carga efectiva teórica calculada para estos sistemas. De esta forma, hemos analizado el efecto de la valencia de los contraiones y de la concentración salina sobre la carga efectiva de los microgeles, lo que nos ha permitido obtener interesantes conclusiones sobre la permeación y condensación iónica en el interior de la red de polímeros.

Para concluir con esta parte de nuestra investigación, en el trabajo número IV hemos seguido un procedimiento completamente diferente a los anteriores, basado en simulaciones de Dinámica Molecular. Esta técnica permite considerar el efecto conjunto de todas las interacciones que aparecen cuando cadenas de polímero se encuentran dispersas en soluciones electrolíticas. Sin embargo, es necesario tener en cuenta que modelar de forma exacta la red polimérica de una partícula de microgel es extremadamente exigente desde el punto de vista computacional, por lo que en su lugar hemos considerado una membrana de cadenas de PNIPAM como modelo. De esta forma, en primer lugar se ha confirmado el comportamiento termosensible de estas cadenas para posteriormente sumergir la membrana en diferentes soluciones de electrolito y estudiar los correspondientes perfiles de densidad iónica tanto para estados expandidos como compactados de los polímeros.

2.2.2 Absorción y distribución de biomoléculas en microgeles

Además de las interacciones microgel-ion, para evaluar el potencial de estas partículas como sistemas de transporte y encapsulación de fármacos en necesario profundizar en el conocimiento de las interacciones entre microgeles y biomoléculas.

Con este objetivo, en el artículo V hemos dejado a un lado el formalismo integral y las simulaciones para llevar a cabo el estudio teórico de la absorción de una molécula heterogéneamente cargada por un microgel en presencia de electrolito 1:1. De esta forma, mediante un procedimiento relativamente sencillo, hemos estudiado el potencial de fuerza media entre el microgel y la molécula para diferentes valores de dipolo eléctrico y carga neta de la molécula. También hemos considerado los efectos dependientes de la concentración salina, la exclusión de volumen y las interacciones hidrófobas. Hemos identificado cinco estados diferentes de absorción en este sistema, desde la completa repulsión de la biomolécula hasta su absorción en el interior del microgel, pasando por estados de adsorción superficial estables y metaestables.

2.2.3 Propiedades interfaciales de microgeles termosensibles

Anteriormente hemos comentado que existe un creciente interés por el estudio de monocapas y otras estructuras de microgeles. Por ese motivo, en el artículo VI de esta tesis hemos abierto una nueva línea de investigación en nuestro trabajo para estudiar las características interfaciales de microgeles termosensibles con el objetivo de explorar sus potenciales aplicaciones como estabilizadores de emulsiones sensibles a estímulos externos.

De esta forma, hemos investigado el comportamiento de microgeles de PVCL en la interfase aire-agua, tanto experimental como teóricamente. El trabajo experimental se ha llevado a cabo mediante diferentes técnicas, tales como estudio de la adsorción, reología dilatacional y monocapas de Langmuir. Por otra parte, los resultados experimentales se han interpretado cualitativamente en términos de los potenciales efectivos entre pares de microgeles.

2.3 Conclusiones

De los trabajos realizados en la primera parte de esta tesis doctoral, en la que se estudia la permeación de iones en el interior de microgeles, se pueden extraer las siguientes conclusiones:

1) Cuando los iones difunden a través de los poros del microgel no sólo sufren el efecto de la interacción electrostática, sino que los efectos de exclusión de volumen determinan el grado de penetración y la distribución de iones en el interior y exterior de la partícula. Este efecto estérico es el responsable del significativo aumento de la carga efectiva del microgel que se observa experimentalmente cuando el microgel se compacta. También se ha demostrado que es necesario incluir la interacción estérica microgel-ion en los modelos teóricos para reproducir con exactitud los perfiles de densidad iónica obtenidos en las simulaciones Monte Carlo.

2) El formalismo integral de Ornstein-Zernike, junto a la ecuación de cierre HNC, en un método fiable para predecir las funciones de distribución radial de iones en el interior y en torno a los microgeles, incluso en casos de partículas con elevada carga eléctrica, iones multivalentes y condiciones de fuerte confinamiento. En este marco teórico, la división de la interacción efectiva microgel-ion en dos términos aditivos, uno electrostático y otro estérico, proporciona resultados satisfactorios. Para calcular el término estérico es necesario modelar la estructura interna del

microgel. Se ha observado que la red de polímeros resulta sorprendentemente bien representada mediante un modelo de monómeros esféricos superponibles aleatoriamente distribuidos, a pesar de que supone una considerable aproximación de la estrucutra real del microgel.

3) La valencia de los contraiones que penetran en el interior de los microgeles juega un papel relevante en varios aspectos. En primer lugar, los contraiones multivalentes neutralizan la carga del microgel de manera mucho más eficiente que los monovalentes, lo que produce valores mucho más bajos de la carga efectiva. Como consecuencia de ello, la transición de fase volumétrica de los microgeles se produce a temperaturas más bajas. Este efecto es más acusado cuanto más carga posean los microgeles. Asimismo, cuanto mayor es la valencia más significativo es el efecto de condensación iónica en el interior de la red de polímeros, lo que se traduce en un fuerte descenso de la movilidad electroforética de los microgeles.

4) En el interior de la red polimérica los perfiles de densidad iónica son homogéneos y se satisface la electroneutralidad. No obstante, en las inmediaciones de la interfase microgel-agua se viola dicha electroneutralidad. Podemos deducir por tanto que la carga efectiva del microgel procede fundamentalmente de la superficie de la red de polímeros.

5) Las simulaciones mediante Dinámica Molecular de un oligómero y una membrana de PNIPAM en agua confirman que los campos de fuerza AMBER y OPLS-AA en combinación con el modelo de agua SPC/E reproducen satisfactoriamente el colapso de las cadenas observado experimentalmente. El hecho de que la temperatura de colapso no varíe entre el oligómero y la membrana hace pensar que las interacciones polímero-polímero no juegan un papel relevante en la transición de volumen. Asimismo, en el caso de una membrana en presencia de electrolito se ha observado el efecto de precipitación salina, más acusado en el caso de NaCl que en el caso de NaI, como se observa también experimentalmente.

De la segunda parte de esta tesis, centrada en el estudio teórico de las interacciones que intervienen en la absorción de biomoléculas por parte de los microgeles, podemos concluir lo siguiente:

6) El potencial de fuerza media total entre el microgel y la biomolécula es el resultado de una compleja interacción en la que intervienen diferentes

fenómenos físico-químicos. Entre ellos, la interacción electrostática juega un papel fundamental en la absorción y la distribución de la molécula en el interior del microgel. Asimismo, la distribución de carga heterogénea en la molécula que produce un dipolo eléctrico es un factor determinante a tener en cuenta, especialmente cuando se persigue la adsorción superficial de la partícula en la corteza del microgel. Este trabajo demuestra que, a pesar del gran número de parámetros que intervienen en la absorción de biomoléculas en microgeles, es posible predecir cualitativamente el comportamiento de estos sistemas mediante un formalismo teórico relativamente sencillo.

Por último, del análisis del comportamiento interfacial de microgeles termosensibles en la interfase aire-agua se han obtenido dos resultados principales:

7) A temperaturas por encima de la temperatura de transición de volumen (VPTT) un mayor número de microgeles compactados alcanzan la interfase. Bajo estas condiciones la superficie acomoda más partículas y la densidad de empaquetamiento aumenta a medida que los microgeles se compactan, lo que resulta en una configuración más estable y resistente a la agregación que a temperaturas más bajas que la VPTT.

8) El análisis de las monocapas de Langmuir proporciona información muy útil sobre la estuctura interna de los microgeles. Efectivamente, mediante el estudio de los cambios en las interacciones microgel-microgel con la disminución de la distancia entre partículas, y la comparación con medidas experimentales del diámetro hidrodinámico, es posible estimar el tamaño de la corteza y el núcleo de los microgeles.

Referencias

[1] Pelton, R.; Hoare, T. In *Microgel Suspensions: Fundamentals and Applications*; Fernandez-Nieves, A., Wyss, H. M., Mattsson, J., Weitz, D. A., Eds.; Wiley-VCH Verlag GmbH & Co. KGaA: Weinheim, Germany, 2011; pp 1–32.

[2] IUPAC, In *Compendium of Polymer Terminology and Nomenclature (IUPAC Recommendations 2008)*; Jones, R. G., Wilks, E. S., Metanomski, W. V., Kahovec, J., Hess, M., Stepto, R., Kitayama, T., Eds.; The Royal Society of Chemistry, 2009; p 443.

[3] Sasa, N.; Yamaoka, T. *Advanced Materials* **1994**, *6*, 417–421.

[4] Murray, M. J.; Snowden, M. J. *Adv. Colloid Interface Sci.* **1995**, *54*, 73–91.

[5] Saunders, B. R.; Vincent, B. *Adv. Colloid Interface Sci.* **1999**, *80*, 1–25.

[6] Zhang, Y.; Guan, Y.; Zhou, S. *Biomacromolecules* **2006**, *7*, 3196–3201.

[7] Saunders, B. R.; Laajam, N.; Daly, E.; Teow, S.; Hu, X.; Stepto, R. *Adv. Colloid Interface Sci.* **2009**, *147-148*, 251–62.

[8] Naficy, S.; Razal, J. M.; Whitten, P. G.; Wallace, G. G.; Spinks, G. M. *J. Polym. Sci., Part B: Polym. Phys.* **2012**, *50*, 423–430.

[9] Zhang, J.; Pelton, R. *Langmuir* **1999**, *15*, 8032–8036.

[10] Li, Z.; Geisel, K.; Richtering, W.; Ngai, T. *Soft Matter* **2013**, *9*, 9939–9946.

[11] Scheidegger, L.; Fernández-Rodríguez, M. Á.; Geisel, K.; Zanini, M.; Elnathan, R.; Richtering, W.; Isa, L. *Phys. Chem. Chem. Phys.* **2017**,

[12] Li, Z.; Ngai, T. *Nanoscale* **2013**, *5*, 1399–1410.

[13] Lyon, L. A.; Debord, J. D.; Debord, S. B.; Jones, C. D.; McGrath, J. G.; Serpe, M. J. *J. Phys. Chem. B* **2004**, *108*, 19099–19108.

[14] Liétor-Santos, J. J.; Gasser, U.; Zhou, J.; Hu, Z.; Fernández-Nieves, A. *Hydrogel Micro and Nanoparticles*; Wiley-VCH Verlag GmbH & Co. KGaA: Weinheim, Germany, 2012; pp 337–368.

[15] Hendrickson, G. R.; Smith, M. H.; South, A. B.; Lyon, L. A. *Adv. Funct. Mater.* **2010**, *20*, 1697–1712.

[16] Hu, L.; Sarker, A. K.; Islam, M. R.; Li, X.; Lu, Z.; Serpe, M. J. *J. Polym. Sci., Part A: Polym. Chem.* **2013**, *51*, 3004–3020.

[17] Mura, S.; Nicolas, J.; Couvreur, P. *Nat. Mater.* **2013**, *12*, 991–1003.

[18] Lee, S. M.; Nguyen, S. T. *Macromolecules* **2013**, *46*, 9169–9180.

[19] Du, A. W.; Stenzel, M. H. *Biomacromolecules* **2014**, *15*, 1097–1114.

[20] Lesher-Perez, S. C.; Segura, T.; Moraes, C. *Integr. Biol.* **2016**, *8*, 8–11.

[21] Ghugare, S. V.; Mozetic, P.; Paradossi, G. *Biomacromolecules* **2009**, *10*, 1589–1596.

[22] Bysell, H.; Månsson, R.; Hansson, P.; Malmsten, M. *Adv. Drug Delivery Rev.* **2011**, *63*, 1172–1185.

[23] Lü, S.; Liu, M.; Ni, B.; Gao, C. *J. Polym. Sci., Part B: Polym. Phys.* **2010**, *48*, 1749–1756.

[24] Smith, M. H.; Lyon, L. A. *Acc. Chem. Res.* **2012**, *45*, 985–993.

[25] Shin, J.; Cherstvy, A. G.; Metzler, R. *Physical Review X* **2014**, *4*, 021002.

[26] Vinogradov, S. V. *Nanomedicine (London, England)* **2010**, *5*, 165–8.

[27] Ramos, J.; Imaz, A.; Callejas-Fernández, J.; Barbosa-Barros, L.; Estelrich, J.; Quesada-Pérez, M.; Forcada, J. *Soft Matter* **2011**, *7*, 5067–5082.

[28] Lu, Y.; Welsch, N.; Dzubiella, J.; Ballauff, M. In *Intelligent Hydrogels*; Sadowski, G., Richtering, W., Eds.; Springer International Publishing: Cham, 2013; pp 113–130.

[29] Ramos, J.; Forcada, J.; Hidalgo-Álvarez, R. *Chem. Rev.* **2014**, *114*, 367–428.

[30] Ramos, J.; Peláez-Fernández, M. A.; Forcada, J.; Moncho-Jordá, A. In *Soft Nanoparticles for Biomedical Applications*; Callejas-Fernández, J., Estelrich, J., Quesada-Pérez, M., Forcada, J., Eds.; The Royal Society of Chemistry: Cambridge, 2014; Chapter 4, pp 1–37.

[31] Das, M.; Mardyani, S.; Chan, W. C. W.; Kumacheva, E. *Advanced Materials* **2006**, *18*, 80–83.

[32] Pelton, R. H.; Chibante, P. *Colloids and Surfaces* **1986**, *20*, 247–256.

[33] Pelton, R.; Pelton, H. M.; Morphesis, A.; Rowell, R. L. *Langmuir* **1989**, *5*, 816–818.

[34] Duracher, D.; Elaïssari, A.; Pichot, C. *J. Polym. Sci., Part A: Polym. Chem.* **1999**, *37*, 1823–1837.

[35] Leobandung, W.; Ichikawa, H.; Fukumori, Y.; Peppas, N. A. *J. Appl. Polym. Sci.* **2002**, *87*, 1678–1684.

[36] López-León, T.; Ortega-Vinuesa, J. L.; Bastos-González, D.; Elaïssari, A. *The journal of physical chemistry. B* **2006**, *110*, 4629–36.

[37] Tagit, O.; Tomczak, N.; Jafarpour, A.; Jańczewski, D.; Han, M. Y.; Vancso, G. J.; Herek, J. L. *Nanotechnology* **2011**, *22*, 265701.

[38] Gottwald, D.; Likos, C. N.; Kahl, G.; Löwen, H. *The Journal of chemical physics* **2005**, *122*, 074903–11.

[39] Quesada-Pérez, M.; Ramos, J.; Forcada, J.; Martín-Molina, A. *The Journal of chemical physics* **2012**, *136*, 244903–9.

[40] Moncho-Jordá, A. *The Journal of chemical physics* **2013**, *139*, 064906.

[41] Gao, Y.; Au-Yeung, S. C. F.; Wu, C.; Yibing Gao,; Steve C. F. Au-Yeung,; Chi Wu, *Macromolecules* **1999**, *32*, 3674–3677.

[42] Vihola, H.; Laukkanen, A.; Valtola, L.; Tenhu, H.; Hirvonen, J. *Biomaterials* **2005**, *26*, 3055–3064.

[43] Imaz, A.; Forcada, J. *Journal of Polymer Science Part A: Polymer Chemistry* **2010**, *48*, 1173–1181.

[44] Daly, E.; Saunders, B. R. *Langmuir* **2000**, *16*, 5546–5552.

[45] Quesada-Pérez, M.; Ahualli, S. A.; Martín-Molina, A. *The Journal of chemical physics* **2014**, *141*, 124903.

[46] Rumyantsev, A. M.; Rudov, A. A.; Potemkin, I. I. *The Journal of Chemical Physics* **2015**, *142*, 171105–5.

[47] Belloni, L. *Colloids and Surfaces A: Physicochemical and Engineering Aspects* **1998**, *140*, 227–243.

[48] Denton, A. R. *Physical Review E* **2003**, *67*, 011804–10. *Erratum–ibid* **2003**, *68*.

[49] Moncho-Jordá, A.; Anta, J. A.; Callejas-Fernández, J. *The Journal of chemical physics* **2013**, *138*, 134902.

[50] Moncho-Jordá, A.; Adroher-Benítez, I. *Soft Matter* **2014**, *10*, 5810–5823.

[51] Rumyantsev, A. M.; Santer, S.; Kramarenko, E. Y. *Macromolecules* **2014**, *47*, 5388–

5399.

[52] Pérez-Fuentes, L.; Drummond, C.; Faraudo, J.; Bastos-González, D. *Soft Matter* **2015**, *11*, 5077–5086.